Characterisation of exoplanet atmospheres using high-resolution spectroscopy

Lennart van Sluijs
University of Oxford
Brasenose College

A thesis submitted for the degree of
Doctor of Philosophy in Astrophysics

Michaelmas 2023

Statement of Originality

I carried out the work in this thesis at the Department of Physics, University of Oxford between January 2021 and September 2023 under the supervision of Prof. Jayne Birkby. The first year of the work from October 2019 to December 2020 was carried out at the Anton Pannekoek Instituut at the University of Amsterdam.

I declare that no part of this thesis has been submitted in support of another degree, diploma, or other qualification at the University of Oxford or any other university. Except where otherwise stated, the work in this thesis is all mine. At the start of each chapter, I explicitly state contributions from collaborators and if parts of the text and figures are based on already published first-authored peer-reviewed articles.

No quotation from this thesis may be published without prior consent or acknowledgment of its author.

Acknowledgements

"There is an art to the business of making sandwiches which it is given to few ever to find the time to explore in depth. It is a simple task, but the opportunities for satisfaction are many and profound. "
-Douglas Adams, Mostly Harmless
from the Hitchhiker's Guide to the Galaxy series

Admittedly, at times during my DPhil I have been tempted to become a simple sandwich maker on another planet, like Arthur Dent in the Hitchhiker's Guide to the Galaxy series; perhaps an urge some fellow students can relate to? Although, jokes aside, at most times I have felt incredibly grateful to be able to work on my passion which is the exploration of our universe. Most importantly, I am thankful to have been surrounded by a group of amazing and supportive people, which have filled my DPhil with unforgettable memories and joyful moments.

A DPhil student is lost without good supervision, so I will start with you, Jayne. Thank you for being a fantastic supervisor. I enjoyed our meetings and always felt encouraged after our science discussions. Anytime I could use help, for example, to submit a job application, conference abstract, or write a paper, you have always been there. You have been so helpful and patient during my numerous climbing injuries. I am glad I took the opportunity to join you in Oxford.

Great collaborators have been essential to the success and enjoyment of my research projects. Vivien, thanks for inviting me to your research group retreat in Nice, I especially enjoyed our whiteboard sessions. Josh, thanks so much for your help understanding the complexities of modelling exoplanet atmospheres. Hayley, thanks for making me understand the complexities of 3D Global Circulation Models. Emily, thanks for offering me a PostDoc position in your group. Matteo, I learned so much about high-resolution spectroscopy from our discussion during the High Res Meetings. Suzanne and Ernst, thank you for making time to be on my board of examiners.

Funding and facilities are essential to conduct research and travel to share science results. My research was funded as part of the exoZoo project that has received funding from the European Research Council (ERC) under the European

Union's Horizon 2020 research and innovation program under grant agreement No 805445. The MEASURE observations were obtained at the MMT Observatory, a joint facility of the Smithsonian Institution and the University of Arizona.

Although I have only spent a few months there, I am glad I have been part of the close community at the Anton Pannekoek Institute. Ben and Eleanor, thanks for all your exozoo support. I enjoyed our walks around the science park at the University of Amsterdam and our coffees in Oxford. Difeng, you have been a bright light during a difficult time for me. I am so happy we got to spend a large part of COVID-19 together in my flat in Amsterdam. The memories we made together are special to me. Dion thanks for the nice chats, your well-written master thesis has been a huge help getting started for me. Niloo, Annelotte, Bob, Kevin, Olivier, Anwesh, and Swapnil thanks for all the nice chats at API and the fun freshers' weekend in Drenthe. Lucas and Susan, thank you for your help in the transition from Amsterdam to Oxford.

The Oxford Astrophysics Department became my new community, and I have been fortunate to meet and befriend many new people. Ashling, thanks for giving me a warm welcome in the Oxford Astrophysics department. Jake, you are a super caring friend, always cheering me up when things are tough. Also thanks for being the energy in the room at all of the Oxoplanet discussion meetings, they made them a lot of fun. Your help and advice on career-related stuff has also meant a lot to me. Sophia thanks for all the laughs, the paper cat, and the walks in University Park during COVID-19 when I had just moved to Oxford. Colette, Luke, and Mitch thanks for the fun chats during our group meetings. Chloe, thanks for introducing me to 'Spoons'. I especially enjoyed our night out at UKExom in Edinburgh. Tobias, thanks for the company during many lunches, I hope we get to share another Cafe Creme sandwich sometime, and I will never forget your stellar Swiss-German karaoke performance. Annabella, Jakob, Tobias, and Joe, thanks for the fun birthday celebrations in the office, the Balliol and Lincoln lunches, and our nights out. Joost, thank you for inviting me to come to Oxford and letting me stay at your place. I also really appreciate your help on research-related projects, such as my ESO proposal, and your help with opacity tables. I have fond memories of our day cycling to Blenheim Palace and an unforgettable karaoke night in Nottingham. Jingxuan, thanks for bearing with me, while 'accidentally' climbing up the steepest side of Arthur's Seat in Edinburgh. Mark, Hamish, Alex, and Thea thanks for the various fun nights out, dinners, and discussions at the Oxoplanets journal club.

The summer of 2022 was particularly eventful for me. One of the highlights climbing up a desert formation and the helicopter ride that followed. Chris, thanks for catching my fall from Castleton Tower, I could not have wished for a better friend to be there when I broke my heel. Our trips to Scotland, Utah, California, and Washington state were awesome adventures. Piotrek, I enjoyed our occasional catch-up lunches, your visit to the Netherlands, and our punting sessions. Emma, thank you for your kindness and support, I especially enjoyed our holiday in France and Italy. All three of you, I will never forget our Wolfson College ball night out. Maddi you are such a sweet, kind, and loving person, I am glad we got to spend time together in Oxford and Berkeley that summer.

It has been a great pleasure to experience the Brasenose College community and many formal dinners. Sunny and Luna, I had a blast at our dinners and brunches together. I am really glad you were my first flatmates here in Oxford. Damayanti, it was short, but lovely having you as my flatmate. Robert, I had a great time rowing together for the Brasenose M2 team. Josh, I got such fun memories from our Toxic performance at the Brasenose Ball, and thanks for the nice coffee catch-ups. Brasenose Porters, I appreciate your help, especially getting around Oxford during the times when I was walking with crutches. Arthur, thanks for everything, especially the charming getaway holiday in Spain and our club nights in Printworks.

One of the things I greatly enjoyed was learning rock climbing in the UK; indoors in Brookes and outdoors with the Oxford Mountaineering Club. Jannik, thanks for teaching me the ins and outs of lead climbing and the fun bouldering sessions in Iffley. Albert, thanks for always pushing me to climb harder. Adam thanks for the fun night out in London, your taste in music and food is excellent. Sasha thanks for the fun climbing weekends with the OUMC and my birthday night out in the Bullingdon. Cica, thanks for being my sweet belayer, I enjoyed our weekends on the south coast so much. Because of you, Dorset became my happy place. Martin, thanks for lending me your sailing gear and our fun gym sessions in Brookes. Alex and Lauren, thanks for the nice Astro climbing sessions.

Sometimes new people come into your life in unexpected ways. Jonathan, I am glad we got to stay in touch after meeting each other in Seattle. Peter and Jorge thank our fun drinks and times at the AAS conference, and our night out in Berlin after our Potsdam conference. Anthony, thanks for the super fun Easter weekend and for showing me around London. Baris, you have forever improved my salad choice at Taylors and I enjoyed our lunches in the University Park together.

Leo, Carlos, Tobias, Ed, and Magnus, thanks for all the nice casual chats in the kitchen, it's been nice sharing a flat and coming home to a laid-back and relaxing atmosphere.

My occasional return trips to the Netherlands were a great way to reconnect with my friends back home. John, I am glad we managed to stay in touch despite my moving abroad. Thanks for coming to visit Oxford, and the fun times at Landjuweel. Nikky, Maurice, and Aron thanks for coming to visit me in Oxford and for the fun weekend of rock climbing. I appreciate I have always been welcome to come over and stay in Amsterdam at your place. Mike and Nina, thanks for the dinners, It is always nice to see you again back home and to catch up. Linde, I loved our sporadic, but sweet phone calls. Kasper and Sonja, it was fun to have you visit and to show you around Brasenose College. Jeroen, we go back to primary school and I am glad to still catch up from time to time.

Last but not least, I want to thank my family. Mom and Dad, thanks for your unconditional support, even though I moved even further away from home. Tessa and Lisa, you are most important to me. Rene and Sander, it is always nice to have a chat with you and I had fun trying new things with you both, from surfing to bird watching. Stern, welcome to the family, you already bring me so much joy. Ria and Frits, your postcards are so lovely and kept me connected to life back home.

It is impossible to name everyone, so if I missed you, please forgive my chaotic memory. I am super grateful for the past four years and excited to continue the exploration of exoplanet atmospheres at the University of Michigan.

Abstract

The characterisation of exoplanet atmospheres is crucial to understanding planet formation, the exploration of extreme atmospheric physics, finding habitable worlds, and searching for extraterrestrial life, but challenged by the overwhelming star-to-exoplanet flux contrast. High-resolution cross-correlation spectroscopy (HRCCS) overcomes this challenge by resolving individual exoplanetary spectral lines and disentangling them from the stellar and telluric lines using their difference in Doppler shift. In this thesis, I demonstrate how HRCCS can constrain the chemistry and dynamics of a range of exoplanet atmospheres. I developed a data reduction pipeline for the MMT Exoplanet Atmosphere Survey to detect carbon monoxide emission lines in the atmosphere of WASP-33 b, the first time in an exoplanet atmosphere. This provides unambiguous evidence of a thermal inversion in its atmosphere. These results are a proof of concept that the ARIES/MMT combination can be used to study exoplanet atmospheres even at R=15,000 and I further investigate the data quality limitations of this survey on the warm sub-Saturn HD 46375 A b. Recently, cross-correlation-to-log-likelihood (CC-to-log(L)) mappings suitable for HRCCS of exoplanet atmospheres emerged which constrain atmospheric abundances and the P-T profile. I use these mappings to constrain the water abundance of τ Böo A b and further constrain the chemistry and P-T structure WASP-33 b. I contributed a new method to use the scale parameter of a CC-to-log(L) mapping with a 3D global circulation model (GCM) to show it is consistent with an eastward hot spot offset in WASP-33 b. This demonstrates that HRS is capable of constraining atmospheric dynamics, even at a spectral resolution of R=15,000. I further compare 1D and 3D simulated datasets to investigate the climate of WASP-18 A b. These models produce very different synthetic spectra, highlighting the need to better understand the physics that needs to be included in realistic simulations of ultra hot Jupiters. In conclusion, these results show the power of 3D GCMs and CC-to-log(L) mappings combined with HRCCS to constrain exoplanet atmospheres.

"Not just beautiful, though–the stars are like the trees in the forest, alive and breathing. And they're watching me."

-Haruki Murakami, Kafka on the Shore

Contents

List of Figures

List of Tables

1
Introduction

The material in this chapter is partly based on the introduction from van Sluijs et al. (2023) and sometimes I have used parts of this work with minor or no changes to the original text to remain concise and preserve the clarity of the underlying message.

"There are infinite worlds both like and unlike this world of ours ...
We must believe that in all worlds there are living creatures and plants
and others things we see in this world ."

-Epicurus, 300 BC

1.1 The discovery of other worlds

Ever since humankind has gazed at the stars, our place in the universe has been one of the greatest mysteries. Scientific advancements of the past century have revealed a vast universe with billions of stars. Many presumed even more numerous faraway worlds orbiting around them. This evokes big questions such as: How do planets form? How common are other planets like Earth? Are some of them habitable? And, do other lifeforms exist on them?

Scientific answers to these questions about *exoplanets*, planetary bodies orbiting other stars than our own Sun, have only just started forthcoming over three decades ago. Since the surprising discovery of exoplanets around the pulsar PSR B1257+12 (Wolszczan & Frail, 1992), new detections have kept exceeding our imagination. Notable discoveries are the detection of a Jupiter-sized companion orbiting extremely close around the Sun-like star 51 Pegasi (Mayor & Queloz, 1995), the tightly packed TRAPPIST-1 ultracool dwarf system at only $\sim$11 pc with seven (super) Earth-sized planets, among which three inhabit the habitable zone (Gillon et al., 2017), and the detection of at least one Earth-sized planet around our closest neighbouring star Proxima Centauri (Anglada-Escudé et al., 2016; Suárez Mascareño et al., 2020).

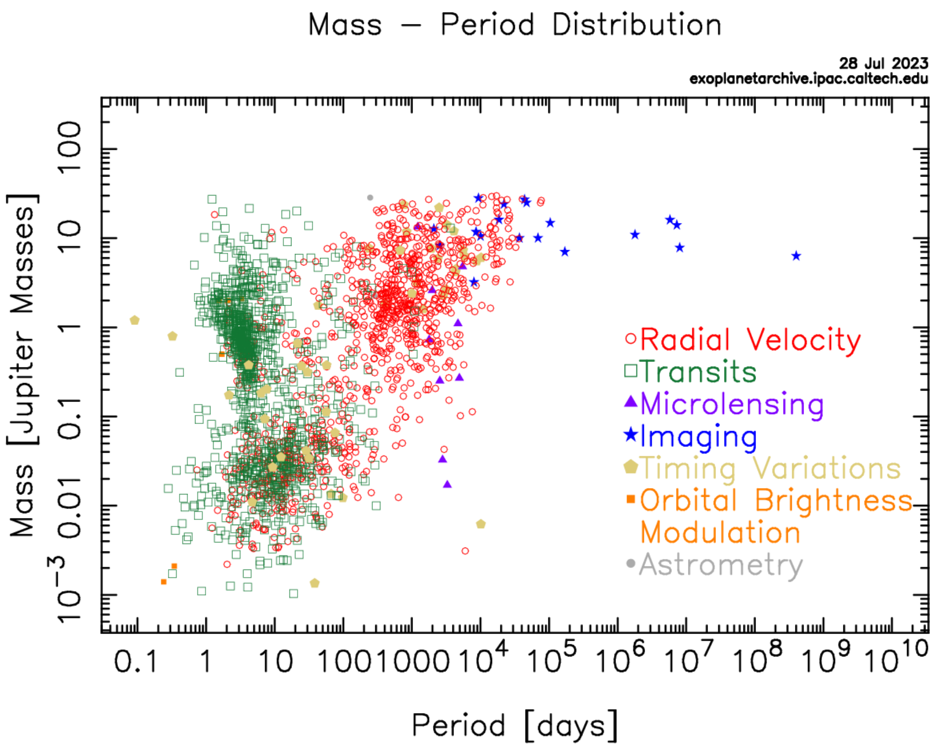

Figure 1.1: Mass as a function of orbital period of all confirmed exoplanets as of 28 July 2023. The colours indicate the discovery method. Most exoplanets have been discovered using the transit method and radial velocity method. Source: `https://exoplanets.nasa.gov/`

In order to detect these faraway worlds, specialized instruments collecting high-quality observations have been built and new data reduction and analysis techniques have been developed. An overview of confirmed exoplanets to date and their discovery methods are shown in Fig 1.1 (for a general review on all detection methods see Fischer et al., 2014). Although some exoplanets have been directly imaged, the majority have been discovered by means of indirect methods. By far the two most successful discovery methods are the *transit method* and *radial velocity method*.

The transit method measures a reduction of the total stellar flux as the exoplanet periodically orbits in front of its star as seen from the Earth, thus blocking part of the light from the stellar surface (for a general review see Deeg & Alonso, 2018). This is similar to how the Moon blocks part of the Sun during a lunar eclipse. Ground-based transit surveys are e.g.: TrES (Alonso et al., 2004), XO (McCullough et al., 2005), SuperWASP (Pollacco et al., 2006; Butters et al., 2010), KELT (Pepper et al., 2008), HATNet (Bakos et al., 2007), MASCARA (Talens et al., 2017) and NGTS (Wheatley et al., 2018). Notable space missions are Kepler (Borucki et al., 2010), CoRoT (Barge et al., 2008) and recently TESS (Ricker et al., 2014).

The radial velocity method detects the wobble of the host star around the exoplanetary system center of mass by measuring the blueshift or redshift of spectral stellar lines (for a recent review see Hara & Ford, 2023). This requires an ultra-stable high spectral resolution spectrograph with wide instantaneous wavelength coverage, e.g. echelle spectrographs. An echelle spectrograph consists of two key optical elements: the echelle grating which disperses the light into high spectral orders to enable a high spectral resolution and a cross-disperser which orthogonally separates overlapping spectral orders to ensure the spectral orders are well separated on the detector. In the (near-)infrared these optical elements require cooling by a cryostat to avoid thermal background. Due to the size of such instruments, e.g. they are all ground-based. A selection of notable instruments are HIRES (Vogt et al., 1994), HARPS (Mayor et al., 2003), CORALIE (Queloz et al., 2000), HARPS-N (Cosentino et al., 2012), HAMILTON (Vogt, 1987) and ESPRESSO (Pepe et al., 2010). The latter is pushing the frontier of the radial velocity method with a sensitivity <10 cm/s, which is required for the detection of Earth-sized exoplanets. This led to the groundbreaking confirmation of Proxima Centauri b (Suárez Mascareño et al., 2020), an Earth-mass exoplanet in the potentially habitable zone orbiting our nearest neighbouring star.

These detection methods have revealed an enormously diverse set of exoplanetary worlds and architectures vastly different from our solar system (e.g. see Fulton et al., 2017; Van Eylen et al., 2018), colloquially referred to as the *exozoo*. There are Jupiter-sized planets orbiting very close to their host stars receiving extreme levels of stellar radiation: the hot Jupiters (HJs). There are also small rocky worlds very close to their host star, often referred to as lava worlds, because they might have a molten surface (e.g. see Barnes et al., 2010; Crossfield et al., 2022; Zieba et al., 2022). From populations studies we now know the most common types of exoplanets are so-called super-Earths and mini-Neptunes (Fulton et al., 2017), exoplanets with masses in between the Earth and Neptune, for which no analogue exists in our own solar system.

To understand the diversity of the exozoo, the field of exoplanets is rapidly evolving away from merely detecting new systems. This is both on a *single system level* towards detailed characterization of the nearest exoplanets and on a *demographic level* towards understanding their formation and evolution processes.

A key area of research covering both levels is the study of their atmospheres. On an individual level, this provides a detailed understanding of their climate and atmospheric composition, both of which are key to test the physics and chemistry in our atmospheric models, evaluating their habitability and assessing their capacity to host extraterrestrial life. On a demographic level, the atmospheric composition holds clues on universal planet formation and evolution pathways and how climate and composition depend on exoplanet size, stellar irradiation environment and system architecture.

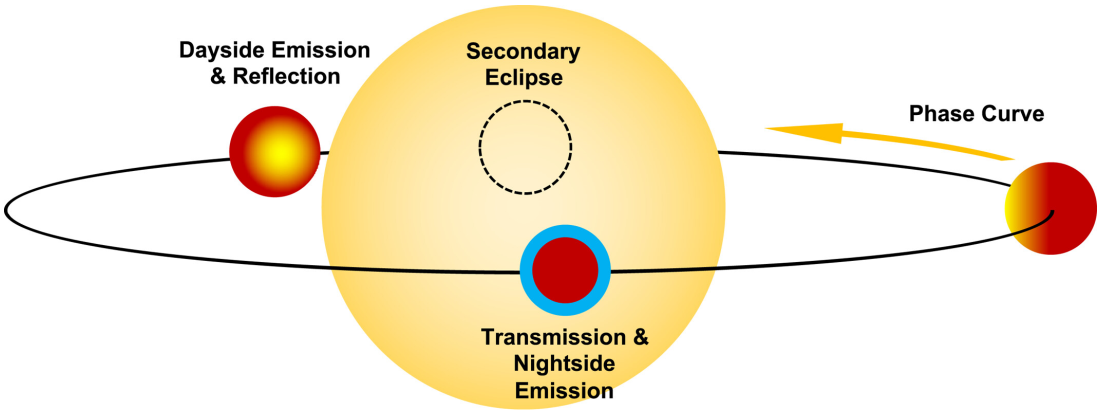

Figure 1.2: Methods to detect a short period exoplanet's atmosphere. First, the light transmitted through the atmosphere can be detected during transit. Second, the reflected/emitted light that disappears during a secondary eclipse can be detected. Lastly, the reflected/emitted light can be detected during the orbit, resulting in a phase curve of the exoplanet. Figure from Gao et al. (2021).

In the rest of this chapter, I will provide the reader with a rudimentary background of previous research required to understand the goal of this thesis, which is to demonstrate the power of Bayesian frameworks combined with HRS to constrain both the chemistry and the dynamics of exoplanet atmospheres. In order to understand the motivations behind this goal I will start by giving a brief overview of general methods used to characterise exoplanet atmospheres in Section 1.2. In my research, I specifically use the high-resolution spectroscopy (HRS) method and I discuss this in more detail in Section 1.3, where I will also introduce how Bayesian frameworks are reshaping HRS methods. I discuss pioneering efforts on constraining chemistry and dynamics within the context of exoplanet atmosphere demographics in Section 1.4. I conclude with an outline my thesis chapters in Section 1.5.

1.2 Characterising exoplanet atmospheres

Detecting an exoplanet's atmosphere is extremely challenging. This is due to the close angular separation (separations of $< 0.005''$ or 0.05 au; Birkby (2018)) and the large contrast ratio between the flux of the star and exoplanet. As seen from our closest neighbouring star, the Earth and Sun are at an angular separation $<1''$ at a contrast ratio of $\sim 10^{-10}$ (at NIR wavelengths). Opportunely, the discovery of HJs, which have a much more favourable contrast ratio of $10^{-3} - 10^{-4}$ (again at NIR wavelengths), has enabled characterisation of exoplanet atmospheres with current observing facilities.

There are three ways to detect a short orbital period exoplanet's atmosphere that overcome the challenging contrast ratio (see Fig. 1.2). First, it is possible to detect the stellar light transmitted through the atmosphere as the exoplanet transits in front of its host star. Absorption by species present in the upper atmospheric layers can create detectable spectral

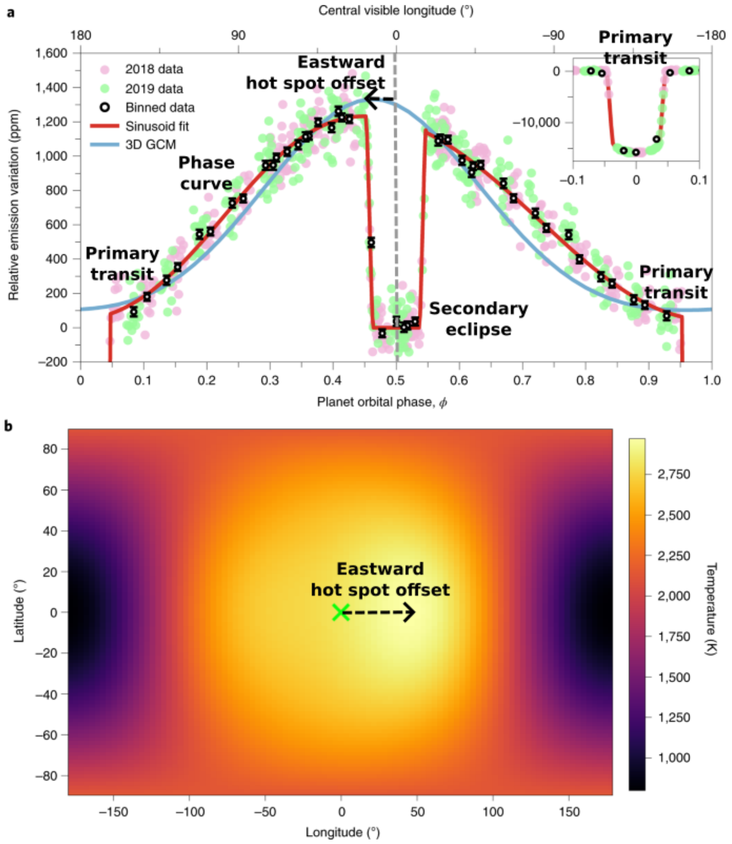

Figure 1.3: WASP-121 b as an example of information that can be obtained from broadband photometry. *Top panel:* two observing runs of WASP-121 b with HST/WFC3. The primary transit, secondary eclipse and phase curve are all clearly visible and indicated. A sinusoidal fit to the phase curve and a prediction from a 3D global circulation model are shown. An offset between the maximum of the phase curve and the half-phase is observed. *Bottom panel:* a 2D spatial temperature map of WASP-121 b constructed from the 1D phase curve. The offset of the maximum in the phase curve is interpreted as a shift of the hottest region of WASP-121 b away from the substellar point: an eastward hot spot offset. Adapted figure from Mikal-Evans et al. (2022).

signatures. This is done by comparing the transit depth difference between in-transit and out-of-transit. Second, one can detect the secondary eclipse, when the emitted light of the exoplanet's atmosphere disappears as it is occulted by the stellar disk. Third, the change in flux as the exoplanet orbits its host star can be observed. These changes are due to seeing more or less of the hotter dayside compared to the cooler nightside. An example of a broadband phase curve observation is shown for the exoplanet WASP-121 b in Fig. 1.3.

The earliest successful technique was transmission spectroscopy demonstrated by the detection of sodium in the atmosphere of HD 209458 b with HST/STIS (Charbonneau et al., 2002). Just a few years later, a secondary eclipse was used to detect thermal emission from the exoplanet Tres-1 b with Spitzer (Charbonneau et al., 2005). Phase curves are challenged by successful removal of systematics, but have been observed for a handful of HJs (e.g. Borucki et al., 2009; Stevenson et al., 2017; Von Essen et al., 2020; May et al., 2021, 2022; Mikal-Evans et al., 2022). All three methods have booked many successes since, with the

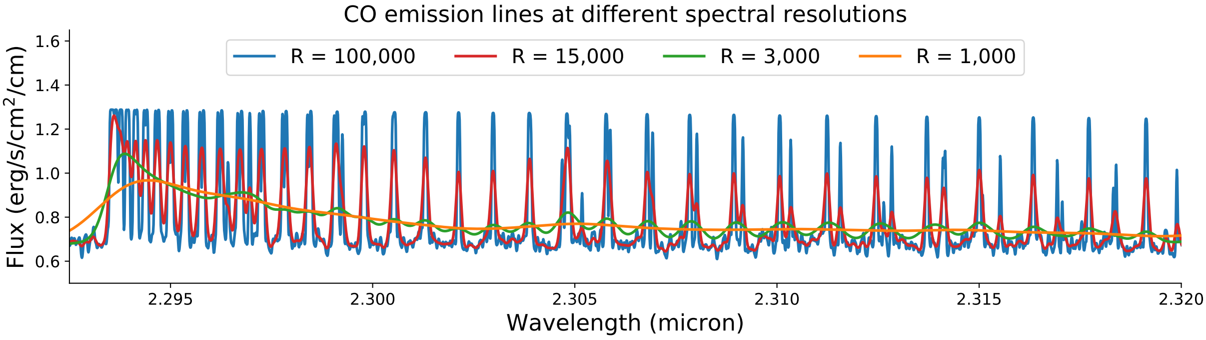

Figure 1.4: CO emission lines at different spectral resolutions. Using HRS (R=100,000) individual lines are resolved, but using LRS (R=3,000) individual lines blend into a broad spectral feature.

key facilities being Kepler, TESS, HST/STIS and WFC3, Spitzer and recently JWST (e.g. see Kreidberg et al., 2018; Sing, 2018; Parmentier et al., 2018; Deming & Knutson, 2020; Radica et al., 2023; Taylor et al., 2023; Ahrer et al., 2023; Feinstein et al., 2023).

A disadvantage of the transit method and the secondary eclipse method is that they both require a rather favourable transiting system geometry. For most exoplanetary systems the stellar radius ($R_\star$) is much larger than the exoplanets radius (R_p), thus $R_\mathrm{p} \ll R_\star$. Under this assumption, the transit probability is given by $\sim R_\star/a$ with a the semi-major axis of the exoplanet's orbit. For a twin Earth-Sun system, this probability is just ~0.5%. Statistically it is expected the nearest habitable Earth-sized exoplanet around an M dwarf (these stars are more common than solar-type stars) will be ~11 pc away (Dressing & Charbonneau, 2015). In light of this statistic, the discovery of the TRAPPIST-1 system at ~11 pc with as many as seven transiting exoplanets was extraordinary (Gillon et al., 2017). But, the nearest non-transiting Earth-sized exoplanet will be an order of magnitude closer to us. The very closest being the detection of two exoplanet around Proxima Centauri (Anglada-Escudé et al., 2016; Suárez Mascareño et al., 2020). These nearby non-transiting exoplanets highlights the importance of a technique that can also characterise non-transiting, short-period exoplanets.

1.3 High-resolution cross-correlation spectroscopy

1.3.1 The method's principle

A very successful technique that does not necessarily require a transiting system is the HRS technique combined with the cross-correlation method, in short: *high-resolution cross-correlation spectroscopy (HRCCS)*. In contrast to transmission spectroscopy and the secondary eclipse method, the HRS method does not necessarily require a transiting system geometry. It allows a wider range of inclinations i, as long as the projected radial velocity is sufficiently large, thus the orientation should not be too close to face-on ($i = 0°$).

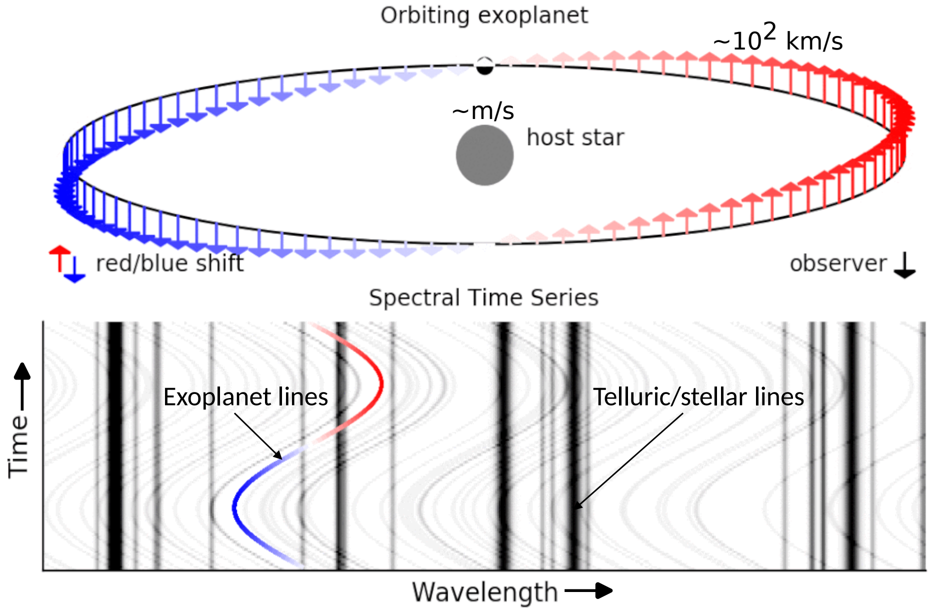

Figure 1.5: The HRCCS method. As the exoplanet orbits its host star, its orbital velocity induces a redshift or blueshift as indicated by the colour and length of the arrows in the top panel. This shifts the spectral lines of the exoplanetary spectrum with respect to the quasi-stationary stellar and telluric lines. The greater the exoplanetary acceleration, the easier it becomes to disentangle the telluric and stellar lines from the exoplanet signal.

At high spectral resolution[1], around $R = 100.000$, spectral lines in the exoplanet's atmosphere, stellar atmosphere, and the Earth's atmosphere (telluric lines) are resolved (see Fig. 1.4, but too faint to detect due to the overwhelming star-to-planet contrast ratio. Each observation of the system contains a combined spectrum of pre-dominantly stellar and telluric lines, with the exoplanetary spectral lines buried within the noise. Therefore, direct fitting of the exoplanetary lines is not possible yet in an individual spectrum.

However, as the planet orbits its host star its orbital velocity will introduce a distinct Doppler shift, which can be used to disentangle the exoplanet lines from the quasi-stationary stellar and telluric lines (see Fig. 1.5). Typical orbital velocities for HJs are ~100 km/s. For the Earth orbiting around the Sun, this is ~30 km/s. The quasi-stationary stellar lines are moving much slower at ~m/s due to the star's motion around the system's center of mass. This order of magnitude difference in radial velocity is the principle behind the HRS method: by removing the quasi-stationary stellar and telluric components, the faint exoplanetary signal remains.

Even if the quasi-stationary components are removed completely, the majority of exoplanetary lines have a very low signal-to-noise ratio[2] (SNR) with a $\mathrm{SNR}_{\mathrm{line}} \leq 1$. This is where the cross-correlation method comes to the rescue. When cross-correlating the residual

[1]With spectral resolution defined as $R \equiv \lambda/\Delta\lambda$ with λ the wavelength and $\Delta\lambda$ the smallest wavelength spacing at which the spectrograph operates.

[2]With the notable exception of some broad and strong spectral lines: Hα, Hβ, Hγ, He II, Ca II and Na I (e.g. Jensen et al., 2018; Seidel et al., 2019; Zhang et al., 2023)

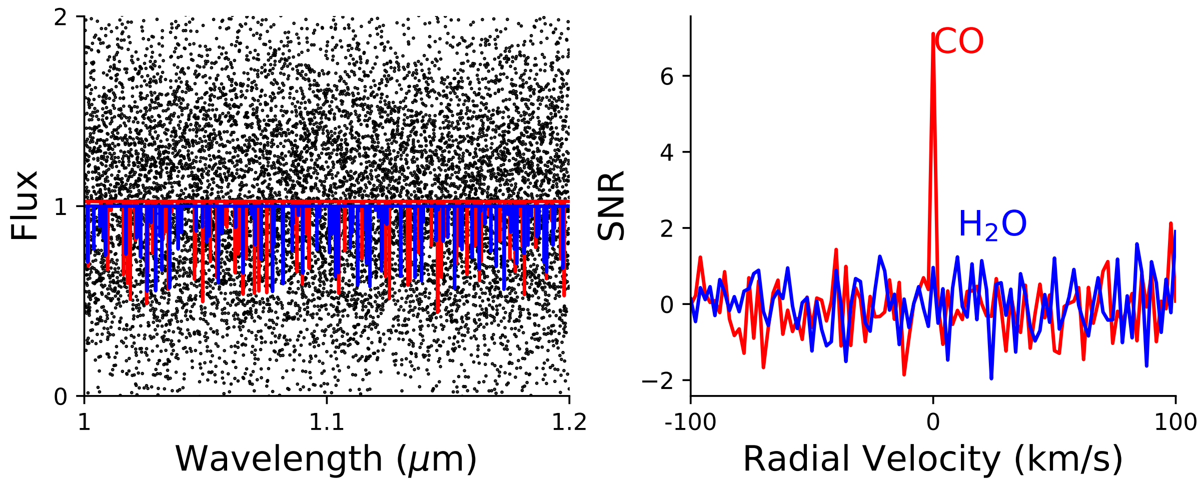

Figure 1.6: *Left panel:* Mock cross-correlation templates for CO (red) and H_2O (blue). The black scatter is an observed mock spectrum for CO after the quasi-stationary components have been removed. Individual exoplanetary lines are buried within the noise with a $SNR_{line} \leq 1$. *Right panel:* SNRs after cross-correlation with a carbon monoxide (CO) and water (H_2O) template. Cross-correlation reveals CO is present at the rest frame velocity, at a SNR=6.6, but H_2O is not detected.

spectra with a synthetic model template of the exoplanet's expected spectrum it essentially combines the signal of all faint spectral lines such that the total SNR of the detection SNR>1 (see Fig. 1.6).

In real data, auto-correlation of the cross-correlation template with itself and incomplete removal of the systematics often cause spurious signals. Therefore, as a sanity check, cross-correlation is done in different trial rest frames. If the signal originates from the real exoplanet, it should peak at the known system velocity v_{sys} and the exoplanet's Keplerian velocity K_p. An example of a real detection is shown in Fig. 1.7.

Another advantage of resolving individual spectral lines is that HRS is sensitive to the spectral line shape, relative line depth, and line position. This means it is uniquely sensitive to distinguish between different molecules present in the exoplanet's atmosphere. Since HRS is sensitive to the unique spectral signature, detections using HRS are often more robust than detections using low-resolution spectroscopy (LRS). This is because it is hard to distinguish different opacity sources due to their broad spectral bands using LRS and systematics have a large impact. An example is the variation of intrapixel sensitivity for the Spitzer telescope, which has proven notoriously hard to correct (e.g. Kilpatrick et al., 2017). Furthermore, winds, rotation, clouds, pressure-temperature structure (P-T structure), and chemical abundances all affect these three spectral line properties. Therefore, the HRS method is sensitive to both the *chemistry* and *dynamics* of an exoplanet atmosphere.

I will discuss the technical aspects of the HRCCS method and template modelling in more detail in the next chapter. First, I present a brief overview of previous work using

Exoplanet	First-time species was detected with HRS
WASP-76 b	Na I (Seidel et al., 2019), Fe I (Ehrenreich et al., 2020), Li I, Mg I, Ca II, Mn I, K I, H I (Tabernero et al., 2021), V I, Cr I, Ni I, Sr II, Co I (Kesseli et al., 2022), H_2O, HCN (Sánchez-López et al., 2022), Ba II (Azevedo Silva et al., 2022), CO (Yan et al., 2023), VO, Ca I, O I, Fe II (Pelletier et al., 2023)
MASCARA-2 b/KELT-20 b	Na I, H I (Casasayas-Barris et al., 2018), Ca II, Fe II (Casasayas-Barris et al., 2019), Fe I (Stangret et al., 2020), Si I (Cont et al., 2022a), Cr I (Borsa et al., 2022), Ni I (Kasper et al., 2023). Mg I, Cr I, Mn I, Ca I (Gandhi et al., 2023)
WASP-121 b	Fe I (Gibson et al., 2020), H I (Cabot et al., 2020), Cr I, V I, Fe II (Ben-Yami et al., 2020), Mg I, Ca I, Ni I, V I (Hoeijmakers et al., 2020a), K I, Li I, Ca II (Borsa et al., 2021b), Sc II (Merritt et al., 2021), Co I, Sr II, Ba II (Azevedo Silva et al., 2022)
WASP-18 A b	H_2O, CO, OH (Brogi et al., 2022)
HAT-P-70 b	Ca II, Cr I, Cr II, Fe I, Fe II, H I, Mg I, Na I, V I (Bello-Arufe et al., 2022) Ca I, Mn (Gandhi et al., 2023)
WASP-189 b	Fe I (Yan et al., 2020), TiO, Fe II, Ti I, Ti II, Cr I, Mg I, V I, Mn I (Prinoth et al., 2022), CO (Yan et al., 2022), Ca I. Ni I (Gandhi et al., 2023)
WASP-33 b	TiO (Nugroho et al., 2017), Ca II (Yan et al., 2019), Fe I (Nugroho et al., 2020b), H I (Yan et al., 2021), OH (Nugroho et al., 2021), Si I (Cont et al., 2022a), Ti I, V I (Cont et al., 2022b), CO (van Sluijs et al., 2023, presented in chapter 3 of this thesis)
KELT-9 b	H I (Yan & Henning, 2018), Fe I, Fe II, Ti II (Hoeijmakers et al., 2018a), Mg I (Cauley et al., 2019), Na I, Cr II, Sc II, Y II, (Hoeijmakers et al., 2019), Ca II (Turner et al., 2020), O I (Borsa et al., 2021a), Si I (Ridden-Harper et al., 2023), Ca I, V I, Ri I, Cr I, Ni I, Sr II, Ba II, Tb II (Borsato et al., 2023)
MASCARA-4 b	H I, Na I, Ca II, Mg I, Fe I, Fe II, Ca I, Cr I, Fe I, Fe II (Zhang et al., 2022a), Ni I, Mn I, V I, (Gandhi et al., 2023) Rb I, Sm I, Ti II, Ba II (Jiang et al., 2023)
MASCARA-1 b	H_2O, CO (Holmberg & Madhusudhan, 2022) Fe I, Cr I, Ti I (Scandariato et al., 2023)
TOI-1518 b	Fe I (Cabot et al., 2021)
WASP-12 b	H I, Na I (Jensen et al., 2018)

Table 1.1: An overview of all species detected in the atmospheres of UHJs using HRS. Only the first reports of detections are listed. Tentative detections (SNR<4) are omitted. This table is complete as of August 2023.

HRS to constrain the chemistry and dynamics of exoplanet atmospheres and how Bayesian frameworks are transforming the HRS methodology.

1.3.2 A brief overview of species detected using HRS

As of today, a total of 55 exoplanets have one or more confirmed detected species in their atmospheres using HRS[3]. For the most recent general review on HRS see Birkby (2018).

HRS is sensitive to different species depending on the wavelength region probed. The optical covers mostly atomic and ionic energy transitions, whereas the infrared covers the rotational-vibrational energy transitions of molecules.

[3]According to the ExoAtmospheres IAX community database, last checked August 2023: http://research.iac.es/proyecto/exoatmospheres/index.php

The first successful detections using HRCCS were in the near-infrared where the planet-to-star contrast ratio is more favourable. Snellen et al. (2010) were the first to successfully use HRCCS and detected a carbon monoxide signal in the atmosphere of the HJ HD 209458 b with CRIRES/VLT. CRIRES's initial success was followed by more detections: CO absorption lines were also found in τ Boötis b, HD 189733 b, β Pictoris b, 51 Peg b and HD 179949 b (e.g. Brogi et al., 2012; Rodler et al., 2012; de Kok et al., 2013, 2014a; Snellen et al., 2014). Additionally, water was detected in the atmospheres of HD 189733 b, GQ Lupi b, and 51 Peg b (e.g. Birkby et al., 2013; de Kok et al., 2014a; Schwarz et al., 2016; Brogi et al., 2016; Birkby et al., 2017). The first combined water and CO detection was found by Brogi et al. (2016). CRIRES was removed from the VLT in July 2014 and has only recently returned as CRIRES+ in October 2021 (Lavail et al., 2016). In the meantime CRIRES's success was followed by other near-infrared spectrographs: e.g. NIRSPEC (McLean et al., 1998), IGRINS (Park et al., 2014; Levine et al., 2018), GIANO (Piskorz et al., 2017a), CARMENES (Quirrenbach et al., 2018), iSHELL (Rayner et al., 2016), SPIRou (Thibault et al., 2012) and IRD (Kotani et al., 2018). These have again detected CO (e.g. Rodler et al., 2013; Flagg et al., 2019), water vapour (Lockwood et al., 2014; Piskorz et al., 2017b; Guilluy et al., 2019; Sánchez-López et al., 2019; Buzard et al., 2020), OH (Nugroho et al., 2021; Brogi et al., 2022), HCN (Sánchez-López et al., 2022) and tentatively methane (Guilluy et al., 2019; Giacobbe et al., 2021).

Following the successful detections in the infrared, in the optical wavelength region *Ultra Hot Jupiters* (UHJs), Jupiter-sized exoplanets with equilibrium temperatures $\geq$2000 K (adopting the definition by Parmentier et al. (2018)), have provided a unique opportunity to characterise the atoms and ions in their atmospheres. The population of UHJs is distinct from the population of cooler HJs as the atmospheres transitions from a (i) water-dominated towards a hydrogen-dominated atmosphere and (ii) from non-inverted P-T structures towards inverted ones (for recent reviews see Showman et al., 2020; Fortney et al., 2021). Notable optical high-resolution spectrographs are: HARPS (Mayor et al., 2003), HARPS-N (Cosentino et al., 2012), HDS (Noguchi et al., 2002), HIRES (Vogt et al., 1994), MAROON-X (Seifahrt et al., 2018), GRACES (Chene et al., 2014) and ESPRESSO (Pepe et al., 2010). At the temperatures of UHJs, molecules break down in their atomic counterparts and both volatile and refractory species are present in gaseous form. Previous studies have detected a wide range of metals either in their atomic and/or ionic form. An overview of all first detections of species in the atmospheres of UHJs using HRS is shown in Table 1.1. Recent studies do not merely detect these atomic and ionic species but can constrain their abundances ratios (e.g. Gandhi et al., 2023; Maguire et al., 2023; Ramkumar et al., 2023).

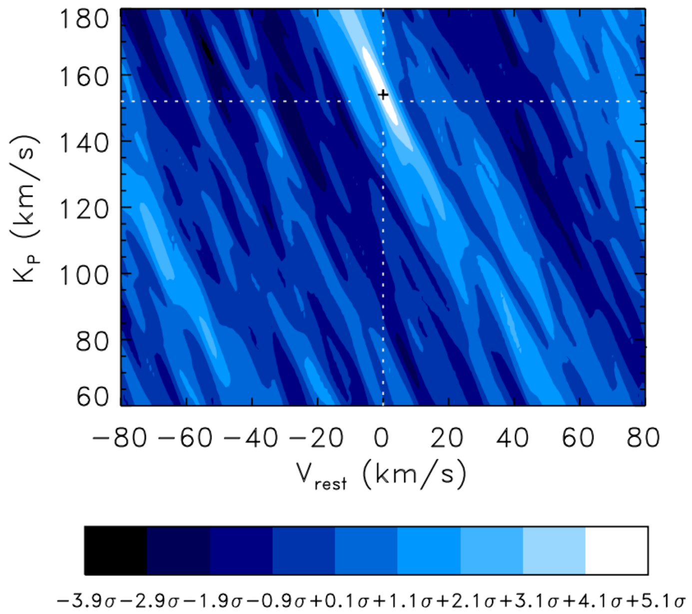

Figure 1.7: Example of a detection using HRCCS. The colours indicate the SNR value after cross-correlating data of the HJ HD 189733 b with a water vapour template. SNR values are shown for each combination of the system velocity (here: $v_{\rm rest}$) and Keplerian velocity ($K_{\rm p}$). The expected velocity offset is indicated by the white dashed cross. The maximum SNR value is indicated by the black plus symbol. Although spurious signals exist at other velocity offsets, the strongest signal aligns well with the expected velocity offset. Therefore, this is a detection of water at $\sim 5\sigma$. Figure adapted from Birkby (2018).

Similar attempts to characterize smaller worlds such as the bloated super Neptune WASP-127 b found a non-detection of sodium (Seidel et al., 2020b). Zhang et al. (2023) successfully detected the resolved helium spectral line in the atmosphere of four young mini-Neptunes. These are important steps to understand the most common type of exoplanets and are pushing the limits towards the goal of ultimately characterising Earth-sized exoplanets with the next generation of extremely large telescopes.

1.3.3 Dynamics of exoplanet atmospheres using HRS

Winds in exoplanet atmospheres move a gas parcel towards or away from us, adding an extra component to the observed radial velocity. Day-to-nightside winds (U)HJs are predicted to have speeds of ∼1-10 km/s (Tan & Komacek, 2019). Winds can affect both transmission spectra (e.g. see Wardenier et al., 2023; Beltz et al., 2023) and emission spectra (e.g. see Beltz et al., 2021; Pino et al., 2022; Brogi et al., 2022). For a handful of HJs, velocity offsets have been observed that are at least in part explained by winds (e.g. Snellen et al., 2010; Brogi et al., 2016; Wardenier et al., 2021; Beltz et al., 2021; Gandhi et al., 2022; Pino et al., 2022; Brogi et al., 2022). The left panel of Fig. 1.8 shows how different wind and rotation patterns induce a phase-dependant net system velocity offset from the exoplanet rest frame velocity and compares them to those observed in the high-resolution emission spectra of the UHJ KELT-9 b.

Faster rotation rates broaden the observed spectral lines (see right panel of Fig. 1.8. Measurement of the broadening, either by cross-correlating directly with a broadened template or indirectly from the width of the cross-correlation peak thus constraints the projected rotational velocity of the exoplanet. For HJs, such spin rates are expected to be similar to their

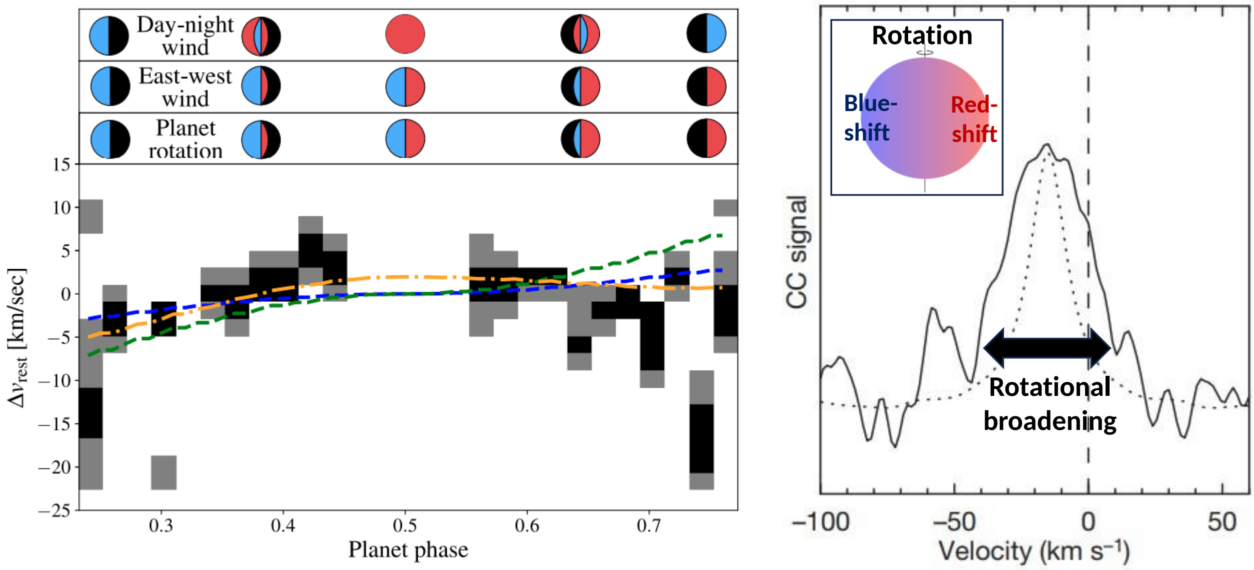

Figure 1.8: Effects of rotation and winds on high-resolution emission spectra. *Left panel:* The top three panels show toy models demonstrating which parts of the exoplanet disk are red- or blue-shifted due to a combination of wind and rotation as a function of orbital phase. Black regions correspond with the night side. The bottom panel shows the expected net offset from the exoplanet rest frame velocity for each of the three models: (i) pure rotation (blue dashed line) (ii) east-west winds of 10 km/s (green dashed line), and (iii) day-to-night wind of 5 km/s (orange dot-dashed line). This is compared to observed velocity offsets in high-resolution spectra of the UHJ KELT-9 b (black and gray are within 1σ and respectively 2σ of the best fit). Adapted from (Pino et al., 2022). *Right panel:* The effect of rotational broadening on the cross-correlation. *Right panel:* The small panel shows which parts of the exoplanet disk are blue-shifted and which parts are red-shifted due to its rotation. This broadens the spectral lines and hence the CCF. An observed example of this is for β Pictoris b, where the dashed line indicates the unbroadened CCF and the solid line is the observed profile. Figure adapted from (Snellen et al., 2014).

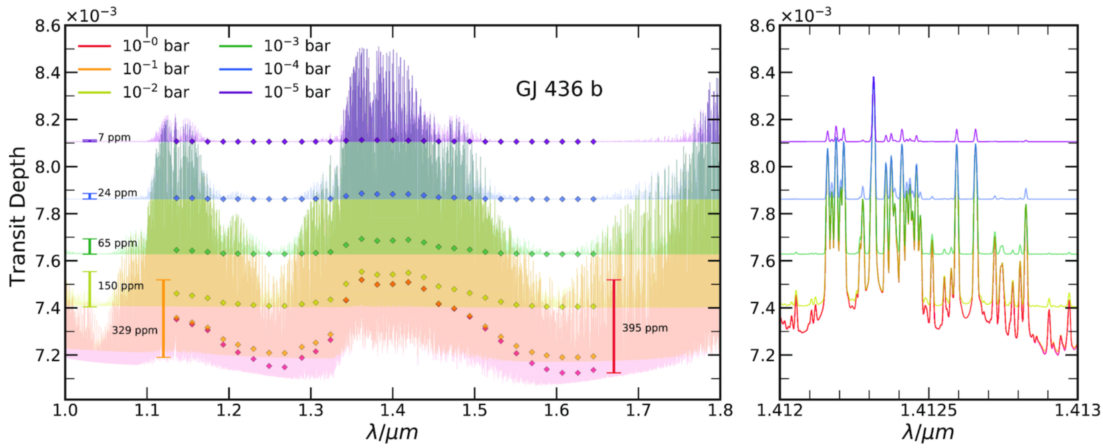

Figure 1.9: Example of a high-resolution transmission spectrum of the exoplanet GJ436 b. The colours indicate cloud decks at different pressure levels. At high-spectral resolution, spectral lines forming above the cloud deck are still resolved. At low-spectral resolution, the same spectral lines form broad or even flat features. The diamond markers in the left panel indicate the HST/WFC3 low-resolution transmission spectra. The right panel shows a zoomed version of the left panel around 1.4125 μm. Figure adapted from Gandhi et al. (2020).

orbital period due to efficient tidal synchronisation as a consequence of their proximity to their host star (Rasio et al., 1996; Showman & Guillot, 2002). For longer-period exoplanets, tidal synchronisation is not as efficient and this enables the comparison of exoplanet spin rates to those predicted by exoplanet formation and evolution models. Snellen et al. (2014) was the first to constrain the spin of an exoplanet when they measured the projected rotational velocity of β Pictoris b at $\sim$25 km/s.

The P-T structure and cloud coverage also affect the spectral line strength. This is because the temperature difference between different probed atmospheric layers essentially sets the contrast between the line core and wings. Cloud formation at intermediate altitudes can block part of the deeper layers, resulting in shallower lines (see Fig. 1.9). This is another advantage of HRS, as the signal of shallower lines is muted at lower spectral resolutions (Gandhi et al., 2020).

Hot spots are a colloquial term referring to the hottest region of HJ atmospheres. Note sometimes the term hot spot also refers to the brightest point in the phase curve, which often coincides, but not necessarily, with the hottest region of the atmosphere. Standard hydrodynamical theory predicts a hot spot offset eastward of the substellar point in UHJs, due to the formation of a strong eastward jet that redistributes heat from the dayside to the nightside (e.g. Showman et al., 2008; Komacek & Showman, 2016; Komacek et al., 2017; Hammond & Lewis, 2021). Evidence for hot spot offsets has been observed (an example was earlier shown for the UHJ WASP-121 b in Fig. 1.3) at a low spectral resolution which is sensitive to absolute flux variation as a function of orbital phase but remains challenging due to systematic effects (e.g. see Zhang et al., 2018; Bell et al., 2021a). Recently some HRS studies suggest the strength of the spectral lines is sensitive to hot spots as well (Herman et al., 2022; Hoeijmakers et al., 2022; Pino et al., 2022; van Sluijs et al., 2023)[4]

1.3.4 Bayesian frameworks

Although cross-correlation has been extremely successful in the detection of species present in exoplanet atmospheres, it is not immediately clear how to link the SNR value of a detection to constraints on the P-T structure and chemical abundances. To solve this problem, *Bayesian frameworks*, structures to compare observed data to a model by using Bayesian statistics, or cross-correlation-to-log-likelihood (CC-to-log(L)) maps, have been developed to provide a statistical framework that can constrain model input parameters (e.g. chemical abundances, P-T structure, orbital phase offsets, Keplerian and system velocity) directly (Zucker & Mazeh, 1994; Brogi et al., 2017; Piskorz et al., 2017a; Gibson et al., 2020). Here I follow the same interpretation from a Bayesian framework as is the standard in the HRS community from Brogi & Line (2019). Brogi et al. (2017) also use these frameworks to naturally combine low- and high-resolution data. This helps to constrain the P-T profile at a wider pressure-range, since low- and high-resolution data probe different layers of the exoplanet's atmosphere (see Fig. 1.4). A technical overview of Bayesian frameworks will be presented in the next chapter.

Buzard et al. (2020) introduced yet another multi-epoch observing strategy based on Bayesian principles. Their data reduction technique directly models the stellar, exoplanet, and noise components simultaneously to correct for the non-random noise in the data set. A potential advantage of their method is that it covers the orbital phase more uniformly than traditional HRS observations. At the moment, a limited number of studies have tested their framework (Buzard et al., 2021b,c).

1.4 Demographics of exoplanet atmospheres

Studying exoplanet atmospheres at a population level, enabled by the steadily growing number of characterised targets, is important for two main reasons. First, studying how HJ atmospheric properties vary as a function of stellar irradiation and exoplanet mass can test our fundamental understanding of extreme atmospheric physics. Second, measurement of the atmospheric composition of a larger sample can expose universal planet formation and evolution pathways.

For close-in giant exoplanets, *Global Circulation Models (GCMs)* predict a transition of the dynamics and chemistry for different equilibrium temperatures (e.g. Perna et al., 2012; Komacek & Showman, 2016; Komacek et al., 2017; Parmentier et al., 2021; Showman et al.,

[4]Results from van Sluijs et al. (2023) on hot spot offsets are presented in chapter 5 of this thesis.

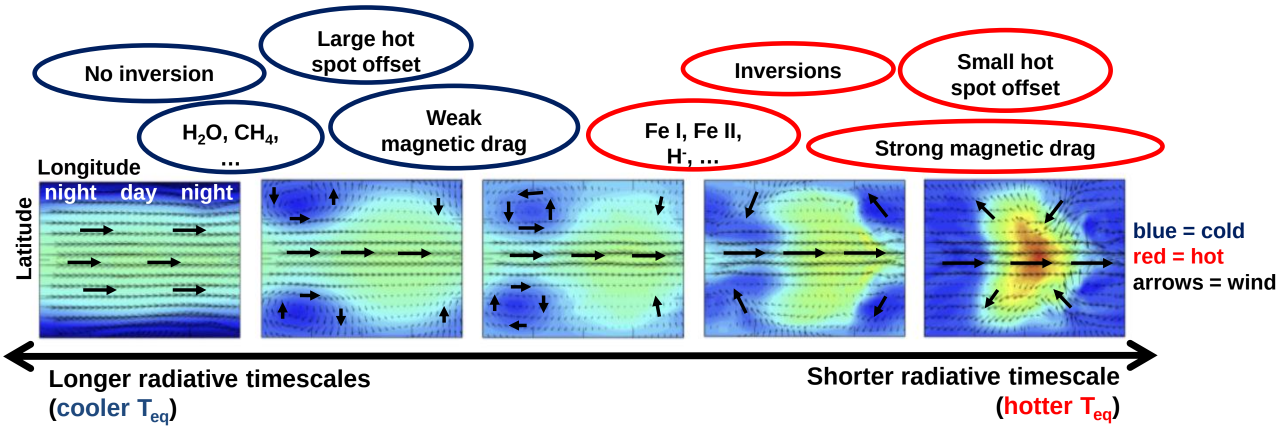

Figure 1.10: Qualitative prediction of the chemistry and dynamics of close-in gas giants from cool to hot. The five panels show spatial temperature maps (blue is cold and red is hot) and flow direction (arrows) of close-in gas giants based on GCMs. Panels from left to right follow decreasing radiative timescale (or increasing equilibrium temperature): 10^7, 10^6, 10^5, 10^4, 10^3 s. Above the panels, a selection of observables that correlate with the radiative timescale are highlighted. Figure adapted from Showman et al. (2020) based on the original from Komacek & Showman (2016).

2020). This is because the efficiency of the global heat-redistribution depends on the balance between the radiative timescale $\tau_{\rm rad}$, how long it takes for heat to re-radiate back into space, and the advection timescale $\tau_{\rm adv}$, how long it takes for a gas parcel to cross from the dayside to the nightside. Calculation shows a transition occurs around a $\tau_{\rm rad}$ $\sim 3\times10^5$ s (Showman et al., 2020). Below this timescale, advection is efficient, thus so is the global heat redistribution; above this timescale, re-radiation is efficient, thus global heat redistribution is inefficient.

This transition affects wind patterns, spatial P-T structure, atmospheric composition, hot spot offsets and magnetic drag (see Fig. 1.10). For long radiative timescales, the cool dayside results in large hot spot offsets, molecular chemistry, no temperature inversions and weak magnetic drag due to the absence of ionic species in the atmosphere. For shorter radiative timescales, the hot dayside results in: small hot spot offsets, and dissociation of molecules into their atomic and ionic counterparts, which in turn contribute to an inverted P-T structure and a larger magnetic drag induced by the motion of charged particles, namely the ions.

To test GCM predictions, there is a need for a population study of exoplanets with a range of masses and equilibrium temperatures. A few population studies using low-resolution spectrographs have been conducted. Sing et al. (2016) find a transition for HJs from cloudy to clear. Zhang et al. (2018) find evidence for larger hot spot offsets for cooler HJs. Baxter et al. (2021) re-analysed Spitzer data, finding evidence for non-equilibrium chemistry in the cooler exoplanet surveyed, indicated by the absence of methane. Mansfield et al. (2020) find evidence of H_2 dissociation and recombination as a function of equilibrium temperatures.

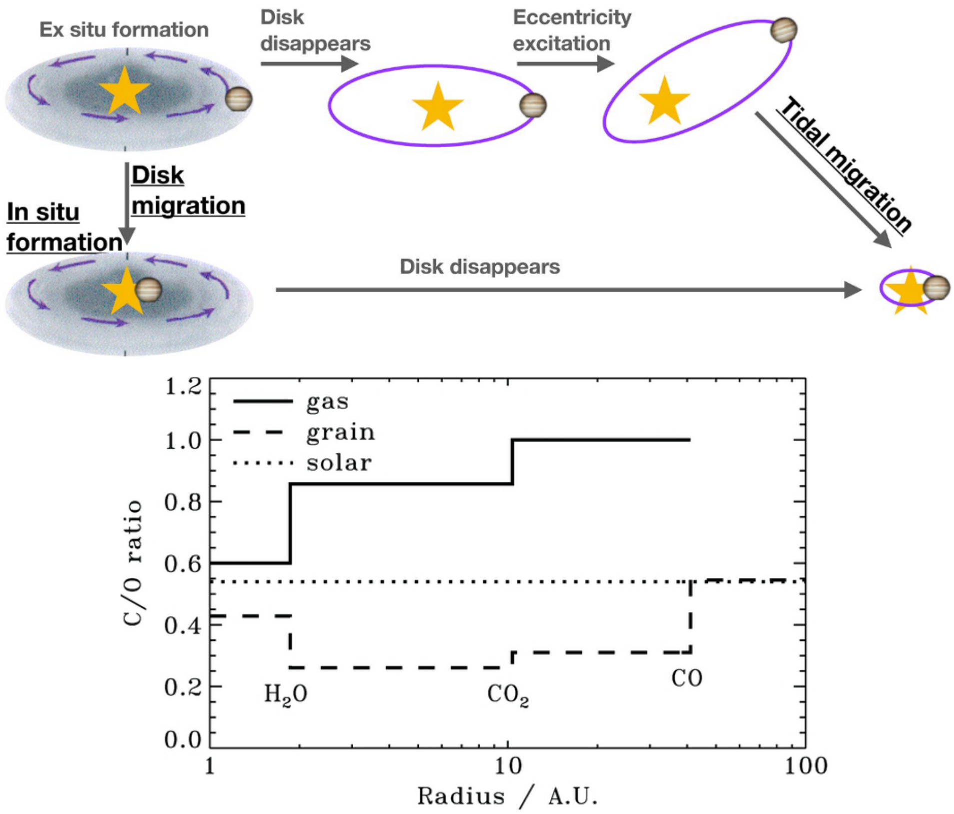

Figure 1.11: Planet formation pathways and their relation to the protoplanetary disk's local composition. *Top panel:* visualisation of three possible formation pathways of HJs: (i) in situ formation (ii) disk migration, and (iii) tidal migration. Figure adapted from Fortney et al. (2021). *Bottom panel:* The effects of snowlines in protoplanetary disks on the C/O of grains and gas at a function of distance to the protostar. Thus measurements of the C/O ratio in exoplanet atmospheres potentially provides insight in their formation pathways. Figure adapted from (Öberg et al., 2011).

There are a couple of ongoing surveys with the JWST. Lastly, there are some ongoing ground-based HRS population studies: HEARTS (Wyttenbach et al., 2017; Seidel et al., 2019; Bourrier et al., 2020; Hoeijmakers et al., 2020a,b; Seidel et al., 2020a,b; Mounzer et al., 2022; Steiner et al., 2023), the "Roasting Marshmallows Survey" (Brogi et al., 2022), ExoGemS (Flagg et al., 2023; Deibert et al., 2023), the SPIRou Legacy Survey (Allart et al., 2023; Moutou et al., 2023; Donati et al., 2023) and MEASURE (van Sluijs et al., 2023, presented in chapter 3 of this thesis).

Comparison of exoplanet atmospheres can also provide clues on planet formation and evolution processes. During the formation, the primordial atmosphere was built from the gas and dust available at the planet's birth location in the protoplanetary disk. This original composition was altered by changes in the systems architecture (such as exoplanet migration), (stellar) radiation environment, enrichment by sub-planetary bodies, geological processes and biological processes.

Fortney et al. (2021) provides an excellent review of the three key possible formation pathways for HJs (see top panel of Fig. 1.11): (i) in situ formation (ii) disk migration, and

(iii) tidal migration. Exoplanet that form in-situ fully accrete and stay at their birth location. Exoplanets that undergo disk migration form in the outer parts of the disk, but due to exchanges of angular momentum with gas in the disk start to migrate inwards while accreting more material. Exoplanets that undergo high-eccentricity fully form in the outer parts of the disk, but after the protoplanetary disk dissipates end up in a highly eccentric orbits, which shrinks and circularises due to tidal interactions between the exoplanet and host star (e.g. Kozai, 1962; Lidov, 1962; Fabrycky & Tremaine, 2007).

An observable that has received particular interest in the C/O ratio. Exoplanets forming inside or outside different snowlines will have accreted different oxygen- and carbon-rich ices (see bottom panel of Fig. 1.11). Therefore, the C/O ratio is thought to be an important indicator of the planet's formation and migration history (e.g. Öberg et al., 2011; Madhusudhan, 2012; Madhusudhan et al., 2014). Similarly, it has been suggested to measure the refractory-to-volatile ratio in UHJs to constrain their accreted rock-to-ice ratio (Lothringer et al., 2020). The rock-to-ice ratio also varies within the protoplanetary disk, thus providing a complementary measurement of the formation location and subsequent evolution. Simulations based on planet formation models linked to protoplanetary disk chemistry by Cridland et al. (2019); Eistrup et al. (2018); Mollière et al. (2022) suggest C/O trends may be present in the HJ population. Khorshid et al. (2022) developed a planet formation code that also suggests a correlation between measurements of the C/O ratio and metallicity and planet formation pathways.

Studies using HRCCS have measured C/O ratios for a handful of exoplanet (e.g. Line et al., 2021; Pelletier et al., 2021; Brogi et al., 2022; Hoch et al., 2023). The high atmospheric temperatures of HJs allow for C/O measurements at a precision comparable or even better than those measured for the cooler Solar System gas planets (e.g. Li et al., 2020). Nonetheless, a larger sample of exoplanets with constrained C/O ratios is required before obtaining any conclusive results on universal planet formation pathways.

1.5 Outline of this thesis

The goal of this thesis is to demonstrate the power of Bayesian frameworks combined with HRS to constrain both the chemistry and the dynamics of exoplanet atmospheres.

In **Chapter 2**, I will describe the technical aspects of the key methods used throughout this thesis. This should provide the reader with a sufficient understanding to follow the subsequent science chapters.

In **Chapter 3** (largely based on van Sluijs et al., 2023), I will describe the science goals and results of the MMT Exoplanet Atmosphere SURvEy, or in short MEASURE. The main goal of this survey is the characterisation of exoplanet chemistry and dynamics for a small population of diverse exoplanets using HRS. I will describe the complex data processing steps to go from raw detector images to molecular detection. For this, I use data from the hottest MEASURE target, the UHJ WASP-33 b, as an example and I find a strong detection of carbon monoxide emission lines using classical HRCCS.

In **Chapter 4** (partially based on van Sluijs et al., 2023), I will describe how to constrain the chemistry of exoplanet atmospheres independent of a detection or not. For a non-detection of the atmosphere, like for a fainter MEASURE target, the sub-Saturn HD 46375 b, I show injection-recovery tests are useful to evaluate the constraining power of the data. For another non-detection, the absence of water in CRIRES τ Boö b observations, I show Bayesian frameworks can still provide meaningful upper limits on chemical abundances. Finally, for a strong detection like CO in WASP-33 b, I show Bayesian frameworks can be used to further constrain P-T structure, and metallicity and distinguish between different heat-redistribution efficiency scenarios.

In **Chapter 5** (largely based on van Sluijs et al., 2023), I will describe the power of Bayesian frameworks to constrain atmospheric dynamics. I will show the scale parameter in the Brogi & Line (2019) CC-to-log(L) mapping is sensitive to the temperature gradient between atmospheric layers. I apply this idea to the strong detection of the carbon monoxide emission lines in the atmosphere of WASP-33 b to show our observations are consistent with an eastward hot spot offset in its atmosphere.

In **Chapter 6** (van Sluijs et al., 2023b, in prep.), I will explore the interplay of chemistry and dynamics by investigating how molecule-dependant velocity offsets can be used to map spatial abundances and wind patterns on an UHJ using HRCCS. Specifically, I investigate if the observed velocity offsets of H_2O, OH, and CO in the atmosphere of WASP-18 A b by Brogi et al. (2022) are naturally reproduced by a GCM or not. I highlight the importance of including 3D effects in Bayesian retrieval framework.

Finally, in **Chapter 7**, I will summarise the main conclusions from this thesis and present some directions for future work.

2
Methods of high resolution spectroscopy

"Don't Panic."

-Douglas Adams, The Hitchhiker's Guide to the Galaxy

As described briefly in the previous chapter, the main challenge in detecting an exoplanet atmosphere is overcoming the large star-planet flux contrast ratio for close-in exoplanets. HRCCS solves this problem by disentangling the star and exoplanet spectral features by their difference in Doppler shift. To resolve individual spectral lines and their Doppler shifts, observations at high spectral resolution are necessary. These observations require large, ground-based, echelle spectrographs. This adds an additional challenge, namely removing the varying telluric lines from each observed spectrum. Since individual spectral lines are buried in the noise, cross-correlation with a spectral template is used to combine the signal of all individual lines.

In summary, successful characterisation of an exoplanet atmosphere with HRCCS requires (i) a procedure to extract the observed spectral time series and removal of the systematics and telluric lines (section 2.1), (ii) a synthetic exoplanet spectrum to use as a cross-correlation template (section 2.2) and (iii) a procedure to cross-correlate the data and template (section 2.3). Finally, section 2.4 will discuss how Bayesian frameworks are used to further constrain properties of exoplanet atmospheres.

2.1 Processing of the spectra

2.1.1 From echellogram to spectrum

Let's define the *echellogram* $F(x, y)$ as the counts per pixel (x, y) on a raw detector image observed by a ground-based echelle spectrograph. Assume this echellogram has been corrected for the dark current (dark correction), the current flowing through the detector in the absence of incident flux, and variation of inter-pixel sensitivity (flat correction). Let's further assume this spectrograph observed an exoplanetary system at a distance d. The host star has a radius $R_\star$ and emits an observed flux $F_\star$. Similarly, the exoplanet has a radius R_p and emits an observed flux F_p. In this case, $F(x, y)$ is equal to

$$F(x,y) = (F_\star(\lambda)R_\star^2 + F_\mathrm{p}(\lambda)R_\mathrm{p}^2) \times d^{-2} \times T(\lambda) \times E(\lambda)^{-1} \times \epsilon(x,y,\lambda), \tag{2.1}$$

where $T(\lambda)$ is the telluric transmission, $E(\lambda)$ the energy of a photon with wavelength λ and $\epsilon(x, y, \lambda)$ an efficiency term that accounts for telescope size, dispersion into echelle traces on the detector, instrumental throughput, and wavelength-dependant pixel sensitivity. This is a complex term, but often we do not need to fully understand the details, as it can be corrected by flat-fielding the science images.

The challenge is to convert $F(x, y)$ into an *observed spectrum* $F(\lambda)$ as a function of wavelength. First one needs to compute $F(s)$, the observed spectrum in counts for each spectral channel s along each echelle trace. This is done by an algorithm that finds the echelle traces on the detector and sums all fluxes within a (weighted) aperture. A wavelength solution $s = s(\lambda)$ is found by calibration against telluric lines or by the use of a spectral calibration lamp, such that the observed spectrum $F(\lambda) = F(s(\lambda))$. A *spectral time series* is defined as a set of N observed spectra, $\{F(\lambda, t) : t \in T\}$ with $T = \{t_1, t_2, ..., t_N\}$ the set of observing times. For one observing run, a spectral time series is computed for each echelle trace, defined as *a spectral order*. Thus a HRS dataset is a set of spectral time series for each spectral order $\{\{F(\lambda, t) : t \in T\}_o : o \in O\}$ with O the total number of spectral orders.

2.1.2 Self-calibration

Opposed to LRS, for HRS the observed spectrum is not calibrated against a reference star. This is because it is time-consuming to switch between targets during the observing run, and, for slit-based echelle spectrographs only, it is difficult to re-point the telescope accurately such that the echelle traces are stable on the echellogram. Instead, a self-calibration approach is adopted for HRS.

This is done for each spectrum in the spectral time series by fitting and dividing out the continuum (e.g. Brogi & Line, 2019) to correct for the variability of the airmass and instrumental throughput over time. To fit the continuum, a common method is to pick a subset of the brightest spectral channels in each spectrum and fit a polynomial to them (e.g. Brogi & Line, 2019). Division of each spectrum by the fitted continuum results in a *normalised spectrum*

$$F(\lambda,t) = \left(1 + \frac{F_\mathrm{p}(\lambda,t)}{F_\star(\lambda,t)} \frac{R_\mathrm{p}^2}{R_\star^2}\right) \times T(\lambda,t). \tag{2.2}$$

This corrects each spectral time series to the same pseudo continuum levels. Smaller variations, for example, due to small time-dependent changes of the spectral blaze function will be corrected for in the post-processing of this data (e.g. with an algorithm such as PCA/SVD/SYSREM, as discussed later in this chapter).

Often the change in stellar Keplerian velocity around the system center of mass is much smaller than the change in Keplerian velocity of the exoplanet. In that case, it is helpful to assume a static stellar spectrum, thus $F_\star(\lambda, t) = F_\star(\lambda)$. For early-type stars, equilibrium temperatures are sufficiently high to dissociate molecules, and few rotational-vibrational transitions exist in the near-infrared. Therefore, the stellar spectrum can often be well approximated by a Planck black body function

$$B(\lambda, T) = \frac{2hc^2/\lambda^5}{e^{\frac{hc}{\lambda kT}} - 1}, \tag{2.3}$$

with $F_\star(\lambda) = B_\star(\lambda, T_\star)$ at the stellar effective temperature $T_\star$.

2.1.3 An overview of different telluric removal methods

It remains an ongoing debate on how to optimally remove the quasi-stationary components (e.g. the telluric lines) from the normalised spectral time series. If the systematics are well understood, these can be removed by fitting for trends with observables such as the airmass, target offset on the spectrograph slit, seeing, or air humidity. The telluric contribution can be modeled directly with codes such as MOLECFIT or TERRASPEC (Rodler et al., 2012; Lockwood et al., 2014; Smette et al., 2015). An advantage of both of these methods is that they provide insight into what is being removed from the data.

If systematics are poorly understood, data-driven approaches often lead to better results. One way is to fit polynomials to any trends in the data as a function of time (e.g. Brogi et al., 2017). Often a Principal Component Analysis (PCA) or Singular Value Decomposition (SVD) (e.g. Wall et al., 2003) is used to clean the data. These approaches have been successfully used (e.g. see de Kok et al., 2013; Birkby et al., 2013; Piskorz et al., 2016, 2017b; Brogi & Line, 2019; Line et al., 2021; Cheverall et al., 2023). Another popular choice is SYSREM (Tamuz et al., 2005), a slightly more sophisticated algorithm based on PCA/SVD which also incorporates errors (e.g. Mazeh et al., 2007; Birkby et al., 2013, 2017; Spring et al., 2022). However, Cabot et al. (2019) found that optimizing parameters of certain data cleaning algorithms such as SYSREM can introduce biases and recommends against such optimization schemes. Sometimes a high-pass filter successfully removes low-frequency trends from each spectrum (for example see Snellen et al., 2010; Brogi et al., 2012, 2013; de Kok et al., 2014a; Brogi et al., 2017; Piskorz et al., 2017a; Herman et al., 2020). Fisher et al. (2020) investigated how supervised machine learning can help clean spectral time series. Meech et al. (2022) used Gaussian Processes to clean the spectral time series. In this thesis, I use SVD because it is computationally fast, easy to implement, and has led to robust detections in previous

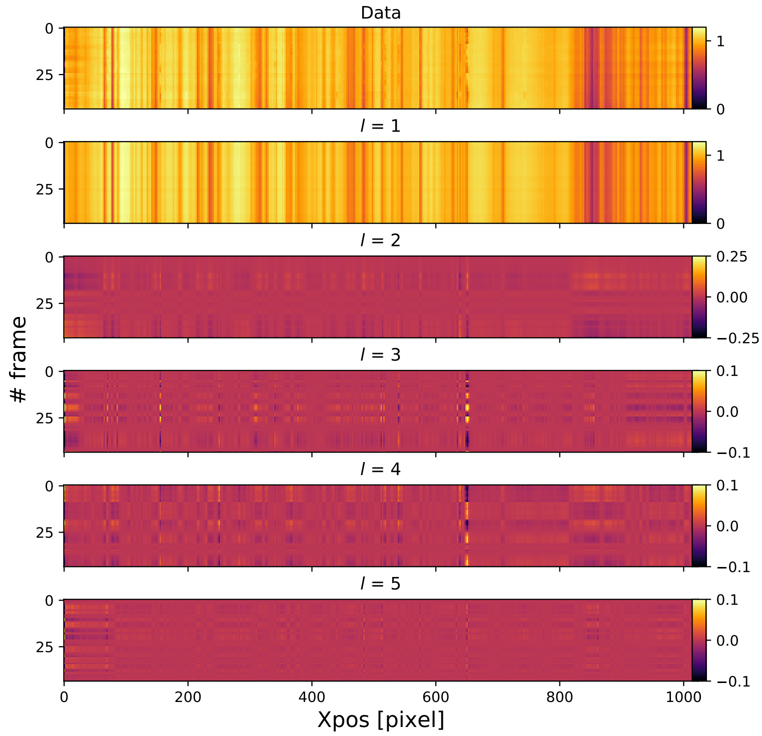

Figure 2.1: Example of SVD of an observed spectral time series. Real data is shown in the top panel where each row represents an observed normalised spectrum. The decomposition of the data into the first five "eigen components" is shown.

HRCCS studies. Alongside SVD, I will sometimes use high-pass filtering in those datasets where low-frequency trends persist after SVD.

2.1.4 Singular Value Decomposition

The SVD algorithm decomposes a spectral time series into multiple orthogonal components. These contributions from each component can be listed from large to small. Since the telluric and stellar lines dominate the spectral time series, they coincide with the first couple of orthogonal components. This provides a clever way to remove only the telluric and stellar lines, without degradation of the exoplanet signal.

An example of the steps of SVD is shown in Fig. 2.1. First, I write the spectral time series in matrix form: $\mathbf{F}$, an $M \times N$ matrix, where each row is an observed spectrum $F(\lambda, t)$ with a total of N spectra and M spectral channels per spectrum. SVD is now given by

$$\mathbf{F} = \mathbf{U}\mathbf{S}\mathbf{V}^T, \tag{2.4}$$

where $\mathbf{U}$ is a matrix of "eigen time series", $\mathbf{V}^T$ is a transposed matrix of "eigen fluxes" and $\mathbf{S}$ a matrix with singular values (in this case they are equivalent to the eigenvalues) s_l on its diagonal and zeros elsewhere. The singular values are ordered monotonically decreasingly: the strongest trend is $l = 0$, followed by $l = 1$, and so on until $l = N$. Since the telluric lines and systematics are the dominating trends, they are captured by the first couple of trends. To re-construct a *cleaned spectral time series*, one computes equation (2.4), but replaces $\mathbf{S}$ by $\mathbf{S}'$ with the only difference between them being that the first k values on the diagonal of $\mathbf{S}'$ have been set zero. There's no pre-defined ideal number of components k to remove, but empirically removing between four and seven components (e.g. Brogi & Line, 2019; Line et al., 2021) is often sufficient to remove the systematics and tellurics; that is to reach a noise level close-to photon-limited. Removing more components risks degradation of the exoplanetary signal as part of the exoplanetary signal will be included in the weaker orthogonal components. Symbols have been changed in this paragraph.

2.2 Modelling exoplanet atmospheres

2.2.1 Radiative transfer

The general problem of computing a synthetic model spectrum can be thought of as iteratively solving the radiative transfer equation through a set of atmospheric layers (e.g. Seager & Deming, 2010). The 1D plane-parallel form of the radiative transfer equation is given by

$$\mu \frac{dI(z, \lambda, \mu, t)}{dz} = -\kappa(z, \lambda, t) I(z, \lambda, \mu, t) + \epsilon(z, \lambda, \mu, t), \tag{2.5}$$

with I the intensity (essentially a beam of traveling photons), the absorption coefficient κ, the emission coefficient ϵ, $\mu = \cos\theta$ with θ the angle between the layer normal and beam direction and z the altitude of the layer. Often this equation is re-written using the optical depth τ, defined by $d\tau \equiv -\kappa dz$:

$$\mu \frac{dI(\tau, \lambda, \mu, t)}{d\tau} = -\kappa(\tau, \lambda, t) I(\tau, \lambda, \mu, t) + B(\tau, \lambda, t). \tag{2.6}$$

This assumes local thermal equilibrium (LTE) and Kirchoff's law $B = \epsilon/\kappa$ (see equation (2.3)). In words, equation (2.6) states that the change in intensity of a beam of photons through a layer of the atmosphere is a balance between the amount of radiation absorbed and the amount of radiation emitted. Built into equation (2.5) are opacity, thermal structure, chemistry, and clouds.

For a single gas, the absorption coefficient is defined as

$$\kappa(\lambda, T, P) = n(T, P)\sigma(\lambda, T, P), \tag{2.7}$$

with n the number density and σ the cross-section which reflects all energy transitions at a wavelength λ that form spectral lines. These spectral line lists either come from laboratory measurements, quantum mechanical calculations, or a combination of both. Popular line list databases used in exoplanet work are HITEMP (Hargreaves et al., 2019), HITRAN (Gordon et al., 2022), and ExoMol (Tennyson & Yurchenko, 2018).

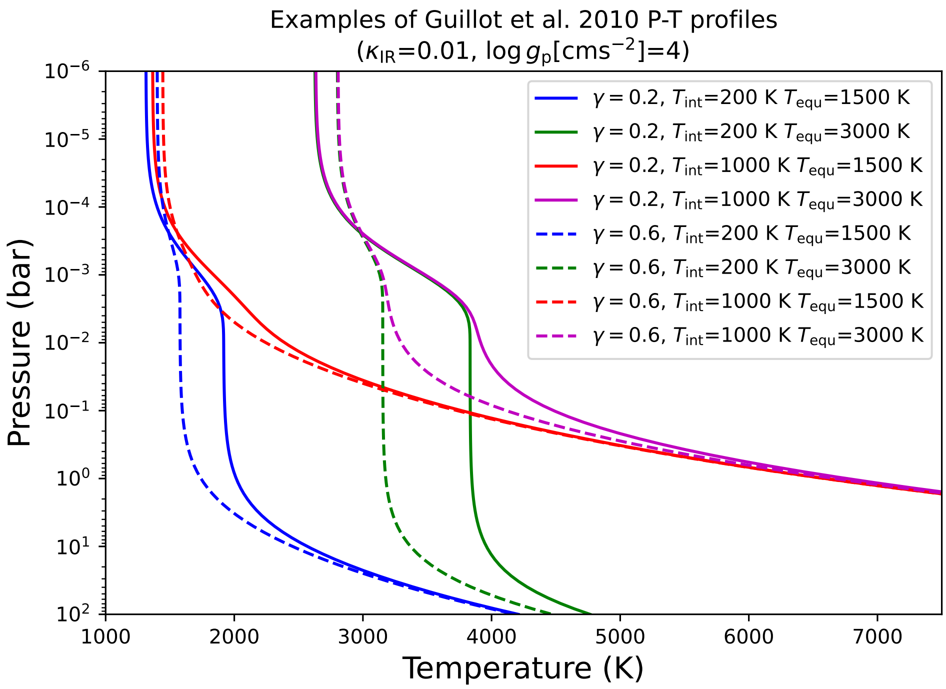

Figure 2.2: Visualisation of a few Guillot (2010) P-T profiles.

2.2.2 Free 1D models

A hierarchy of approaches with different levels of complexity exists to solve the radiative transfer equation. *Free 1D models* are the most simple solution as they assume a parametrised P-T structure and chemical structure. Examples of free 1D modelling codes used in this thesis are PHOENIX (Hauschildt et al., 1997) and PETITRADTRANS (Mollière et al., 2019).

There are a few commonly used parametrisations for P-T structures. These have been tested either against Solar System measurements or against the output from more complex modelling codes. The analytical atmospheric P-T profile from Guillot (2010) is given by

$$T^4 = \frac{3T_{\rm int}^4}{4}\left(\frac{2}{3}+\tau\right)+\frac{3T_{\rm equ}^4}{4}\left[\frac{2}{3}+\frac{1}{\gamma\sqrt{3}}+\left(\frac{\gamma}{\sqrt{3}}-\frac{1}{\gamma\sqrt{3}}\right)e^{-\gamma\tau\sqrt{3}}\right] \tag{2.8}$$

with the $T_{\rm int}$ the internal temperature, $T_{\rm equ}$ the equilibrium temperature, γ the ratio between the optical and infrared opacity and with τ the optical depth. The optical depth can be computed using $\tau = (P\kappa_{IR})/g$, with P the pressure, κ_{IR} the atmospheric opacity in infrared wavelengths, and g the gravity. For exoplanets and stars, it is the convention to report the logarithm of the gravity as

$$\log g = \log \frac{GM_{\rm p}}{R_{\rm p}^2}[{\rm cms}^{-2}], \tag{2.9}$$

with G the universal gravitational constant and g in cgs units. A visualisation of a few Guillot (2010) P-T profiles is shown in Fig. 2.2.

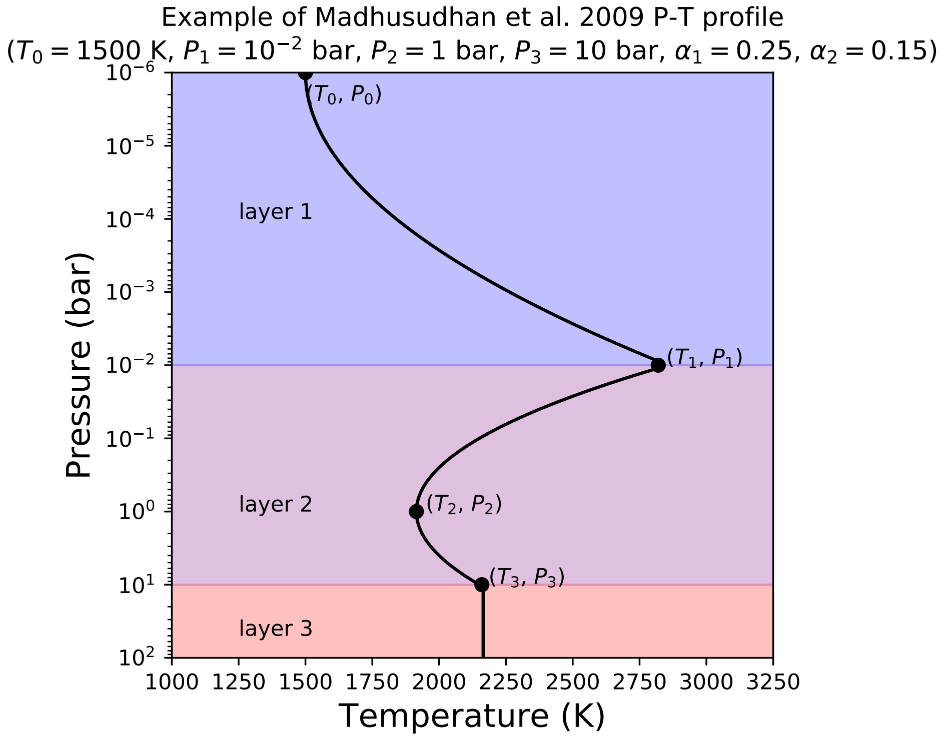

Figure 2.3: Visualisation of a Madhusudhan & Seager (2009) P-T profile. The three atmospheric layers and critical P-T points are indicated.

Another commonly used P-T parametrisation by Madhusudhan & Seager (2009) is given by

$$T(P) = \begin{cases} \frac{1}{\alpha_1} = \ln^2\left(\frac{P}{P_0}\right) + T_0 & P_0 \leq P < P_1 \\ \frac{1}{\alpha_2} = \ln^2\left(\frac{P}{P_2}\right) + T_2 & P_1 \leq P < P_3 \\ T = T_3 & P \geq P_3 \end{cases} . \tag{2.10}$$

This parameterisation defines three layers with boundary pressures P_1 and P_2. By fixing the temperature at the top of the atmosphere T_0 and the gradients of the inversion α_1 and α_2 one can solve for T_2 and T_3 at the boundaries between the layers. A visualisation is shown in Fig. 2.3.

The main advantage of the parametrisation by Guillot (2010) is the clear physical interpretation of the input parameters, as it couples radiative transfer and advection. However, this also means the parametrisation was derived using certain approximations about radiative transfer and advection in the exoplanet atmospheres, which might not be appropriate. Compared to the parametrisation by Guillot (2010), the parametrisation by Madhusudhan & Seager (2009) is more flexible, but the physical interpretation of the input parameters is not as clear-cut. In this thesis, I will use both parametrisations, depending on the dataset analysed.

To compute chemical abundances, one needs to know the P-T structure and assume a certain gas composition. Often the gas composition is assumed to have equal to solar elemental abundances. This approximation is appropriate only to first order, as the gas and grain composition within a protoplanetary disk can vary as a function of the birth location of the exoplanet, enhancing certain elements (an example of this was shown for the C/O ratio in the bottom panel Fig. 1.11), therefore sometimes an enhanced metallicity or different elemental ratios are used. Chemical codes containing a network of chemical reactions and reaction rates combined with the elemental abundances, LTE and the P-T structure are used to determine the expected ionic/atomic/molecular abundances. In the simplest free 1D models, a constant chemical abundance profile with altitude is assumed. Although free 1D model codes can provide meaningful priors on chemical abundances, it is important to point out that the chemistry and thermal structure are not inherently connected. Therefore, unphysical chemical abundances can be assumed for a given P-T structure.

Combining the P-T structure and chemical structure with the right opacity list, the absorption coefficient and emission in each atmospheric layer can be computed. Subsequently, equation (2.6) can iteratively be solved for each atmospheric layer. The output exoplanet synthetic spectrum is the flux at the topmost layer of the atmosphere.

2.2.3 Self-consistent 1D models

Self-consistent 1D models solve for the P-T structure and chemistry by solving for the underlying physics: the radiative transfer equation, the equation of hydrostatic equilibrium, and the equation of energy conservation. An example used in this thesis is the PHOENIX modelling code, which is capable of computing self-consistent 1D models (alongside free 1D models). Thus, a key difference between free 1D models and 1D self-consistent models is that the latter connects the chemistry and thermal structure. This is done by iteratively solving for the chemistry and thermal structure. For example, given the assumed P-T structure, the atomic/ionic/molecular abundances are updated assuming LTE. This in turn affects absorption and emission processes in the atmosphere altering the P-T structure slightly. For a convective atmosphere, convection processes also need to be included. A convergence criterium is used to terminate iteratively solving for the P-T structure and chemical structure of the atmosphere.

An advantage of 1D self-consistent models is that the output spectrum is computed based on the underlying physical processes in the atmosphere. Some disadvantages are that (i) it takes longer to compute a single synthetic model spectrum and (ii) the model is only as complete as the underlying physical processes included. Often disequilibrium processes like non-local thermal equilibrium (NLTE) chemistry, photochemistry, cloud formation, and aerosol production are neglected. It needs to be decided on a case-by-case basis whether more exotic physics is important. This depends on the type of exoplanet, levels of stellar irradiation and the atmospheric layers probed by observations (e.g. whether it is a transit or emission spectrum), and the constraining power of the data.

2.2.4 3D GCMs

Atmospheric circulation distributes heat and chemicals over the exoplanet by advection and convection processes (e.g. Showman et al., 2020). The inclusion of global circulation requires solving the Navier-Stokes fluid dynamics equations. The non-linearity of these equations makes them computationally expensive to solve. Nonetheless, some GCM codes solve these equations directly. Others make assumptions such as local hydrostatic balance to simplify the computation. Different ways to treat opacities have been adopted. Most codes assume circulation in HJs is driven by stellar irradiation and a synchronous planet rotation. In this thesis, I use the output from the SPARC/MITgcm (Showman et al., 2009).

Regardless of the exact implementation, qualitatively all GCMs of close-in giant planets predict the same things: (i) eddy and jet structure on a global scale (ii) a large dayside-to-nightside temperature gradient, and (iii) an eastward jet (e.g. Knutson et al., 2007; Showman & Guillot, 2002; Showman et al., 2009; Heng et al., 2011; Rauscher & Menou, 2012; Amundsen et al., 2016; Cho et al., 2015; Mendonça et al., 2018). Since GCMs produce spatial maps (for example see Fig. 1.10) of the global winds, cloud structure, rotation, P-T structure, and chemical abundances, their synthetic model spectra are often much more complex than those from 1D models. Moreover, an output synthetic model spectrum can be computed along the changing line of sight as the exoplanet orbits its host star. Thus a synthetic disk-integrated model spectrum can be computed at each observed orbital phase.

2.3 Cross-correlation

2.3.1 The Pearson cross-correlation coefficient

Cross-correlation of the observed spectrum with a modeled synthetic exoplanet spectrum is needed to combine the faint signal of many exoplanetary lines buried in the noise. Several different ways to compute cross-correlation coefficients are in use throughout previous studies. In this thesis, I use the Pearson cross-correlation coefficient defined for two vectors X and Y as

$$\rho_{X,Y} = \frac{\mathrm{cov}(X,Y)}{\sigma_X \sigma_Y}, \tag{2.11}$$

where the covariance is defined as

$$\mathrm{cov}(X,Y) = \frac{1}{N}\sum_i (x_i - \mu_X)(y_i - \mu_Y), \tag{2.12}$$

with μ the mean and σ the standard deviation. The division by $\sigma_X\sigma_Y$ ensures the Pearson cross-correlation coefficient is normalised such that $\rho_{X,Y} \in [-1,1]$. Let F be the vector representation of the observed spectrum with entries for each spectral channel. Furthermore, let $F_{\mathrm{m}}(v)$ be the synthetic model spectrum shifted to a Doppler velocity v by applying

$$\lambda_s = \lambda\sqrt{\frac{1+v/c}{1-v/c}}, \tag{2.13}$$

with c the speed of light, λ the rest frame wavelengths and λ_s the wavelengths in the shifted rest frame. Now if we take $X = F$ and $Y = F_{\mathrm{m}}(v)$, the *cross-correlation function (CCF)* is defined as

$$CCF(v) = \rho_{F,F_m(v)}. \tag{2.14}$$

2.3.2 SNR detections in velocity space

A large CCF value does not always mean the exoplanet atmosphere is detected. This is because correlated noise and auto-correlation often persist in the data. Therefore, the difference in Doppler velocity between a real exoplanetary signal and spurious signals is used to detect the exoplanet atmosphere. The exoplanet Keplerian velocity can be computed from its orbital period P, eccentricity e, and inclination i using

$$K_{\mathrm{p}} = \left(\frac{2\pi G}{P}\right)^{1/3} \frac{M_\star \sin i}{(M_{\mathrm{p}} + M_\star)^{2/3}} \frac{1}{\sqrt{1-e^2}}. \tag{2.15}$$

Lets assume the exoplanet orbits on a circular orbit $e = 0$ seen edge-on $i = 90°$, such that equation 2.15 reduces to

$$K_{\mathrm{p}} = \left(\frac{2\pi G}{P}\right)^{1/3} \frac{M_\star}{(M_{\mathrm{p}} + M_\star)^{2/3}}. \tag{2.16}$$

For such as system, when observed from the Earth, the exoplanetary lines have a total Doppler velocity

$$v = v_{\mathrm{bary}} + v_{\mathrm{sys}} + K_{\mathrm{p}} \sin \phi_{\mathrm{p}}, \tag{2.17}$$

where v_{bary} is the barycentric velocity, the Earth's velocity around the Sun; v_{sys} the system velocity, the stellar velocity as seen from the barycenter and ϕ_{p} the orbital phase at which the exoplanet is observed. The orbital phase can be computed at each time t as

$$\phi_{\mathrm{p}} = \frac{t - T_0}{P} \bmod \mathrm{P} \tag{2.18}$$

where T_0 is a reference time for which $\phi_{\mathrm{p}} = 0$. For a transiting system, this corresponds with a reference mid-transit point time. The barycentric velocity can be computed given the

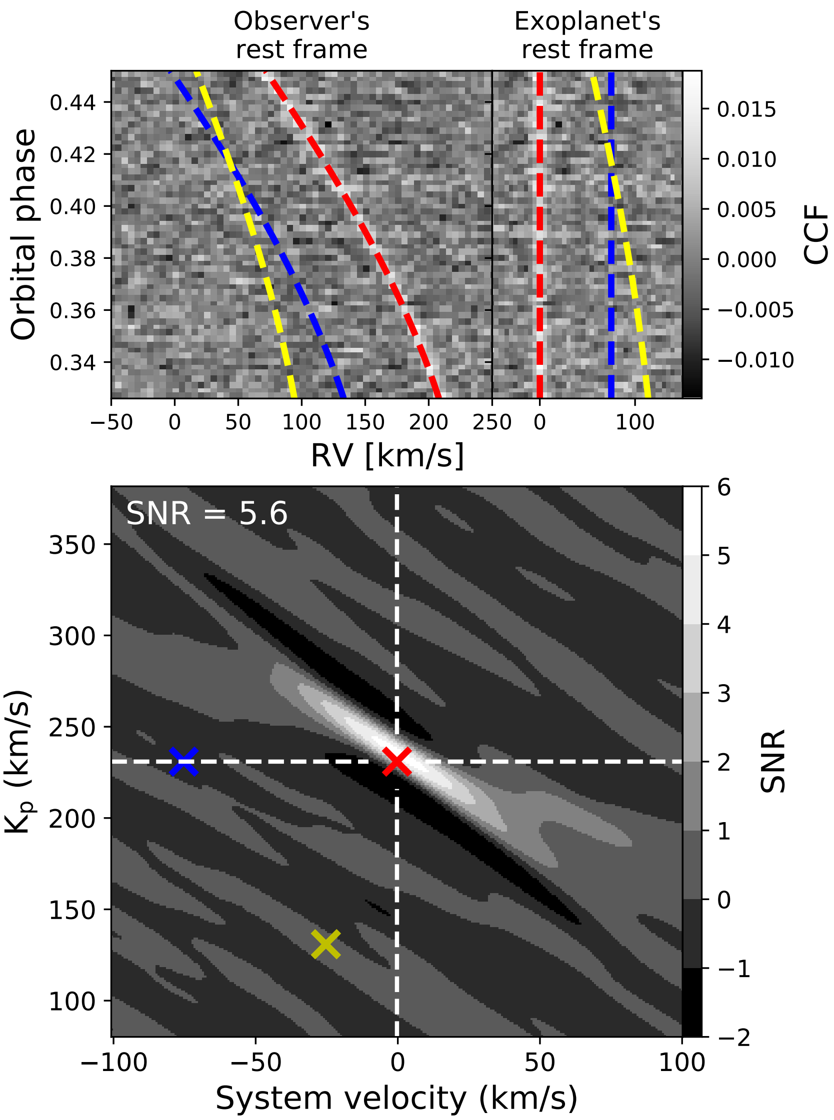

Figure 2.4: *Top-left panel:* example of a CCF time series for a simulated exoplanet. RV trails for three $(v_{\rm sys}, K_{\rm p})$-values are shown as dashed lines. *Top-right panel:* The same, but in the exoplanet's rest frame. *Bottom panel:* Corresponding SNR-map in velocity space. The three $(v_{\rm sys}, K_{\rm p})$-values are indicated by the cross-shaped markers using the same colours. The red line aligns with the true exoplanetary signal at a $SNR = 5.6$

times of observation[1]. Thus, the Doppler velocity in equation (2.17) is a function of $v_{\rm sys}$ and $K_{\rm p}$.

Multiple methods have been used in previous studies to convert cross-correlation values to SNR values. The main method used in this thesis computes the SNR from the CCF time series. When using HRCCS it is common practice to explore a 2D grid of trial ($v_{\rm sys}$, $K_{\rm p}$)-values. An example is shown in Fig. 2.4 where the top panel shows a cross-correlation time series with Doppler velocity trails for three ($v_{\rm sys}$, $K_{\rm p}$)-values indicated. For each of these trails, the cross-correlation time series is interpolated to the new rest frame, in other words, where the trail is a vertical line at $v = 0$. In this new rest frame, all CCF values are summed along the time axis such that the mean at each Doppler velocity $\overline{CCF(v)} = \frac{1}{N}\sum_{t\in T} CCF(v,t)$ is computed. The exoplanet signal has a width $v_{\rm in-trail}$ set by the convolution of the rotational broadening and instrumental profile (IP) of the spectrograph. The set of in-trail velocities is $\{v : |v| \leq v_{\rm in-trail}\}$ and the set of out-of-trail velocities is $\{v : |v| > v_{\rm in-trail}\}$. Now the SNR is computed in each trial reference frame as

$$SNR(v) = \frac{S(v)}{N(v)} = \frac{\sum_{\rm in-trail} \overline{CCF(v)}}{\sqrt{\sum_{\rm out-of-trail}\left(\overline{CCF(v)} - {\rm mean}(\overline{CCF(v)})\right)^2}}. \tag{2.19}$$

Note that since $\overline{CCF(v)}$ is a time-averaged quantity, so is the SNR. A SNR is computed for each ($v_{\rm sys}$, $K_{\rm p}$) combination on a 2D grid. An example is shown in the bottom panel of Fig. 2.4 with the three points corresponding to the trial trails indicated.

An alternative way to compute the SNR is to interpolate and sum all cross-correlation values for each trial ($v_{\rm sys}$, $K_{\rm p}$)-value. This results in a map of $\overline{CCF(v_{\rm sys}, K_{\rm p})}$-values. The signal map is set equal to this map. The noise map can be estimated by computing the standard deviation of the map in a region outside of the expected exoplanetary ($v_{\rm sys}$, $K_{\rm p}$)-values. The SNR map is equal to the signal map divided by the noise map. I use both methods in this thesis, depending on the dataset analysed.

[1] I use the PYTHON package BARYCORRPY to compute the barycentric velocity

2.3.3 Estimating the SNR a priori

It is often useful to compare the measured SNR detection in velocity space to a priori estimates of the SNR, for example, to check whether the observed SNR was expected, especially in the case of a non-detection. When using HRCCS, to the first order, the expected SNR of the planet SNR_{p} is given by

$$SNR_{\mathrm{p}} = \frac{S_{\mathrm{p}}\sqrt{N_{\mathrm{lines}}}}{\sqrt{S_{\star} + \sigma^2_{\mathrm{bg}} + \sigma^2_{\mathrm{read}} + \sigma^2_{\mathrm{dark}}}}, \tag{2.20}$$

where S_{p} is the observed planet's flux, $S_{\star}$ the observed stellar flux, N_{lines} the number of resolved spectral lines (approximating all line are equally strong)[2], σ_{bg} the noise from the sky and telescope background, σ_{read} the detector read-out noise and σ_{dark} the detector dark current (Snellen et al., 2015). In the photon-limited regime, Equation 2.20 reduces to

$$SNR_{\mathrm{p}} = \left(\frac{S_{\mathrm{p}}}{S_{\star}}\right) SNR_{\star}\,\sqrt{N_{\mathrm{lines}}}, \tag{2.21}$$

where $\mathrm{SNR}_{\star}$ is the stellar continuum SNR (Birkby, 2018). For emission spectroscopy, the contrast ratio between bolometric fluxes can be estimated from the planet-to-star ratios of the effective temperature and radii:

$$\frac{S_{\mathrm{p}}}{S_{\star}} = \left(\frac{T_{\mathrm{p}}}{T_{\star}}\right)^4 \left(\frac{R_{\mathrm{p}}}{R_{\star}}\right)^2. \tag{2.22}$$

When comparing the fluxes within a certain bandpass this ratio will vary between

$$\frac{S_{\mathrm{p}}}{S_{\star}} = \left(\frac{T_{\mathrm{p}}}{T_{\star}}\right) \left(\frac{R_{\mathrm{p}}}{R_{\star}}\right)^2 \tag{2.23}$$

in the Rayleigh-Jeans limit ($h\nu \ll k_B T$), and

$$\frac{S_{\mathrm{p}}}{S_{\star}} = \left(\frac{\exp -h\nu/k_B T_{\mathrm{p}}}{\exp -h\nu/k_B T_{\star}}\right) \left(\frac{R_{\mathrm{p}}}{R_{\star}}\right)^2 \tag{2.24}$$

in the Wien limit ($h\nu \gg k_B T$).

The SNR of the star can be calculated using an instrument-specific exposure time calculator given the known magnitude of the star. The number of lines can be estimated from the line list of the model spectrum of the species one is trying to detect, by counting lines above a certain threshold line strength. In summary, equation (2.21) captures that HRCCS works best for exoplanetary systems with (i) a bright star, (ii) a high planet-to-star contrast ratio, and (iii) for species that have many well-separated lines in the observed wavelength region; and for instruments with (i) a large photon-collecting area, (ii) a high throughput and (iii) which operate at a spectral resolution sufficient to resolve many spectral lines.

[2]Note this is only a simplified approximation as in general different spectral lines, particularly from different molecules, will contribute differently to the overall SNR.

2.3.4 Constraining the mass of non-transiting exoplanets

Close-in non-transiting systems are detected using the radial velocity method by measurement of the projected stellar velocity around the center of mass $K_\star \sin i$. Thus only the projected exoplanetary mass $M_\mathrm{p} \sin i$ is measured, but not the true planetary mass, resulting in an exoplanetary mass lower limit.

With HRS, detection of the exoplanetary atmosphere will result in the measurement of the projected Keplerian velocity $K_\mathrm{p} \sin i$. Assuming the exoplanetary system is a two-body system and using preservation of angular momentum, the ratio between the exoplanet mass and stellar mass is given by

$$\frac{M_\mathrm{p}}{M_\star} = \frac{K_\star}{K_\mathrm{p}}. \tag{2.25}$$

Since the projected $K_\star$ and K_p are both measured, one can solve for the true stellar mass and exoplanet mass.

2.4 Bayesian frameworks

Bayesian frameworks are a structure to compare observed data to a model by using Bayesian statistics. In Bayesian statistics, the *likelihood function* is the joint probability of observing data as a function of parameters of a statistical model. A Bayesian goodness of fit metric maximises the likelihood function.

In practice, in HRCCS of exoplanet atmospheres, the data is the observed spectrum and the model is the synthetic exoplanet spectrum. This synthetic model spectrum is computed by a forward model of choice given a set of input parameters, which generally include a P-T profile parameterisation, chemical abundances, and velocity offsets. Note that when comparing the data and model it is essential that both the data and model have been processed homogeneously.

For LRS, it is common practice to use the chi-squared (χ^2) goodness of fit estimator. The χ^2-value between the observed spectrum and the synthetic model spectrum is defined as

$$\chi^2 = \sum_{s \in S} \frac{(F_s - F_{m,s})^2}{\sigma_{F_s}^2}, \tag{2.26}$$

where the sum is taken over all spectral channels S. This is converted to the reduced chi-squared defined as

$$\chi_\nu^2 = \frac{\chi^2}{\nu}, \tag{2.27}$$

the chi-squared per degrees of freedom $\nu = N - M$ with N the number of observations and M the number of free parameters in the forward model. Ideally, $\chi_\nu^2 = 1$ if the model matches the data well. If $\chi_\nu^2 \gg 1$ the model is a poor match to the data and if $\chi_\nu^2 < 1$ the model is overfitting the data or the errors are underestimated. The LRS likelihood function is defined as

$$\log L_{\text{LRS}} = -\frac{\chi^2}{2}. \tag{2.28}$$

2.4.1 CC-to-log(L) mapping

For HRS, compared to LRS the direct use of the chi-squared is problematic because it is self-calibrating, rather than calibrated in flux or measured in comparison to a reference star. Imperfect normalisation and residual broadband structure when using HRS imply $F_s - F_{m,s}$ in equation (2.26) is poorly defined, which inhibit the use of a chi-squared (Brogi & Line, 2019). Instead of a chi-squared, cross-correlation is insensitive to the broadband normalisation and combines the signal of all faint SNR<1 lines. The challenge with HRCCS thus becomes to define a Bayesian goodness of fit estimator that naturally includes the CCF.

Zucker (2003) defined a CC-to-log(L) mapping as

$$\log L = -\frac{N}{2} \log 1 - CCF^2. \tag{2.29}$$

Although useful, this mapping is limited by the quadratic CCF^2 term, which means it is not possible to distinguish between positive and negative correlation. This implies indifference between absorption or emission lines, severely limiting constraints on the P-T parameterisation.

Brogi & Line (2019) improved upon this by introducing a new CC-to-log(L) mapping, as a way to include the cross-correlation into the likelihood with preservations of the sign of the CCF. Their mapping defines the log-likelihood as

$$\log L = -\frac{N}{2} \log \left(s_f^2 - 2R + s_g^2\right) \tag{2.30}$$

with $s_g^2 = \sigma_{F_m}^2$ the model variance, $s_f^2 = \sigma_F^2$ the data variance, $R = cov(F, F_m)$ the cross-covariance between the model and data and N the total number of data points. They also show that this equation can be rewritten entirely in terms of the Pearson cross-correlation coefficient and data and model variances.

More recently, Gibson et al. (2020) introduced another CC-to-log(L) mapping[3]

$$\log L = -\frac{N}{2} \log 2\pi - N \log \beta - \sum_{s \in S} \log \sigma_s - \frac{1}{2}\chi^2, \tag{2.31}$$

, where they define χ^2 as

$$\chi^2 = \sum_{s \in S} \frac{(F_s - aF_{m,s})^2}{\beta \sigma_{F_s}^2}. \tag{2.32}$$

[3]I changed their notation slightly to remain consistent with the rest of this chapter.

Their CC-to-log(L) mapping is similar to the one by Brogi & Line (2019), apart from introducing two free scale parameters a to scale the model (see section 2.4.2) and β to scale the observed errors in the data.

Combining LRS with HRS within a Bayesian framework can improve the overall constraints of exoplanet atmospheres, as this takes advantage of the broader instantaneous wavelength coverage and continuum information from LRS and the sensitivity of HRS to unique spectral signatures, spectral line contrast, spectral line position, and spectral line shape. The total likelihood function is the sum of the LRS likelihood and the HRS likelihood function (Brogi & Line, 2019), thus

$$\log L = \log L_{\text{LRS}} + \log L_{\text{HRS}}. \tag{2.33}$$

Combining LRS and HRS has been done for a few HJs to improve constraints on their chemical abundances and P-T structures (Brogi et al., 2017; Brogi & Line, 2019; Kasper et al., 2023). Particularly, Brogi & Line (2019) shows a combination of simulated low-resolution spectra combined with high-resolution spectra of the HJ HD 209458 b improves constraints on the deeper part of the P-T profile and metallicity.

2.4.2 The scale parameter

Due to the self-calibration in HRCCS, the scaling of the data to the model is often poorly known. Alongside this, the model may not include all necessary physics to be at the same scale as the data.

If the scaling of the model or data is unknown, it can be useful to introduce a scale parameter a into the log-likelihood map given by equation (2.30). Substitution of $a \times F_m$ into F_m into the equation 2.30 the new log-likelihood mapping becomes

$$\log L = -\frac{N}{2} \log \left(s_f^2 - 2aR + a^2 s_g^2 \right). \tag{2.34}$$

Ideally, the maximum likelihood is retrieved at $a = 1$, which implies there is no need to scale the model to match the data.

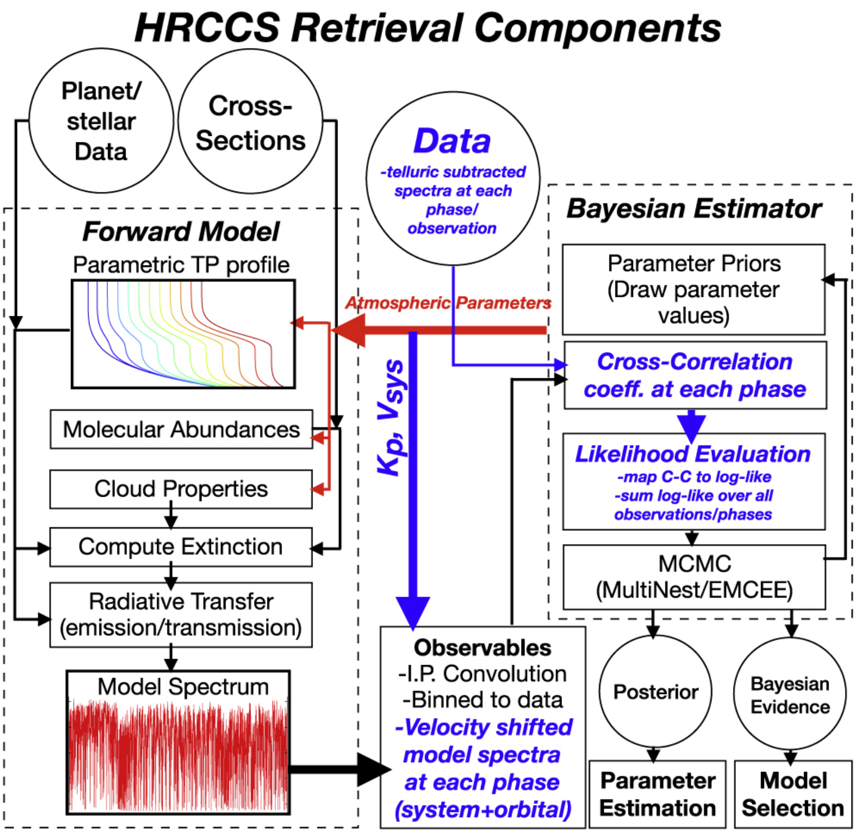

Figure 2.5: Flow chart of a HRCCS retrieval framework. Adapted from Brogi & Line (2019).

2.4.3 Wilks' theorem

The best matching model maximises the log-likelihood, but it is not immediately clear from equation (2.30) how to constrain model input parameters. Wilk's theorem (Wilks, 1938) can be used to calculate the errors on model input parameters. Let $\Delta \log L$ be the difference between the log-likelihood and the maximum log-likelihood value. Wilks' theorem states that $-2\Delta \log L$ follows a chi-squared distribution with a number of degrees of freedom M, where M is again the number of free parameters in the model. The cumulative chi-squared distribution function has an analytical solution, thus one can compute the confidence interval for each $\Delta \log L$-value[4]. This confidence interval can be converted to a standard error, for example, a 68%-confidence interval, would correspond with a standard error of 1σ.

2.4.4 HRCCS retrieval frameworks

A HRCCS retrieval framework provides a systematic way to compare the data and model to find and constrain the model input parameters that best match the data. A key component is the forward model which computes a synthetic model spectrum from a set of trial input parameters. This synthetic model spectrum is compared to the real data using

[4]In PYTHON this can be done by using the `stats.chi2.cdf` function

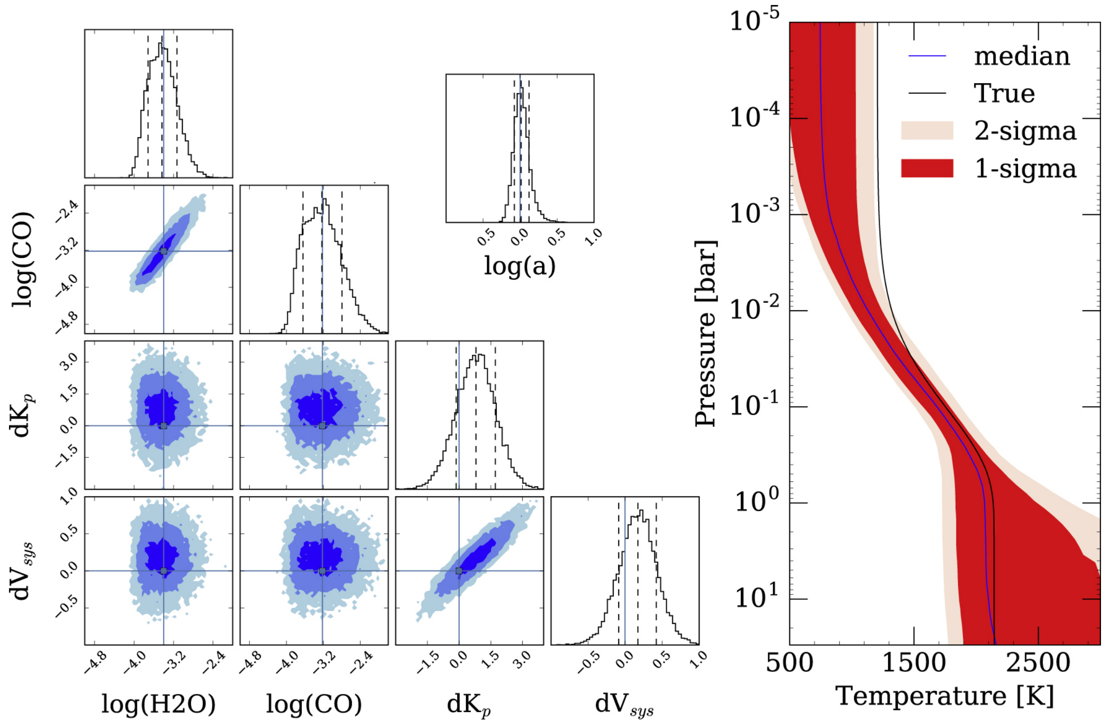

Figure 2.6: An example of the output from a HRCCS framework. The posterior distributions and constraints for the abundance of H_2O, abundance of CO, systemic velocity offset, Keplerian velocity offset, and scale parameter are shown. The CO and H_2O abundances are correlated and so are the velocity offsets. The right panel shows the constraints on the P-T profile. The input parameters for the simulation are indicated by the cross-wires in the corner plot and as the true value in the P-T profile plot. Retrieved constraints are close to the simulation input parameters. Adapted from Brogi & Line (2019).

a Bayesian estimator, such as the log-likelihood mapping by Brogi & Line (2019). To explore the multi-dimensional input parameter space efficiently, a Markov chain Monte-Carlo (MCMC) method is used which creates samples of random variables based on their predefined prior distribution. A flow chart of an example HRCCS retrieval framework is shown in Fig. 2.5.

As a retrieval iteratively computes many (~100,000) synthetic spectra, the forward model needs to be fast, and computation times per iteration are usually a fraction of a second. Therefore, most often 1D free models are used, although sometimes 1D self-consistent models can be used too. These codes are sometimes optimised to use GPUs, to decrease computation time significantly. Long-running GCMs are not included in this framework. The output of a HRCCS retrieval framework is a posterior distribution for each of the model input parameters. From this posterior distribution, the best-fit parameters and their error can be computed. An example of the output of a HRCCS retrieval is shown in Fig. 2.6. For exoplanet atmospheres, a HRCCS retrieval framework thus provides a powerful way to constrain P-T structure and chemical abundances directly.

3
MMT Exoplanet Atmosphere Survey: the case of CO in WASP-33 b

The material in this chapter is partly based on van Sluijs et al. (2023) and sometimes I have used parts of this work with minor or no changes to the original text or figures, to remain concise and preserve clarity of the underlying message. The observations that are a part of MEASURE were obtained by the following people: Jayne Birkby, and Joshua Lothringer with the help of Craig Kulesa and Don McCarthy. The PHOENIX 1D templates were computed by Joshua Lothringer. The 3D GCM templates of WASP-33 b were computed by Elspeth K. H. Lee.

In this Chapter, I will describe the key science goals and analysis of the MMT Exoplanet Atmosphere Survey (MEASURE). The final data product of this survey is a set of high-resolution spectral observations of eleven exoplanets obtained with the ARizona Infrared imager and Echelle Spectrograph (ARIES, McCarthy et al. (1998)) on the 6.5-m MMT, a telescope in Arizona, USA. It contains a diverse set of worlds ranging from HJs to sub-Saturns and covering a wide range of masses, temperatures, and stellar irradiance. I will first explain the scientific motivation and target selection of MEASURE. Next, I will describe the instrumental setup and observing strategy in more detail. I will use the observations of the Ultra Hot Jupiter (UHJ) WASP-33 b as an example to show the power of MMT/ARIES to characterise exoplanet atmospheres. To reduce the data from MEASURE I developed a processing pipeline. Finally, I present some key results and evaluate the performance of ARIES/MMT in the context of high-resolution spectroscopy characterisation of exoplanet atmospheres. These results include the detection of CO emission lines in the atmosphere of WASP-33 b, the first time this has been reported in an exoplanet atmosphere, which provides unambiguous evidence for a thermal inversion in the atmosphere of this UHJ.

3.1 The MEASURE targets

The eleven exoplanets observed as part of MEASURE are shown in Fig. 3.1. Table 3.1 contains an overview of the key properties of these exoplanets and their host stars. Their temperatures range from ∼1400-3400 K, while their stellar irradiance covers about two orders of magnitudes ∼10^8-10^{10} erg/s/cm^2/cm and masses of ∼1-5 M_J.

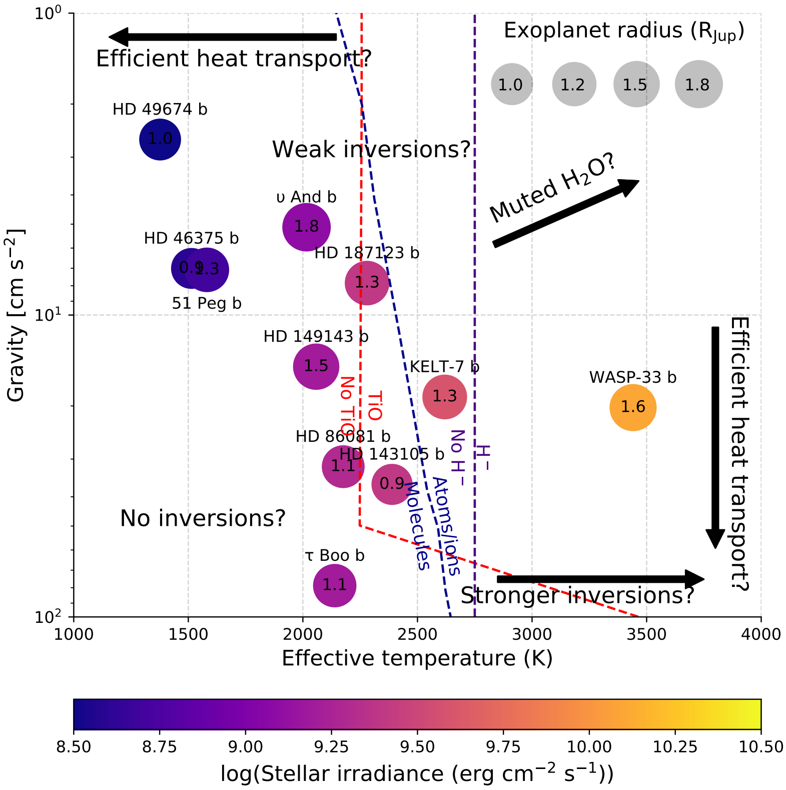

Figure 3.1: Overview of all targets observed by MEASURE as a function of effective temperature and gravity. The colour indicates the exoplanets effective temperature assuming all radiation is absorbed (Bond albedo equals zero) and is instantly re-radiated (no advection, $f = 2/3$). Their radii are indicated by the size of the circle and the number at the center. Theoretical predictions for transition regions of interest are indicated and were adopted from Fig. 1 of Brogi et al. (2022).

On a single system level, this dataset can be used to characterise the chemistry and dynamics of these worlds in detail. On a demographic level, it enables a comparison of these worlds to see how atmospheric dynamics and chemistry vary over a wide range of temperatures, stellar irradiance, and masses. On a demographic level, this wide range covers various theoretical transition regions of interest, namely: (i) a transition from atmospheres with TiO to atmospheres without TiO, (ii) a transition from molecules towards mainly atoms/ions in the atmosphere, (iii) a transition from atmospheres without dissociation of H_2O into H^- towards atmospheres with dissociation into H^- and muted H_2O features, (iv) a transition from non-inverted to inverted P-T structures, and (v) a transition from efficient to inefficient heat transport.

		Planetary parameters					Stellar parameters		
Name	**Transits?**	**Period (days)**	**Radius[a] (R_{Jup})**	**Mass[b] (M_{Jup})**	**Eccen-tricity**	T_{eq} **(K)**	T_{eff} (K)	**Radius ($R_{\odot}$)**	**Mass ($M_{\odot}$)**
WASP-33 b	Yes	1.219870 $\pm$0.000001	1.593$\pm$0.074	2.093$\pm$0.139	0.0	2782$\pm$41	7430$\pm$100	1.44$\pm$0.03	1.5$\pm$0.03
KELT-7 b	Yes	2.734770 $\pm$0.000004	1.60$\pm$0.06	1.39$\pm$0.22	0.0	2048$\pm$27	6768$\pm$7	1.81$\pm$0.07	1.76$\pm$0.25
HD 143105 b	No	2.1974 $\pm$0.0003	1.22[a]	1.21$\pm$0.06	<0.07	2389[c]	6380$\pm$60	$1.65^{+0.01}_{-0.02}$	1.51$\pm$0.11
HD 187123 b	No	3.096583 $\pm$0.0000008	1.27[a]	0.523$\pm$0.043	0.0103 $\pm$0.0059	2280[c]	5790^{+158}_{-115}	$1.15^{+0.05}_{-0.06}$	$1.04^{+0.11}_{-0.16}$
HD 86081 A b	No	2.1378 $\pm$0.0000031	1.21[a]	1.48$\pm$0.23	0.0119 $\pm$0.0047	2176[c]	5939	1.46$\pm$0.14	1.21$\pm$0.28
τ Böo A b	No	3.3124568 $\pm$0.0000069	1.14[a]	5.95$\pm$0.28	0.011 $\pm$0.006	2139[c]	6466^{+115}_{-97}	$1.43^{+0.04}_{-0.05}$	$1.32^{+0.24}_{-0.18}$
HD 149143 b	No	4.07182 $\pm$0.000001	1.22[a]	1.33$\pm$0.15	0.0167 $\pm$0.0040	2058[c]	5856	1.44$\pm$0.08	1.20$\pm$0.20
υ And b	No	4.617033 $\pm$0.000023	1.25[a]	0.6876$\pm$0.044	0.02150 $\pm$0.00070	2016[c]	6157$\pm$112	1.56	1.3
51 Peg b	No	4.230785 $\pm$0.000036	1.27[a]	$0.46^{+0.06}_{-0.01}$	0.013 $\pm$0.012	1581[c]	5758^{+101}_{-120}	$1.17^{+0.06}_{-0.04}$	$1.03^{+0.17}_{-0.09}$
HD 46375 A b	No	3.02573 $\pm$0.000065	0.894[a]	0.226$\pm$0.019	0.226 $\pm$0.019	1514[c]	5285$\pm$112	0.91$\pm$0.02	0.92
HD 49674 b	No	4.94737 $\pm$0.000098	0.553[a]	0.10$\pm$0.01	0.090 $\pm$0.090	1377[c]	5602$\pm$21	1.02$\pm$0.01	1.03 $\pm$ 0.11

[a]In the case of non-transiting systems, the radius was estimated using the mass-radius relation as encoded in the PYTHON FORECASTER package (Chen & Kipping, 2017). [b]In the case of non-transiting systems, the inclination is unknown and this quantity is the mass times the sine of the inclination angle. [c]These have been calculated using the mass-lower limit in the case of non-transiting planets, assuming an albedo of zero and re-radiation efficiency of 2/3.

Table 3.1: Planetary and stellar properties of the eleven exoplanets observed as part of MEASURE. Values are from the NASA Exoplanet Archive unless explicitly stated otherwise.

3.2 ARIES and observing strategy

Eleven MEASURE targets were observed with ARIES. ARIES can cover, but not instantaneously, wavelengths from 1μm to 5 μm and at spectral resolutions of 2,000-30,000. For the eleven MEASURE targets, the echelle spectrograph mode was used, obtaining spectra with an instantaneous wavelength coverage between 1.37-2.56 μm covering 26 spectral orders. These have been observed in the highest spectral resolution mode, using the $1'' \times 0.2''$ slit and the f/5.6 camera mode, aiming for the instrumental upper limit of $R = 30,000$. The observations were obtained in combination with the f/15 adaptive secondary mirror and adaptive optics system at the 6.5-m MMT Observatory on Mt Hopkins in Arizona, USA. The adaptive secondary mirror provides a low thermal background while augmenting the total throughput of the instrument. The simultaneously operated ARIES imager was used for in-slit guiding, with occasional manual offsets made to correct any sustained drift during an exposure not corrected by the AO guiding system.

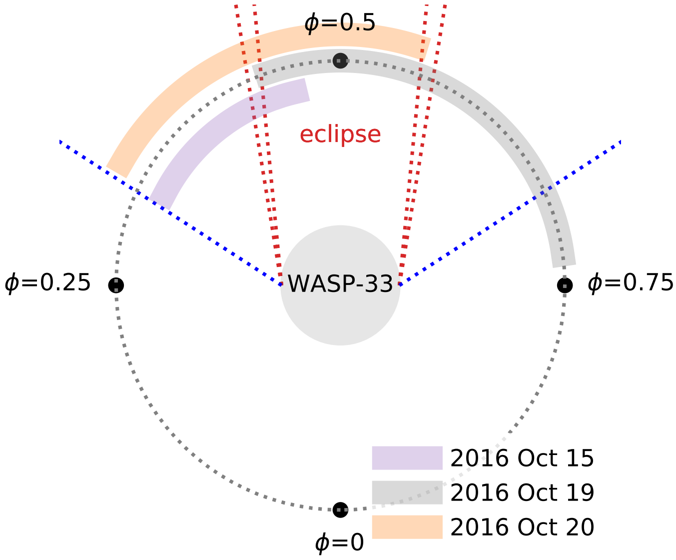

Figure 3.2: Orbital phase (ϕ) coverage for each observing night of the WASP-33 data set. WASP-33 b orbits its host star in a retrograde orbit. As can be seen, all nights contain some spectra taken during the full eclipse of WASP-33 b. The blue dotted line indicates up to which phases I have symmetric phase coverage for both the pre- and post-eclipse data.

At the beginning and end of each half-night, a set of calibration images were observed. This included a set of dark frames obtained using a blank in the filter wheel and the ARIES entrance covered to prevent any light from entering the instrument with exposure times similar to the flats and sciences. The flat fields were observed with the grating in, using an incandescent light bulb arranged such that its light reflected off an aluminized board into the dichroic of ARIES. A thorium-argon lamp was used in a similar manner at the start of the night to focus the spectrograph, but used the observed telluric absorption lines for simultaneous wavelength calibration. An overview of all data obtained as part of MEASURE on each of the targets is given in Table 3.2. This includes both day- and night-side data on all of the targets.

Target	Observed dates (UT)	Observed times (UT)	Phase range	Total observing time (h)
WASP-33 b	15/10/2016	08:08-12:10	0.32-0.45	4
	19/10/2016	03:30-11:45	0.44-0.72	8
	20/10/2016	05:25-11:47	0.32-0.54	6
	10/02/2017	02:21-03:15	0.85-0.88	1
	11/02/2017	02:07-02:37	0.66-0.68	0.5
KELT-7 b	20/02/2016	03:06-04:44	0.16-0.18	1.5
	21/02/2016	02:24-06:14	0.51-0.57	4
	23/02/2016	06:23-07:12	0.31-0.32	1
	26/02/2016	02:53-06:19	0.35-0.40	3.5
	17/10/2016	06:37-12:43	0.97-0.06	6
	09/02/2017	06:27-07:33	0.02-0.04	1
	11/03/2017	02:35-06:00	0.93-0.98	3.5
	14/03/2017	02:20-05:00	0.02-0.07	2.5
HD 143105 b	20/02/2016	08:13-13:13	0.99-0.08	5
	21/02/2016	09:07-13:14	0.46-0.54	4
	24/02/2016	07:54-12:39	0.80-0.89	4.5
	25/02/2016	07:50-12:23	0.26-0.34	4.5
	26/02/2016	07:28-10:44	0.70-0.77	3
	26/05/2016	08:52-11:33	0.69-0.74	2.5
	11/03/2017	06:25-13:10	0.16-0.29	7
	13/03/2017	02:34-04:53	1.00-0.04	5
	14/03/2017	06:16-13:00	0.52-0.65	7
HD 187123 b	24/05/2016	10:45-12:03	0.72-0.74	1.5
	14/10/2016	02:39-06:44	0.79-0.85	4
	20/10/2016	02:44-03:40	0.73-0.74	1
HD 86081 A b	21/02/2016	06:39-08:19	0.05-0.09	1.5
	03/12/2017	05:09-08:54	0.83-0.91	4
τ Böo A b	19/02/2016	11:02-13:05	0.61-0.63	2
	23/02/2016	07:52-13:21	0.78-0.85	5.5
	26/02/2016	11:56-12:46	0.73-0.74	1
	26/05/2016	03:26-08:45	0.80-0.86	5
	09/02/2017	08:01-11:21	0.93-0.97	3.5
	10/03/2017	09:41-12:57	0.31-0.30	3
HD 149143 b	12/03/2017	09:12-12:57	0.43-0.46	4
υ And b	27/10/2015	08:22-11:10	0.65-0.67	3
	01/11/2015	05:50-07:11	0.71-0.72	1.5
	15/10/2016	02:10-11:09	0.26-0.34	8
	16/10/2016	02:33-12:25	0.48-0.57	10
51 Peg b	27/10/2015	01:34-07:55	0.58-0.64	6.5
	31/10/2015	03:19-08:03	0.54-0.59	4.5
HD 46375 A b	31/10/2015	08:27-12:41	0.58-1.00	4
	01/11/2015	08:07-12:49	0.93-0.39	5
HD 49674	12/03/2017	02:34-04:53	0.58-1.00	2
	13/03/2017	02:48-07:11	0.93-0.06	7

Table 3.2: Details of the observing runs for each target in the MEASURE survey. Times have been rounded up to the closest half hour.

3.3 MEASURE observations of WASP-33 b

3.3.1 Introduction to WASP-33 b

One well-studied UHJ for which a thermal inversion was predicted by atmospheric modelling is WASP-33 b. This planet orbits every 1.22 days around an A5 star (Collier Cameron et al., 2010). The first observational evidence of a thermal inversion of WASP-33 b's atmospheric profile was excess infrared emission observed by Spitzer from secondary eclipse observations (Deming et al., 2012; Zhang et al., 2018) and NIR low-resolution HST/Wide Field Camera 3 spectra, possibly due to TiO (Haynes et al., 2015).

As WASP-33 is a δ Scuti pulsator (Herrero et al., 2011). In low-resolution data, these pulsations show up as continuum variation due to variability of the stellar flux, which needs to be corrected (e.g. Zhang et al., 2018). In high-resolution data, it can show up as correlated noise in the CCF. This is caused by the deformation of the spectral lines as the pulsations induce irregular blue and redshift on different parts of the stellar disk. If a species is present in both the star and exoplanet, the stellar line profile is not stationary and therefore residuals persist when cleaning the data with an algorithm like SVD. These residuals show up as correlated noise in the CCF. The effect of stellar pulsations has been observed in the detection of neutral iron lines in WASP-33 b by Nugroho et al. (2020b) and Herman et al. (2022).

Attempts to follow up the tentative low-resolution detection of TiO in the atmosphere of WASP-33 b using high-resolution spectra have led to inconclusive results so far. Nugroho et al. (2017) detected the optical TiO molecular signature using the High Dispersion Spectrograph on the Subaru Telescope. Herman et al. (2020) analysed emission and transmission spectra from the Echelle SpectroPolarimetric Device for the Observation of Stars (ESPaDOnS) on the Canada-France-Hawaii Telescope and the High-Resolution Echelle Spectrometer (HIRES) on the Keck telescope, but as they find a non-detection of TiO they are unable to constrain the presence or absence of a thermal inversion. The detection by Nugroho et al. (2017) was later challenged by a re-analysis of the same data by Serindag et al. (2021) who found a weaker signal using the updated TiO ExoMol TOTO line list. There is thus a lack of a current consensus regarding the observational evidence for TiO in the atmosphere of WASP-33 b.

Several new detections show that WASP-33 b must have a thermally inverted atmosphere. This is in line with predictions that alongside TiO and VO, atomic/ions in UHJs can contribute to inverted P-T structures (Lothringer et al., 2018; Gandhi & Madhusudhan, 2019). Recently, emission lines of FeI (Nugroho et al., 2020b; Cont et al., 2021a), neutral Si (Cont et al., 2021b), and OH (Nugroho et al., 2021) have been detected. Nugroho et al. (2021) also only marginally detect H_2O, consistent with a low water abundance on the dayside due

Date (UTC)	Total exposure time (min)	No. spectra	Phase Coverage	SNR*
2016 Oct 15	220	44	0.331-0.469	91
2016 Oct 19	465	93	0.461-0.731	26
2016 Oct 20	370	74	0.337-0.554	71

*This quantity refers to the median SNR per wavelength element as measured from the extracted and normalised spectral time series of the 23rd spectral order around the 2.3μm CO emission region.

Table 3.3: Observational parameters of the WASP-33 data set for each night.

to water dissociation into OH and H^- at these temperatures. Other atmospheric detections for WASP-33 b include Ca II (Yan et al., 2019), the hydrogen Hα, Hβ and Hγ Balmer lines (Cauley et al., 2021; Yan et al., 2021; Borsa et al., 2021c), tentative evidence for AlO (Von Essen et al., 2019), and lastly, Kesseli et al. (2020) place upper limits on the Volume Mixing Ratio (VMR) for FeH based on their null detection.

In this chapter, I will report the first detection of CO emission lines in the atmosphere of WASP-33 b using observations with the MMT/ARIES combination as reported in my first-authored paper (van Sluijs et al., 2023). First, this result demonstrates the capability of MMT/ARIES to characterise exoplanet atmospheres and I will use these results to assess its performance. Second, via the detection of CO emission lines, I provide unambiguous evidence of a thermal inversion in the atmosphere of WASP-33 b. The detection of CO emission lines in the atmosphere of WASP-33 b has now been confirmed by later studies, (Yan et al., 2022; Finnerty et al., 2023), highlighting the significance of these first findings and providing confidence in these results. CO emission lines have now also been confirmed in other UHJs besides WASP-33 b, namely in the atmospheres of WASP-189 b, WASP-18 A b, WASP-76 b and MASCARA-1 b (Brogi et al., 2022; Holmberg & Madhusudhan, 2022; Yan et al., 2022, 2023).

3.3.2 Observations of WASP-33

The same observing setup and strategy as previously described in Section 3.2 were used. In total 211 spectra of the WASP-33 system were obtained with an exposure time of 300 s per frame. An overview of the observed orbital phase coverage is shown in Fig. 3.2 and listed in Table 3.3. Orbital phases have been calculated using a period of $P = 1.21986967$ d and a primary transit time of 2454590.17936 BJD (Smith et al., 2011) using equation (2.18). The three observing nights cover both pre- and post-eclipse orbital phases, but the post-eclipse data covers significantly more of the orbit, almost to quadrature, where the planet shows half its day-side and half its night-side to the Earth.

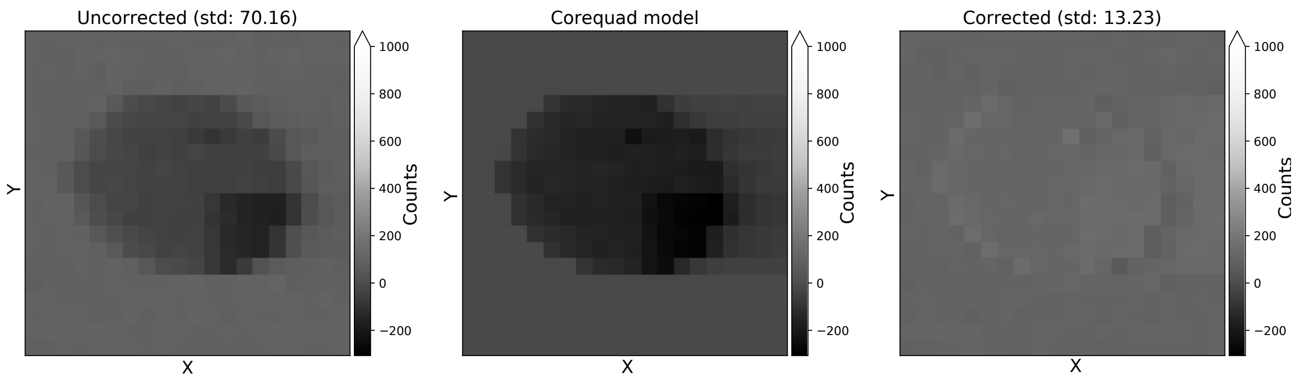

Figure 3.3: Result of the cross-talk correction. Each panel shows a prominent ghost image on one of the quadrants. *Left:* the ghost-like image pre-correction. *Middle:* the ghost image model produced by CORQUAD. *Right:* the ghost like image post-subraction of the CORQUAD-model.

3.4 Pre-processing pipeline

In this section, I describe the pre-processing of the MEASURE data: how to turn the raw detector science, dark, and flat frames captured with the ARIES/MMT combination into a wavelength-calibrated spectral time series. I describe the final version of the pre-processing pipeline here. This pipeline is now publicly available on my Github[1]. All examples are shown for the first night of the WASP-33 observations obtained as part of the MEASURE.

3.4.1 Cross-talk correction

ARIES experiences cross-talk between the four quadrants of its detector which needs to be corrected. Cross-talk occurs when a source in one quadrant creates a negative mirror image or ghost in another quadrant. These ghost images for ARIES are distinctly cross-shaped, negative shadows at the same position in all other three quadrants on the detector. This effect is apparent in all dark, flat, and science frames. I use the C-based CORQUAD routine provided by the ARIES team[2] to correct for the cross-talk. Three input parameters define the convolution kernel size for each detector quadrant. The parameter space is explored using a grid-based search to find the best cross-talk convolution kernels, which I define as those that minimize the standard deviation in a 10×10 box around a visually identified prominent shadow feature. The size of this box was chosen by trial and error to be sufficiently large to encompass most distinct ARIES cross-talk features, without including too much background. I apply the CORQUAD routine using the best convolution kernels parameters to all dark, flat, and science frames, before any further data reduction. Fig. 3.3 shows the

[1] `https://github.com/lennartvansluijs/ARIES`

[2] See `http://66.194.178.32/~rfinn/pisces.html`. A Python-based version is available at: `https://github.com/jordan-stone/ARIES`

result of applying the crosstalk correction to one of the prominent ghost images in one of the quadrants.

3.4.2 Dark correction

In each science and flat frame part of the electron count can be attributed to the thermal background, the so-called dark current, which needs to be subtracted. First, the individual dark frames may still contain cosmic rays and hot pixels, which show up as bright outliers, and these need to be corrected in each individual dark frame before combining them into a master dark. I identify hot pixels as $\geq 3\sigma$-outliers. Hot pixels are cross-shaped and I replace them with the median of their neighbours outside of a cross-shaped footing in an 11×11 box around each hot pixel. Second, I median combine all frames of identical exposure time into a master dark. Essentially these dark frames estimate the total dark current in each individual science/flat frame given their exposure time. This is done uniquely for each exposure time at which sciences/flats were observed, as the dark current might not scale linearly with exposure time. Finally, to complete the dark correction, I subtract the appropriate master dark from each science and flat frame.

3.4.3 Flat correction

The flat correction involves two key steps. First, all flats contain fringes arising from Fabry-Pérot interference between the optical elements of the instrument, which needs to be removed. These fringes in the flat field introduce modulation in the continuum that would be erroneously divided into the science flat during flat field correction, reducing the sensitivity of later procedures. Second, I follow the standard flat procedure, where I create a master flat and divide this out of each science frame to correct for inter-pixel variations in the images.

To remove the fringes from the flats, I developed a modified version of the flat fringe correction by Stone et al. (2014). The procedure is shown in Fig. 3.4. The key idea of the procedure is to first 'straighten' the curved traces of the flats on the detector, such that they appear as straight lines. For this, I use the solution of all 26 spectral orders to calculate a 2D polynomial transform to dewarp the flat frame. In the 'straightened' reference frame, I can model the fringes more easily, because the fringe pattern will only be a function of the transformed x-coordinate. After creating a fringe model in this reference frame, I can transform the model back to the original data rest frame using the inverse 2D polynomial transform. This way the fringe model can be subtracted from the data in the original rest frame, and therefore there is at no point any interpolation or alteration of the original pixel-by-pixel noise properties.

In practice, I use the *getthem* routine from the publicly available Python package CERES by Brahm et al. (2017) to fit the echelle traces as 4th-order polynomials using a 10-pixel wide aperture. I fit each row by a 7th-order polynomial to create a dewarped illumination model, essentially representing the dewarped blaze function. This model is subtracted from the dewarped flat frame to reveal the dewarped flat fringes. Most fringes have frequencies <0.025 pixel^{-1}. Therefore, I apply a 6th-order Butterworth high-pass filter with a cut-off frequency $f_c = 0.025$ pixel^{-1} to create a dewarped fringe model. I then use the inverse 2D polynomial transform to warp the fringes model. I remove the fringes from the observed flat frame by subtracting the warped fringes model. As mentioned before, it is key this subtraction is done in the observed coordinate frame such that the observed flat was not interpolated by a transform operation, thus preserving any inter-pixel systematics.

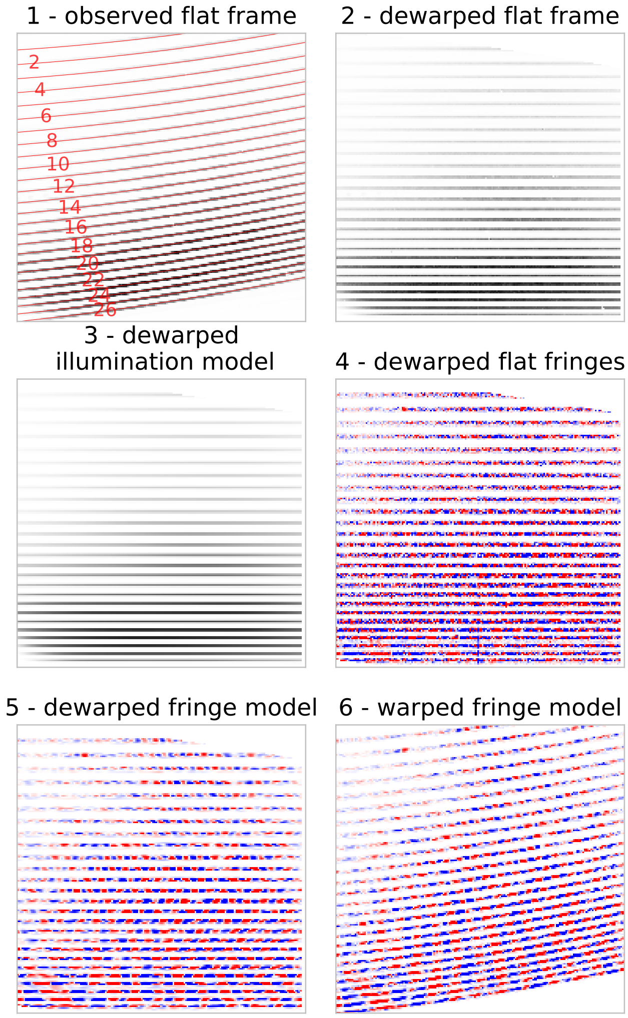

Figure 3.4: Flat fringe correction illustrated in six steps: (1) the observed flat frame with the fitted echelle traces overlaid in red (numbered from blue-to-red). (2) the flat frame after applying a 2D polynomial transform to straighten the echelle traces. (3) the 4th order polynomial row-by-row illumination model. (4) fringes revealed by dividing the dewarped illumination model from the dewarped flat frame. (5) row-by-row low-pass filter fringe model. (6) final fringe model after applying the inverse 2D polynomial transform.

After defringing all flats, I perform a hot pixel correction similar to the one done for the dark frames and create a master flat. The ARIES detector has a central column of dead pixels. I correct this column by replacing it with the median of the two neighbouring columns in the master flat or science frames. To create an outlier pixel map from the master flat, I first normalize the master flat by dividing out the illumination model and identifying pixels with values outside of the [0.5, 1.5] range as outliers. I combine the outlier pixel map from the master flat with the master dark hot pixel map and replace all master flat hot pixels with the fit from the illumination model. For each science frame, I correct each flagged pixel by their closest neighbours in the dispersion direction of the spectrograph. Finally, the master flat is divided out of all of the science frames.

The science frames still contain fringes at this stage, but it is much harder to fit these fringes due to the discontinuity of the echelle traces in the science frames. Instead, I correct these by applying a high-pass filter to the extracted spectral time series in the post-processing stage of the pipeline. However, it is still important that the flat frames were fringe-corrected before division from each science frame to avoid introducing additional fringing in the sciences, as the fringe patterns in the sciences and flats are distinct.

3.4.4 Spectral order extraction

After the flat correction, the spectral orders in the science frames are ready to be extracted. I cannot directly fit the detector echelle traces for the science frames as these fainter traces are often disrupted due to telluric absorption lines. Instead, I use the continuous master flat traces as a reference by using the CERES RETRACE routine. This treats the initial set of master flat traces as an aperture mask and cross-correlates it with each science frame to determine the drift in the cross-dispersion direction. This drift may be caused due to changes in the direction of the gravity vector on ARIES since the instrument is mounted on the back of the moving telescope. The effect of drift on the echelle traces during the course of an observing night is shown in Fig. 3.5. These drifts are on the order of several pixels a night, so I cannot assume the echelle traces are stationary during the course of one observing run. The final science echelle traces are the master flat trace solutions with the time-dependent drift in the x- and y-direction linearly added to them.

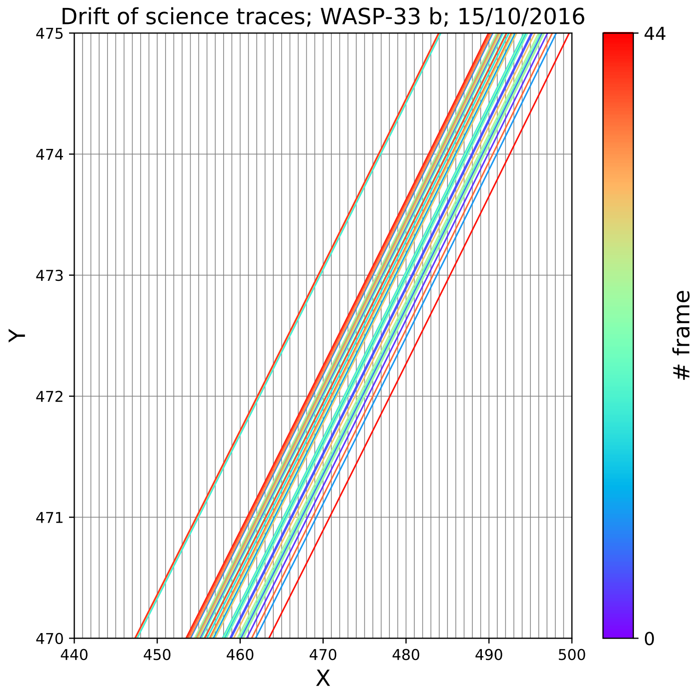

Figure 3.5: Drift of the echelle traces on the science frames for the observing night of 15/10/2016 of WASP-33 b. Discontinuous jumps of several pixels are observed.

Once I have a solution for the science traces of each spectral order on each frame I use the CERES MARSH-algorithm (Marsh, 1989)[3] to extract the 1D spectra for each spectral order from each frame. The MARSH-algorithm assigns appropriate weights to each pixel on the echelle trail to maximise the output spectrum signal-to-noise ratio. The algorithm has the advantage of fitting for variations in the profile shape, which occurs commonly due to varying focus of the instrument or change of pointing which causes variations of the incident flux on the slit. The MARSH-algorithm is thus an excellent algorithm to extract 1D spectra for cross-dispersed echelle spectrographs such as ARIES. I use the algorithm with a 5-pixel aperture radius and clipping $>5\sigma$ outliers to ignore remaining hot pixels for example due to cosmic rays. In the first step of the MARSH algorithm, the optimal weights are calculated. Secondly, these weights are used to sum the flux in the trace of each science frame.

The result of the spectral extraction for one of the frames is shown in Fig. 3.6. I have highlighted specific features of interest. Telluric lines are clearly visible in some of the orders already by eye (see orders 1-2). Because I did not remove the science fringes, a fringe pattern can still be seen superimposed on some of the orders (see pixels > 512 for orders 18-22). Rather than correcting for this on an image frame level, I will correct for these by high-pass-filtering the spectra during the post-processing stage. Although most-outliers are filtered by the pre-processing steps, some spectra still show significant outliers (see order 22). These also need to be corrected in the post-processing stage of the pipeline.

The final result after extraction of all spectral orders from all the science frames is a raw unaligned spectral time series. The result for the first observing night of WASP-33 b is shown in the top panel of Fig. 3.7.

3.5 Post-processing pipeline

The post-processing of the data involves turning the raw, unaligned, and uncalibrated spectral time series into a residual, aligned, and wavelength-calibrated spectral time series. An overview of the spectral time series after each subsequent step is shown in Fig. 3.7.

[3]This is a generalisation of the Horne optimal extraction algorithm (Horne, 1986), which is also commonly used to extract echelle traces from detector images. The Marsh algorithm works better, especially for highly tilted echelle spectra that cross many columns.

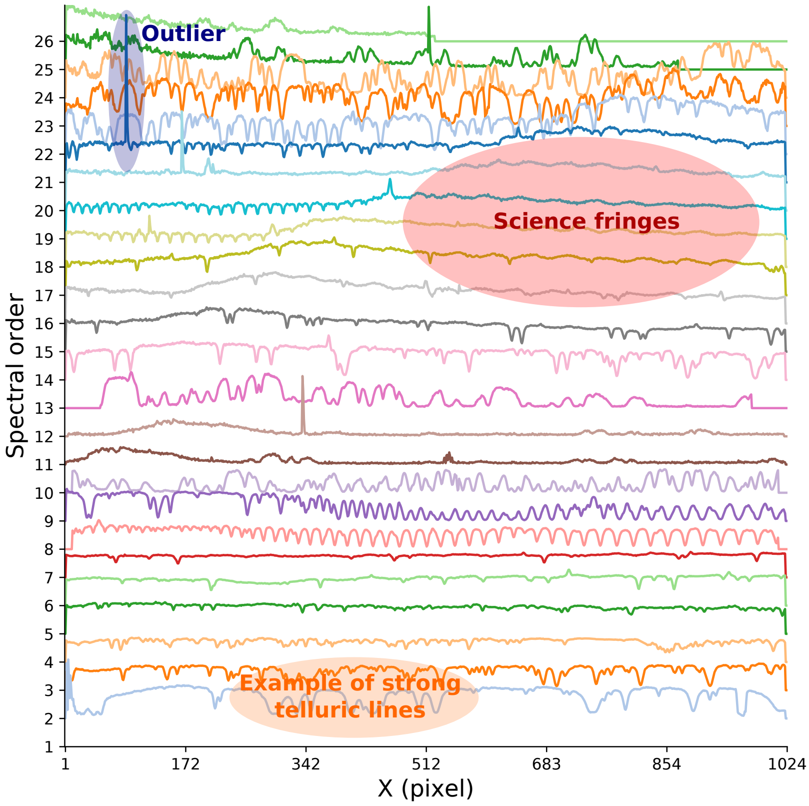

Figure 3.6: Example of the spectra extracted for each of the 26 spectral orders on a single science frame using the MARSH-algorithm. The spectral orders roughly cover a wavelength range from 1.4 to 2.6 μm. I have highlighted features of interest that require correction in the post-processing.

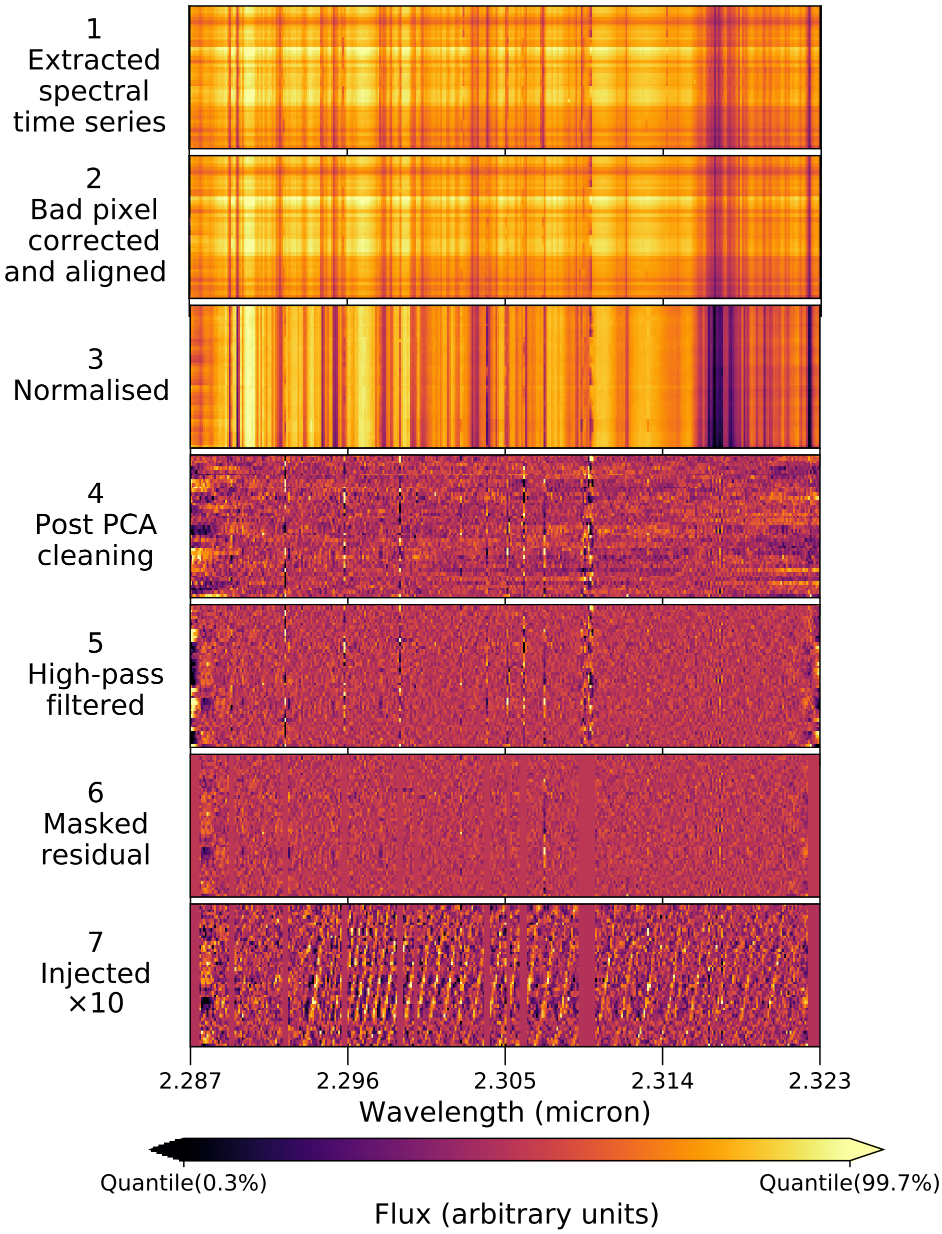

Figure 3.7: Example of post-processing procedure of a spectral time series for order 23 (2.28-2.32 μm) for the first observing night of WASP-33 b. *First panel:* The extracted spectral time series from the processed detector image is shown in the top panel. *Second panel:* after bad pixel/column correction and alignment with respect to the first spectrum. *Third panel:* normalised by the median of the 50 brightest pixels per spectrum. *Fourth panel:* after removing the first 7 components using Principal Component Analysis. *Fifth panel:* After applying a high-pass-filter with cutoff-frequency of 0.02 pixel^{-1}. *Sixth panel:* After masking the columns with the worst residual structure. *Seventh panel:* same as the previous panel, but with a WASP-33 b model injected at $\times 10$ the nominal strength into the spectral time series between panels 2 and 3.

3.5.1 Bad pixel/column correction

In each spectral time series, some bad pixel columns or detector artifacts may still be present in the spectral time series. To reveal these anomalies, I normalise each spectrum by the median of each row, followed by subtracting the mean of each column.

I use a Blob Detection Algorithm (an edge-detection algorithm), which uses a Laplacian of the Gaussian Filter to detect outliers, as described in more detail by Kong et al. (2013). In this application, I identify features of the size of a single pixel. These outliers are corrected by interpolating in the dispersion direction over the closest nearby good pixels. I ignore any convolution boundary effects here as they only affect the edge pixels and these will be clipped during the post-processing stage of the pipeline.

Bad columns in the spectral time series are identified by taking the median of each spectral channel and applying a median filter using a three-pixel width then subtracting this from the original. As before I use the Blob Detection Algorithm to identify 5σ-outliers in the residual time series which are considered bad columns and are corrected by interpolation from their nearest neighbouring good columns in the dispersion direction. I iteratively performed the bad pixel and column correction procedure five times to ensure all outliers were corrected. In total, only $\sim$0.2% of all pixels are identified as outliers.

3.5.2 Alignment of spectra

Effects such as instrumental flexure, variation of the air mass, or misalignment of the star on the spectrograph slit, can all cause sub-pixel drift of the spectra across the detector. I need to align the spectra to correct for these effects, or else they will leave residuals later in the telluric line removal procedure. The data themselves are used as a reference: the first spectrum of every night is used as a reference spectrum, thus the alignment will be in the telluric rest frame of the first spectrum. The alignment procedure is done in three steps. Firstly, the reference spectrum is cross-correlated with each frame. Secondly, I fit a Gaussian to the CCF to determine the drift on a sub-pixel level for each frame. Finally, I shift each spectrum using linear interpolation to align it with the reference spectra. The final result is shown in Fig. 3.7, panel 2.

3.5.3 Telluric wavelength calibration

After alignment, I perform wavelength calibration using the observed telluric lines. I do not use lines from a standard lamp, because for high-resolution spectroscopy the wavelength solution needs to be precise for each science frame. ARIES does not have an instantaneous standard lamp, so the solution for each frame will deviate from one take at the start or the end of the observing run. Additionally, the standard lamp does not have sufficient lines in some spectral order to provide an accurate wavelength solution.

I generate a telluric model using ATRAN[4] (Lord, 1992). For each aligned spectral order I cross-match by-eye telluric lines in the model to the corresponding telluric lines in the median of the observed spectra[5]. I robustly fit a polynomial to all these visually identified wells for each order to obtain a wavelength solution. Robust here refers to the fact that I iteratively clip $\geq 5\sigma$ outliers and refit a polynomial until no more outliers are found. By default, I fit 3rd-order polynomials, but for some orders where there are few absorption lines towards the edges of the detector, I fitted 2nd-order polynomials instead, to avoid massive deviation of the wavelength solution towards the edges. All these fits were manually inspected to ensure a proper wavelength solution was obtained. For some orders, the wavelength solutions were poorly constrained due to strong residual science fringes and/or weak telluric absorption features. For these reasons, I excluded orders 7-9 and 11 from the rest of the analysis. This may impact the power of this dataset to constrain molecules with many transitions in this wavelength region such as H_2O, but e.g. not CO as this molecule has no spectral lines in this wavelength region. The wavelength solution and root mean square (RMS) deviation for each spectral order are shown in Fig. 3.8 for the first observing night.

3.5.4 Throughput correction

Throughput variations can be caused by variations in airmass and misalignment of the target on the slit. I correct for these variations by dividing by the mean of the brightest 50 pixels per spectrum as per the procedure described in Brogi & Line (2019). The final result of the throughput correction is a normalised spectral time series as shown in Fig. 3.7, panel 3.

[4] https://atran.arc.nasa.gov/cgi-bin/atran/atran.cgi

[5] In subsequent analysis of other MEASURE targets I have automated this and eliminated the need for manually checking each spectral order. This procedure is described further in Section 4.2.1.

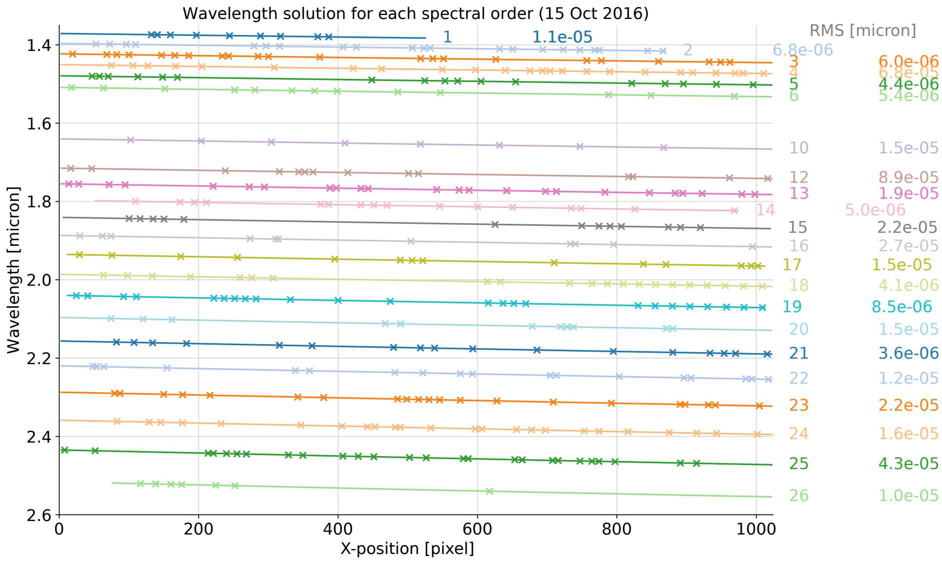

Figure 3.8: Wavelength solution for each spectral order for the first observing night. For each order, the points indicate visually identified telluric absorption lines, and the lines indicate the best-fit polynomial. The root mean square (RMS) values of the difference between the points and the wavelength solution are noted to indicate the quality of the fit for each spectral order. Some masked orders for which no good wavelength solution was found have been omitted.

3.5.5 Telluric removal

Quasi-stationary trends mostly due to the telluric lines still dominate the spectra. To remove these, Principal Component Analysis (PCA) is used to decompose the spectral time series. In the implementation, I perform a Singular Value Decomposition (similar to de Kok et al., 2013; Line et al., 2021). A visual inspection of other ARIES observations of other systems indicates that using seven Principal Components works well to balance telluric removal and retrieve an injected exoplanet signal at a high SNR, so I adopt this also for WASP-33 b. However, I emphasize that keeping the number of PCA components fixed for all spectral orders and all observing nights is at the sacrifice of order/night-specific systematic effects and noise. However, previous studies have shown optimising the number of PCA components for each order/night can produce artificially large spurious SNRs (e.g. (Cabot et al., 2020; Spring et al., 2022)). The result of the PCA cleaning is shown in panel 4 of Fig. 3.7.

Remaining low-frequency residuals persist due to several effects: (1) throughput variations due to small offsets of the target position on the spectrographs slit entrance; (2) residual airmass variations; (3) echelle trace drift on the detector due to the changing gravity vector during the observations, causing instrumental flexure; and (4) uncorrected science frame fringes. I found a 6th-order Butterworth high-pass filter with a cutoff frequency of 0.02 pixel^{-1} to remove most of these trends, that is by visual inspection the majority of fringes are removed. This frequency was chosen to be just below the typical fringe frequency reported previously in Section 3.4.3. The result of the high-pass filtering of the residuals is shown in panel 4 of Fig. 3.7.

3.5.6 Masking

The remaining bad columns in the residual time series are masked. This is done by identifying $> 3\sigma$ outliers in the residual matrix and flagging columns with more than five outliers. I combine flagged columns if there are more than two columns within a five-pixel-wide sliding window. Additionally, the columns in a 50-pixel window from the edge of the detector are masked by default. Masked columns are shown in panel 6 of Fig. 3.7.

3.6 Observed instrumental performance

MEASURE is the first survey aiming to characterise exoplanet atmospheres using high-resolution spectra from ARIES/MMT and therefore it is key to measure the observed instrumental performance and compare it to the theoretical instrumental performance. I use a data-driven approach where I measure the instrumental throughput, spectral resolving power, and Precipitable Water Vapour (PWV) from the telluric lines in the normalised spectral time series. The instrumental throughput is measured directly from the total SNR for each spectrum by measuring the SNR of the continuum in each frame and dividing it by the average continuum SNR. The observed resolving power and PWV are measured by following the procedure described by Chiavassa & Brogi (2019). They cross-correlate the normalised spectral time series with a telluric model and evaluate the log-Likelihood defined by Zucker (2003).

The cross-correlation is sensitive to variations in the shape of the continuum, which can result in incorrect measurements of the PWV and spectral resolving power. Therefore, I fit for the shape of the continuum in each observation and divide it out of each observation, before cross-correlation with a telluric model. The continuum correction is done in the following way: (1) a median filter removes any possible 5σ outliers (2) each spectrum is binned and the maximum of each bin is calculated (3) I fit a low 3rd-order polynomial to these local maxima and (4) I divide out this polynomial fit from each spectrum.

The TELFIT code is used to compute telluric spectra (Gullikson et al., 2014). I chose to use TELFIT over ATRAN as it can be called easily and iteratively from a custom PYTHON script, whereas ATRAN uses a web-based graphical interface. I fix the airmass to the logged airmass for each frame which I obtain from the raw FITS-header information, instead of keeping it a free parameter as done by Chiavassa & Brogi (2019). The Markov Chain Monte Carlo (MCMC) PYMULTINEST (Buchner et al., 2014) package is used to explore the 2-dimensional parameter space with the PWV and spectral resolving power as free parameters.

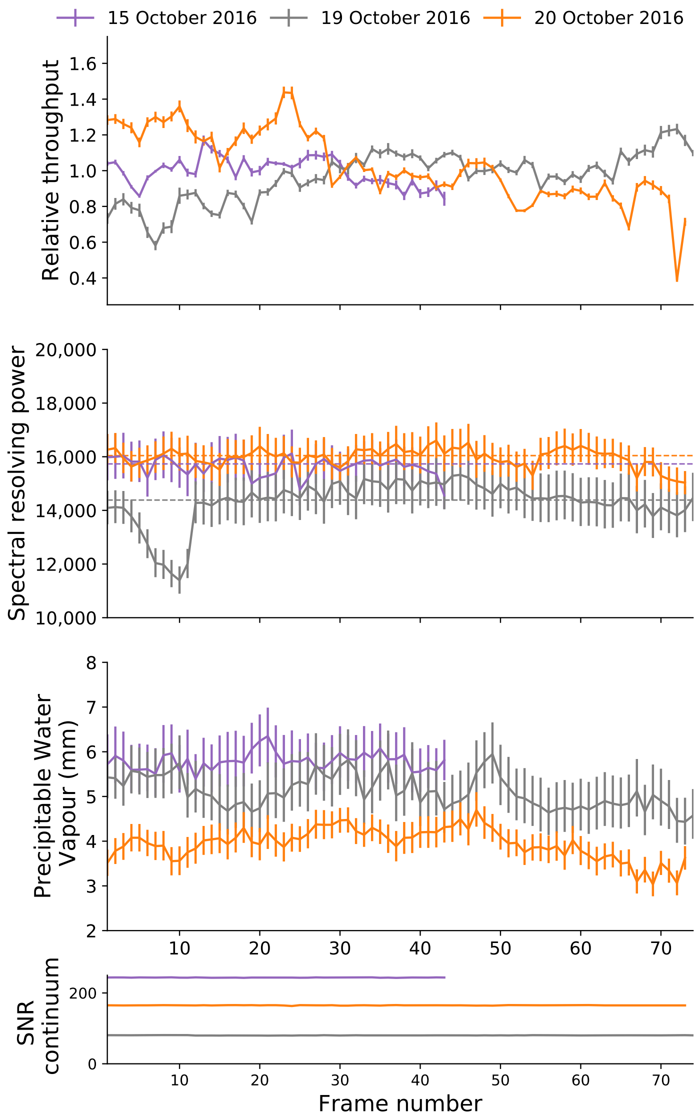

Figure 3.9: Relative throughput, spectral resolving power, PWV and continuum SNR for each observing night of the WASP-33 system, as measured from order 23 which is centered around the CO 2.3 μm spectral feature. The dashed lines indicate the median resolving power used to convolve the spectral templates for each night. The overall consistently reduced resolution of ARIES is hypothesised as sub-optimal focusing of the spectrograph.

The measured relative throughput, instrumental resolving power, and PWV are shown in Fig. 3.9. A key result is that the measured spectral resolving power $R = 14,000 - 16,000$, is notably lower than the nominal specification for ARIES of $R = 30,000$. I hypothesize this large offset may be due to the sub-optimal focus of the spectrograph resulting in consistently lower observed spectral resolution. The other fluctuations of spectral resolving power in the course of each night could be due to a combination of target misalignment on the slit entrance, instrumental instability, and occasional opening of the AO loop. This analysis also highlights the importance of measuring the spectral resolving power from the observations when using HRCCS, as the cross-correlation templates will need to be convolved to the appropriate spectral resolution later on. If I used the theoretical instrumental spectral resolution here, I would have features at a higher spectral resolution in the model template compared to the data, likely resulting in a poorer match and thus lower cross-correlation values.

3.7 HRCCS of WASP-33 data

Despite the relatively low spectral resolution, I will now show that ARIES/MMT still has the capability to successfully characterise an exoplanet atmosphere using the high-resolution cross-correlation spectroscopy technique. I follow the SNR-method HRCCS methodology as previously described in Section 2.3.2 to three nights of WASP-33 b data. In Section 3.7.1 I describe the models I used as cross-correlation templates. In Section 3.7.2 I describe the results from cross-correlating the residual time series with these model templates. Finally, I present in Section 3.8 the key result that came out of this analysis, namely the first detection of CO emission lines in an exoplanet atmosphere. This also proves that the ARIES/MMT combination has the capability to characterise an exoplanet atmosphere. This was one of the key science questions I aimed to address in this chapter.

3.7.1 Cross-correlation templates

To create cross-correlation templates for the exoplanet WASP-33 b I use 1D free models (see Section 2.2.2). These are computed with the atmosphere modelling code PHOENIX, which has been used to model stellar and exoplanetary spectrum (Hauschildt et al., 1997, 1999; Barman et al., 2001, 2011; Allard et al., 2011; Lothringer et al., 2018; Lothringer & Barman, 2019). The modelling approach used here for WASP-33 b is described in more detail in Lothringer et al. (2018), which I will summarise here.

This grid of models has varying P-T structures and atmospheric metallicity. A range of metallicities is explored with metallicity values of $0.1\times$, $1\times$, $10\times$, and $100\times$ Solar metallicity. For the P-T profiles, the parametrisation from Madhusudhan & Seager (2009) is used. It is

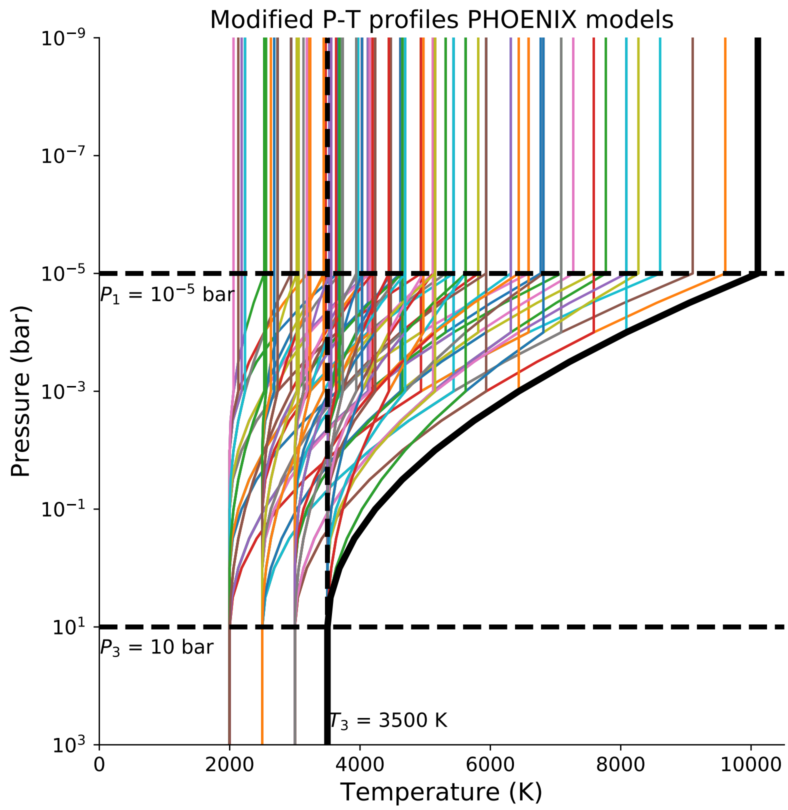

Figure 3.10: Overview of all modified PHOENIX P-T profiles explored. For the hottest P-T profile (bold black) the P_1, P_3 and T_1 are annotated.

modified to have an isothermal upper atmosphere. These simple structures use four parameters to describe the temperature throughout the atmosphere: P_1, P_3, T_3 and α. The deepest layer of the atmosphere ($P > P_3$) is at a temperature T_3. The temperature then varies until it reaches the tropopause at a pressure P_1, as set by α, the gradient of the inversion[6]. At lower pressures where $P < P_1$ the temperature is set equal to the tropopause temperature. A wide range of P-T profiles is explored with upper atmosphere temperatures from 2000 K to about 10,100 K, shown in Fig. 3.10. In total 576 forward models were run.

Another small subset of these models is computed to explore how removing a single opacity source affects the significance of the planet detection: the best matching model without H_2O, without CO, and without OH is computed again. This is done in order to identify potential absorbers or emitters in the atmosphere while keeping the P-T profile fixed. Line lists for the investigated opacity sources were taken from: CO (Goorvitch, 1994), OH (Barber et al., 2006), and H_2O (Rothman et al., 2009).

Alongside these 1D models, I also use full 3D templates which were simulated using a 3D Global Circulation Model (GCM).

[6]This follows the second line of equation (2.10), where $\alpha_2 = \alpha$ and one solves for T_2 at the boundary pressure P_3 where $T = T_3$.

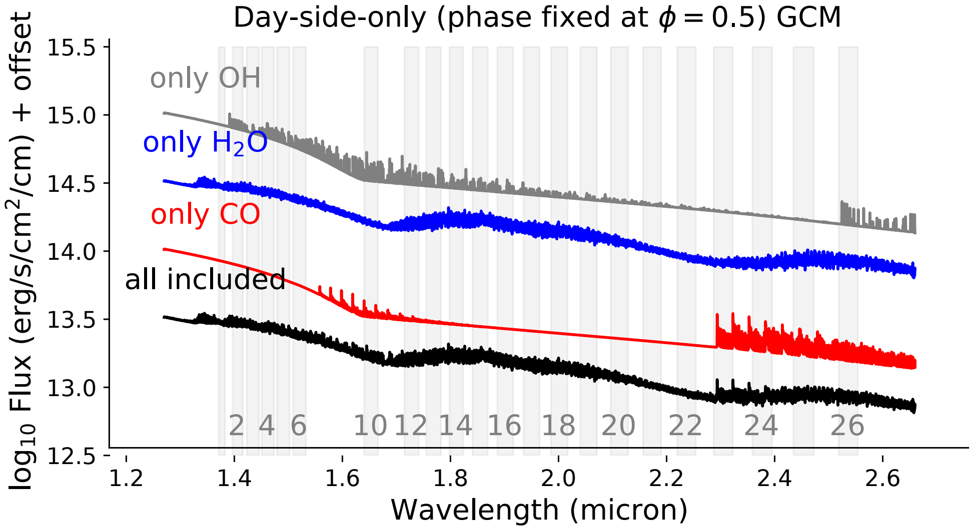

Figure 3.11: WASP-33 b GCM synthetic emission spectra convolved to the observed spectral resolution of $R = 15,000$. All spectra are day-side-only (i.e. fixed at phase $\phi = 0.5$) GCM spectra with all opacity sources included or only specific molecules included. The different models have been offset by 0.5 with respect to the "all included"-case along the y-axis for visual purposes. The ARIES spectral orders are indicated by the gray bars.

The SPARC/MITGCM (Showman et al., 2009) code is used with input parameters for WASP-33 b as described in Parmentier et al. (2018). The GCM output is then post-processed using the gCMCRT 3D RT code (Lee et al., 2021) to create template emission spectra. The 3D GCM modelling for WASP-33 b is described in more detail in Section 5.3.1. In this chapter, I will focus on results from cross-correlation with GCM templates at a fixed phase of $\phi = 0.5$. These are dayside-only models with the inclusion of all opacity sources, just CO, just H2O, and just OH. An overview of these cross-correlation templates is shown in Fig. 3.11.

3.7.2 SNR-analysis

Following the methodology described in Section 2.3. I cross-correlate with all 576 forward models 1D PHOENIX models with modified structure and/or abundances. I explore cross-correlation values on a 31×31 grid in ($v_{\rm sys}$, $K_{\rm p}$)-space centred around values of ($v_{\rm sys}$, $K_{\rm p}$) = (-0.3, 230.9) km/s. These central values are based on the previously reported detection of OH by (Nugroho et al., 2020b). This grid is explored within the range of ±100 km/s for $v_{\rm sys}$ and ±150 km/s for $K_{\rm p}$ on a 31×31 grid. For all 576, I compute the SNR and check whether the $v_{\rm sys}$, $K_{\rm p}$ are close to the expected planetary system parameters. Those exposures were taken in between the first and last contact of the eclipse of WASP-33 b (see Fig. 3.2), when the planet is not fully visible, are excluded from the SNR calculation to avoid dilution of the combined CCF signal. Not all spectral orders are equally sensitive when cross-correlating with the spectral template. Lower sensitivity is expected for the bluer ARIES orders because of poorer data quality, due to lower throughput, stronger fringes, and weaker spectral features in the

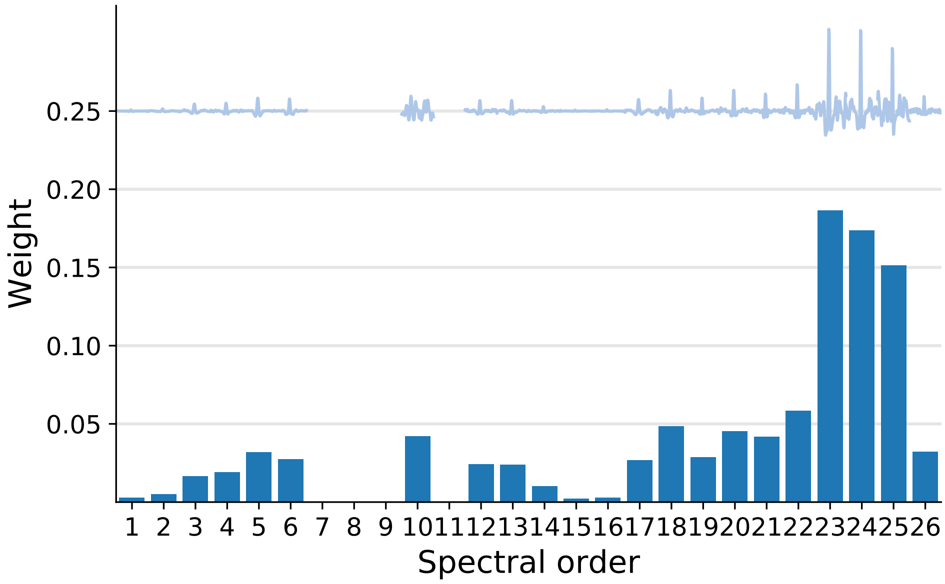

Figure 3.12: Example of the weights per spectral order after cross-correlation with a PHOENIX model spectral template. Weights are calculated from the SNR of the difference between the injected and observed CCF, indicated by the miniature CCF above each order. Orders 7-9 and 11 were excluded from the analysis in the wavelength calibration step. Orders 23-25 around the CO 2.3μm spectral feature are naturally assigned the highest weights, as these data are predominantly sensitive to CO emission lines.

models. To account for both, I use an order-specific weighting scheme in the SNR method to combine the CCF matrices, based on the data quality and model. To calculate the weights I follow Spring et al. (2022), where I first inject the model (before PCA cleaning) into the observations using the expected model strength and orbital parameters (using the values reported by Nugroho et al. (2020b)). I create a Cross-Correlation Function (CCF) matrix for each injected order, and then subtract its corresponding observed (no injection) CCF matrix. For each order, I calculate the SNR of this CCF difference. For each order n, weights w_n are assigned proportionally to this SNR and normalised such that $\sum_{n=1}^{N} w_n = 1$, where N is the total number of spectral orders included. An example of the weighting scheme is shown in Fig. 3.12. The reddest order (23-25) has the largest weights, which can likely be attributed to the $\sim$2.3 micron densely-packed CO spectral feature which overlaps with these spectral orders.

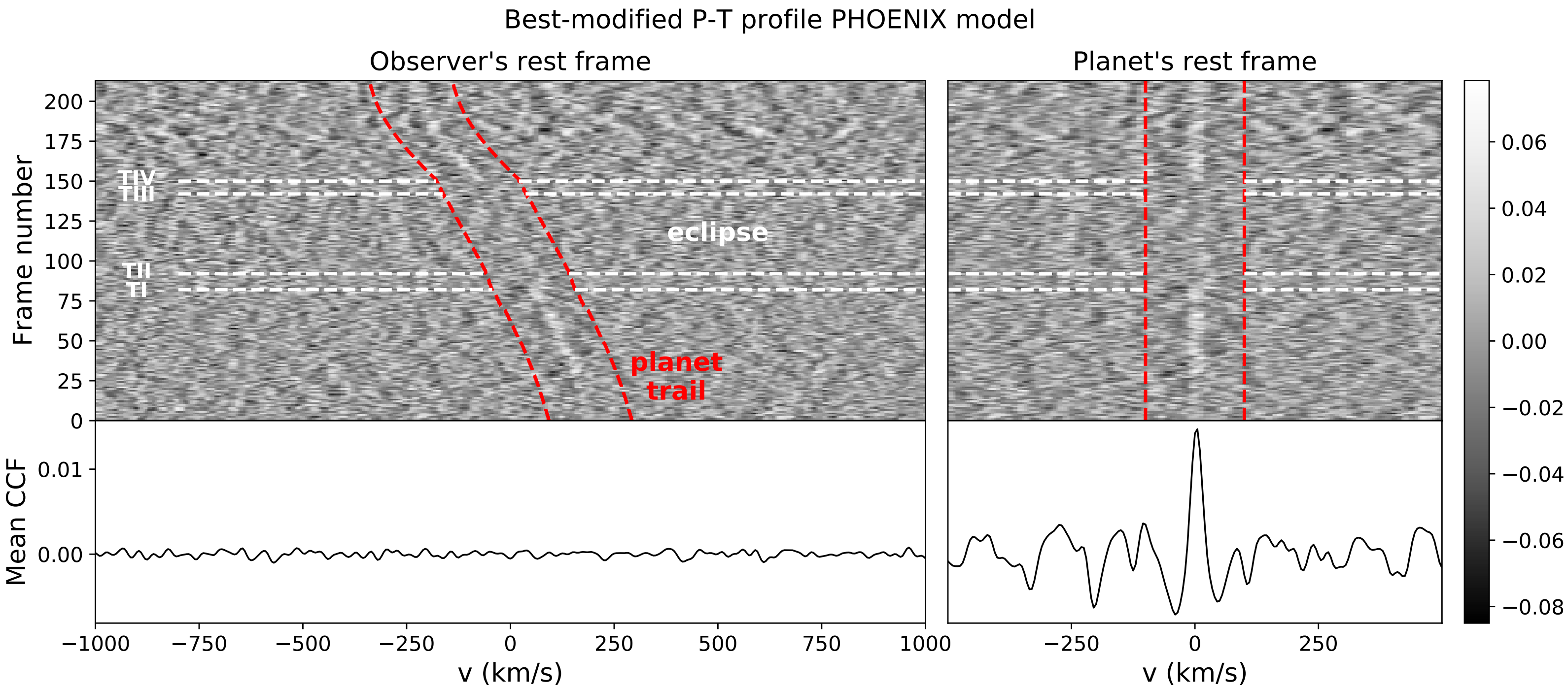

Figure 3.13: CCFs for the best-modified P-T profile detected at a SNR of 7.9σ. *Top-left:* The CCF for each frame including all three observing nights. Frames are sorted by orbital phase but are not equally spaced. The start/end of ingress/egress is indicated by the white dashed lines labeled TI-TIV for the four contact points. The two red lines are centered around the planet's radial velocity trail. The planet is clearly visible as a curved white trail. *Top-right:* Same as the top-left panel, but shifted to the planet rest frame. The planet is clearly visible as a vertical white trail. *Bottom-left:* the mean CCF along the y-axis. Frames, where the planet is not fully visible (in between TI-TIV), were excluded when computing the CCF to prevent dilution of the planet signal. *Bottom-right:* same as the bottom-right panel, but shifted to the planet's rest frame.

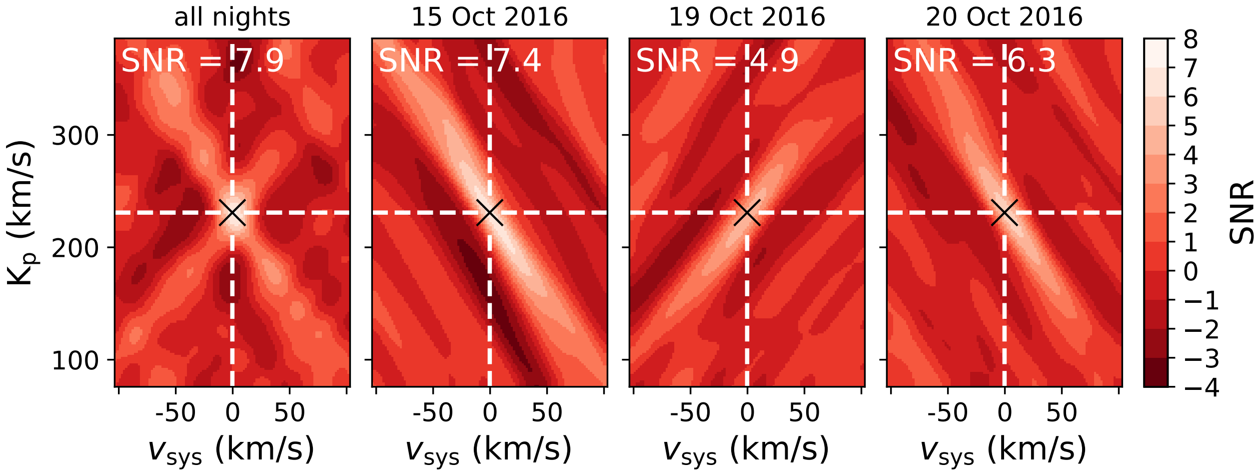

Figure 3.14: SNR as a function of the system velocity v_{sys} and orbital velocity K_p for the best PHOENIX (1D) modified P-T profile model. The gray cross-symbol marks the maximal SNR location. The dashed white grid indicates the expected location at (v_{sys}, K_p) = (-0.3, 230.9) km/s based on the OH detection by Nugroho et al. (2021). This detection is in agreement with their (v_{sys}, K_p)-value.

3.8 Results of HRCCS of WASP-33 data

3.8.1 Detection of the exoplanet atmosphere

The model that results in the highest SNR detection is a modified PHOENIX model. The highest SNR model includes all investigated opacity sources (opacities of CO, OH, and H_2O plus the H-H and H-He continuum opacity sources) and has the following P-T profile parametrization: $T_3 = 2000$ K, $P_3 = 1$ bar, $P_1 = 10^{-3}$ bar, $\alpha = 0.17$ and a metallicity of $10\times$ Solar. The CCF matrix of this best-matching model is shown in Fig. 3.13. As shown in the top row of Fig. 3.14 this model gives $SNR = 7.9\sigma$ when all nights are combined in velocity-space, and the SNR-values are higher during pre-eclipse orbital phases than post-eclipse. In the calculation of the SNR, I assume the distribution of the cross-correlation values is Gaussian and not impacted significantly by any residual correlated noise. To assess this, I plot the distribution of the cross-correlation values in-trail (the three most central columns that cover the width of the planet trail) and out-of-trail (outside of the ten most central columns to generously exclude the width of the planet trail). The result, based on the best matching model described above in this section, is shown in Fig. 3.15 for the highest SNR PHOENIX modified P-T profile spectral template. To quantify whether the samples are normally distributed, I performed a Shapiro Wilks Test on the in-trail and out-of-trail samples (that is after aligning to the planet's rest frame). Both samples pass the test with p-values > 0.05 ($p_{in-trail} = 0.75$ and $p_{out-of-trail} = 0.09$). Therefore, the distribution of the cross-correlation values follows a normal distribution, and I conclude the effect of residual correlated noise on the SNR measurement is negligible.

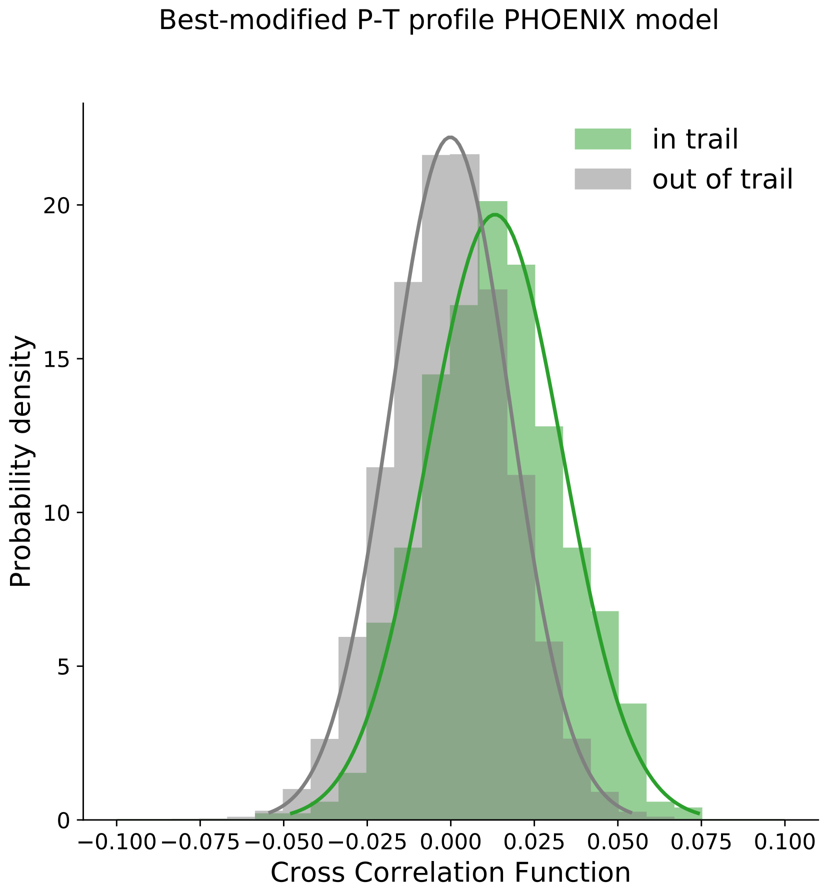

Figure 3.15: Histogram showing the probability density of the cross-correlation values in-trail (three most central columns) and out-of-trail (outside of the ten most central columns) of the exoplanet's velocity trail after aligning to the planets rest frame. Values are shown for the PHOENIX best modified P-T profile model. The over-plotted solid lines are Gaussian fits to the distributions, which are well described by the Normal function.

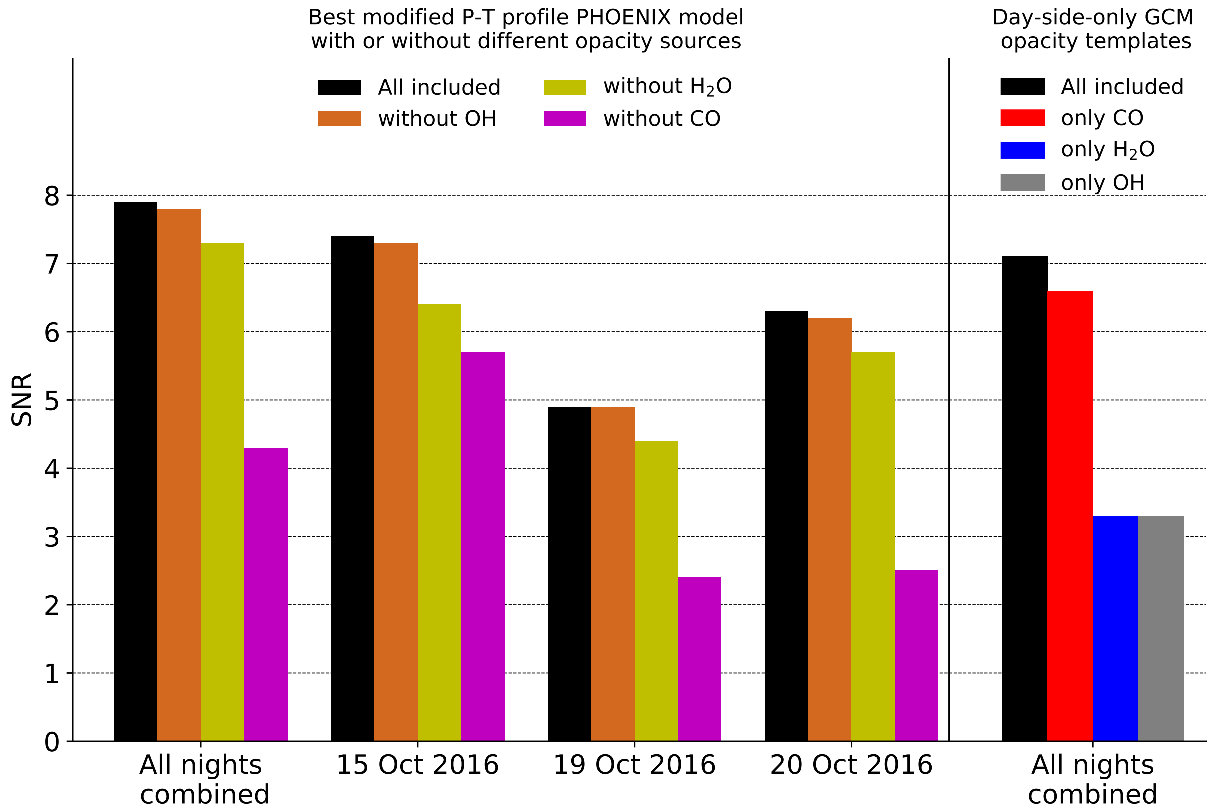

Figure 3.16: SNR results for the models with different opacity sources included or excluded. *Left panel*: results from the PHOENIX best modified P-T profile models for the cases of all opacity sources included and with a single opacity source excluded, respectively models with OH, H_2O and CO excluded. Only the models without CO result in a significant drop in the SNR when compared to the all-included case. *Right panel*: Results from the dayside-only GCM for the cases of all opacity sources included and respectively with only CO, only H_2O and only OH included. From all opacity sources, only CO remains robustly detected.

3.8.2 Detection of CO emission lines

To determine if any one particular species was contributing the majority of the detected signal, I fixed the P-T profile to the best-matching modified P-T profile PHOENIX model (all opacities included) and then ran the SNR-analysis for each individual night without CO, H_2O and OH, respectively. The results are shown in Fig. 3.16. Exclusion of CO significantly impacts the SNR every night and drops from 7.9σ to 4.3σ for all nights combined. On the other hand, the exclusion of OH and H_2O only marginally reduces the measured SNR, indicating that these data are not sensitive to these species at their abundance with this data. However, on the first night of pre-eclipse data, I still detected the planet signal to relatively high SNR, despite the exclusion of CO (the corresponding SNR matrices are shown in Fig. 3.17). This suggests that other species in the model are summing to give a detection, but I do not identify these individual species. The data on the third night, which covers the same orbital phase, is of lower quality and may explain why a similar feature is not seen during this night.

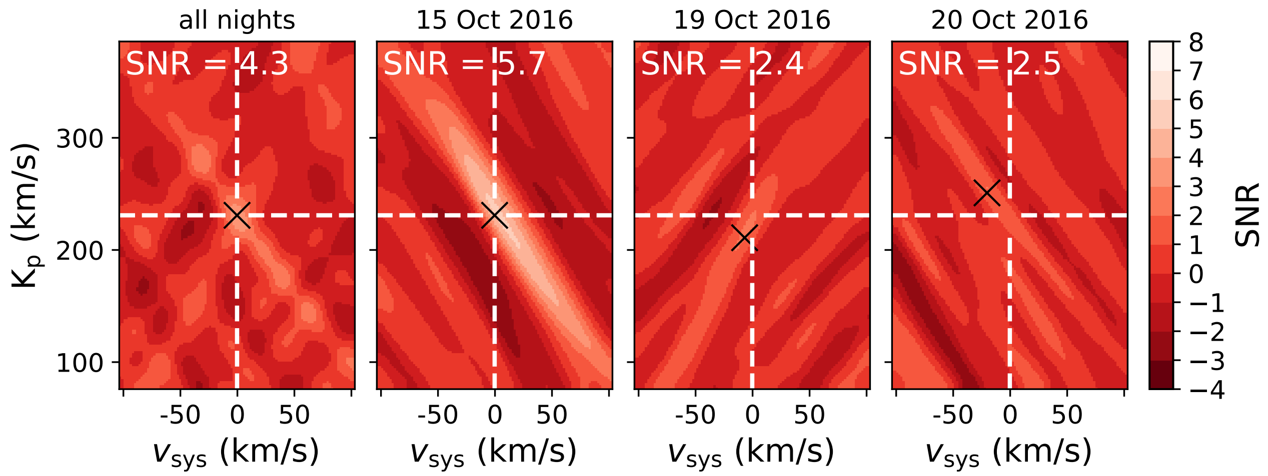

Figure 3.17: Same as Fig. 3.14, but for the best modified P-T profile PHOENIX model without CO.

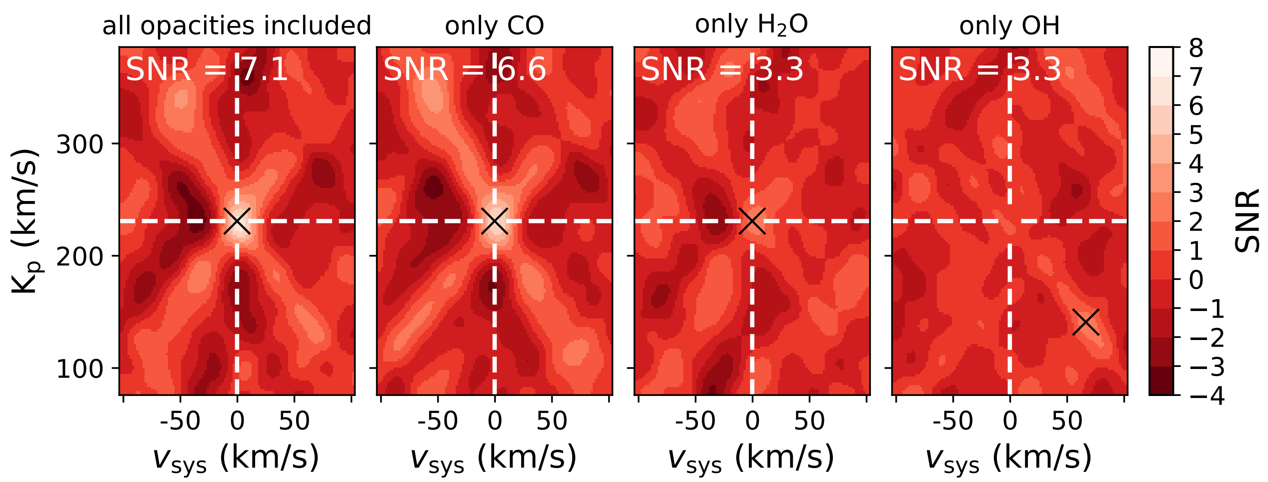

Figure 3.18: Same as Fig. 3.14, but for the GCM dayside-only templates.

I also assess in the day-side-only GCM model if any single species contributes the majority of the detection. The SNR results for single species models are shown in the right panel of Fig. 3.16 and the corresponding SNR-plots are shown in Fig. 3.18. From all opacity sources, only the CO GCM model results in a significant SNR of 6.6σ. The GCM H_2O spectral template has $SNR = 3.3\sigma$, which is insufficient for robust detection in HRCCS as previous work demonstrated spurious signals at a SNR $\leq 4\sigma$ often persist (Cabot et al., 2020; Spring et al., 2022), even though it appears at the expected planet velocity. OH is not detected.

Although a sufficient SNR is crucially important to claim the detection of an opacity source, comparing SNRs of models with different opacity sources included or excluded is statistically not robust. In Chapter 4 I will show how novel Bayesian frameworks can help us to compare these models within a robust statistical framework.

3.9 Discussion

3.9.1 Thermal structure and composition of WASP-33 b

The detection of CO emission lines with the modified PHOENIX P-T profiles provides unambiguous evidence for a thermal inversion in the atmosphere of WASP-33 b. A non-inverted atmosphere would have exhibited absorption lines instead. This is in agreement with previous observations of other atomic and molecular lines in emission in the atmosphere of WASP-33 b (e.g. Deming et al., 2012; Haynes et al., 2015; Zhang et al., 2018; Nugroho et al., 2020b; Cont et al., 2021a,b; Herman et al., 2022) and expected from atmospheric modelling of UHJ atmospheres (e.g. Lothringer et al., 2018; Gandhi & Madhusudhan, 2019). However, up to this detection with ARIES/MMT, no suitable high-resolution spectrographs were operational around the required wavelength region ($\sim$2.3μm) which covers the CO emission band.

From all molecular templates investigated in this work, only CO has resulted in a robust detection. Only the exclusion of CO had a significant impact on the SNR of the planet signal. It does remain somewhat puzzling however that I still detect the PHOENIX best-modified model without CO at a SNR $= 5.8$ in the first night of pre-eclipse data. I cannot attribute these to H_2O or OH alone in terms of the SNR, and no significant contributions from iron lines in the ARIES wavelength range are expected either.

I do not detect the model without CO during the third night, despite covering similar orbital phases. This may be explained by the better observing conditions during the first observing night relative to the third observing night (see SNR measurements in Table 3.3). Although there have been many detections of CO absorption lines (Snellen et al., 2010; Brogi et al., 2012; Rodler et al., 2012; de Kok et al., 2013; Rodler et al., 2013; Lockwood et al., 2014;

de Kok et al., 2014a; Brogi et al., 2016), this is the first reported detection of CO emission lines using the HRCCS technique, using only the large Doppler-shift induced by the planet's orbital motion, that is without the aid of High Contrast Imaging.

Previous works have indicated both water (Haynes et al., 2015) and OH (Nugroho et al., 2021) in the atmosphere of WASP-33 b, but I do not make a robust detection of these molecules in the ARIES data. To demonstrate that the very weak GCM H_2O signal in the data can be caused by non-planetary residuals e.g. tellurics, I ran the analysis using only frames obtained when the planet is not visible i.e. during the full eclipse of WASP-33 b. Spurious signals due to telluric or stellar residuals should persist whereas signals originating from WASP-33 b should disappear. For H_2O I found that a signal is still retrieved at the same offset ($v_{\rm sys}$, $K_{\rm p}$)-position albeit with larger errors, while the CO signal was not obtained at the expected planet ($v_{\rm sys}$, $K_{\rm p}$)-position anymore. This supports the interpretation that any H_2O signal in the ARIES data is caused by non-planetary residuals.

The non-detection of OH with ARIES/MMT is not necessarily surprising either when compared to the OH detection by Nugroho et al. (2021) using Subaru/IRD data. The bluer wavelength region (0.97-1.75 μm) covered by Subaru/IRD with respect to ARIES/MMT contains stronger OH emission lines and Subaru/IRD has a higher spectral resolution ($R = 70,000$). Thus, the lack of OH detection with ARIES can likely be explained by the poorer data quality of the spectral orders covering the OH-line dense regions compared to CO-line dense regions. The synthetic GCM spectrum in the left-top panel of Fig. 3.11 shows OH line dense regions in the wavelength range of the bluer ARIES spectral orders and order 26 at the far red-end. As explained in Section 3.7.2, lower weights are assigned to the bluer ARIES orders which have a lower throughput and contain residual fringing. The reddest order 26 falls at the edge of the detector and is consequently of poorer data quality. Lastly, telluric absorption is strong in some OH line-dense spectral orders. Due to the high dissociation temperature for CO, the abundances of CO are approximately constant in and outside of the hotter and cooler regions of the planet, at the pressures probed by HRCCS (Lodders & Fegley, 2002). This is in line with the modelling results of WASP-33 b by Tsai et al. (2021) who also found CO to be the only molecule that can be stable against dissociation. This is in contrast to other molecular species such as OH, H_2O or TiO which dissociate on the day-side (at least up to temperatures of $\sim$4000 K at a pressure of 10^{-4} bar). For example, for H_2O this will result in an abundance difference of several orders of magnitude between the day- and night-side. Since I assume Solar metallicity and the Solar C/O value is $\sim$0.54 (Asplund et al., 2009; Caffau et al., 2011), the CO abundance will not really depend on the varying H_2O abundance, but rather the limiting factor to form more CO will be the amount of carbon-atoms available. This is regardless of the extra freed-up oxygen atoms that become available as water dissociates at higher day-side temperatures. For species other than CO, their abundance has a strong temperature dependence and introduces a degeneracy between the effects of the atmospheric abundance (or the dissociation rate) and thermal structure, complicating the interpretation of the line contrast. This stability of CO against dissociation means the CO line contrast is a reliable tracer of the thermal structure of the atmosphere. I therefore advocate for CO as a better probe of the thermal structure and inversions of UHJs compared to H_2O in HRCCS.

3.9.2 Robustness of CO as a temperature tracer in the presence of stellar activity

The CCF trail inside the planet radial velocity trail in Fig. 3.13 is distinct. I do not see contaminating signatures of the host star's δ Scuti pulsations. On the contrary, the contamination by stellar pulsations can be seen clearly in the cross-correlation analyses of neutral iron emission lines (Nugroho et al., 2020a; Herman et al., 2022). This is not exclusive to WASP-33 b; any pulsating star with opacity sources present in both the star and planet will contaminate HRCCS. This contamination limits the available effective orbital phase coverage, as frames obtained at phases close to secondary eclipse have to be either heavily processed to remove the stellar pulsations (Johnson et al., 2015; Temple et al., 2017; van Sluijs et al., 2019) or disregarded (Nugroho et al., 2020a; Herman et al., 2022). In contrast to atomic species often present in both the planet and star, CO is dissociated in the hot stellar atmosphere of early-type A/F stars. These types of stars are also more likely to be pulsating stars due to their location within the Hertzprung-Russel diagram's instability strip (e.g. Gautschy & Saio, 1996). Although this depends on the abundance of CO and pressure range probed, here it highlights a further advantage of using CO in the NIR to probe the atmospheric temperature structure and inversions of UHJ around hot pulsating stars.

3.9.3 Low-resolution limit for HRCCS technique

For the HRCCS technique, to the first order, the SNR of the planet is generally given by equation (2.20), which reduces to equation (2.21). These observations are photon-limited thanks to the bright host star. However, residual noise, likely from residual telluric lines, persists in the final CCF time series (see Fig. 3.13), but the impact of this is substantially mitigated by the large Doppler shift of WASP-33 b.

For UHJs, one cannot be aided by High Contrast Imaging to spatially resolve the exoplanet and increase the planet-to-star contrast ratio, due to the small angular separation between the star and exoplanet. One thus relies solely on disentangling the exoplanet's lines from its Doppler shift induced by its orbital motion. The exoplanet's SNR can thus be increased in two ways: First, one can increase the photon collecting power such that the $\mathrm{SNR}_{\star}$ increases, or second one can increase the total number of spectral lines observed by either expanding the instantaneous wavelength coverage or the spectral resolving power.

Since SNR is proportional to $\sqrt{N_{\mathrm{lines}}}$ it is crucial to have a sufficiently high spectral resolution to resolve more lines. Previously, the lowest spectral resolution at which HRCCS unaided by high contrast imaging was successfully demonstrated was $R = 25,000$, as shown by the detection of water vapour in the atmosphere of τ Böo with the pre-upgraded NIRSPEC1.0/Keck combination as reported by (Lockwood et al., 2014). Other evidence for a detection of the thermal spectrum of HD 88133 b, also with NIRSPEC1.0/Keck was reported by Piskorz et al. (2016) using a multi-epoch approach, but later on disputed (Buzard et al., 2021a). The detection with ARIES/MMT shows Doppler-only HRCCS can still be used even at spectral resolutions as low as $R = 14,000 - 16,000$ given a sufficiently high orbital velocity.

The detection of WASP-33 b at this lower spectral resolution provides proof-of-concept that HRCCS is still possible at a lower resolving power when there is a sufficiently large orbital Doppler shift, despite less and diluted spectral lines being observed. Therefore, one can potentially trade off spectral resolving power for photon collecting power. This is particularly interesting for short-period exoplanets where no high spectral resolving power is required to resolve their large orbital Doppler shifts. Examples include other UHJs (for example KELT-9b) or terrestrial lava worlds (for example CoRoT-7b) as both have orbital velocities of similar order of magnitude as WASP-33 b, given they have inclinations close to edge-on.

3.10 Conclusions

In this work, I presented the first analysis of HRS observations from the NIR spectrograph ARIES mounted behind the MMT targeting WASP-33 b. I developed a public pre-processing pipeline for ARIES to extract a spectral time series from the raw detector images. I use the HRCCS technique with PCA to characterise WASP-33b's atmosphere using the SNR method. The primary conclusions of this work are the following:

1. I present the first robust detection (7.9σ) of CO emission lines using HRCCS in an exoplanet atmosphere. The detection of CO emission lines in the atmosphere of WASP-33 b is unambiguous evidence of an inverted P-T profile.

2. I find no evidence of stellar pulsations affecting the infrared detection of CO, in contrast to previous detections of atomic emission lines in the optical. This mainly impacts observations aiming to observe orbital phases close to zero (or equivalently velocities close the stellar radial velocity). I advocate that CO is therefore an advantageous and good probe of the thermal atmospheric structure of UHJs at pressures seen with HRCCS.

3. At a measured resolving power of $R \sim 15,000$, these observations show that HRCCS can be used even at spectral resolutions of $R \sim 15,000$ when using only the large Doppler-shift induced by the exoplanet's orbital motion to disentangle its spectrum from its host star and telluric. That is without the use of any spatial information from High Contrast Imaging. Thus spectral resolving power can be traded for photon collecting power in cases where the induced orbital Doppler shift is sufficient to move the planet spectrum over multiple pixels such as expected for close-in terrestrial lava planets and UHJs.

4. These results are a proof-of-concept of the ARIES/MMT combination that can be used to study and characterise exoplanet atmospheres.

4
Chemistry and thermal structure with Bayesian frameworks: the cases of HD 46375 A b, τ Böo A b and WASP-33 b

---

The material in this chapter is partly based on van Sluijs et al. (2023) and sometimes I have used parts of this work with minor or no changes to the original text or figures, to remain concise and preserve the clarity of the underlying message. The observations that are a part of MEASURE were obtained by the following people: Jayne Birkby, and Joshua Lothringer with the help of Craig Kulesa and Don McCarthy. The τ Böo A b dataset was downloaded from the ESO archive and reduced by Jayne Birkby. The opacities used in the HRCCS retrieval of τ Böo A b were calculated using the HELIOS-K code and provided by Joost Wardenier. The PHOENIX 1D self-consistent model templates were computed by Joshua Lothringer. The 3D GCM templates of WASP-33 b were computed by Elspeth K. H. Lee.

In the previous chapter, I demonstrated the capability of ARIES/MMT to detect species in exoplanet atmospheres using the high SNR detection of CO emission lines in the atmosphere of WASP-33 b as an example. However, this is also the hottest target in the MEASURE data set, and as I start pushing the instrumental limits towards the cooler, fainter systems, non-detections or tentative detections are expected. The SNR is a useful metric to test for the detection of species but does not provide insight into whether the SNR is low due to low chemical abundances or lack of quantity or quality of data.

In this chapter, I will introduce how novel Bayesian frameworks can constrain chemical abundances, in the case of a strong SNR detection SNR>5, but also in the case of a SNR non-detection $SNR \ll 5$. I will also introduce an injection-recovery test to check if the data quality and quantity are sufficient to detect the exoplanet atmosphere. I will apply these to data of the exoplanets HD 46375 A b, τ Böo b, and again WASP-33 b. HD 46375 b is a sub-Saturn mass exoplanet is and one of the lowest-mass planets observed as part of MEASURE, pushing the limits of survey. τ Böo b is an UHJ with the tension between results from two previous studies on whether this is a water-rich or water-poor world. I will use archival CRIRES data to investigate the discrepancy between these two studies. Lastly, I will reassess WASP-33 b, but this time with the addition of self-consistent models. I will highlight how a Bayesian framework can add additional constraints to the chemistry and thermal structure of this UHJ in the case of a high SNR detection.

The modelling approaches (section 4.3), and cross-correlation and likelihood methodologies (section 4.4) in this chapter are of a different level of complexity for each of these three targets. I used different approaches because there are different goals for the different datasets:

- For HD 46375 b, the first goal is to demonstrate whether ARIES/MMT has the capability of detecting signals from cooler and lower-mass targets. The second goal is to constrain its mass from the observed projected Keplerian velocity by means of equation (2.25). A significant SNR detection in (v_{sys},K_{p})-space should provide sufficient evidence to address both goals. Therefore, I use a grid of forward models with PETITRADTRANS and cross-correlation to investigate this dataset.

- For τ Böo A b, the goal is to constrain its water abundance, to resolve the tension between a water-rich and water-poor scenario in the literature (Pelletier et al., 2021; Webb et al., 2022). Therefore, I deploy a full HRCCS retrieval framework (adapted from Line et al., 2021) alongside forward modelling and cross-correlation.

- For WASP-33 b, the first goal is to highlight how Bayesian frameworks can provide additional constraints on the chemical composition and P-T structure alongside the SNR method. The second goal is to show what additional information can be learned from self-consistent 1D models, compared to the results from free 1D models which were presented in Chapter 3 of this thesis. Therefore, a new suite of self-consistent PHOENIX 1D models of WASP-33 b are introduced, and I use CC-to-log(L) mapping combined with Wilks' theorem.

4.1 Introduction

I will now briefly summarise the literature on the exoplanets HD 46375 b and τ Böo b. An overview of previous literature on WASP-33 b was given in Section 3.3.1.

4.1.1 HD 46375 A b

The HD 46375 system is a relatively bright widely separated (346 ± 13 au or $10.352 \pm 0.061''$) double star system with an apparent magnitude of $V = 7.91$ (Mugrauer et al., 2006; Anderson & Francis, 2012). The primary star is classified as G9V (Grieves et al., 2018) and the secondary as M0V (Terrien et al., 2012). The system is at a distance of ~33 pc (Gaia Collaboration et al., 2021). The primary star has a mass of 0.91 ± 0.01 $M_{\odot}$, a radius of 1.01 ± 0.01 $R_{\odot}$, an effective temperature of 5199.0 ± 15 K and metallicity $+0.27 \pm 0.06$ dex (Rojas-Ayala et al., 2012; Bonfanti et al., 2016; Grieves et al., 2018).

The primary star hosts a Saturn-mass exoplanet HD 46375 A b, which was detected using the radial velocity method by the Keck High-Resolution Echelle Spectrograph (Marcy et al., 2000). It has an orbital period of $P = 3.02538 \pm 0.00006$ d and slightly eccentric orbit $e = 0.0524^{+0.0229}_{-0.032}$ (Wang & Ford, 2011). No transit has been detected, which constrains the inclination of the orbit $i < 83°$ (Henry, 2000). Gaulme et al. (2010) use a light curve observed with the CoRoT observatory to search for phase variations in reflected light. They find a tentative detection of a signal compatible with the orbital period of HD 46375 A b and infer a relatively high albedo between 0.16 and 0.33. They do point out longer baseline observations are required to unambiguously confirm the reflected light phase variations are originating from HD 46375 A b.

Given the system is non-transiting, detection of the exoplanet using high-resolution spectroscopy has the potential to constrain K_{p} from which the true planetary mass can be calculated using equation (2.25). Few atmospheres of warm sub-Saturns have been characterised using HRCCS. A comparison with hotter more massive exoplanets will be useful to understand how chemistry and dynamics vary as a function of gravity and effective temperature. Measurements of abundance ratios such as M/H and C/O will be helpful to constrain formation pathways. Finally, this tests the capability of MEASURE to characterise target systems with a fainter planet-star contrast ratio.

4.1.2 τ Böo A b

τ Böo is a widely separated (224 au or 14.39") double star system with a primary F7-star Gray et al. (2001) and a secondary M-dwarf (Hale, 1994). Butler et al. (1997) discovered a planet around the primary star τ Böo A b, that has a mass of $M_\mathrm{p} = 5.90^{+0.35}_{-0.20}$ $\mathrm{M_{Jup}}$ (Lockwood et al., 2014), estimated equilibrium temperature of $T_\mathrm{eq} = 2139$ K and estimated radius of $R_\mathrm{p} = 1.14$ $\mathrm{R_{Jup}}$. This exoplanet is non-transiting (Baliunas et al., 1997). The orbital parameters of this system were well constrained by Justesen & Albrecht (2019) and all three bodies are orbiting each other in a co-planar orbit. Follow-up observations aiming to detect the reflected light of τ Böo A b did not detect any significant signals (Charbonneau et al., 1999; Collier Cameron et al., 1999; Leigh et al., 2003; Rodler et al., 2010) and a meta-analysis of all these previous studies by Hoeijmakers et al. (2018b) constrain a planet-to-star contrast ratio to $< 1.5 \times 10^{-5}$ and albedo to < 0.12 in the optical.

The first detection of the exoplanet atmosphere of τ Böo A b used HRCCS to detect CO absorption lines using CRIRES around the 2.3 μm wavelength band (Brogi et al., 2012; Rodler et al., 2012). Lockwood et al. (2014) also detect CO absorption lines in the exoplanet's emission spectra but with Keck/NIRSPEC. Most recently Pelletier et al. (2021) uses CFHT/Spirou to constrain the CO abundance at VMR $\log \mathrm{CO} = -2.46^{+0.25}_{-0.29}$.

Despite the clear detection of CO in the atmosphere, there have been inconclusive results in different studies on the detection of water. Brogi et al. (2012) and Rodler et al. (2012) did not find conclusive evidence for water in the atmosphere. However, using a multi-epoch approach, Lockwood et al. (2014) detect water in the atmosphere of τ Böo A b at 6σ. On the contrary, Pelletier et al. (2021) find no water and constrain the water abundance at VMR $\log \mathrm{H_2O} < 5.66$ (at 3σ) using a novel Bayesian retrieval framework. Follow-up work by Webb et al. (2022) contradicts this upper limit and finds a detection of water at a VMR $\log \mathrm{H_2O} = -3$ in a single night of CARMENES data. In this work, I will analyse complementary CRIRES data around the $\sim$3.5 micron region, which covers strong water absorption features. The aim is to constrain the water abundance of τ Böo A b and thus help resolve the discrepancy between multiple literature studies.

4.2 Observations and data processing

I will briefly describe the MEASURE observations of HD 46375 A b and archival CRIRES τ Böo b observations.

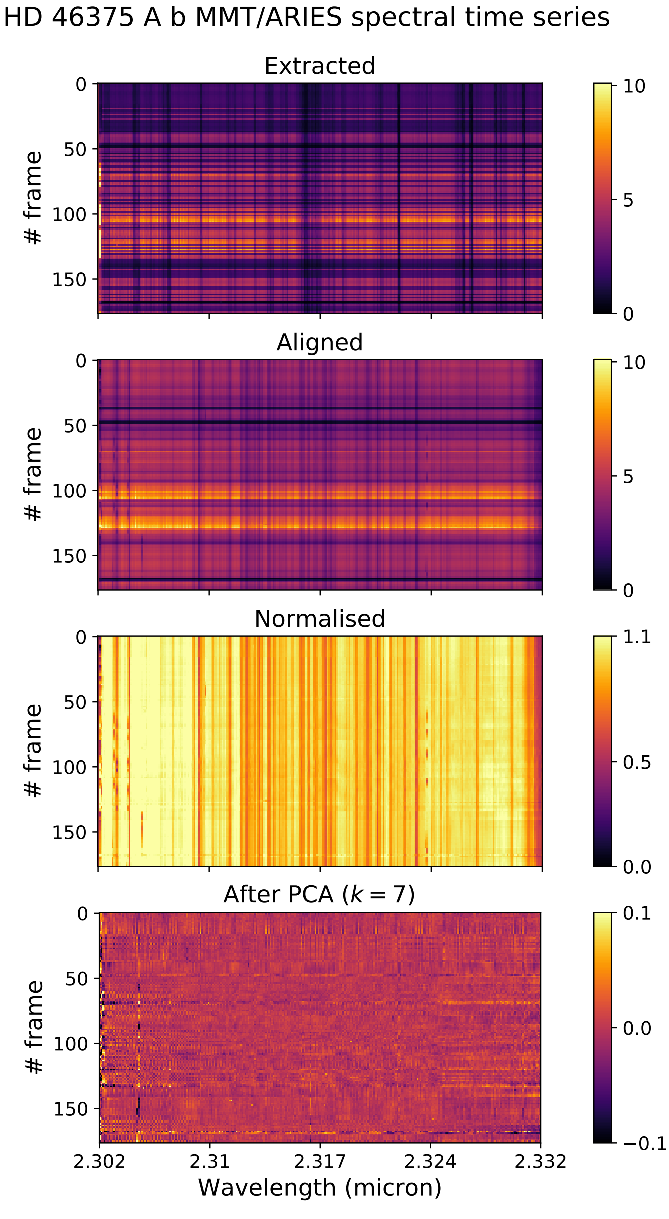

Figure 4.1: Processing of the 23rd spectral order of the HD 46375 A b ARIES/MMT dataset. The extracted spectral time series is shown in the top row, the aligned spectral time series in the second row, the normalised spectral time series is shown in the third row, and the fourth row shows the spectral time series after cleaning with seven iterations of PCA.

4.2.1 ARIES/MMT observations of HD 46375 A b

I analyse a single night of dayside observations of HD 46375 A b obtained on the 1st of November 2015. There is an additional observing night covering the nightside, but I estimate the planet-star contrast is too low to detect the nightside in a single observing night. The target has been observed for a total of $\sim$5 hours on the dayside. A total of 177 frames were obtained with an exposure time of 90 seconds per frame. Alongside science frames, flat and darks were obtained to be used for the data calibration. I use the pre-processing pipeline as described previously in Section 3.4 to reduce the raw detector images to a spectral time series. I largely follow the post-processing steps as described in Section 3.5. To avoid a manual wavelength calibration for each new data set analysed by the pipeline, I developed an automatic wavelength calibration. The algorithm starts with an initial guess of the wavelength solution, based on the polynomial solution found for the WASP-33 b data set. Visual comparison of this initial guess shows the wavelength solution is close, but misaligned on the level of a few spectral channels. This is not unexpected, as there is about a year between the HD 46375 A b data set and the WASP-33 b dataset. I use an MCMC algorithm[1] to explore the parameter space of the polynomial coefficients. I drew a total of $N = 10,000$ with a burn-in of $N = 1,000$, which I found to balance the computation time and accuracy of the wavelength solution. I manually inspect the wavelength solution for each spectral order to ensure goodness of fit. In the rest of my analysis, I exclude orders 7-9, 15, 21, and 24 as I find they have particularly bad fringing or few telluric lines, resulting in an inaccurate wavelength solution. Using the same methodology as for WASP-33 b I measure the spectral resolving power. I find this data has a spectral resolving power of $\sim$16,000, comparable to the WASP-33 b observations, again lower than the instrumental specification for ARIES. I remove the quasi-stationary trends following the same steps as for the WASP-33 b data. The result is shown in the fourth row of Fig. 4.1, a de-trended spectral time series, ready to be compared by a model template by means of cross-correlation.

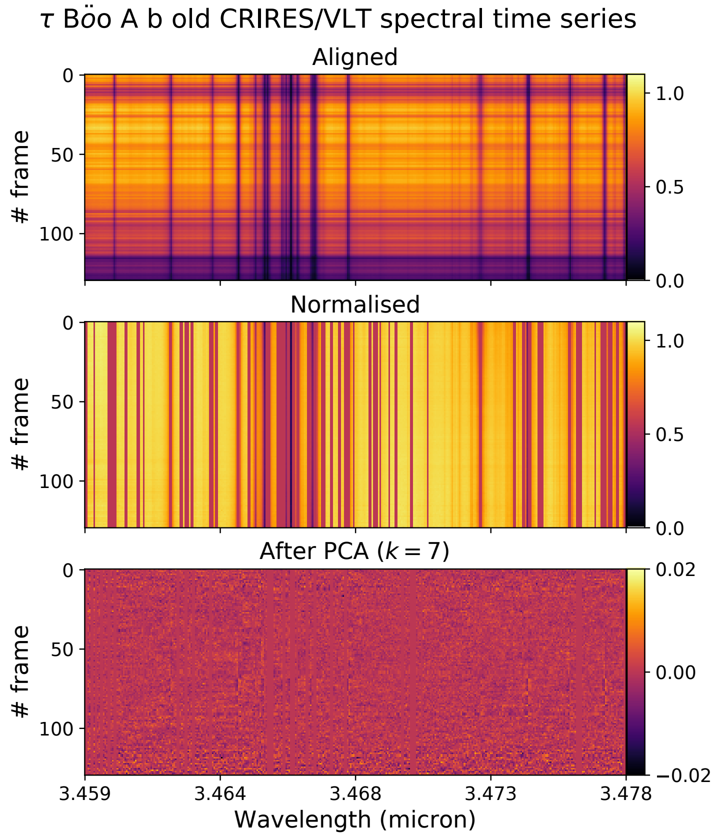

Figure 4.2: Processing of the first spectral order of the τ Böo A b old CRIRES/VLT dataset. The aligned spectral time series is shown in the top row, the normalised spectral time series is shown in the second row, and the third row shows the spectral time series after cleaning with seven iterations of PCA.

4.2.2 CRIRES observations of τ Böo A b

τ Böo A b has been observed with old CRIRES as part of the program 092.C-0660(A) with PI J. L. Birkby to provide a detailed atmospheric characterisation of the non-transiting exoplanet τ Böo A b. This observing program aimed to constrain the abundances of important C- and O-bearing molecules to constrain the C/O ratio and link it to planet formation and evolution pathways. The observations were obtained around the 3.5 μm wavelength region to target absorption features of CO, CH_4, and CO_2 in the exoplanet's emission spectrum (de Kok et al., 2014b). Combined with the previous detection of CO around 2.3 μm (Brogi et al., 2012; Rodler et al., 2012), also with CRIRES, these constraints can be used to calculate the C/O ratio.

These data have been downloaded directly from the online ESO data archive[2]. The raw detector images have been reduced with the default data processing pipeline as provided by the instrument team[3]. After extraction of the spectral time series by the CRIRES processing pipeline, alignment and wavelength calibration were done separately. I use my post-processing steps as described in Section 3.5 to reduce this data. I tried PCA with three, five, and seven components, but these qualitatively gave the same result and I fixed the number of iterations to seven. Science fringes were not present in the CRIRES data, thus I did not use a high-pass filter. The result is a detrended spectral time series for all of the four CRIRES spectral orders. The result of each step in the analysis is shown in Fig. 4.2.

4.3 Modelling of the exoplanet atmospheres

I will now describe how I modelled the exoplanet atmospheres of τ Böo b and HD 46375 A b. I will also introduce a new set of self-consistent PHOENIX models of the exoplanet WASP-33 b. Different modelling approaches have been adopted for each of the three targets depending on the different goals of the analyses (as described at the start of this chapter).

4.3.1 Modelling HD 46375 A b with petitRADTRANS

I use the publicly available PETITRADTRANS[4] Python package to calculate emission spectra of the exoplanet HD 46375 A b (Mollière et al., 2019). To forward model the exoplanet atmosphere with PETITRADTRANS one has to make assumptions on certain atmospheric

[1] The PYTHON package EMCEE is used.
[2] http://archive.eso.org/eso/eso_archive_main.html
[3] https://www.eso.org/observing/dfo/quality/CRIRES/pipeline/pipe_reduc.html
[4] https://petitradtrans.readthedocs.io/en/latest/

Parameter	Symbol	Unit	Value(s)
Reference pressure	P_0	Pa	0.01
IR opacity	κ_{IR}	-	0.01
Ratio between optical and IR opacity	γ	-	0.4
Internal temperature	T_{int}	K	0
Stellar metallicity	$Z_\star$	$Z_\odot$	1.75
Mean molecular weight (H-He mixture)	μ	u	1.7065
Planetary mass $\times$ sin i	M_{p}	M_{Jup}	0.23
Inclination	i	$^\circ$	45, 64.2, 83.5
Equilibrium temperature	T_{eq}	K	1250, 1500, 1750
Mass fraction H_2	X	-	0.74
Mass fraction He	Y	-	0.24
Mass fraction H_2O	$Z_{\mathrm{H_2O}}$	-	0.001 $\times Z_\star$
Mass fraction CO	Z_{CO}	-	0.01 $\times Z_\star$
Mass fraction CO_2	$Z_{\mathrm{CO_2}}$	-	0.00001 $\times Z_\star$
Mass fraction CH_4	$Z_{\mathrm{CH_4}}$	-	0.0000001 $\times Z_\star$
Mass fraction Na	Z_{Na}	-	0.00001 $\times Z_\star$
Mass fraction K	Z_{K}	-	0.000001 $\times Z_\star$

Table 4.1: Input parameters to generate atmospheric models of the exoplanet HD 46375 A b with the PETITRADTRANS Python package.

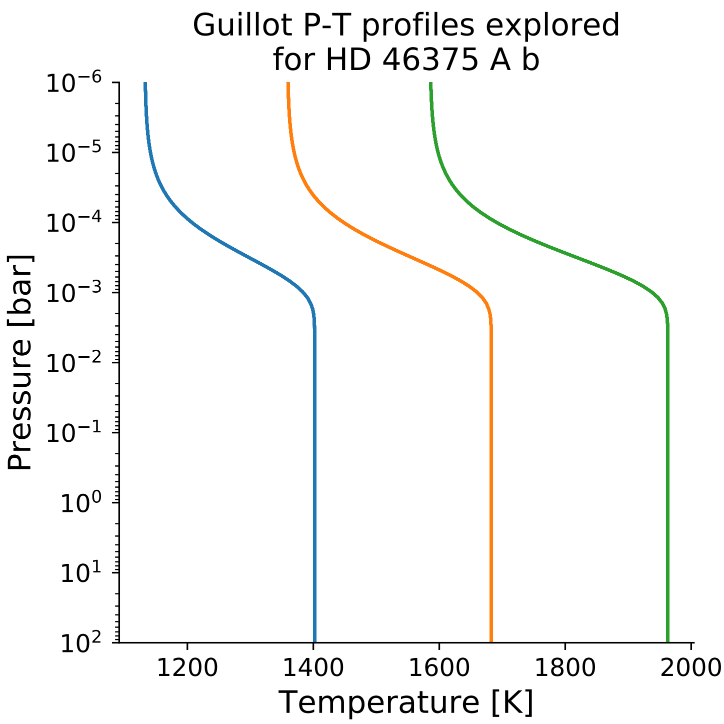

Figure 4.3: All P-T profiles explored when modelling the exoplanet atmosphere of HD 46375 A b with PETITRADTRANS. All of these use the Guillot P-T profile parametrisation (see equation (2.8) with the parameters listed in Table 4.1.

and planetary parameters. These parameters are summarised in Table 4.1. As this is a non-transiting system, inclinations above 83.5° are ruled out. Inclinations below $\sim$45° are unlikely to result in a significant radial velocity signal to detect the exoplanet. Therefore, I explore inclinations within 45°-83° as listed in Table 4.1.

The equilibrium temperature depends on the properties of the atmosphere such as the re-radiation efficiency and albedo. I explore a range of temperatures around the estimated equilibrium temperature of $T_{\mathrm{eq}} = 1514$ K for instantaneous re-radiation and albedo of zero (absorbing all incoming radiation). At these temperatures HJ models predict an atmospheric composition containing H_2, He, H_2O, CO, CO_2, CH_4, Na and K. The line lists of these molecules are available online in a format suitable for use with PETITRADTRANS and come from a variety of sources (e.g. HITEMP, see Rothman et al., 2010, 2013; Piskunov et al., 1995; Hargreaves et al., 2020). The stellar metallicity is measured by Fischer & Valenti (2005). For all other parameters, I assume typical values of the right order of magnitude for an HJ based on previous modelling efforts (e.g Lothringer et al. (2020)). In total, I compute nine PETITRADTRANS models of HD 46375 A b to cover the range of possible inclinations and effective temperatures.

The spectra are generated the following way. First, I assume a Guillot global P-T structure which is given by equation (2.8) (Guillot, 2010). Using the assumed inclination, I calculate the planetary mass. I use the FORECASTER[5] Python package to estimate the planetary radius from the planetary mass (Chen & Kipping, 2017). The gravity is calculated using equation (2.9). I define a total of 100 pressure layers in between logarithmically-equally-spaced atmospheric pressures between $10^{-6} - 10^{2}$. Using the atmospheric composition, P-T structure, gravity and mean molecular weight, PETITRADTRANS calculates the output planetary emission spectra using the radiative transfer equations (Mollière et al., 2019). An overview of the P-T profiles explored is shown in Fig. 4.3 and an example of one of the emission spectra is given in Fig. 4.4.

[5] `https://github.com/chenjj2/forecaster`

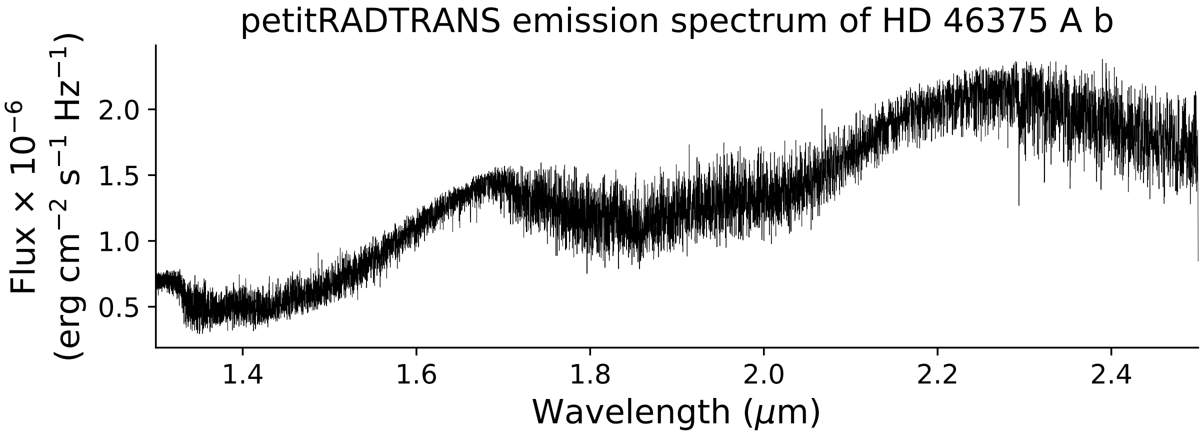

Figure 4.4: Example of one of the emission spectra explored when modelling the exoplanet atmosphere of HD 46375 A b with PETITRADTRANS convolved to the observed spectral resolution of $R = 15,000$. This model assumes an inclination i=64.2 ° and an effective temperature of $T_{\rm eq}$=1500 K. All other parameters as listed in Table 4.1.

4.3.2 Modelling τ Böo A b with a Bayesian retrieval framework

Rather than computing a grid of models, I model the atmosphere of τ Böo A b using a Bayesian retrieval framework for high-resolution emission spectra. The framework is adopted from Line et al. (2021), where they use it to compute and run a HRCCS retrieval on observations of the exoplanet WASP-77 A b. I use their code for this, with modifications to the opacity source line lists included and adjusting the input parameters to those of the τ Böo A system.

In my HRCCS retrieval on the τ Böo A b dataset, I include five opacity sources H_2O, CH_4, CO_2, HCN, TiO (references to these opacities can be found in Table 1 in Lee et al. (2022)). These opacity sources are expected to be relevant absorbers in the 3.5μm wavelength range. Fewer opacity sources are included compared to the forward model of HD 46375 A b. This was done to reduce the number of free parameters in the HRCCS retrieval and speed up the computation of the forward model in each step. The remainder of the atmospheric composition is assumed to be a H_2+He mixture (at a number density ratio $n_{\rm He}/n_{\rm H_2} = 0.176$, similar to the assumption by Line et al. (2021)). The atomic opacities were calculated using the HELIOS-K code Grimm et al. (2021). The abundances of all of these opacity sources are included as free parameters in the retrieval. The retrieval framework P-T profile parametrisation by Madhusudhan & Seager (2009) as given by equation (2.10). Cloud physics is not explicitly included in the HRCCS retrieval. The offset from the expected Keplerian velocity $\Delta K_{\rm p}$ and $\Delta v_{\rm sys}$ system velocity are included as free parameters. I explore velocity offsets around the values reported Pelletier et al. (2021) of $v_{\rm sys}$=-15.4 km/s and $K_{\rm p}$=108.2 km/s. The scale parameter a introduced by Brogi & Line (2019) is also included, which allows for additional stretching of the emission lines in the template spectrum. Lastly, a small phase

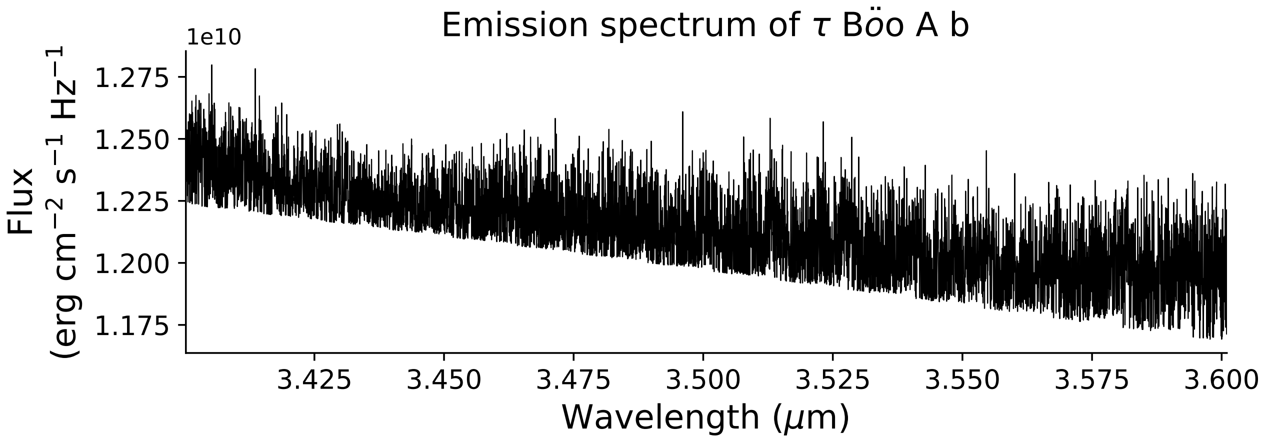

Figure 4.5: Example of an output emission spectrum of τ Böo A b from the HRCCS retrieval code by Line et al. (2021) at CRIRES spectral resolution of $R = 100,000$. The input parameters are based on those from Pelletier et al. (2021) and (Webb et al., 2022) when available and otherwise I made a reasonable guess (see text for parameter values).

offset term is included to account for errors in the ephemeris. I set the projected rotational velocity of the τ Böo A b to $v \sin i = 4.5/\mathrm{km/s}$ and convolve the synthetic model spectrum with a Gaussian kernel with a FWHM equal to the projected rotational velocity. Similarly, each model is also convolved to the spectral resolving power of CRIRES $R = 100,000$.

An example of an output spectrum generated by this forward modelling approach is shown in Fig. 4.5. This model is generated using the abundances and P-T profile as reported by Pelletier et al. (2021): $\log \mathrm{CH_4} = -3.78$ (upper limit), $\log \mathrm{HCN} = -5.57$ (upper limit), $T_0 = 3000$ K, $\log P_1 = 0$, $\log P_2 = -2$, $\log P_3 = -6$. However, I use the higher water abundance $\log \mathrm{H_2O} = -3$ from Webb et al. (2022). I use the higher water abundance to ensure that if water is present in the real data, there are water lines in the synthetic model as well. For the other parameters, no literature priors are available and I assume low VMRs $\log \mathrm{CO_2} = -9$, $\log \mathrm{TiO} = -9$ and $a_1 = a_2 = 0.5$.

4.3.3 Self-consistent 1D PHOENIX models of WASP-33 b

In addition to the PHOENIX 1D free models with modified structure and/or abundances, as introduced in Section 3.7.1, the PHOENIX code is also capable of running self-consistent models. The WASP-33 b self-consistent PHOENIX models are similar to the extremely irradiated HJ models presented in Lothringer et al. (2018). As explained in Section 2.2.3, self-consistent atmosphere models solve the atmosphere structure and composition iteratively, calculating the spectrum at each iteration and comparing it to radiative equilibrium. For these models, the radiative-convective boundary is usually below the highest pressure. Therefore, no convective adjustments were made as the speed of convergence was sufficient. Temperatures are then modified and iteratively updated to radiative equilibrium after which the chemistry is calculated based on chemical LTE and the spectrum is re-calculated. This process was repeated until the temperature corrections were below a convergence criterium, such that the atmosphere was in radiative and chemical equilibrium.

Each spectrum was calculated for a broad wavelength range from 10 to 10^7 nm. For WASP-33 b, the exoplanetary parameters from Haynes et al. (2015) were used(as summarised in Table 1 of Lothringer et al., 2018). A grid was used with varying atmospheric metallicity and a heat re-radiation efficiency f defined by Madhusudhan & Seager (2009) as

$$F_{\mathrm{p}} = (1 - A_{\mathrm{B}})(1 - f)F_{\mathrm{s}}, \tag{4.1}$$

where A_{B} is the Bond Albedo. In equation (4.1), the $(1 - A_{\mathrm{B}})$ term describes how much of the irradiation is reflected back into space, and the $(1 - f)$ term describes how much of the heat is transported to the nightside. Metallicities values explored are $0.1\times$, $1\times$, and $10\times$ Solar metallicity. For the heat re-radiation factors f the explored values are: $f = 1/4$ for dayside and nightside heat redistribution, $f = 1/2$ for dayside-only heat redistribution, and $f = 2/3$ for instantaneous heat re-radiation.

These self-consistent models include (see Lothringer et al., 2018): bound-free opacity from H, H^-, He, C, N, O, Na, Mg, Al, Si, S, Ca, and Fe, free-free opacity from H, Mg, and Si, and scattering from e_-, H, He, H_2. These models also include opacities for TiO and VO, but as explained in Lothringer et al. (2018), TiO and VO are not the sole cause of temperature inversions in extremely irradiated HJs. Temperature increase at these pressures is likely due to the absorption of short-wavelength radiation by absorbers like atomic Fe and the lack of coolants such as H_2O. Such hot temperatures result in the thermal dissociation of most molecules in the atmosphere including H_2 and H_2O (see Fig. 4.6). The abundance of CO, with the strongest molecular bond, is also reduced, but to a lesser extent compared to other potential molecular opacity sources. The resulting spectra, shown in Fig. 4.7, have CO emission lines with signatures of H_2O and other molecules muted due to thermal dissociation combined with the isothermal lower atmosphere.

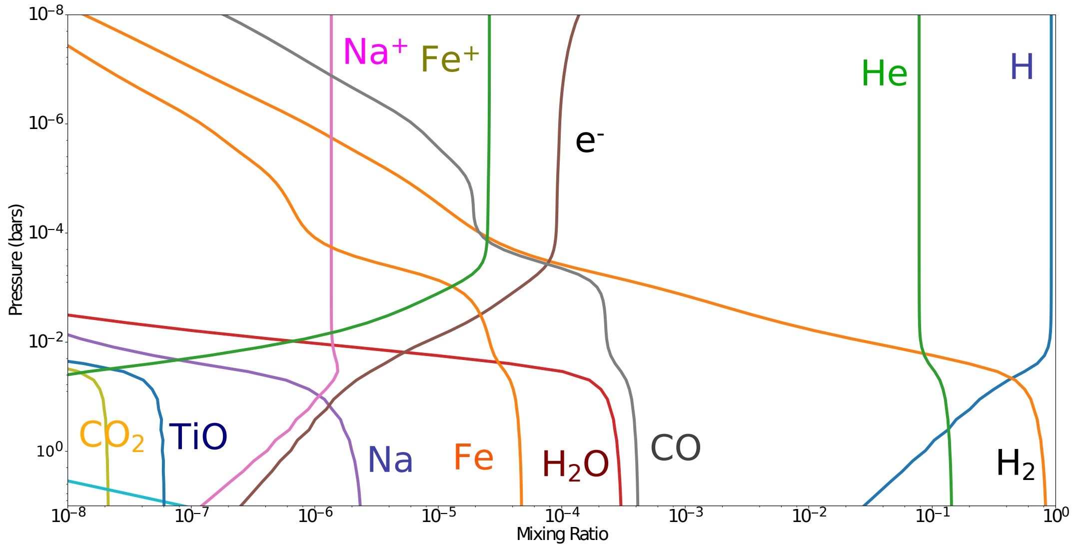

Figure 4.6: Mixing ratios in chemical equilibrium as functions of pressure for different species in the self-consistent PHOENIX 1D model atmospheres of WASP-33 b. This is for the day-side-only heat redistribution model $f = 0.5$ at $\times 1$ Solar metallicity.

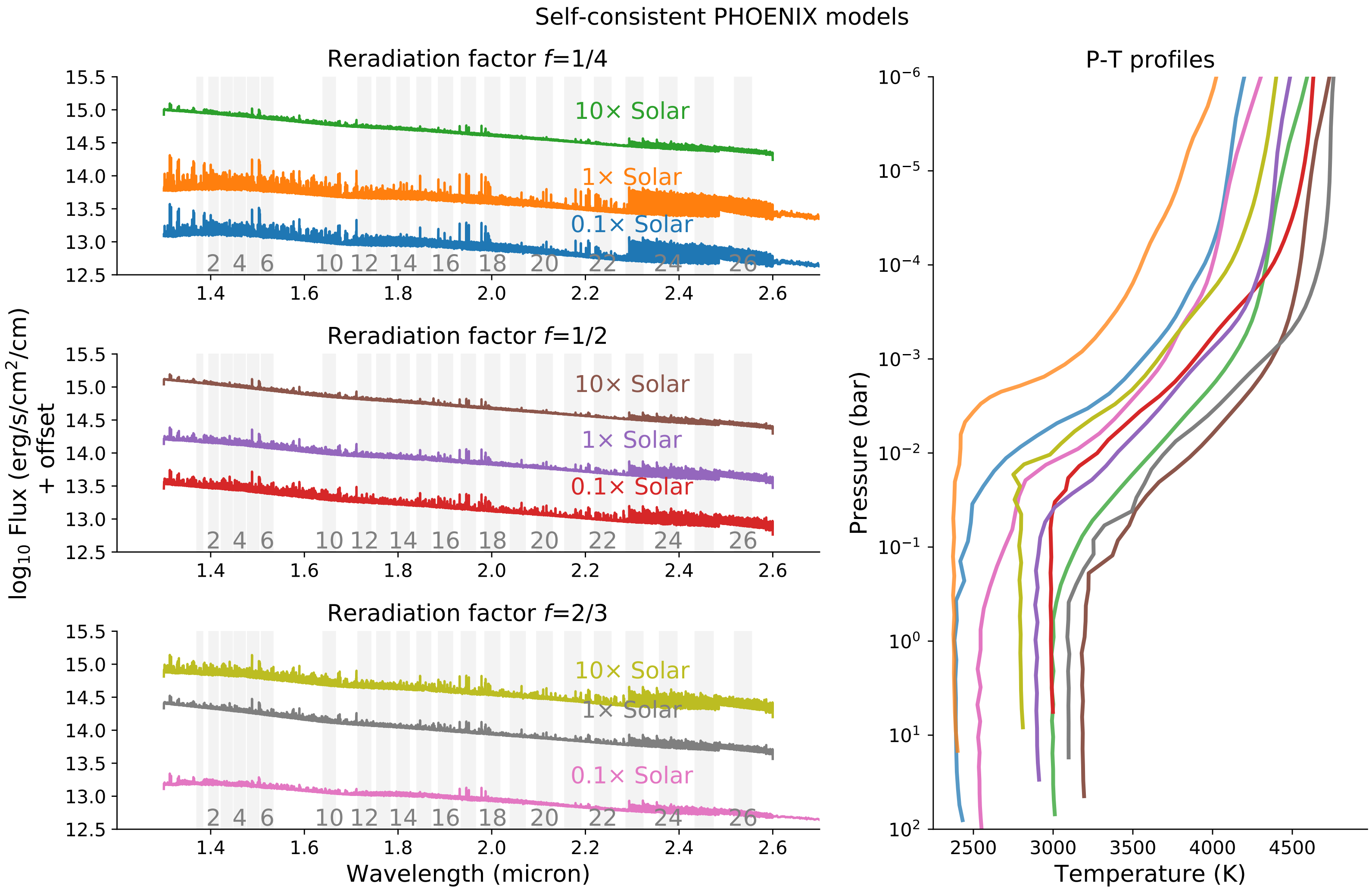

Figure 4.7: WASP-33 b 1D PHOENIX self-consistent synthetic emission spectra. *Left panels*: PHOENIX self-consistent spectra convolved to the observed spectral resolving power of $R = 15,000$ as a function of the metallicity and re-radiation factor f: $f = 1/4$ for full heat-redistribution, $f = 1/2$ for day-side-only heat-redistribution and $f = 2/3$ for instantaneous re-radiation. Different metallicity models have been offset by 0.75 along the y-axis with respect to the 0.1×Solar model. The ARIES spectral order wavelength ranges included are indicated by the gray bars. *Right panel:* corresponding PHOENIX self-consistent P-T profiles.

4.4 Cross correlation and Bayesian methods

I will now describe the cross-correlation and Bayesian methods used for each of the three targets. Different approaches have been adopted for each of the three targets depending on the different goals of the analyses (as described at the start of this chapter).

4.4.1 SNR-maps of HD 46375 A b

For HD 46375 A b I use the SNR method and cross-correlate each of the nine PETITRADTRANS models with the detrended spectral time series. I follow the same approach as for WASP-33 b, where I also create a model-dependent spectral order weighting scheme by injecting the signal into the data at an offset velocity. I cross-correlate the model template with trial velocities between -1000 km/s and +1000 km/s. This is done in steps of 5 km/s, sufficient for the measured spectral resolving power of ∼16,000. After combining all spectral order cross-correlation matrices with the appropriate weights, I shift the combined cross-correlation matrix into the planet rest frame for a range of $v_{\rm sys}$ and $K_{\rm p}$ values. I search around $v_{\rm sys} = -0.98$ km/s (Soubiran et al., 2018) within a range of ±50 km/s. I use equation (2.25) to calculate the true semi-major amplitude based on the assumed inclination. For $i = 83°$, the maximum allowed inclination given the planet is non-transiting, and the projected semi-major amplitude is 139 km/s. I explore values around this within a range of ±100 km/s, gain with a step-size of 5 km/s. This range in $K_{\rm p}$-values is sufficiently large for the inclinations explored between 45° and 83°. I calculate the SNR-maps similar to the methodology used for the WASP-33 b data set as described previously in Section 2.3.2.

4.4.2 Bayesian retrieval of τ Böo A b

I use the Bayesian retrieval framework using uniform priors around the best initial guess as shown in Fig. 4.5. The retrieval framework uses PYMULTINEST to explore the multidimensional parameter space. The code uses GPU parallelization to speed up the computation of each forward model. It takes a total of ∼1 day to run the retrieval algorithm on a single NVIDIA GeForce RTX 2080 GPU. The output of the algorithm are posterior distributions for each of the forward model free parameters.

Alongside running a full retrieval framework, I also create SNR maps. I explore a velocity grid with $v_{\rm sys}$ values in the range of -100 km/s to 100 km/s ($v_{\rm sys} = -15$ km/s has been reported by Pelletier et al. (2021)). I search around $K_{\rm p} = 108.2$ km/s, the value reported by Pelletier et al. (2021), within a range of ±100 km/s. I use a step size of 1 km/s, sufficient for these CRIRES observations at a spectral resolving power of $R = 100,000$. The SNR maps are calculated in a slightly different way since the retrieval framework internally processes the data and model homogeneously. This is done by running Singular Value Decomposition, to remove tellurics/systematics, once on the data and storing the 5 principal component eigenvectors. For each model, the effect of telluric lines/systematics is reintroduced by reconstructing a matrix from these stored eigenvectors and injecting the artificial exoplanetary signal into this matrix. This way, the model and data are processed homogeneously and it is not necessary to introduce a spectral order weighting scheme. The cross-correlation value for each trial ($v_{\rm sys}$, $K_{\rm p}$)-point is calculated directly. In velocity space, I use a region outside of the expected planetary velocity to determine the standard deviation of the background cross-correlation values. The entire map in velocity space is divided by this value to create a SNR map.

4.4.3 Wilks' Theorem and the Bayesian analysis of WASP-33 b

Alongside applying the SNR method to the self-consistent models, I introduce log-likelihood mapping and a simple Bayesian retrieval framework. First, the cross-correlation values for each evaluated model can directly be converted to a likelihood value using equation (2.30). Each set of models (modified structure and/or abundances; self-consistent) can then be compared amongst themselves using Wilks' Theorem (see Section 2.4.1), where the sigma-values are always with respect to the highest likelihood model on the grid of models evaluated.

Additionally, I use PYMULTINEST to explore the parameter space around three parameters: $K_{\rm p}$, $v_{\rm sys}$, and the scale parameter a, as described in Section 2.4.2. This is done to further constrain the $K_{\rm p}$, $v_{\rm sys}$ values for the different opacity models. The final result of this analysis is posterior distributions of these three parameters for the different opacity source models.

4.5 Results

4.5.1 SNR results of HD 46375 A b

The SNR-maps for each of the nine PETITRADTRANS models are shown in Fig. 4.8. As shown, the exoplanet atmosphere is not detected at the expected velocity offset, although all models do show a positive correlation at this location. There is a very small, but negligible difference between the $T_{\rm eq} = 1250$ K models and the hotter models. Changing the inclination, which affects the mass, radius, and gravity of HD 46375 A b has no effect on the detection significances or structure in the SNR-maps. The trail plot for the petitRADTRANS 1D model with an inclination $i = 64^\circ$ and effective temperature $T = 1500$ K is shown in Fig. 4.9. Note the noise is lowest during the middle of the observing run as the continuum SNR was highest during this part of the run.

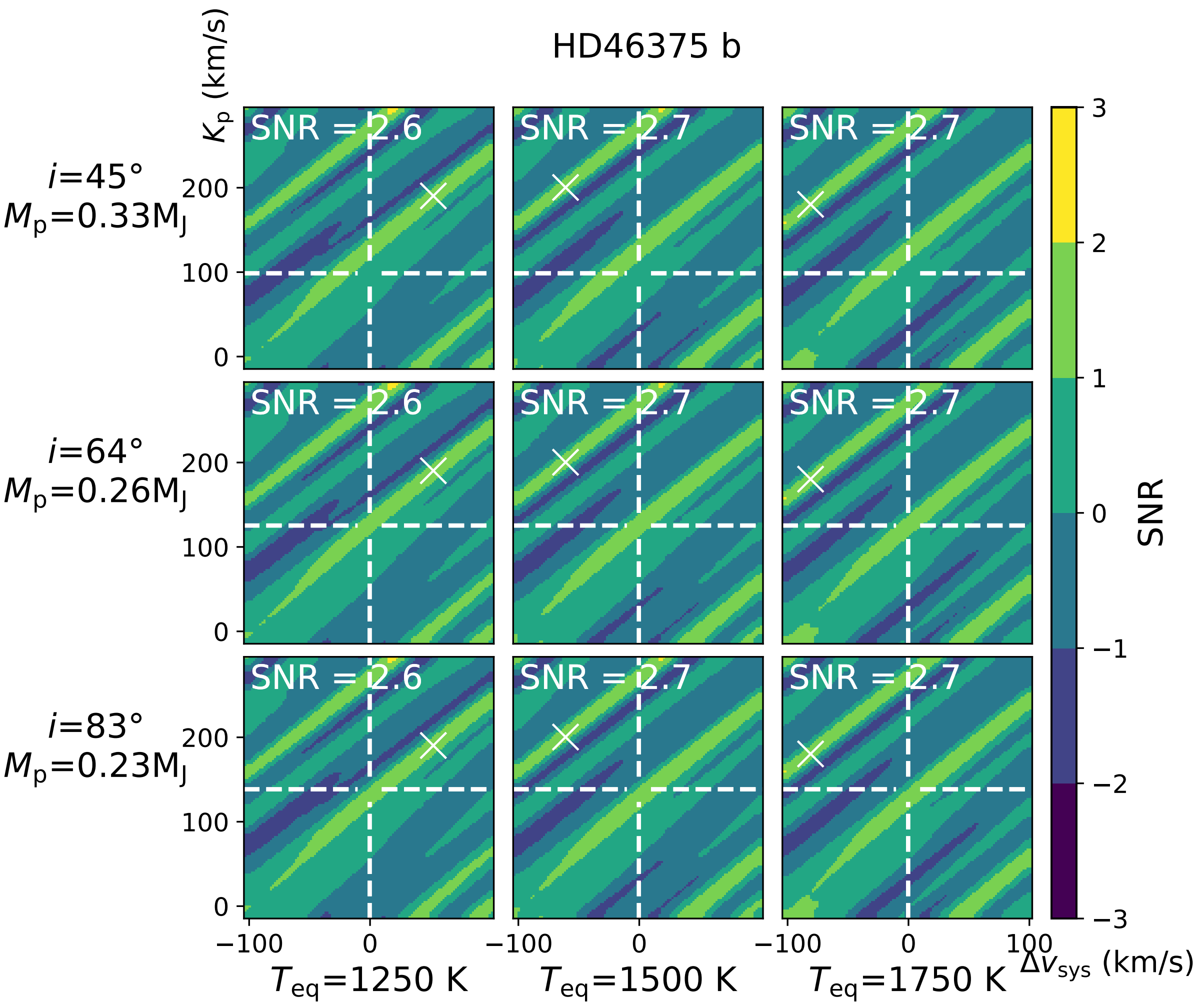

Figure 4.8: SNR maps in velocity space for a range of HD 46375 A b PETITRADTRANS models with varying inclinations and equilibrium temperatures. Each SNR-map is a function of the system velocity v_{sys} and orbital velocity K_p. The white cross symbol marks the maximal SNR location. The dashed white grid indicates the expected location in velocity space for each inclination.

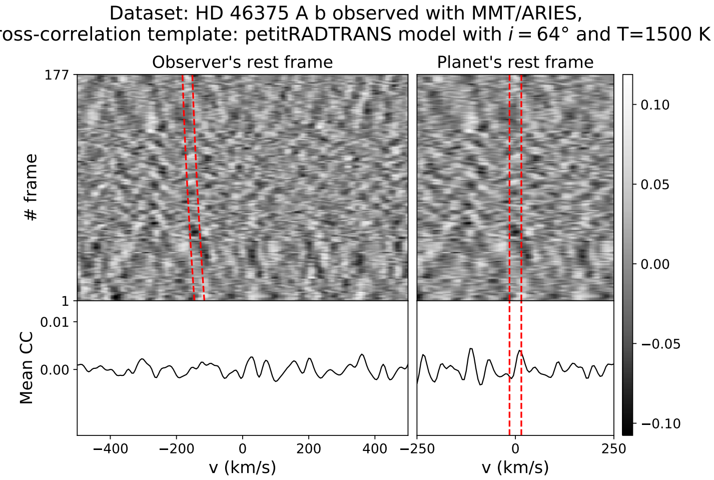

Figure 4.9: CCFs for the HD 46375 A b dataset observed with MMT/ARIES. The cross-correlation template is a synthetic model spectrum computed by petitRADTRANS with an inclination $i = 64°$ and effective temperature $T = 1500$ K. Frames are sorted by orbital phase. The two red lines are centred around the expected planet radial velocity trail. *Top-right:* Same as the top-left panel, but shifted to the expected planet rest frame. *Bottom-left:* the mean CCF along the y-axis. *Bottom-right:* same as the bottom-right panel, but shifted to the planet's rest frame.

4.5.2 SNR and Bayesian retrieval results of τ Böo A b

The SNR-maps after cross-correlation with two templates: one with our best initial guess based on previous work from Pelletier et al. (2021) with the water abundance set to the value found by Webb et al. (2022), and the best model found by running the HRCCS retrieval in this work. Both are shown in Fig. 4.10. The left-most panel shows cross-correlation with the forward model with input parameters from Pelletier et al. (2021), but a higher water abundance from Webb et al. (2022). The model is not detected, with only SNR=1.4 at the expected ($v_{\rm sys}$, $K_{\rm p}$)-location. Many spurious signals of much higher significance exist in the surrounding velocity space. The CCF trail plot is shown in Fig. 4.11 and shows a lot of residual correlated noise.

The right-most panel of Fig. 4.10 shows the cross-correlation with the maximum-likelihood model, in other words the synthetic model spectrum with the best-fit parameters inferred by the HRCCS retrieval framework. This model is also not-detected in the data with a SNR=2.1 at the expected ($v_{\rm sys}$, $K_{\rm p}$)-location. Again many spurious signals of higher significance exist in the neighbouring velocity space. Fig. 4.12 shows the corresponding CCF trail plot for this model. There is visually a lot less correlated noise compared to Fig. 4.11.

Despite the non-detection of the exoplanet atmosphere, with the Bayesian framework the water abundance, thermal structure, and other free parameters can still be constrained. An overview of all the posterior distributions for each of the forward model parameters is

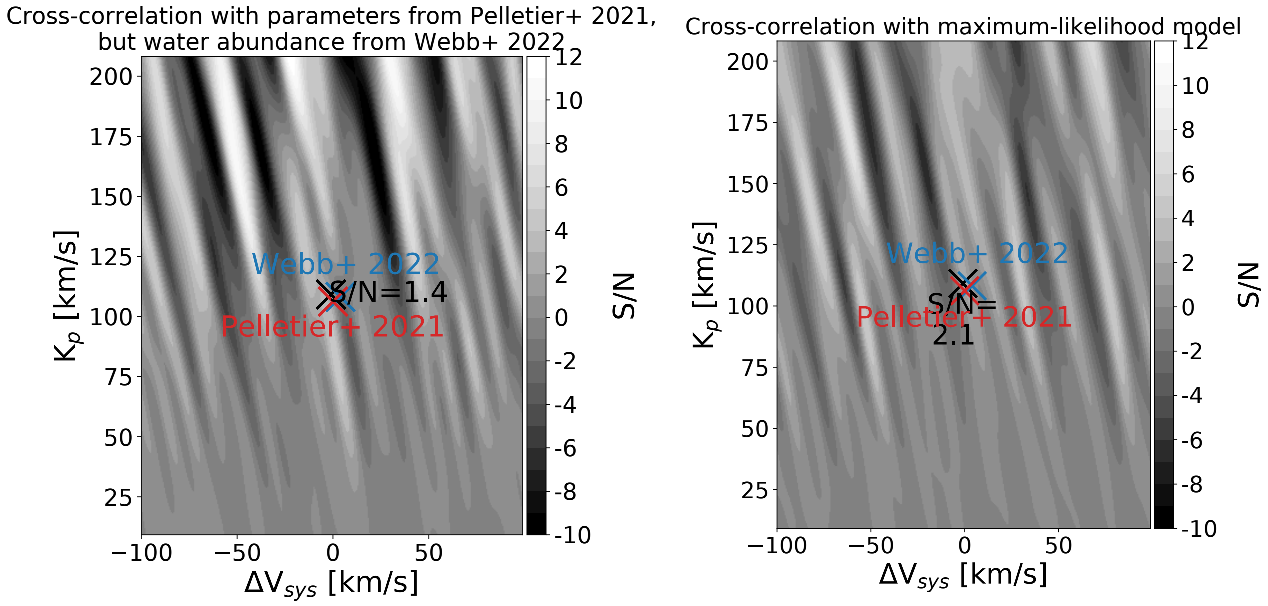

Figure 4.10: SNR maps in velocity space of the τ Böo A b old CRIRES/VLT dataset. The black cross marks the expected (v_{sys}, K_{p})-location. The red and blue crosses indicate the (v_{sys}, K_{p})-values found by Pelletier et al. (2021) and Webb et al. (2022) respectively. *Left panel:* shows SNR-values when cross-correlating with the forward model based on reported values Pelletier et al. (2021) with a water abundance from Webb et al. (2022). The atmosphere is not detected with only SNR=1.4 at the expected location. *Right panel:* shows SNR-values when cross-correlating with the maximum-likelihood model after running the Bayesian retrieval framework. The atmosphere is again not detected with only SNR=2.1 at the expected location.

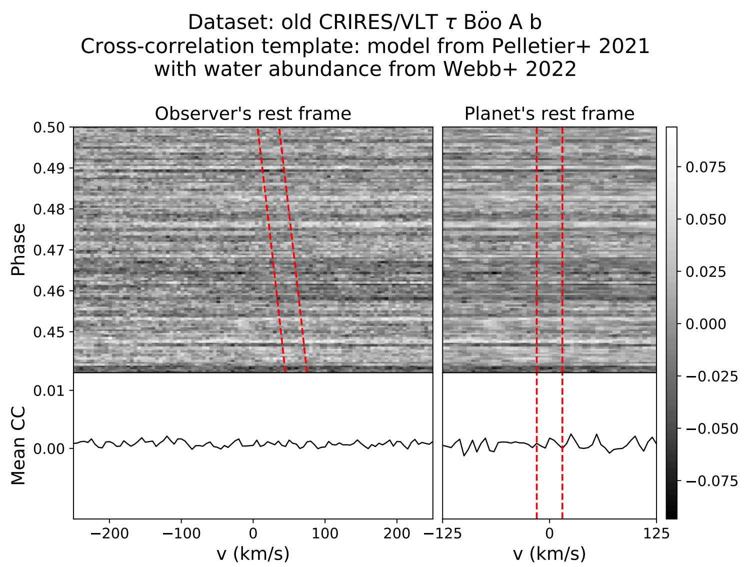

Figure 4.11: CCFs for the τ Böo A b dataset observed with old CRIRES/VLT. The cross-correlation template is the one corresponding with the synthetic model spectrum based on the parameters from Pelletier et al. (2021), but with a modified water abundance from Webb et al. (2022). Frames are sorted by orbital phase. The two red lines are centred around the expected planet radial velocity trail. *Top-right:* Same as the top-left panel, but shifted to the expected planet rest frame. *Bottom-left:* the mean CCF along the y-axis. *Bottom-right:* same as the bottom-right panel, but shifted to the planet's rest frame.

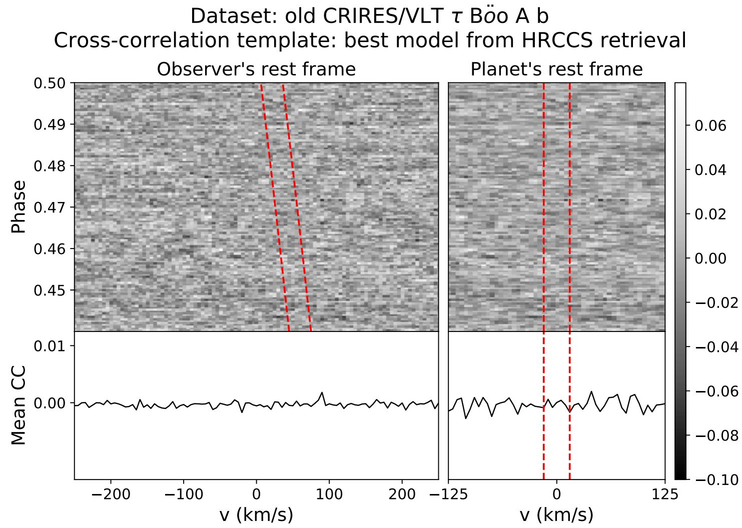

Figure 4.12: CCFs for the τ Böo A b dataset observed with old CRIRES/VLT. The cross-correlation template is the one corresponding with the best HRCCS retrieval output model. Frames are sorted by orbital phase. The two red lines are centred around the expected planet radial velocity trail. *Top-right:* Same as the top-left panel, but shifted to the expected planet rest frame. *Bottom-left:* the mean CCF along the y-axis. *Bottom-right:* same as the bottom-right panel, but shifted to the planet's rest frame.

shown in Fig. 4.13. All abundance constraints are indeed upper limits, consistent with a non-detection of the atmosphere of τ Böo b.

I compare my constraints of the water abundance with previous work in Fig. 4.14. I find a water abundance of $\log H_2O = -6.41^{+3.25}_{-3.22}$. Pelletier et al. (2021) found a water abundance upper limit of $\log H_2O = -8 \pm 1.5$. Webb et al. (2022) found a water abundance of $\log H_2O = -3$, but they do not provide an error on this value. This result has a slight preference for the water-poor scenario, generally the constraints cover a wide range of water abundances from a water-poor to a water-rich atmosphere.

4.5.3 Self-consistent model and results from Bayesian framework of WASP-33 b

In addition to the SNR method, I will now show how comparison with log-likelihood space can add constraints on the chemistry and thermal structure of the atmosphere of WASP-33 b. First, I compare the best-matching PHOENIX modified model with the rest of the models in the suite, as well as that of the best-matching self-consistent PHOENIX model, to give confidence intervals for the alternative P-T profiles, fixed at 10 $\times$ Solar metallicity. This was calculated using Wilks' Theorem and is shown in Fig. 4.15. I used seven free parameters: four for the P-T parametrisation, two for the velocity offsets, and one for the metallicity. The best-matching modified P-T profile is slightly cooler than the best-matching self-consistent PHOENIX model, and inverted P-T profiles with an upper and lower atmosphere temperature difference close to the best-matching model are favoured. Both can be understood by

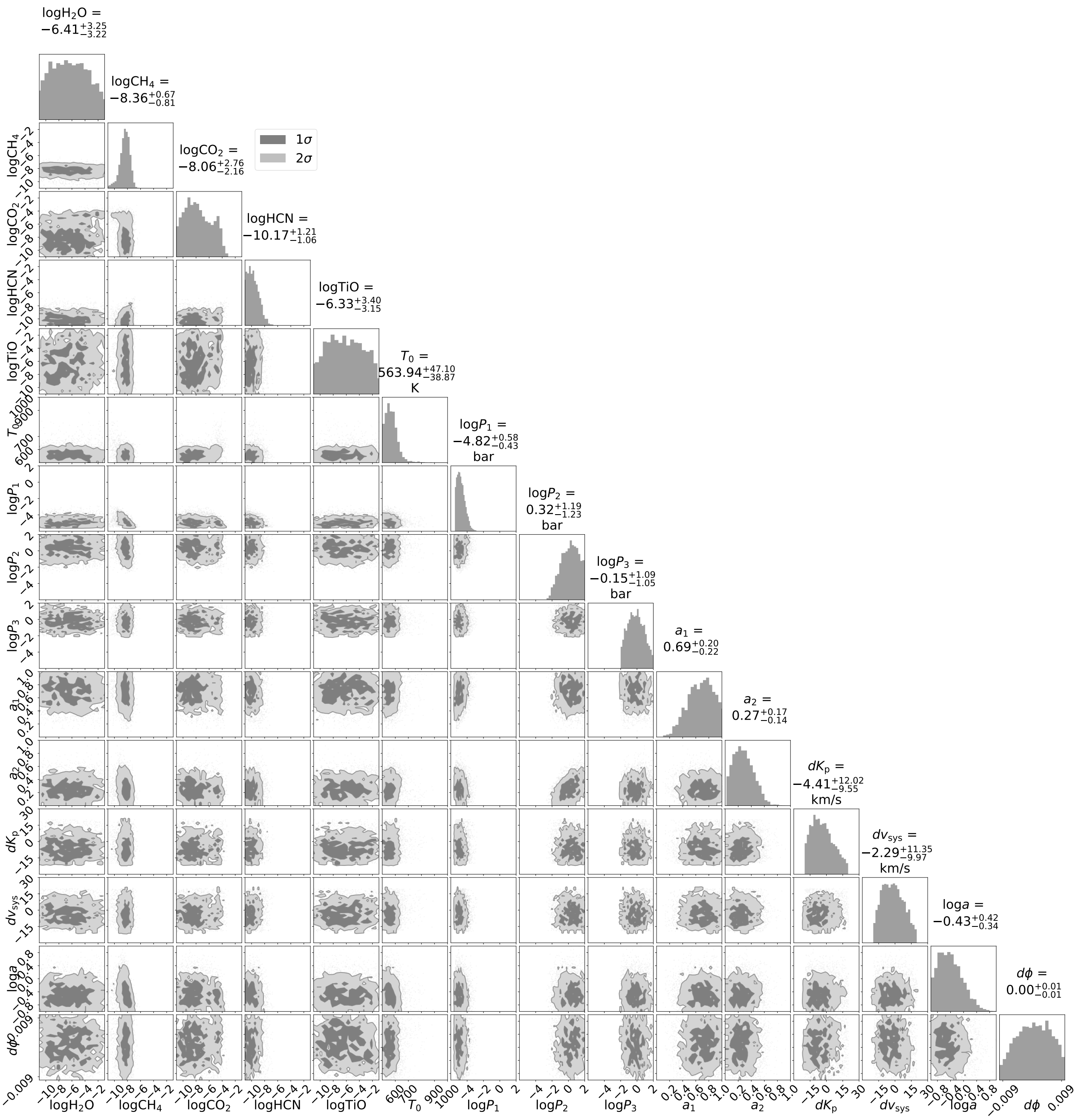

Figure 4.13: Overview of all posterior distributions and parameter constraints produced as output by the retrieval framework for the τ Böo A b old CRIRES/VLT data.

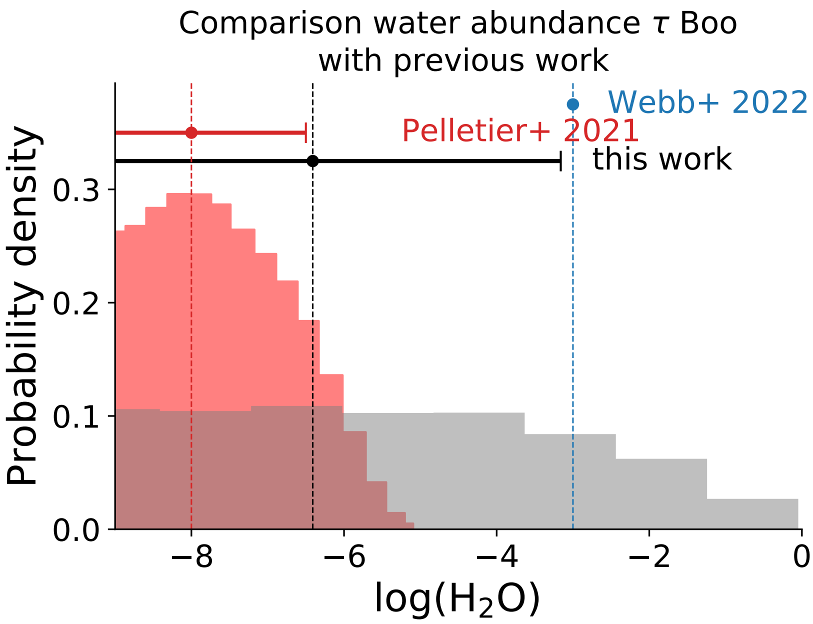

Figure 4.14: Constraints on the water abundance in the atmosphere of τ Böo A b found by this work, Pelletier et al. (2021) and the value reported by Webb et al. (2022). The error bar indicates 1σ-errors on the measured water abundance (Webb et al. (2022) do not report an error on their measured water abundance). Within 1σ the model has a weak preference for a water-poor atmosphere over a water-rich one but generally does not constrain the water abundance.

the fact that the data is sensitive to the relative line strength with respect to the continuum, which is set by the upper and lower atmosphere temperature contrast, the thermal gradient. On the contrary, the data is less sensitive to the absolute temperature due to loss of the continuum information in the HRCCS processing, resulting in a range of absolute lower and upper atmosphere temperatures inside the calculated 1σ-confidence interval.

I also ran the same analysis using Wilks' Theorem to compare the models with a single opacity source excluding the model with all opacity sources included for the best-modified P-T profile PHOENIX model (see left-panel of Fig. 4.16). I find for all nights combined models without CO are significantly worse ($\sigma = 11.1$). Interestingly, there also seems evidence models without H_2O ($\sigma = 5.4$) and marginal evidence OH ($\sigma = 3.4$) are worse which I will discuss further in Section 4.6.3.

The self-consistent PHOENIX models allow us to assess its heat-redistribution efficiency and metallicity. The highest log-likelihood in the PHOENIX self-consistent model suite corresponds to a day-side-only heat-redistribution efficiency $f = 0.5$ and a metallicity of $1\times$ Solar. Confidence intervals comparing the self-consistent PHOENIX models computed using Wilks' Theorem are shown in Fig. 4.17, where I use a visualisation similar to that recently shown by Giacobbe et al. (2021). I use four free parameters: one for the metallicity, one for the heat redistribution efficiency, and two for the velocity offsets. Models with high re-radiation factors $f \geq 1/2$ and high metallicity $\geq 1\times$ Solar are favoured and are within 1σ

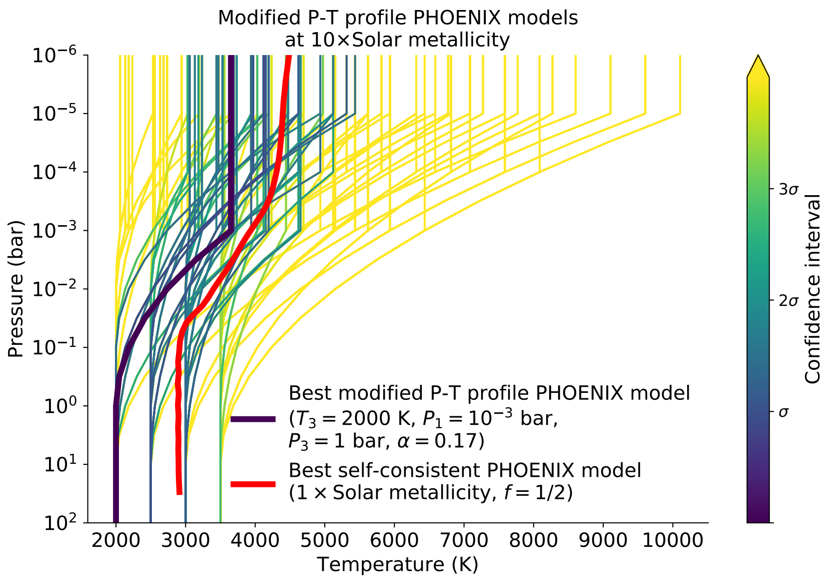

Figure 4.15: Confidence intervals for the modified P-T profile PHOENIX models at 10× Solar metallicity of WASP-33 b. These are for all observing nights combined and were calculated using Wilks' Theorem. The P-T profile of the best-modified structure model, the one with the highest log-likelihood, is plotted in dark green and has the following parametrisation: $T_3 = 2000$ K, $P_1 = 10^{-3}$ bar, $P_3 = 1$ bar, $\alpha_2 = 0.17$. All confidence intervals here are with respect to this best model. The confidence intervals are converted to their corresponding σ-value. The best self-consistent PHOENIX model's P-T profile, at 1× Solar metallicity and with a heat reradiation factor $f = 1/2$, is plotted in red for comparison.

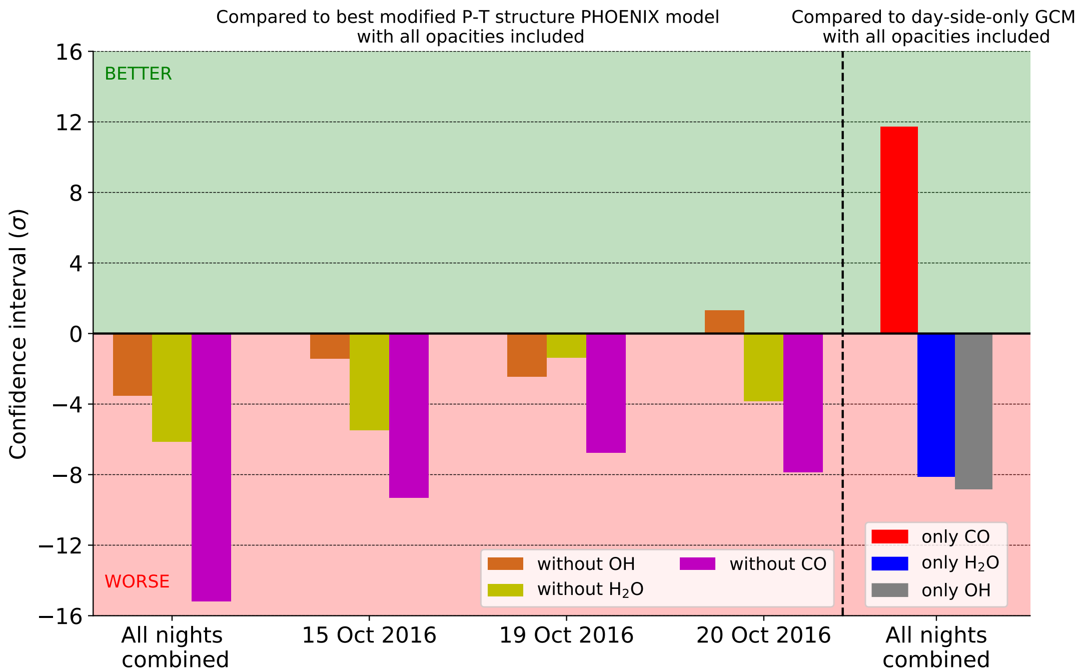

Figure 4.16: Comparison of the best-modified P-T profile PHOENIX model (left-panel) and day-side-only GCM (right-panel) with all opacity sources included to models without/only certain opacity sources included for WASP-33 b. A negative confidence interval indicates the model is worse compared to the model where all opacity sources are included, whereas a positive confidence interval indicates the model is better. Confidence intervals are calculated using Wilks' Theorem.

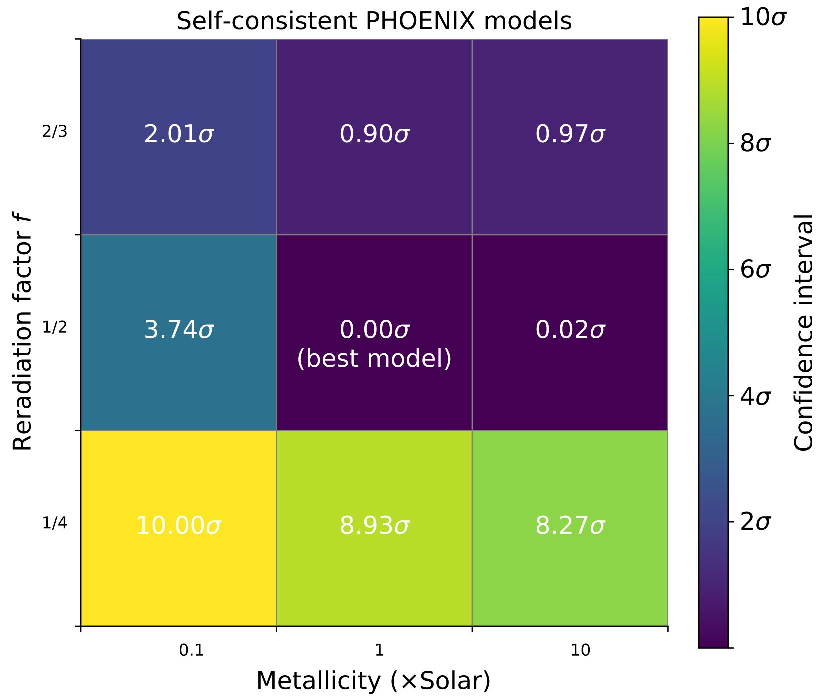

Figure 4.17: Confidence intervals for the PHOENIX self-consistent model grid for all observing nights of WASP-33 b combined using Wilks' Theorem. The best model, the one with the highest log-likelihood, is indicated. By definition of Wilks' Theorem, all confidence intervals here are with respect to this best model. The confidence intervals are converted to their corresponding σ-value, which are annotated in the center of each tile. Models with $f \geq 1/2$ and metallicity $\geq 1\times$ Solar are all within 1σ.

of the best-matching model. I note that the higher SNR for the modified PHOENIX models compared to the self-consistent PHOENIX models is not necessarily surprising given the additional free parameters in the model and the larger number of models explored in the suite. The results from SNR-analysis using this maximum-likelihood self-consistent model are shown in Fig. 4.18 and the corresponding CCF trail is shown in Fig. 4.19. I detect this model at a high SNR=7.6 at the expected location in velocity space. The exoplanetary trail is clearly visible in the CCF time series.

4.6 Discussion

4.6.1 Non-detection of the atmosphere of HD 46375 A b

The non-detection of the exoplanet atmosphere HD 46375 A b can have multiple possible explanations. It may be that the data quality or quantity is insufficiet to detect the exoplanet atmosphere in the first place. To check this hypothesis I first use a rudimentary calculation to check if the expected SNR of the observed stellar spectrum is sufficiently high to detect

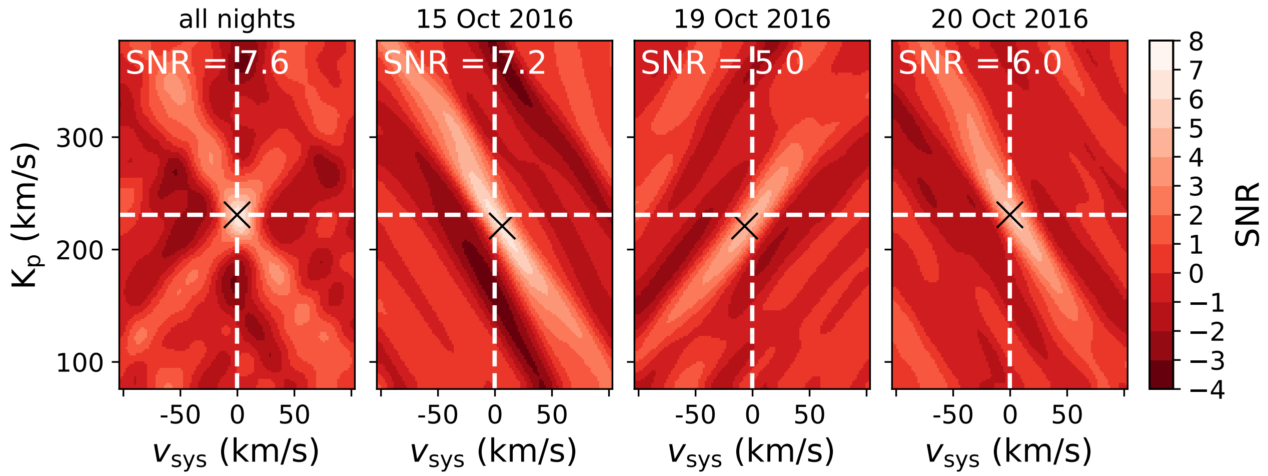

Figure 4.18: SNR as a function of the system velocity v_{sys} and orbital velocity K_{p} for the best self-consistent PHOENIX (1D) model for the WASP-33 b dataset. The black cross symbol marks the maximal SNR location. The dashed white grid indicates the expected location at (v_{sys}, K_{p}) = (-0.3, 230.9) km/s based on the OH detection by Nugroho et al. (2021). This detection is in agreement with their (v_{sys}, K_{p})-values for all nights combined.

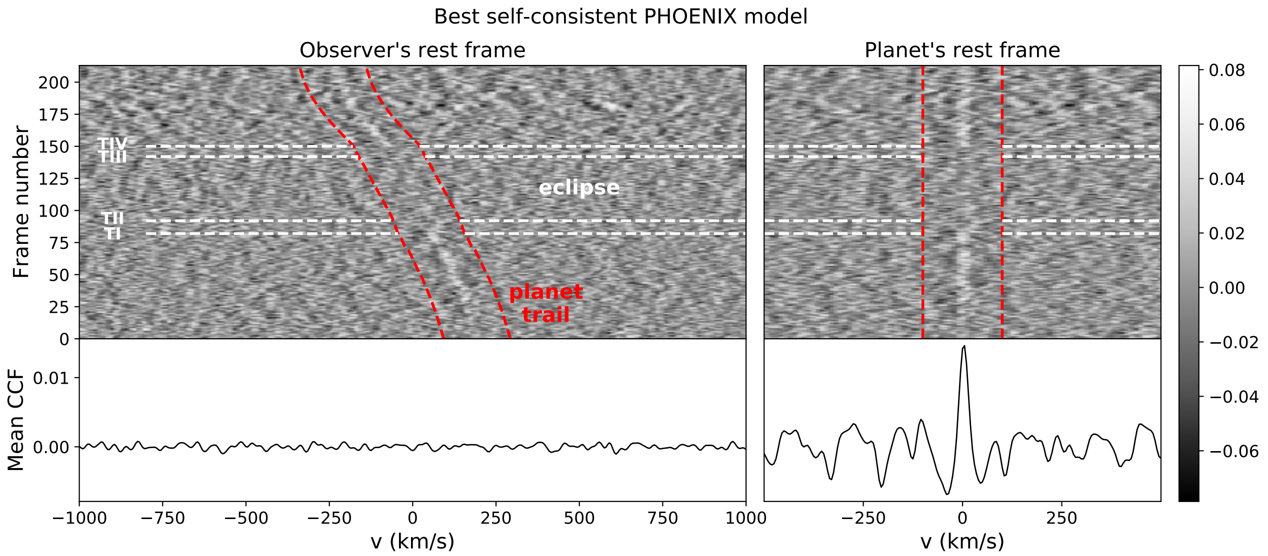

Figure 4.19: CCFs for the best self-consistent model detected at a SNR of 7.6 for the WASP-33 b MMT/ARIES dataset. *Top-left:* The CCF for each frame including all three observing nights in the observer's rest frame. Frames are sorted by orbital phase but are not equally spaced. The start/end of ingress/egress is indicated by the white dashed lines labeled TI-TIV for the four contact points. The two red lines are centered around the planet's radial velocity trail. *Top-right:* Same as the top-left panel, but shifted to the planet rest frame. *Bottom-left:* the mean CCF along the y-axis. Frames, where the planet is not fully visible (in between TI-TIV) were excluded when computing the CCF to prevent dilution of the planet signal. *Bottom-right:* same as the bottom-right panel, but shifted to the planet's rest frame.

the exoplanetary atmosphere in this data set. The expected signal-to-noise ratio can be calculated using equation (2.21), which requires estimates of the continuum SNR, the number of spectral lines in the wavelength range, and the planet-to-star contrast ratio.

I use the model template from Fig. 4.4 to estimate the number of lines. This model was convolved to the observed spectral resolving power of this dataset at $R = 16,000$. I first need to remove the continuum. I do this by splitting the whole model wavelength range into 100 bins of equal size. For each bin, I select the 25 lowest/highest data points, excluding 2σ-outliers from each sample. I fit a second-order polynomial through these data points to estimate the lower/upper continuum in each of the 100 bins. I then stretch the model such that the upper continuum corresponds with a value of 1 and the lower continuum with a value of 0. To count the number of lines, I calculate the number of local minima below a threshold value, where this threshold value corresponds with lines deeper than 10% of the continuum within the spectral order wavelength range. I count a total of $N_{\mathrm{lines}} = 12,3000$.

The SNR of the continuum is calculated from the normalised spectral time series by estimating the median signal and noise in time. To calculate the average signal, I take the median spectrum along the time axis. In this median spectrum, I select the 200 brightest spectral channels and assume these correspond with the continuum level. For each of these spectral channels, I compute the noise as the standard deviation of all the values in time. The signal-to-noise is calculated for each spectrum as the median signal within that spectral channel divided by the noise value within that spectral channel. The median of all 200 SNR-values for each spectral order is computed and I find a median $SNR = 51$.

The contrast ratio can be computed using equation (2.22). I use radii and effective temperatures as listed in Table 3.1. I calculate a contrast ratio of 8.6×10^{-5}. During the observing night, a total of 177 frames were obtained. Inserting all of these values into equation (2.21) and multiplying by $\sqrt{N_{\mathrm{frames}}}$, I compute an expected detection of the exoplanet atmosphere at a SNR of 6.5. I interpret this value as an upper limit on the observed SNR, as it assumes the data is photon-shot-noise limited and free of any correlated noise. Thus a SNR of 6.4 shows under ideal circumstances, the SNR should be sufficient to robustly detect (SNR>5) the exoplanet atmosphere of HD 46375 A b in the ARIES/MMT dataset.

Since the calculation predicts this data is potentially sensitive to a detection of the exoplanet atmosphere, I use an injection of an artificial signal into this data to test this hypothesis. I inject the model from the central panel in Fig. 4.8 into the data at a system velocity offset of $\Delta v_{\mathrm{sys}} = +50$ km/s, this is to avoid overlap with the expected location of the exoplanetary trail in the data. I inject at $\times 1$, $\times 10$, $\times 100$ the expected planet-star contrast ratio. The results are shown in Fig. 4.20. I find no change in the structure of the SNR-maps. This suggests

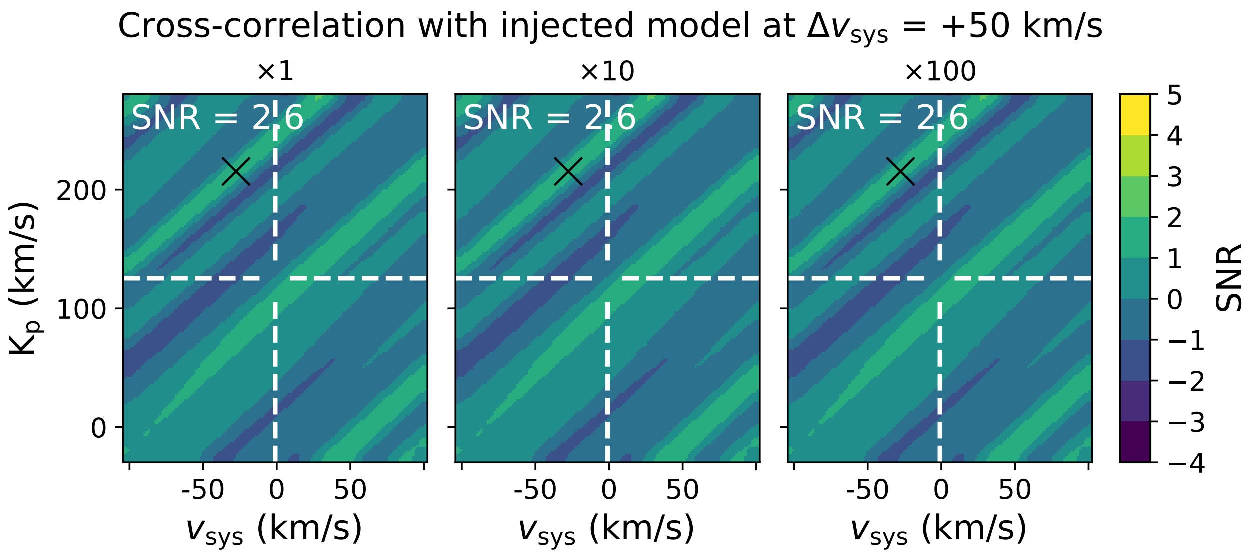

Figure 4.20: Injected cross-correlations for the HD 46375 A b MMT/ARIES dataset. Same as the central panel of Fig. 4.8, but for the data with an artificial signal injected at $\times 1$, $\times 10$ and $\times 100$ the expected strength at a system velocity offset of $\Delta v_{\rm sys} = +50$ km/s. The injection of an artificial signal at these strengths does not affect the structure of these SNR-maps.

these data are insensitive to detection of the exoplanet atmosphere even when injected at much higher strengths.

This implies the data quality is likely insufficient to reach the required level of sensitivity. A likely explanation is that the cleaning does not fully remove the noise to photon-shot-noise limited white noise. Evidence for this is seen in the CCF time series shown in Fig. 4.9 where correlated noise is present. A combination of correlated with noise, with fewer resolved spectral lines by ARIES/MMT may have pushed the SNR in the real observations below the detection threshold. Lastly, there is the option the exoplanet atmospheric signal is hiding in this data, but the nine PETITRADTRANS output spectra are a poor match to the actual exoplanetary spectra, resulting in the non-detection.

4.6.2 Non-detection of the atmosphere of τ Böo A b and upper limits on the water abundance

Since I also do not detect the atmosphere of τ Böo b I also calculate the expected SNR using equation (2.21). Following the same method as for HD 46375 A b, I find $N_{\rm lines} = 751$, $SNR_\star = 261$ (with a continuum SNR of ~113-351 depending on which of the four CRIRES spectral orders are used) and $F_{\rm p}/F_{\rm s} = 7.8 \times 10^{-5}$. These observations have $N_{\rm frames} = 130$. I calculate an expected detection of the exoplanet atmosphere at a SNR$= 6.4$, thus in principle, this data should have the sensitivity required to robustly detect a signal (SNR>5) from τ Böo b.

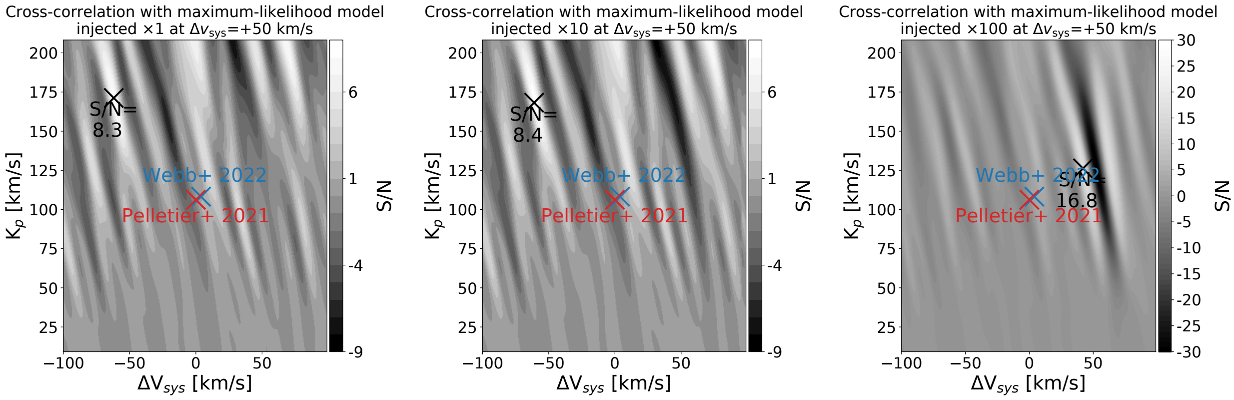

Figure 4.21: Cross-correlation for the τ Böo A b old CRIRES/VLT dataset. The same as Fig. 4.10, but for the data with an artificial signal injected at $\times1$, $\times10$ and $\times100$ the expected strength at a system velocity offset of $\Delta v_{\rm sys} = +50$ km/s. Only the strongest injection $\times100$ shows a cross-correlation peak around the expected location in velocity space.

To test this hypothesis further I run injection-recovery tests. As previously, I inject the maximum-likelihood model into the data at a velocity offset of $\Delta v_{\rm sys} = +50$ km/s, again to avoid overlap with the expected location of the exoplanetary trail in the data. The model is injected at $\times1$, $\times10$, and $\times100$ the expected planet-star contrast ratio. The cross-correlation results of this are shown in Fig. 4.21. Only the strongest injection $\times100$ shows a significant difference in the structure of the cross-correlation map in velocity space with a signal close to the injected system velocity. The weaker injections at $\times1$ and $\times10$ the expected strength show no changes in the structure of the cross-correlation maps in velocity space. This suggests that the data is not sensitive to the exoplanet model at the expected strength. Again it is likely the dataset is not cleaned down to a photon-limited white noise level. Possibly the observing conditions were not ideal during the observing night.

Since the injection suggests the data is insensitive to a detection of the atmosphere of τ Böo A b unless injected at a strength two orders of magnitude higher than expected, the non-detection of τ Böo A b could also A be due to a low water abundance in its atmosphere, since water is the dominant opacity source in the observed wavelength range. The recovery of a very strong injected signal suggest that a very high water abundance may have been detectable. This is supported by the Bayesian framework which excludes very high water abundances, and I find an upper limit on the water abundance of $< 10^{-3}$ with 1σ confidence. This is reflected by the posterior distribution, which is different from the uniform prior distribution. As the data can only provide weak constraints on the water abundance, it thus has a small preference for the water-poor scenario observed by Pelletier et al. (2021).

Further analysis of the MEASURE τ Böo b data will likely improve these constraints, by adding more data, but also by adding complementary wavelength coverage to the CRIRES data. However, the short exposure times in this dataset make it relatively large and thus

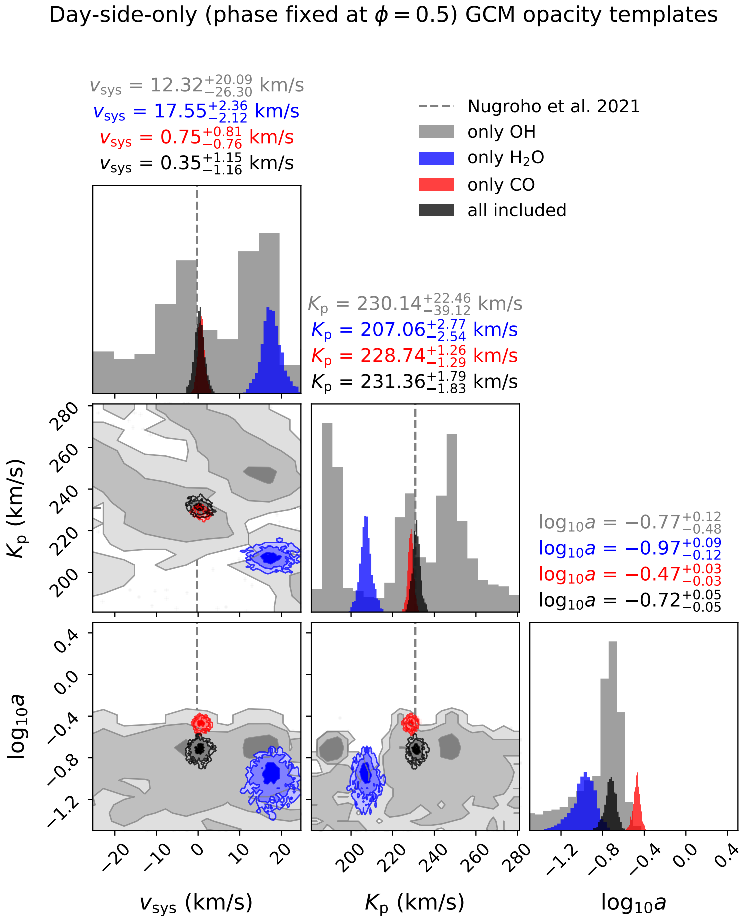

Figure 4.22: Posterior distributions from the CC-to-log(L) framework based on Brogi & Line (2019) shown for the GCM day-side-only spectral templates for different opacity sources are included for the WASP-33 b ARIES/MMT dataset. All results are shown for all nights combined. The contours indicate the 1σ, 2σ, and 3σ confidence intervals. All frames with phases during the eclipse have been excluded from this analysis to prevent dilution of the planetary signal. The dashed black grid indicates the expected location at (v_{sys}, K_p) = (-0.3, 230.9) km/s based on the OH detection by Nugroho et al. (2021).

time-consuming to analyse in detail. Moreover, τ Böo b has been observed one other night with CRIRES, albeit under poorer observing conditions. The addition of this night may also help to increase the constraining power of the data.

4.6.3 Chemistry and thermal structure of WASP-33 b

In this chapter, I showed that a Bayesian retrieval framework can provide additional constraints of the chemistry and thermal structure of the atmosphere of WASP-33 b to the SNR-detection presented in the previous chapter. Although, I do not explore non-inverted or isothermal P-T profiles, my highest log-likelihood P-T profile (see Fig. 4.15) shows temperature contrasts with well constrained upper- and lower limits when including a thermal inversion layer. The likelihood-analysis thus reflects the detection of emission lines providing unambiguous evidence for a thermal inversion in the atmosphere of WASP-33 b.

As presented in the previous chapter, from all molecular templates investigated in this work, only CO has resulted in a robust detection. This is further supported by the CC-to-log(L) results shown in Fig. 4.22 where only CO has similar constraints on the velocities compared to when all opacity sources are included: $v_{\rm sys} = 0.75^{+0.81}_{-0.79}$ km/s, $K_{\rm p} = 228.74^{+1.26}_{-1.29}$ km/s. If I compare the same models in terms of the CC-to-log(L) framework, I find exclusion of water or OH does result in a significantly worse model (see Fig. 4.16), perhaps suggesting a marginal detection of these species or the combined set of all other opacity sources, besides CO, during the first night.

I investigate whether the weak signal from the dayside-only GCM H_2O-only template is due to stellar or telluric contamination. To do this, I run a CC-to-log(L) analysis using only frames obtained when the planet is not visible i.e. during the full eclipse of WASP-33 b.

In this analysis, I include $v_{\rm sys}$, $K_{\rm p}$, and $\log a$ the logarithm of the scale parameter, as free parameters. I constrain these parameters by running the PyMultiNest Markov chain Monte Carlo algorithm exploring the three-dimensional likelihood space. The output of this algorithm are posterior distributions from which error contours can be computed.

Spurious signals due to telluric or stellar residuals should persist whereas signals originating from WASP-33 b should disappear from the planet's expected ($v_{\rm sys}$, $K_{\rm p}$)-location. For H_2O I found that a signal is still retrieved at the same offset ($v_{\rm sys}$, $K_{\rm p}$)-position albeit with larger errors, while the CO signal disappeared from the expected planet ($v_{\rm sys}$, $K_{\rm p}$)-position. This supports the interpretation that any H_2O signal in the ARIES data is caused by non-planetary residuals.

4.7 Conclusions

In this chapter I analysed the non-detections of the exoplanet atmospheres of HD 46375 A b and τ Böo A b. I show these non-detections are significant, as my injection-recovery tests show the data is sensitive to these models. For τ Böo A b, I show how a Bayesian framework can still constrain atmospheric properties despite the non-detection. Lastly, for WASP-33 b, I show that complementary to the SNR analysis presented in the previous chapter, the introduction of self-consistent PHOENIX (1D) models and a Bayesian framework result in additional constraints of the chemistry and thermal structure.

From the analysis of these three targets, I conclude the following key points:

1. I found the SNR values from the cross-correlation maps are consistent with the results from injection-recovery tests. Still, the observations of HD 46375 A b and τ Böo A b are not sensitive to the majority of tested models. This demonstrates that injection-recovery tests are a good way to evaluate the constraining power and quality of HRS datasets.

2. The reduced spectral resolving power and data quality of the MEASURE observations challenge observations of cooler, lower-mass targets like HD 46375 A b with MMT/ARIES.

3. HRCCS with a strong detection that can be combined with Bayesian frameworks to further constrain P-T structure and chemistry. I demonstrated this using MEASURE data of WASP-33 b which shows a strong detection of CO emission lines. Constraints on the P-T profile show HRS data is sensitive to the temperature gradient of the inversion layer but less sensitive to the absolute temperatures of the lower atmosphere. The exclusion or inclusion of different opacity sources compared within a Bayesian retrieval framework confirms the unambiguous detection of CO in emission in the atmosphere of WASP-33 b.

4. HRCCS with a non-detection can be combined with a Bayesian framework to still provide useful upper limits. I demonstrated for the non-detection of the atmosphere of τ Böo A b, Bayesian frameworks enabled me to infer constraints on the abundance of water. Within 1σ there is a slight preference for a water-poor atmosphere scenario, in line with results by Pelletier et al. (2021) and at slight tension with results from Webb et al. (2022).

Overall, these results highlight the power of Bayesian frameworks in constraining the chemistry and P-T structure of exoplanet atmospheres both for detections and non-detections with HRCCS.

5 Dynamics with Bayesian frameworks: an eastward hot spot offset in WASP-33 b

The material in this chapter is partly based on van Sluijs et al. (2023) and sometimes I have used parts of this work with minor or no changes to the original text or figures, to remain concise and preserve clarity of the underlying message. The 3D GCM synthetic model spectra of WASP-33 b and corresponding opacity lists were computed by Elspeth K. H. Lee.

In this chapter, I will demonstrate Bayesian frameworks combined with HRS can constrain the atmospheric dynamics of HJs. Specifically, I focus on offsets in the hottest region of their atmospheres, so-called hot spot offsets. As described in the introduction of this thesis, models of HJs predict different hot spot offsets for different stellar irradiation environments and planet gravities. Thus, this new method provides a novel way to test dynamical predictions from HJ GCMs and assess our understanding of their extreme atmospheric physics.

5.1 Introduction to hot spot offsets

Hydrodynamical simulations predict the thermal structure of HJs to be asymmetric around the sub-stellar point. This asymmetry arises from the competition between heat transport by winds of planetary-scale waves and the radiative cooling of the parcel of gas (e.g. Showman & Guillot, 2002; Perez-Becker & Showman, 2013). In standard hydrodynamical simulations, the gas flow follows the direction of rotation, resulting in an eastward hot spot offset. Hence the majority of GCM codes predict eastward offsets[1] (e.g. Perna et al., 2012; Komacek & Showman, 2016; Komacek et al., 2017; Parmentier et al., 2021; Showman et al., 2020).

The strength of the hot spot offsets, in other words, how many degrees eastward the hottest point is from the substellar point, depends on the atmospheric radiative timescales.

[1]This assumes these eastward offsets are observed at near-infrared wavelengths, where the reflected light from the exoplanet can be neglected. Note that reflected light must be addressed at optical wavelengths, complicating the interpretation of observed offsets.

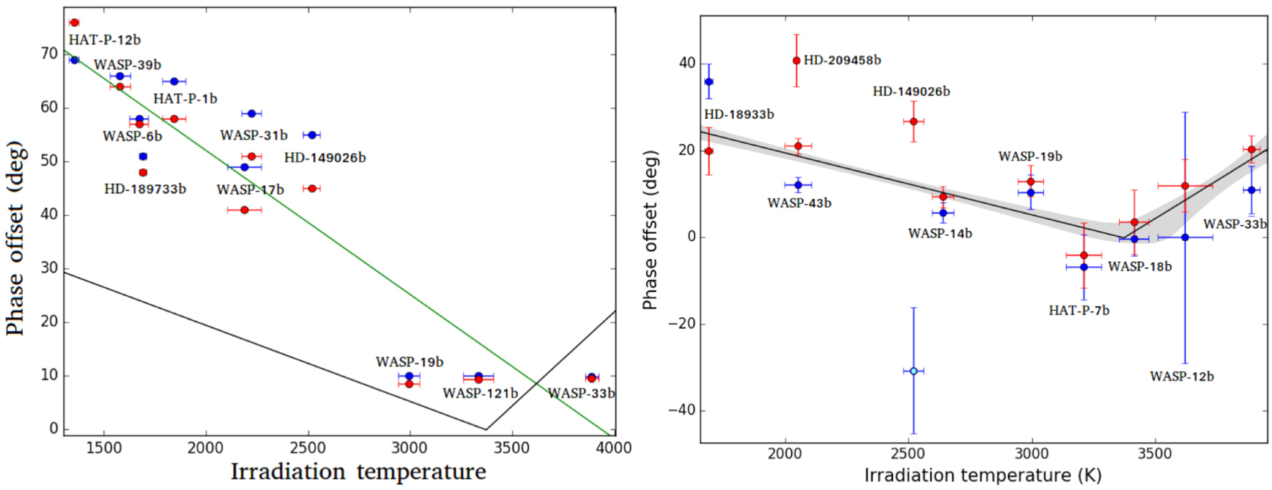

Figure 5.1: Overview of phase offsets as a function irradiation temperature observed with Spitzer. *Left panel:* predictions of phase offsets by GCMs for both of the Spitzer bandpasses (again indicated by blue and red). The trend predicted by the (non-magnetohydrodynamical) GCMs is indicated by the green line. The black line is the same as the observed trend from the right panel. Figure adapted from Zhang et al. (2018). *Right panel:* The blue points indicate the 3.6μm bandpass and the red points are the 4.5μm results. The black line is the best-fit bilinear model, and the gray region is the 1σ confidence interval.

For short radiative time scales (e.g. the coolest HJs), heat redistribution is efficient, resulting in large hot spot offsets. The opposite is true for long radiative time scales (e.g. UHJs). A prediction by GCMs of hot spot offsets as a function of the effective temperature is shown in the left panel of Fig. 5.1.

Notably, GCMs including magnetic effects predict deviations of phase offsets for the hottest UHJs (e.g. Hindle et al., 2019, 2021; Beltz et al., 2022). This is due to predictions of strong magnetic drag as their atmospheres become largely ionised due to extreme stellar irradiation. Therefore, for the hottest UHJs, magnetohydrodynamic GCMs predict westward hot spot offsets (Hindle et al., 2019), or even oscillating hot spot offsets (Hindle et al., 2021).

Previous studies observing phase curves of HJs have constrained hot spot offsets (e.g. Schwartz et al., 2017; Zhang et al., 2018; Dang et al., 2018; Keating et al., 2020; Bell et al., 2021b; May et al., 2022). They do this by measuring the continuum flux of the HJ as it orbits its host star. As more of the hotter dayside becomes visible, higher levels of continuum flux are observed. Thus a peak in the continuum flux levels corresponds to when the hottest part of the HJ is visible. An example of this was shown in Chapter 1 for WASP-121 b (see top panel Fig. 1.3). Since close-in HJs are tidally locked, the orbital phase where this peak occurs coincides with the hot spot offset away from the substellar point: a peak at half-phase implies no hot spot offset, a peak before half-phase implies an eastward hot spot offset and a peak after half-phase implies a westward offset.

An analysis of Spitzer phase curves by Zhang et al. (2018) agrees with the predicted trend of large eastward offsets for the coolest HJs towards small phase offsets for the UHJs (see right panel of Fig. 5.1). However, the GCMs predict larger phase offsets than those observed. Moreover, there is disagreement on how the observed phase offsets depend on the observed bandpass compared to the predicted trend by the GCMs. This suggests either that GCMs overpredict the heat redistribution efficiency or exclude important physics such as clouds or magnetism. Another possibility is that there are uncorrected biases in the observed phase offsets, particularly the removal of the systematics in Spitzer data has proven to be challenging (e.g. Bell et al., 2021b). Robust observations over a large wavelength range (e.g. from the optical to the near-infrared), and a solid theory that includes all relevant atmospheric processes, are both required to fully understand these phase offsets.

An example of an UHJ where a few studies suggest an offset hot spot is WASP-33 b. Zhang et al. (2018) found a phase angle offset by $-12.8 \pm 5.8°$ in the Spitzer 3.6¯m-band, consistent with an eastward hospot. On the contrary, Von Essen et al. (2020) found a $28.7 \pm 7.1°$ phase angle offset in the optical with TESS, suggesting a westward offset hot spot instead, although they mention host star variability may introduce a spurious westward offset. Recently, Herman et al. (2022) reported line-contrast variations and a $22 \pm 12°$ westward phase offset from their detection of Fe-I emission lines using HRCCS.

Complementary constraints on hot spot offsets from an alternative and independent method, such as HRCCS, are valuable to address the tension between phase curve observations and GCM predictions. In Section 5.2, I will introduce how the phase-dependant scale parameter within the Brogi & Line (2019) CC-to-log(L) mapping indicates a hot spot offset by tracing the phase-dependant variation of the spectral line contrast. I will apply this idea to real data of WASP-33 b, where the strong detection of CO enables tracing the phase-dependant variations of CO emission lines through the scale parameter. In Section 5.3 I introduce a 3D GCM of WASP-33 b and describe how to constrain the phase-dependence of the scale parameter in the WASP-33 b dataset. In Section 5.4 I compare the results from 1D models and the 3D GCM. In Section 5.5 I show the observed variation in the scale parameter is consistent with an eastward hot spot offset in the atmosphere of WASP-33 b. In Section 5.6, I conclude this chapter.

5.2 Hot spot offsets with HRCCS

In hydrodynamical GCMs with eastward hot spot offsets, the P-T structure inside the hot spot region has the weakest thermal gradient. This is a natural consequence of the predicted global wind patterns, that redistribute heat from the dayside to the night-side. In these models, air west of the hot spot is experiencing a transition from cold to hot. This transition happens first at low pressures and propagates downwards. This naturally makes a very strong thermal gradient at this transition region between the cold and hot profile and happens at the pressure these observations probe. Once air flows from the hot spot to the cold side the cooling happens more homogeneously over the P-T profile, leading to a less steep gradient.

The goal of Section 5.2.1 is to show that for HRCCS, phase-dependant variations of the line-contrast can be related to the longitudinal variation of the P-T structure through the scale parameter in the Brogi & Line (2019) CC-to-log(L) mapping. Consequently, HRCCS is also sensitive to the location of the hot spot offset. I will describe two ways in which the scale parameter can indicate a hot spot offset using HRCCS. In Section 5.2.2 I will compare my method to two other studies that also used HRCCS to constrain phase offsets.

5.2.1 How the CC-to-log(L) scale parameter indicates hot spot offsets

I will show that for HRCCS phase-dependent variations of the line contrast can be related to longitudinal variation of the P-T structure based on a simple atmospheric toy model. This atmospheric toy model assumes (i) constant abundances with longitude and latitude, (ii) constant abundances with altitude, and (iii) a cloud-free atmosphere. These approximations are appropriate on the hot cloud-free dayside of UHJs and when targeting a molecule with a high dissociation temperature. An example of such a molecule is CO, which has a high dissociation temperature due to its strong covalent bond (Lothringer et al., 2018).

In my toy atmospheric toy model, the exoplanet atmosphere is modelled by a simple P-T structure $P(T)$ with three layers: a lower atmosphere at T_1, an upper atmosphere at T_2 and a transition layer in between (see black lines in the right panel of Fig. 5.2). P-T parametrisations with three layers are commonly used to model HJ atmospheres (for example see Madhusudhan & Seager, 2009). I assume an inverted atmosphere, thus $T_2 > T_1$, as expected from UHJ models (e.g. Lothringer et al., 2018; Arcangeli et al., 2018; Evans et al., 2018; Gandhi & Madhusudhan, 2019). Now let our targetted molecule have two energy transitions with corresponding wavelengths λ_1 and λ_2. Furthermore, assume an optically thick atmosphere at pressures with temperature $T = T_1$, optically thin at pressures with temperatures $T > T_1$, and optically thick at the transition wavelengths λ_1 and λ_2. The spectrum of this toy model

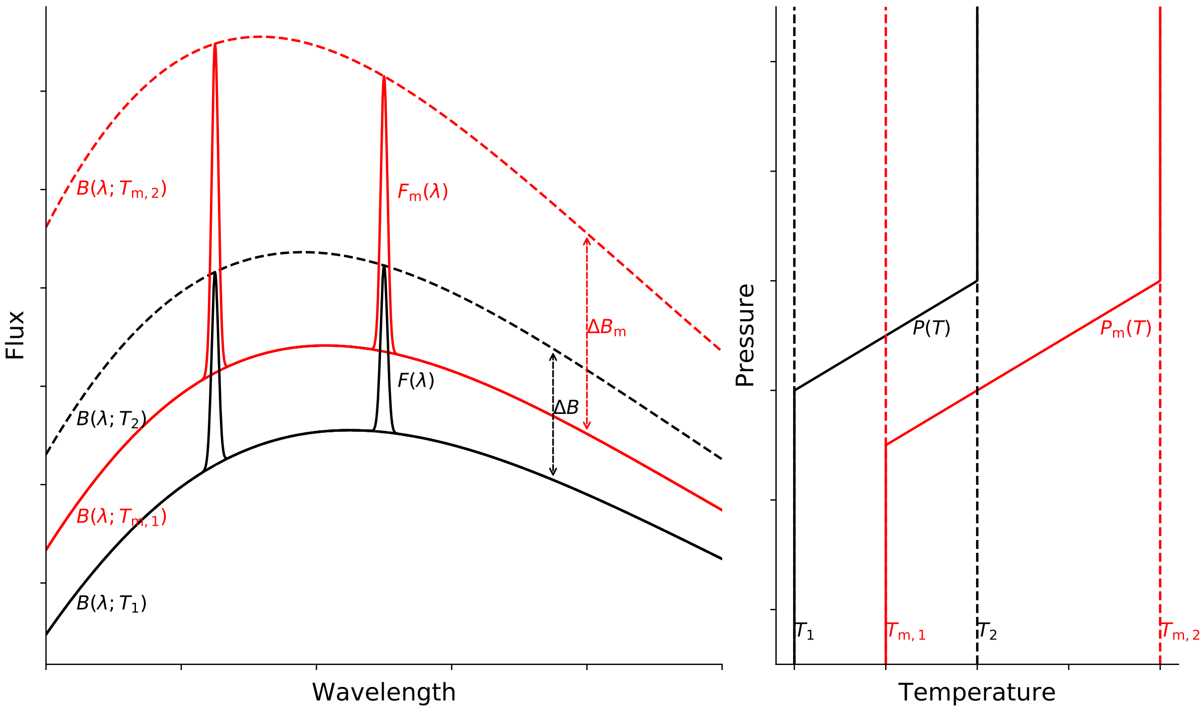

Figure 5.2: Simplified example of an exoplanet atmosphere with two spectral emission lines. This assumes an inverted atmosphere with a lower layer temperature T_1 and an upper layer temperature T_2 with a gradual transition region in between. The black curve $F(\lambda)$ shows flux variations of the data given the assumed black P-T profile $P(T)$ in the right panel. Finally, I assume the real atmosphere is modelled by some forward model, which may or may not match the real data, as shown in red, parametrised by lower and upper layer temperatures $T = T_{m,1}$ and $T = T_{m,2}$ with the same temperature gradient. This results in the flux $F_m(\lambda)$ in the left panel and P-T profile P_m(T) in the right panel. The transition pressures between the atmospheric layers do not necessarily coincide between the forward model and the data.

$F(\lambda)$, follows a black body curve $B(\lambda; T_1)$ with emission lines at λ_1 and λ_2 that reach a peak brightness temperature of T_2 (see black lines in the left panel of Fig. 5.2.

Let us assume that this toy model exoplanet atmosphere was observed using HRCCS and the goal is to constrain its P-T structure by comparing it to a grid of forward models. Let this forward modelling code create a trial model, which may or may not match the observed toy model, using the same P-T parametrisation $P_m(T)$, but with a lower atmosphere at $T = T_{m,1}$ and an upper atmosphere at $T = T_{m,2}$. This results in a modelled synthetic spectrum $F_m(\lambda)$ (see red lines in the left and right panels of Fig. 5.2). Note that in this example, it is not required that the transition between the atmospheric layers in our forward model and toy model occur at the same pressure levels, but they do have the same temperature difference.

Now imagine this toy model was observed using a high-resolution spectrograph and the data is processed using a typical processing procedure to clean the telluric/stellar lines. This processing will remove the exoplanet continuum, because of the self-calibration of HRS data. Thus the line contrast in my processed data is given by $\Delta B = B(T_2) - B(T_1)$ and the processed model has a line contrast of $\Delta B_\mathrm{m} = B_(T_{\mathrm{m},2}) - B_(T_{\mathrm{m},1})$. Thus the line contrast is set by the difference in temperature between the lower and upper atmosphere, regardless of the pressure levels where the line forms.

Within the Brogi & Line (2019) CC-to-log(L) mapping, the model is multiplied with a scale parameter a. Thus, for the scale parameter that matches the data

$$\Delta B = a\Delta B_{\mathrm{m}}. \tag{5.1}$$

This equation relates the line contrast in the data to the line contrast in the model through the scale parameter. Note that there is no unique value of ($T_{\mathrm{m},1}$, $T_{\mathrm{m},2}$) that matches the requirement of equation 5.1, but rather there is a set of combinations of ($T_{\mathrm{m},1}$, $T_{\mathrm{m},2}$) that result in the same difference in flux ΔB_{m} between the upper and lower atmosphere. Thus high-resolution spectra are sensitive to the gradient of the inversion, but not to the absolute temperatures themselves. This is different from low-resolution spectra where the flux is usually calibrated against a reference star, thus the continuum is preserved and therefore the data is sensitive to absolute temperatures.

For a 'real' 3D exoplanet, the gradient of the inversion layer is not constant with longitude. As an observer sees the combined flux of different longitudes as a function of the orbital phase, the line contrast is also a function of the orbital phase, thus $\Delta B = \Delta B(\phi)$. Now lets look at two cases: (i) the is data cross-correlated with a phase-independent 1D model such that ΔB_{m} is constant (ii) the data is cross-correlated with a phase-dependant 3D model such that $\Delta B_{\mathrm{m}} = \Delta B_{\mathrm{m}}(\phi)$

In the first case, the line contrast is directly proportional to the scale parameter. Thus a maximum/minimum in $\Delta B(\phi)$ corresponds with a maximum/minimum of $a(\phi)$. This implies that if the CC-to-log(L) mapping finds variation of the scale parameter with the orbital phase, those phases with the lowest scale parameter correspond with the longitudes with the weakest thermal gradient or the hot spot region.

In the second case, only if the 3D phase-dependent model matches longitudinal variations of the gradient of the P-T profile in the data, such that $d(\Delta B)/d\phi = d(\Delta B_{\mathrm{m}})/d\phi$, the scale parameter is constant with orbital phase. Thus if the CC-to-log(L) mapping finds a constant scale parameter, it indicates the model matches the variation of the thermal gradient in the data. Such a 3D model can be a GCM, which naturally includes a hot spot offset.

In conclusion, I find two ways in which HRCCS can indicate a hot spot offset: (i) when the data is compared to a phase-independent 1D model and the scale parameter is lowest orbital phases offset from half-phase, and (ii) when the data is compared to a phase-dependant 3D GCM that includes a hot spot offset, and a consistent scale parameter between for all phases is found.

5.2.2 Comparison to previous studies

Only two previous studies link phase-resolved high-resolution spectra to a phase offset, namely Herman et al. (2022) and Hoeijmakers et al. (2022).

Herman et al. (2022) use the Bayesian framework by Gibson et al. (2020) (which has the same model scaling parameter as Brogi & Line (2019)) to constrain a phase-offset. They model phase-dependant variations in their observations by the following equation:

$$A_p(\phi) = \alpha(1 - C\cos^2(\pi(\phi - \theta))), \tag{5.2}$$

where $A_p(\phi)$ is equivalent to the scale parameter a within the Bayesian framework described by Brogi & Line (2019). The parametrisation comes from the modelling of low-resolution phase curve observations, where the variation of the normalised continuum flux is well described by a $\cos^2(x)$-function with a phase offset θ and a day-to-nightside contrast ratio C. The multiplication by α in equation 5.2 allows for additional scaling, but should ideally be retrieved at $\alpha = 1$.

Hoeijmakers et al. (2022) model variations in the strength of their CCF as a function of phase by

$$CCF = Ae^{\frac{-(v-v_t)^2}{2\sigma_w^2}} \cdot (0.5 + 0.5\cos 2\pi(\phi_t - \theta - \pi)^\gamma + C, \tag{5.3}$$

where A is the peak amplitude of the emission, v_t the sum of the system velocity and orbital velocity, σ_w the Gaussian line-with, γ the index of the phase function, C a constant offset and θ the offset angle of peak emission.

Both equation 5.2 and equation 5.3 models are based on parametrisation common for low-resolution phase curves. However, careful interpretation of the retrieved parameters is required when adapting this parametrisation to HRCCS. This is because in HRCCS the processing steps will remove the continuum information and therefore the shape of the normalised continuum flux. As argued in the previous section, the model scaling follows the line contrast which is set by the temperature gradient in the P-T structure, but not the continuum flux. Indeed, Hoeijmakers et al. (2022) write themselves it should not be expected that "... line emission is described by the same phase-function as broad-band continuum emission.".

This difference has important consequences on the interpretation of phase variation of the scale parameter. In the next sections, I will demonstrate this based on the strong detection of CO emission lines in the atmosphere of WASP-33 b as reported in Chapter 3.

5.3 Methods

In Chapter 3 and 4, I modelled the atmosphere of WASP-33 b using 1D models, that is models that do not have longitudinal/latitudinal variations of the P-T structure, chemical structure, and circulation. To capture dynamics, including hot spot offsets, a full 3D model needs to be deployed. In Section 5.3.1 I will describe the 3D GCM of WASP-33 b. In Section 5.3.2 I describe the methods used to constrain phase dependence in the scale parameter in the 1D and 3D model.

5.3.1 3D GCM of WASP-33 b

For the 3D GCM, the output from a SPARC/MITGCM (Showman et al., 2009) of WASP-33 b. The simulation set-up is similar to the study by Parmentier et al. (2018) for different UHJs. The GCM output was post-processed using the GCMCRT 3D RT code (Lee et al., 2021) to provide high-resolution emission spectra that account for variation in the spectra throughout the orbital phases of the observation. Line-list data from various sources are used, namely: OH (Hargreaves et al., 2019), H_2O (Polyansky et al., 2018), CH_4 (Hargreaves et al., 2020), CO (Li et al., 2015), CO_2 (Yurchenko et al., 2020), NH_3 (Coles et al., 2019), HCN (Barber et al., 2014). Cross-sections were calculated using the HELIOS-K opacity code (Grimm et al., 2021) and interpolated between 1.27-2.66 μm at a resolution of R = 100,000.

The resulting synthetic high-resolution emission spectra include the effects of Doppler shifting of spectral lines. These are due to winds and planetary rotation in observer's the line of sight for each phase. All molecular species listed above as well as collision-induced absorption coefficients of the H2-H-He from Karman et al. (2019) and H^- from John (1988) were included.

The resulting phase-dependent GCM spectra of the gCMCRT are shown in Fig. 5.3 and P-T profiles are shown in Fig. 5.4. It is computationally expensive and resource-intensive to run the spectral calculation, as it uses a Monte Carlo radiative transfer method on many GPUs. Therefore, synthetic spectra at nine phases were uniformly sampled over the phase coverage during the three observing nights. For those spectral templates required at intermediate phases, I linearly interpolate these spectral templates in phase.

The GCM predicts a hot spot at $+8^\circ$ east from the substellar point, which results in an asymmetry between P-T profiles west or east from the sub-stellar point. As the planet rotates in the same direction as it orbits its host star, More of the hot spot region pre-eclipse is seen compared to post-eclipse. This results in phase-dependent variations in both the continuum and relative line strengths. The variations of the CO line contrast are shown in Fig. 5.5. This result is qualitatively in line with the toy model described in Section 5.2.1.

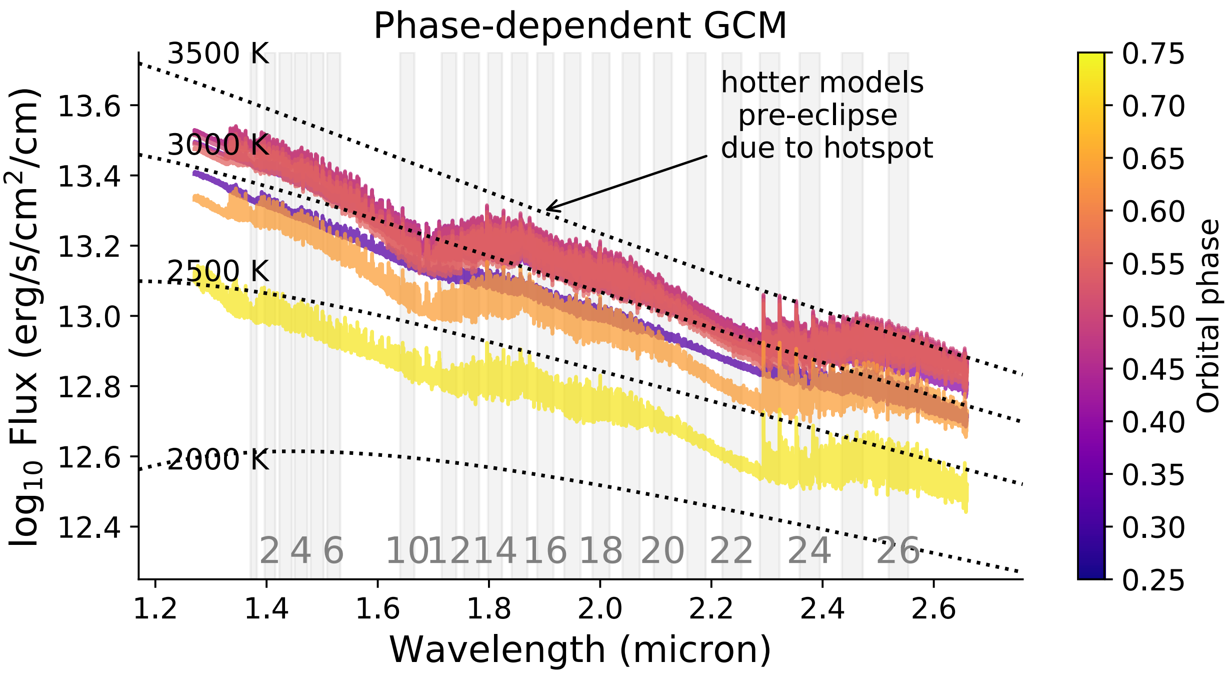

Figure 5.3: WASP-33 b GCM synthetic emission spectra at different orbital phases convolved to the observed spectral resolution of $R = 15,000$. Planck black body curves are plotted at a range of temperatures. The GCM predicts hotter models pre-eclipse compared to post-eclipse due to a hotspot approximately $+8°$ eastward seen from the substellar point.

As noted by de Kok et al. (2014b), while the overall flux on cooler night sides may be lower, the relative line-to-continuum strength, which HRCCS is sensitive to, is strong. This suggests then that the phase-dependant change in the relative line strengths from the GCM will also be detectable as WASP-33 b proceeds in its orbit.

5.3.2 Methods used to compare the 1D and 3D models

First, for the 3D GCM, I run a SNR-analysis following the same method as previously used on the 1D models as described in Section 3.7.2. Second, I investigate the phase dependence of the scale parameter in the MEASURE WASP-33 b dataset. This is done using a similar CC-to-log(L) analysis as described in Section 4.6.3 to obtain posterior distributions and constraints of v_{sys}, K_{p} and $\log a$. I do this separately for the 1D and 3D models and for the pre-eclipse and post-eclipse datasets. Note in Fig. 3.2 that for the WASP-33 b MEASURE dataset, the post-eclipse phase coverage on the second night is longer than the pre-eclipse coverage from the other two nights. To enable a direct comparison, I split the post-eclipse spectra of the second night into a subset of data that contains only the symmetric phases corresponding to the pre-eclipse coverage.

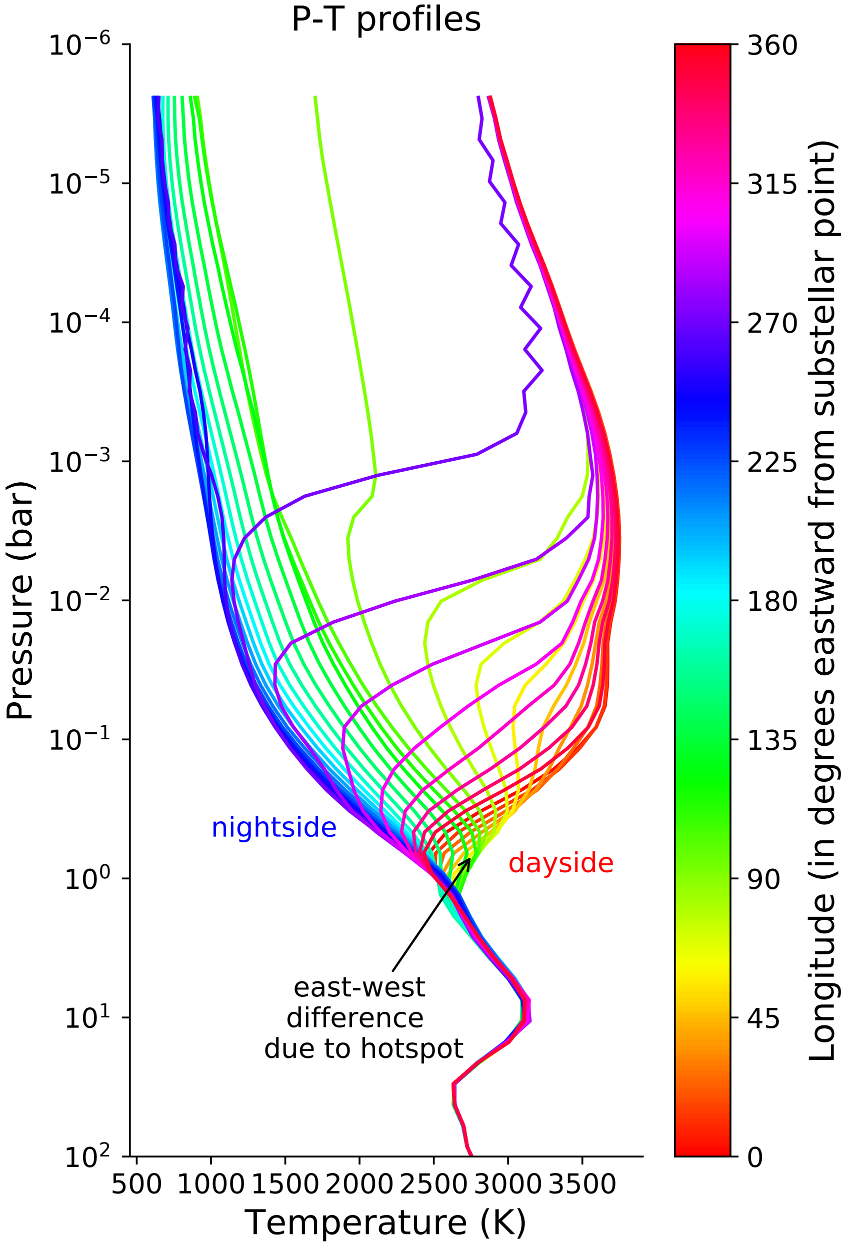

Figure 5.4: WASP-33 b GCM P-T profiles as a function of longitude, where 0° is defined as the substellar point and increases towards the eastward direction as seen from the substellar point.

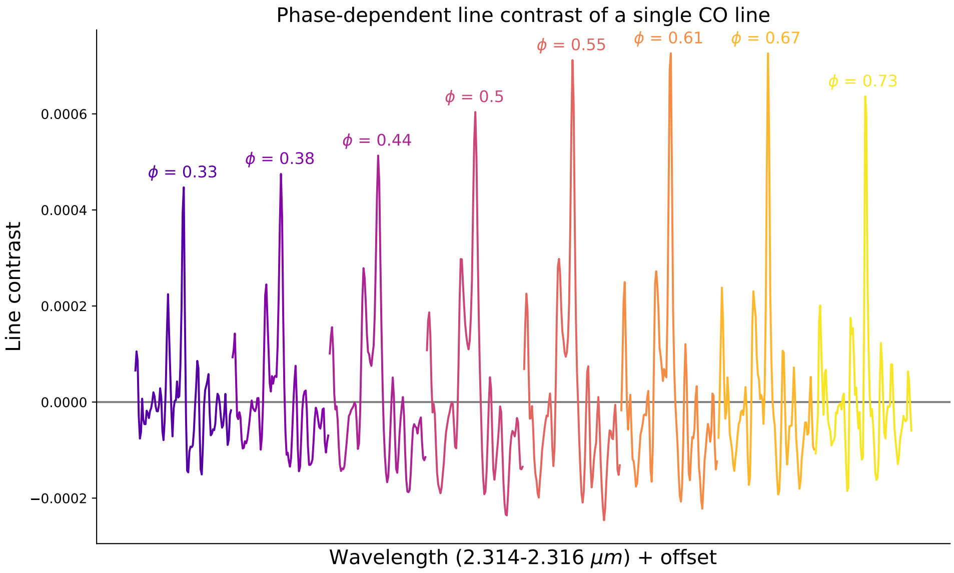

Figure 5.5: Line contrast (flux - mean(flux)) of a single CO line (2.314-2.316 μm) in the disk-averaged phase-dependent GCM synthetic spectrum as a function of orbital phase (ϕ) coverage of WASP-33 b. The phase-dependent variations show shallower lines pre-eclipse compared to post-eclipse for symmetric phases around the secondary eclipse. This is due to a shallower average temperature gradient in the pre-eclipse phases compared to post-eclipse.

5.4 Results

An overview of the results from the S/N-analyses and the scale parameter discrepancy between pre-eclipse and post-eclipse symmetric phases is shown in Table 5.1. I will first elaborate on the results from the 1D models, followed by the results from the 3D GCM.

5.4.1 Results from the 1D PHOENIX models

Fig. 5.6 shows the results from the log(L)-to-CC mapping for the best-matching modified PHOENIX model, giving the posteriors for the systemic velocity, orbital velocity, and the

Model	**Highest S/N**	**$\Delta \log(\mathbf{a})$ (symmetric phases)**
Modified P-T profile PHOENIX models (1D)	7.9	$0.21^{+0.03}_{-0.03}$
Self-consistent PHOENIX models (1D)	7.6	$0.24^{+0.03}_{-0.03}$
Day-side-only (fixed orbital phase $\phi = 0.5$) GCM (3D)	7.1	$0.27^{+0.03}_{-0.04}$
Phase-dependent GCM (3D)	7.1	$0.13^{+0.03}_{-0.03}$

Table 5.1: Overview of the highest SNR of the sets of models explored and their corresponding scaling parameter a from the CC-to-log(L) mapping for the WASP-33 b MEASURE dataset. The final column shows $\Delta \log(a)$ i.e. the difference between the mean of the pre-eclipse (first and third night) scaling parameter and that for the post-eclipse data subset for which there is symmetric phase coverage: $\Delta \log(a)$=$\log(a_{\mathrm{post-eclipse}})$ - $\log(a_{\mathrm{pre-eclipse}})$. The $\log(a)$ scaling parameter has a value of zero when the model is a good description of the data. The phase-dependent GCM gives the smallest discrepancy in $\log(a)$, indicating that it is accounting for the phase dependence of the scaling parameter.

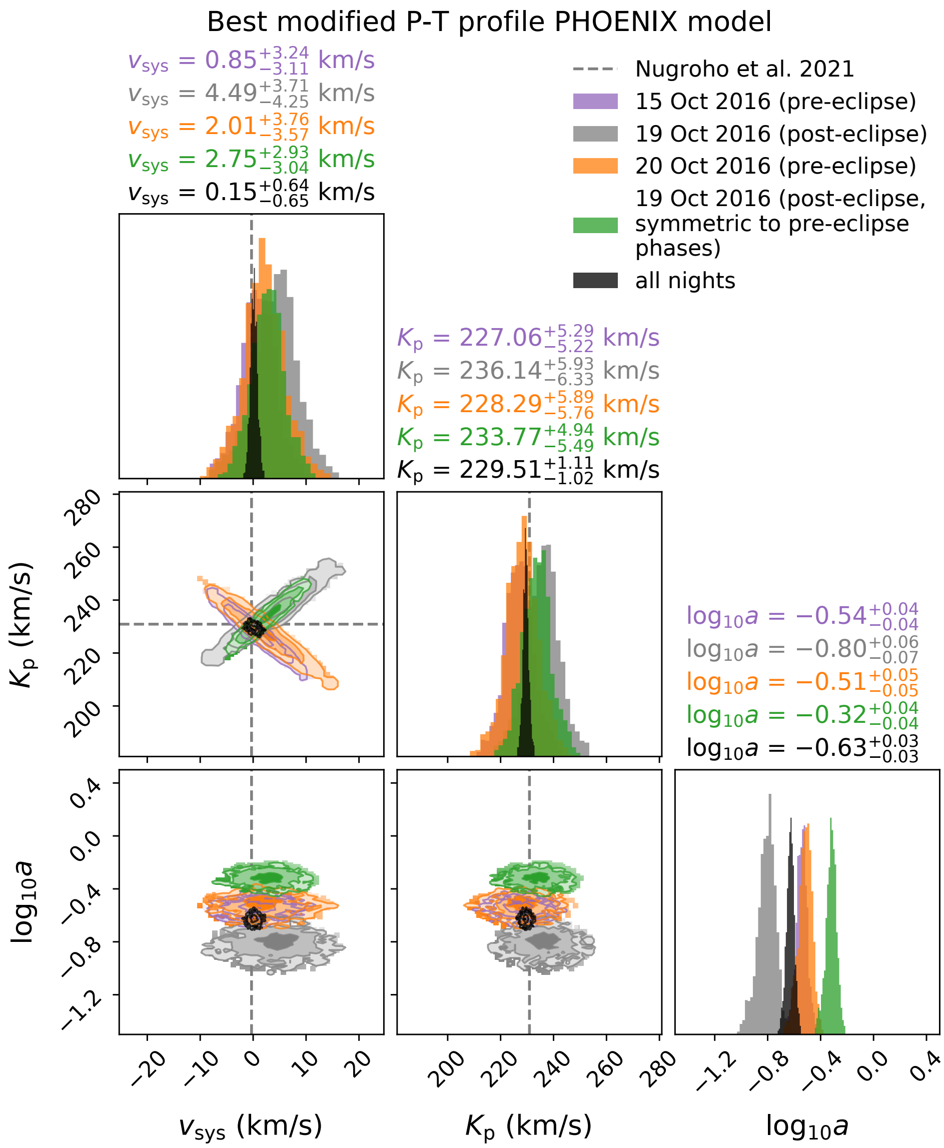

Figure 5.6: Posteriors from the CC-to-log(L) framework based on Brogi & Line (2019). Results are shown for the best-matching modified PHOENIX model of WASP-33 b. The contours indicate the 1σ, 2σ, and 3σ confidence intervals. All frames with phases during the eclipse have been excluded from this analysis to prevent dilution of the planetary signal. Results are shown for individual observing nights, all nights combined, and for the subset of post-eclipse phases that are symmetrically matched with the pre-eclipse phases (see Fig. 3.2). The dashed black grid indicates the expected location at (v_{sys}, K_p) = (-0.3, 230.9) km/s based on the OH detection by Nugroho et al. (2021).

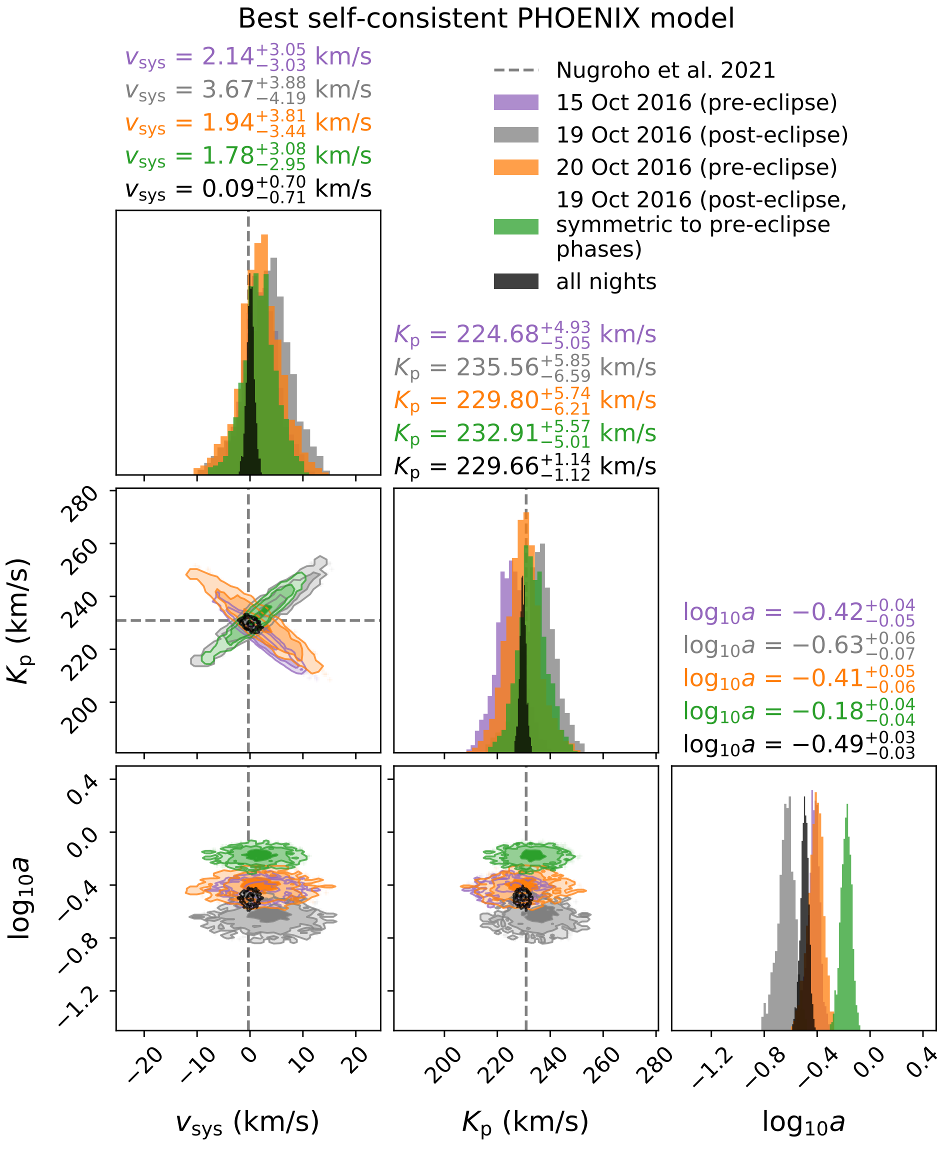

Figure 5.7: Same as Fig. 5.7, but for the best-matching self-consistent PHOENIX model of WASP-33 b.

scaling parameter. The planet is detected at $v_{\rm sys} = 0.15^{+0.64}_{-0.65}$ km/s and $K_{\rm p} = 229.53^{+1.11}_{-1.02}$ km/s with this highest SNR spectral template, in agreement with previous literature e.g. ($v_{\rm sys}$, $K_{\rm p}$) = (-0.3, 230.9) km/s (Nugroho et al., 2021). The scale factor posterior distribution, which would have $\log(a) = 0$ for a perfectly matched model, and systematically offset to smaller values, indicating that the model does not fully encapsulate all of the physics and chemistry to describe the atmosphere. Most striking is the phase dependence of the scale parameter between the pre-eclipse and the symmetric post-eclipse phases. The same is qualitatively seen in Fig. 5.7 for the best-matching self-consistent PHOENIX model. The discrepancy between their scale parameters is significant. However, all nights are in agreement with their ($v_{\rm sys}$, $K_{\rm p}$)-values within 2σ.

5.4.2 Results from the 3D GCM

To first check for general consistency between the GCM and the results from the PHOENIX 1D models, I perform the S/N analysis using the day-side-only (i.e. no phase dependence) 3D GCM with all opacities included. This is detected at $S/N = 7.1\sigma$, which is slightly lower than the PHOENIX models, and found at the expected ($v_{\rm sys}$, $K_{\rm p}$)-values for all nights combined (see top panel of Fig. 5.8 and the corresponding cross-correlation trail is shown in the top panel of Fig. 5.9).

In terms of their likelihood, I find a ratio of peak likelihoods of +59.2 between the best PHOENIX 1D model and GCM suggesting the best PHOENIX 1D model is preferred over the GCM. However, I cannot compare the GCM and PHOENIX 1D models quantitatively in terms of their likelihood as they are drawn from different underlying parameter spaces. I will discuss the preference of the best 1D PHOENIX model over the GCM in more detail in the next section.

The results are qualitatively similar to the PHOENIX spectral templates, again with offsets in $\log(a)$ for the different phase ranges, but with larger error margins (see Fig. 5.10). I hypothesize these larger error contours may be due to the broadening of the lines by planet rotation in the GCM spectral template and its overall lower SNR detection. The broad agreement with the trend for offsets in $\log(a)$ is confirmed by the day-side-only GCM and thus I proceed to allow the GCM to have phase dependence and determine if this resolves the $\log(a)$ scaling discrepancy.

The phase-dependent GCM provides a different cross-correlation template for each observed spectrum at each phase, where the spectrum corresponds to a P-T profile that is a combination of all the profiles from different longitudes visible across the planet disk at that time. The phase-dependent GCM is similarly detected at $SNR = 7.1\sigma$ at the expected ($v_{\rm sys}$,

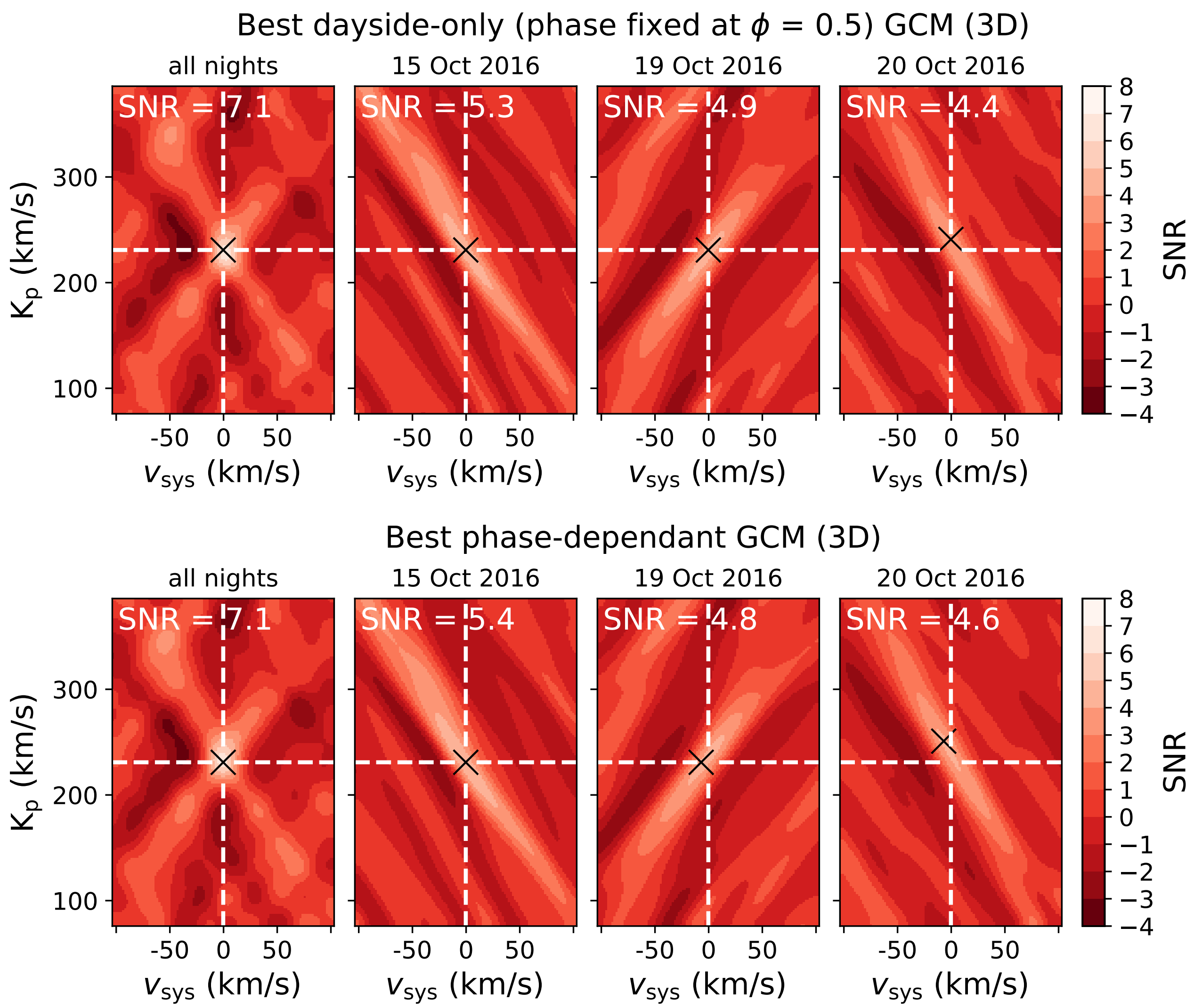

Figure 5.8: SNR as a function of the system velocity v_{sys} and orbital velocity K_p for the dayside-only (phase fixed at $\phi = 0.5$ (top panel) and phase-dependant (bottom panel) (3D) GCM templates of WASP-33 b. The black cross symbol marks the maximal SNR location. The dashed white grid indicates the expected location at (v_{sys}, K_p) = (-0.3, 230.9) km/s based on the OH detection by Nugroho et al. (2021). This detection is in agreement with their (v_{sys}, K_p)-values for all nights combined.

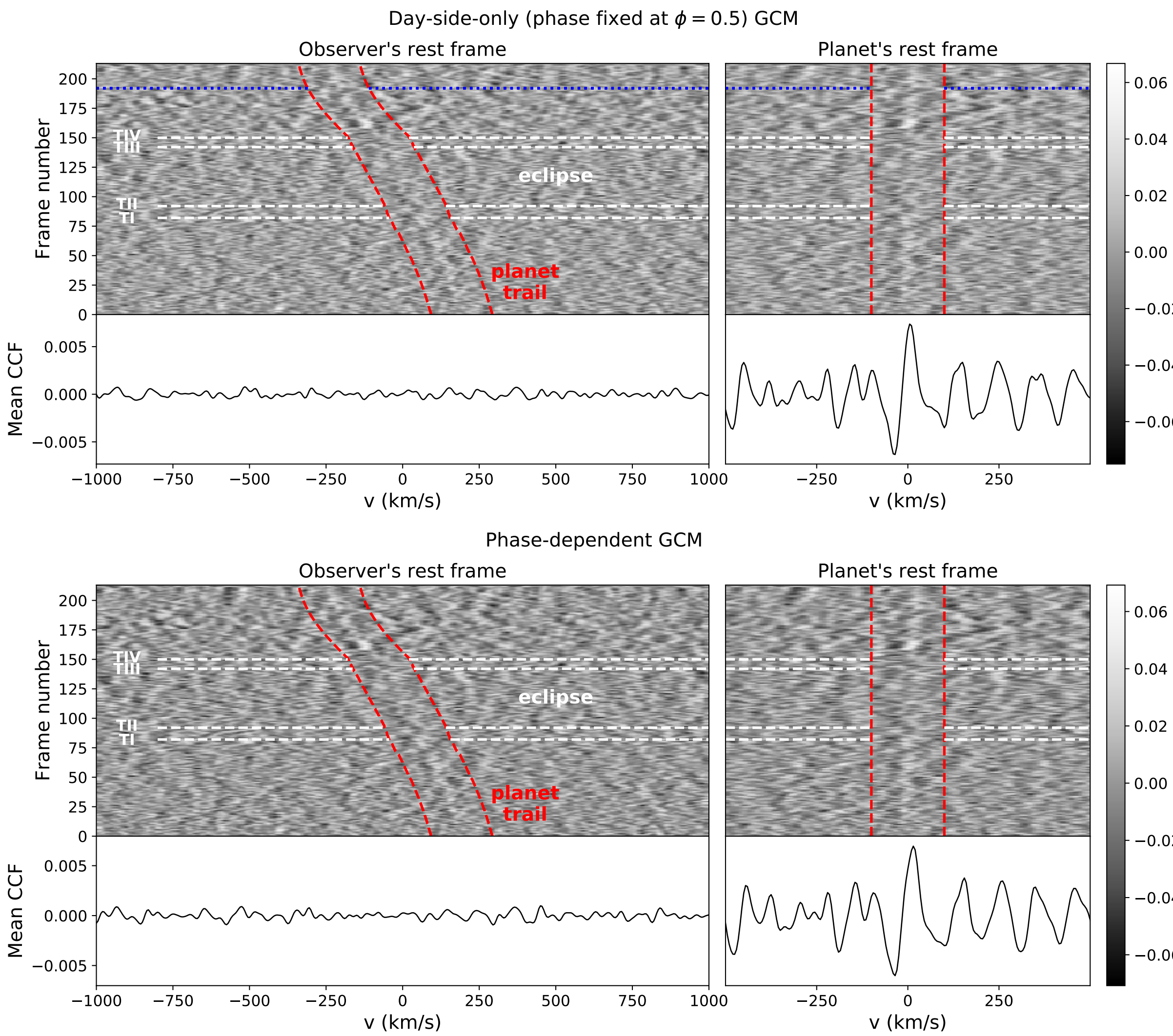

Figure 5.9: Same as Fig. 3.13, but for the GCM dayside-only model (top panel) and the GCM (3D) phase-dependant model (bottom panel).

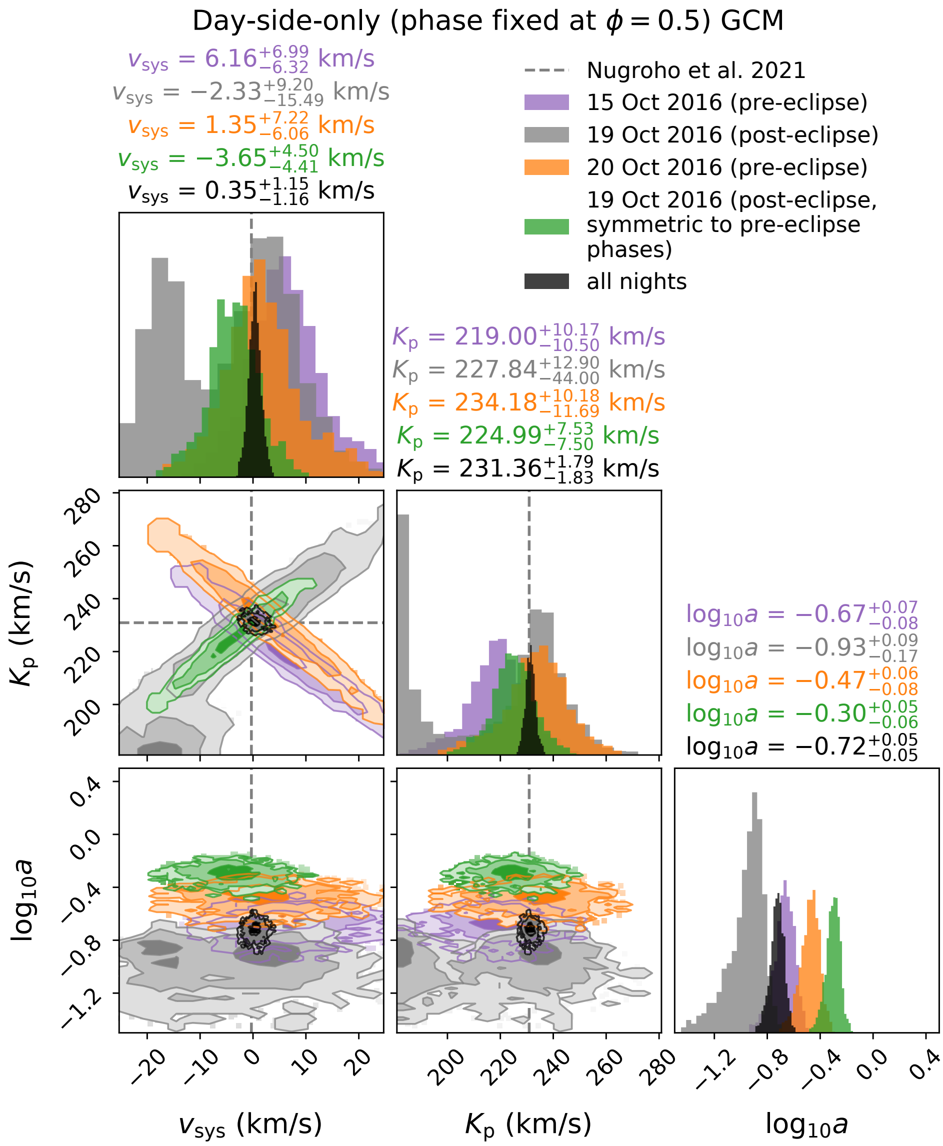

Figure 5.10: Same as Fig. 5.7, but for the dayside-only GCM model of WASP-33 b. The phase-dependent offsets of the scale parameter between pre- and post-eclipse are qualitatively similar to the 1D PHOENIX models.

K_p)-location for all night combined (the corresponding CCF time series are shown in the bottom row of Fig. 5.9 and the $K_\mathrm{p} - v_\mathrm{sys}$ maps are shown in the bottom panel of Fig. 5.8)

However, the results from the CC-to-log(L) mapping shown in Fig. 5.11 are notably different for the scaling parameter. The phase-dependent GCM appears to resolve the majority of the $\log(a)$ discrepancy between the pre-and post-eclipse symmetric phases and brings all the data sets into broad agreement within 2σ. Although the phase-dependent GCM resolves most of the log(a) discrepancy seen for the 1D PHOENIX models, indicating that the inclusion of 3D dynamical effects such as hot spots and orbital phase brightness variation is a better match to the data, it does not fully describe the atmosphere of WASP-33 b. While the 1D model results in a higher SNR detection, differences in full chemistry, or compensating with other parameters may enable a better match, but only once scaled in the log-likelihood framework. The scaling parameter for the 1D models still indicates greater correction is needed for these models than the GCM. Thus there is scope for future work to improve on 3D models for UHJs to give a more comprehensive description of the atmosphere that would result in a higher SNR than the 1D models. This missing physics in the GCM may account for the overall lower SNR, compared to the SNR found for the best 1D PHOENIX models.

5.5 An eastward hot spot offset in WASP-33 b

The phase-dependent line contrast can then be understood in the context of the GCM spectral template. First, the eastward hot spot results in a hotter continuum and thus greater overall brightness for pre-eclipse phases as shown in Fig. 5.3. But, since the post-processing of the high-resolution spectra removes the continuum information I argue these data are insensitive to these variations. Fig. 5.4 then shows that the GCM predicts thermal profiles that are shallower in the eastward-shifted hot spot and steeper on the western part of the day side. Overall, this leads to a disk-integrated temperature gradient that is shallower during pre-eclipse when it contains the eastward hot spot (where the line-of-sight is centred on longitudes $\sim 17 - 61°$), and steeper during post-eclipse when it contains more of the western day-side hemisphere (centred on longitudes $\sim 277 - 341°$). Consequently, the average line contrast associated with these temperature gradients will be shallower during pre-eclipse and stronger during post-eclipse. For a fixed line contrast amongst all phases, such as the PHOENIX models or the day-side-only GCM, this results in a smaller scale parameter pre-eclipse compared to post-eclipse, as observed in the dataset. But for the 3D phase-dependent model, this results in a more consistent scale parameter between the pre-eclipse and post-eclipse data, again as observed in the dataset. Therefore, I conclude that despite the insensitivity to the absolute brightness variations of the hot spot, the phase-dependent variation of

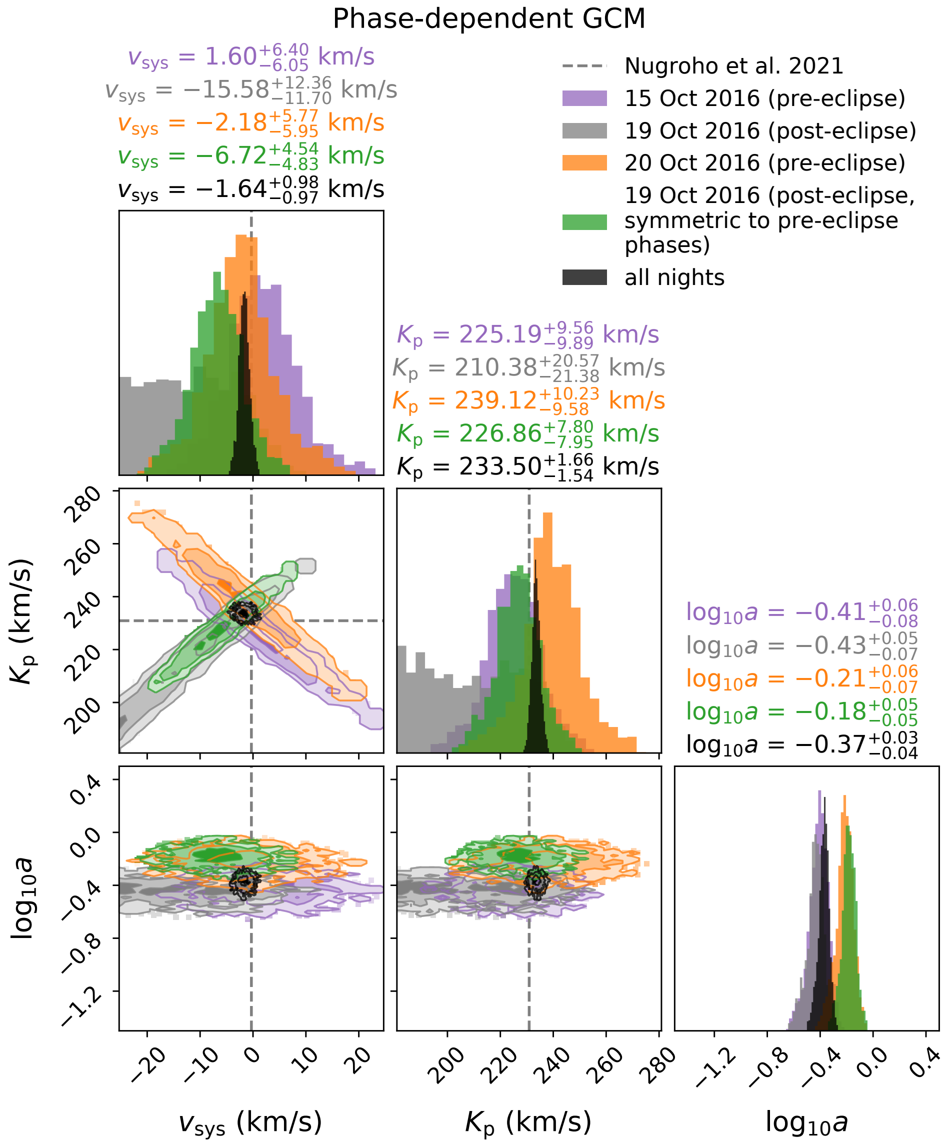

Figure 5.11: Same as Fig. 5.7, but for the phase-dependant GCM (3D) of WASP-33 b. The phase-dependent offsets of the scale parameter between pre- and post-eclipse are now in closer agreement.

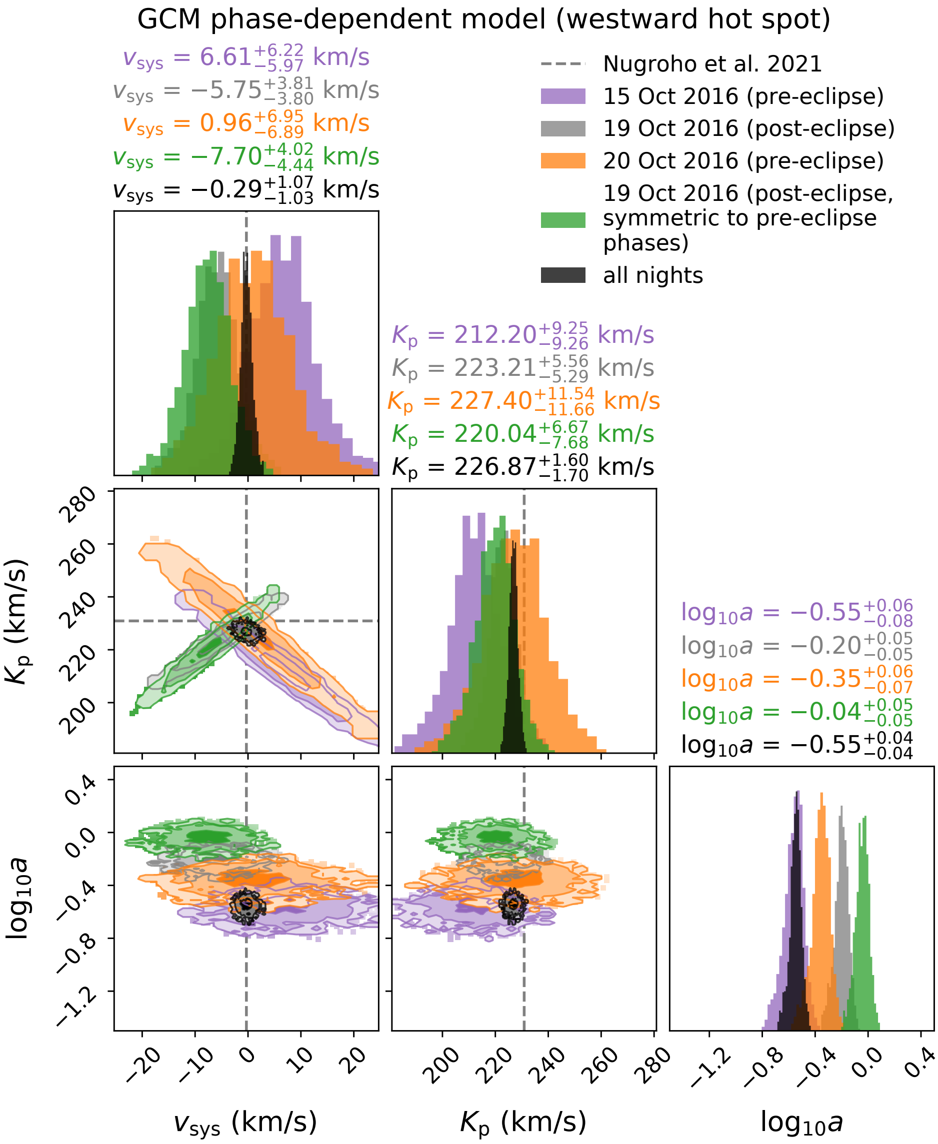

Figure 5.12: Same as Fig. 5.7, but results are shown for the GCM phase-dependent model where all phases have been mirrored such that eastward offsets become westward, effectively turning the model into one with a westward hot spot offset. The phase offsets between pre- and post-eclipse are now in lesser agreement compared to the eastward hot spot offset model.

the scale parameter is still sensitive to the 3D nature of the atmosphere and consistent with an eastward offset hot spot scenario.

These results are all in agreement with the derivations presented in Section 5.2.1, where a larger line contrast is expected for a steeper thermal gradient. It is worth noting that the results presented here are also in agreement with Herman et al. (2022) as they also find a larger scale parameter post-eclipse compared to pre-eclipse, although they do not directly interpret this as implying their data is consistent with an eastward hot spot offset. This is because they do not compare their observations to a full 3D GCM and do not link their phase offset directly to the thermal gradient of the P-T profile.

As a check, I also investigate if this result is robust against the alternative scenario of a westward offset hot spot. Such a scenario is not predicted by the GCM but might arise from magnetohydrodynamical effects on the atmospheric dynamics (Hindle et al., 2021). Including magnetohydrodynamical physics in the GCM is beyond the scope of this work. Instead, I simply mirror the phase-dependent GCM model such that eastward phases become westward and vice versa, effectively turning the eastward offset model into a westward offset model. The result is shown in Fig. 5.12. The discrepancy between pre- and post-eclipse phases has significantly increased ($\Delta \log(a) = 0.41^{+0.03}_{-0.04}$) due to the even shallower line contrast post-eclipse compared to pre-eclipse. I conclude a model with a westward hot spot offset is inconsistent with these data, and that the asymmetry therefore is consistent with an eastward offset.

The lower SNR of the phase-dependent GCM compared to the PHOENIX models may seem unexpected at first, also in the light of results from Beltz et al. (2021) who find a significant increase of the SNR-detections for the exoplanet HD 209458b when using a 3D GCM compared to a 1D model. In part, this may be explained by the lower spectral resolution of this data compared to Beltz et al. (2021) as the 3D effects of the line shape and Doppler shift of the spectral lines will be more pronounced at higher spectral resolutions where they can be resolved. I also compare a single GCM (N=1) to a larger suite of PHOENIX models (N=576 modified models and N=9 self-consistent models), which is an unfair comparison. Instead, a fairer comparison would be to fully explore a larger suite of self-consistent and GCM models exploring the probable parameter space, but such an analysis is computationally very expensive.

Lastly, it may be explained by the current limitations of the GCM, mainly the exclusion of Fe and Fe^+. Lothringer et al. (2018) find Fe and Fe^+ are important opacity sources in the atmospheres of UHJ that contribute to their thermal inversions. Nonetheless, I emphasize the phase-dependent change of the P-T profile with longitude is robust to the choice of exclusion of iron opacities in the GCM. This is because the global circulation of UHJs does not depend on the details of the local P-T profiles. Instead the phase-dependent variation of the thermal gradient and thus line contrast should be seen as a natural outcome of having a shifted hot spot. Thus the results should quantitively be the same regardless of whether iron opacities were included or not.

I do not find significant evidence for a relative blue-shift pre-eclipse compared to post-eclipse that would further indicate an eastward hot spot. Such net Doppler shifts are predicted of ∼1-3 km/s as the hot spot rotates in and out of the observer's view while orbiting its host star (Zhang et al., 2017; Beltz et al., 2021). However, the velocity resolution is only ∼4-6 km/s for the individual observing nights. Moreover, the SNR∼5 when splitting the detection in a pre- and post-eclipse part. Thus I cannot detect such Doppler shifts at this spectral resolution and SNR.

I note that when including all orbital phases out to quadrature in the post-eclipse night, the scaling parameter prefers shallower lines (grey contours in the corner plots) despite the strong line contrasts shown in Fig. 5.5. Quadrature phases add a smaller contribution to the overall SNR, as relatively more night-side is visible. The rate of change of the radial velocity for close-to-quadrature phases is small, and therefore PCA-cleaning will be more effective in the removal of the exoplanetary signal; this has also been reported by Brogi et al. (2022) and Pino et al. (2022). I thus emphasize it is key to only compare symmetric phases, ensuring both the pre-eclipse and post-eclipse frames included were homogeneously processed by the post-processing steps.

I further find a systematic bias towards small scaling parameter $\log a < 0$ in all models. Rather than the choice of input parameters for the single GCM or missing physics, I consider that the data-cleaning steps of the HRCCS can affect the line shape and strength of the exoplanetary signal. PCA likely degrades more of the planetary signal at lower resolution, where the lines spread across multiple pixels. One way to solve this is to apply PCA to the model and data uniformly. However, it is computationally expensive to run PCA for each iteration of the CC-to-log(L) computation by PyMultiNest.

As an alternative, I investigated these effects by injecting the best modified PHOENIX model at $a = 1$ into the frames observed during the eclipse of WASP-33 b. Since the change in radial velocity would be relatively large during the eclipse, potentially making it more robust against PCA, I shifted the injected model in phase to cover similar radial velocities as observed during the first observing night. I found a scale parameter of $\log a = -0.23^{+0.03}_{-0.03}$ for the recovered signal. This result supports the hypothesis that these data-cleaning steps cause at least part of the bias toward lower scale factors. Given that I apply the data processing in a homogeneous way to all data sets, and while I do not give large weight to the absolute values of $\log(a)$, I still give weight to the interpretation of the relative differences. Adopting novel model-filtering techniques such as the one introduced by Gibson et al. (2022) may resolve the issue of comparing asymmetric phase coverage pre- and post-eclipse and alleviate the systematic bias towards lower scaling parameters.

5.6 Conclusions

In this chapter, I demonstrated that line contrast variations of a molecule with a high dissociation temperature in an UHJ atmosphere, such as CO, are related to longitudinal variation of the gradient of the P-T structure. These line contrast variations are revealed by phase-dependent variation of the scale parameter within a Bayesian framework. I investigate whether the CO emission lines in the atmosphere of the UHJ WASP-33 b observed in the MEASURE data show such phase-dependent variation of the scale parameter. The results show that the exoplanet spectral line contrast is greater just after the secondary eclipse than before. I demonstrate that the P-T profiles from a phase-dependent GCM that includes an eastward offset hot spot can explain the majority of the phase dependence in $\log(a)$. The inclusion of a scaling parameter in the CC-to-log(L) mapping can thus reveal the longitudinal phase-dependent thermal structure of the atmosphere, even in spectra that lack the resolving power required to detect the additional induced Doppler shift caused by the offset hot spot.

These results demonstrate the power of Bayesian frameworks combined with phase-resolved high-resolution spectra of exoplanet atmospheres to constrain atmospheric dynamics even at moderate spectral resolution $R = 15,000$.

6
Combining chemistry and dynamics: investigating the climate of WASP-18 A b

The 3D GCM models and opacity tables of WASP-18 A b presented in the chapter were computed by Hayley Beltz. The results presented in this chapter will be a part of van Sluijs et al., 2023b, which is currently in preparation.

6.1 Motivation

Velocity offsets are commonly observed in exoplanet atmospheres with HRCCS in both transmission (e.g. Ehrenreich et al., 2020; Zhang et al., 2022b; Casasayas-Barris et al., 2022) and emission spectra (e.g. Brogi et al., 2022). For transmission spectra, these asymmetries have been proposed to be caused by a difference in chemistry, P-T structure, cloud deck, and wind flow between the trailing and leading limb (e.g. Ehrenreich et al., 2020; Wardenier et al., 2023; Beltz et al., 2023). In emission spectra, they have been proposed to be caused by spatial variations of the P-T structure and chemical abundances (e.g. Beltz et al., 2021). If a signal forms mostly on one side of the exoplanet this leads to asymmetries in the line profile, where the line profile is formed pre-dominantly on the blue or red-shifted side of the planet. Fig. 6.1 (adapted from (Hoeijmakers et al., 2022)) excellently demonstrates how a signal originating from different parts of the exoplanet, translates into (v_{sys}, K_{p}) velocity offsets.

An UHJ where significant velocity offsets have been observed using emission HRS is WASP-18 A b (Brogi et al., 2022). This UHJ was discovered by Hellier et al. (2009) using the WASP-South transit survey (Pollacco et al., 2006). WASP-18 is a widely separated (26.7″ or 3300 au) binary system: the host star is of the F6 spectral type and the secondary companion is a faint M7.5 star (Csizmadia et al., 2019; Fontanive et al., 2019). WASP-18 A b has a radius close to Jupiter's radius $\sim$1.1 R_{Jup} (Southworth et al., 2009), but is much more massive than

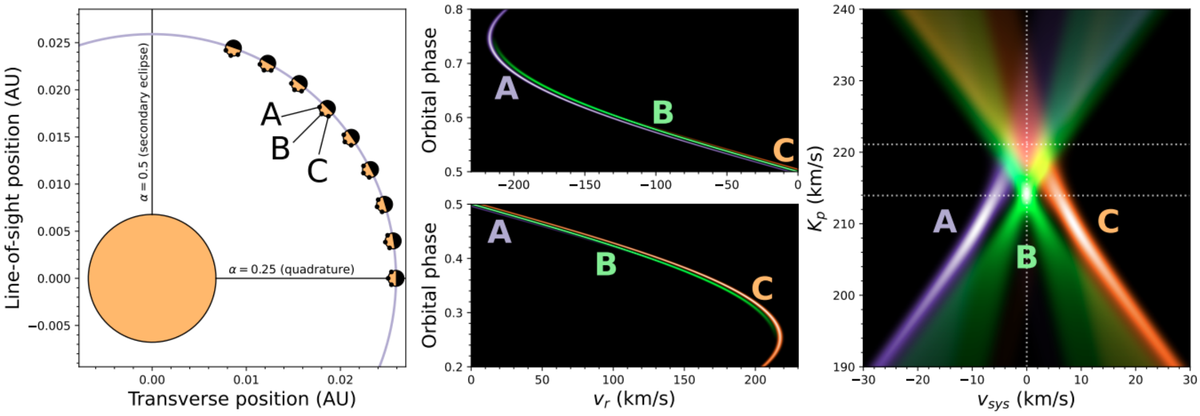

Figure 6.1: Toy model for velocity offsets in HRS emission spectra. *Left panel:* shows a synchronously rotating exoplanet orbiting its host star. Three points on the planet are indicated: near the morning limb (A), the sub-stellar point (B), and the evening limb (C). *Middle panel:* shows the CCF time series for each of the three points. They have slightly different Doppler velocity offsets from the exoplanet's orbital Doppler velocity. The top-middle panel shows post-eclipse phases and the bottom-middle panel shows pre-eclipse phases. *Right panel:* resulting SNR maps in (v_{sys}, K_{sys})-space. Signals originating from different points on the exoplanet show distinct peaks in their SNR map. Figure adapted from Hoeijmakers et al. (2022).

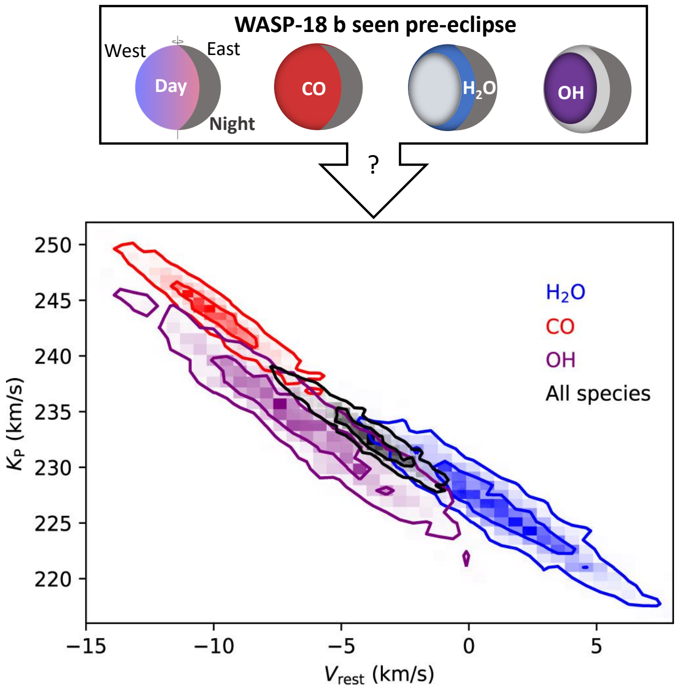

Figure 6.2: *Top panel:* A schematic view of WASP-18 A b at an orbital phase $\phi = 0.375$, close to the whole phase range observed by Brogi et al. (2022). The dayside is blue-shifted and the night-side is red-shifted. The three other panels show spatial variation of chemical abundances for an UHJ toy model. Regions with a relatively high chemical abundance of CO, H_2O, and OH are coloured. *Bottom panel:* the observed velocity offsets in the atmosphere of WASP-18 A b when considering different species when combining orbital phases between 0.326-0.452 (adopted from Brogi et al., 2022). These observations can only be explained in part by the toy model.

Jupiter with a mass of $\sim$10.4 M_{Jup} (Pearson, 2019). Initial evidence suspected orbital decay of WASP-18 A b's orbit Hellier et al. (2009), but follow-up studies did not support this (Wilkins et al., 2017; Cortés-Zuleta et al., 2020a).

The recent HRCCS analysis of WASP-18 A b using IGRINS by Brogi et al. (2022) shows a tentative molecule-dependant velocity offset when cross-correlating with OH, H_2O, and CO (see bottom panel Fig. 6.2). They argue these velocity offsets up to $\sim$10 km/s are much larger than the instrumental sensitivity ($\sim$0.2 km/s). These offsets are also much larger than expected from uncertainties in the lines lists for H_2O and CO (Gandhi et al., 2022), and line list inaccuracies should only translate into a system velocity offset (v_{sys}), but not a Keplerian velocity offset.

Therefore, Brogi et al. (2022) present the possibility these offsets are due to dynamical 3D effects in the atmosphere of WASP-18 A b. The spatial abundances of OH, H_2O, and CO, are correlated with the local P-T structure. Since the molecular lines form on different parts of the exoplanet, the peak of the SNR detection of each molecule is expected to shift to a distinct location (v_{sys}, K_{p})-space as explained earlier by Fig. 6.1.

For an UHJ, the region around the substellar point is where the H_2O molecules dissociate and OH is formed. This side appears blue-shifted at the pre-eclipse phases observed by Brogi et al. (2022) (see top panel Fig. 6.2). At these phases, the OH signal will form mostly on the blue-shifted dayside. Similarly, at these phases, the H_2O signal forms mostly on the day-to-night terminator, which has a net zero velocity offset. The OH signal is thus expected to be blue-shifted relative to H_2O, qualitatively in line with their IGRINS observations.

CO is expected to be distributed uniformly over the exoplanet's dayside disk. Therefore it should largely follow the exoplanet's Keplerian velocity and system velocity. Beltz et al. (2022) predicted a relative blue shift of the pre-eclipse H_2O signal by $\sim$2 km/s compared to the CO signal using 3D models including magnetic drag for another UHJ, namely WASP-76 b. This is opposite to the relative red shift of the H_2O signal observed by Brogi et al. (2022). Moreover, the magnitude of the observed velocity offsets is much larger than $\sim$2 km/s. Since the global circulation patterns of UHJs depend mostly on their equilibrium temperature, which is very similar for WASP-18 A b and WASP-76 b ($\sim$100 K difference Chakrabarty & Sengupta, 2019; Saha, 2023), velocity offsets of similar magnitudes are expected.

In the absence of winds, the maximum velocity offset between two signals originating from different sides of the exoplanet equals

$$v_{\mathrm{max}} = 2 \times v_{\mathrm{rot},} \sin i, \tag{6.1}$$

twice the projected rotational velocity. This is when one signal forms on the equatorial far-most red-shifted limb and the other on the equatorial far-most blue-shifted limb of the disk.

Parameter	Symbol	Unit	Value(s)	Source
Exoplanet radius	R_p	R_Jup	1.165	(Southworth et al., 2009)
Exoplanet gravity	$\log g$	cm/s^2	4.35	(Southworth et al., 2009)[a]
Stellar radius	$R_\star$	$R_\odot$	1.444	(Southworth et al., 2009)
Transit midpoint time	T_0	BKJD	2454590.17936	(Southworth et al., 2009)
System velocity	v_sys	km/s	-0.3	(Brogi et al., 2022)
Keplerian velocity	K_p	km/s	230.9	(Brogi et al., 2022)
Eccentricity	e	-	0.008	(Nymeyer et al., 2011)
Stellar effective temperature	$T_\star$	K	6400	(Southworth et al., 2009)
Inclination	i	$^\circ$	86.0	(Southworth et al., 2009)

[a]This value was computed from their reported exoplanet mass and radius using equation (2.9).

Table 6.1: Overview of relevant exoplanet and stellar parameters of the WASP-18 A system.

In this equation v_rot is the rotational velocity, and i is the inclination. The rotational velocity is given by

$$v_\mathrm{rot} = \frac{2\pi R_\mathrm{p}}{P}, \tag{6.2}$$

with exoplanet radius R_p and where I assumed a synchronously rotating planet $P_\mathrm{rot} = P$. Using the values for WASP-18 A b from Table 6.1, I find $v_\mathrm{max} = 9$ km/s. Thus the observed velocity offsets are close but marginally exceed this velocity offset upper limit. However, winds can add a component to the Doppler velocity of the order of ~1-2 km/s (e.g. Showman et al., 2020).

Regardless of the nature of these velocity offsets, they are concerning in the way HRCCS retrieval frameworks are run to constrain molecular abundances. These retrievals usually use the same system velocity offset and Keplerian velocity offset for all included opacity sources. As shown in Fig. 6.2, for WASP-18 A b this implies fixing the velocity offset at the wrong location for the different opacity sources. This would result in a forward model with spectral lines offset to the observed spectral lines. Varying the abundances of the spectral lines at the wrong shifted wavelengths may bias measurements of chemical abundance or simply produce an incorrect result when using a HRCCS retrieval. This problem is unique to HRS as the velocity offsets are too small to be resolved using LRS.

These puzzling observed velocity offsets demonstrate the need for more realistic simulations of WASP-18 A b using complex 3D GCMs to understand what part can be explained from the interplay between chemistry and dynamics. In Section 6.2 I will introduce two models of WASP-18 A b. First, I introduce a free 1D model with the atmospheric input parameters as inferred by Brogi et al. (2022). For this, I use the forward model code described in Line et al. (2021), which was also used to compute synthetic model spectra of τ Böo A b in Chapter 4. Second, I introduce a 3D GCM, the same as was used for another UHJ by Beltz et al. (2022). In Section 6.3, I use both models to create simulated mock HRS datasets, with similar orbital phases and observing conditions as the observations described in Brogi et al.

(2022). In Section 6.4 I describe the cross-correlation analysis to check if my simulations reproduce velocity offsets and I will briefly investigate the effect on inferred parameters from a HRCCS retrieval. Results from this analysis are presented in Section 6.5, discussed in Section 6.6, and I will conclude in Section 6.7.

6.2 Models of WASP-18 A b

6.2.1 The free 1D model

I use a free 1D model to create a synthetic model spectrum similar to the one used as a cross-correlation template by Brogi et al. (2022). For this, I use the forward model that is part of the HRCCS retrieval code described by Line et al. (2021). This forward model was described earlier in Section 4.3.2 where it was used to model the atmosphere of τ Böo A b.

The forward model input parameters are summarised in Table 6.2. The chemical abundances are taken as reported by Brogi et al. (2022). In Brogi et al. (2022) the P-T parameterisation by Guillot (2010) was used, but the forward model I am using requires input parameters using the P-T parameterisation by Madhusudhan & Seager (2009). Therefore, I chose the P-T parameters such that the P-T profiles are very similar, by visually matching the output P-T profile to the one reported by Brogi et al. (2022). Alongside computing a synthetic spectrum with all opacity sources included, I also compute three models with the opacities of respectively only OH, only H_2O, and only CO included. For the stellar model, I am using a PHOENIX model template with the stellar parameters listed in Table 6.1.

The opacity sources included are OH, H_2O, and CO from the ExoMol database (Tennyson & Yurchenko, 2018). The spectra are computed over the wavelength range of IGRINS, the instrument from Brogi et al. (2022), from 1.45 to 2.45 μm. The model is generated at an oversampled resolution of $R = 125,000$ compared to the data which is at a resolution of $R = 45,000$. The synthetic spectrum is shown in Fig. 6.3. Since the P-T structure has an inverted profile, the spectrum contains emission lines. Shorter wavelengths show strong OH lines, intermediate wavelengths are dominated by water features and the reddest orders show a dense forest of CO emission lines.

Parameter	Symbol	Unit	Value(s)
OH abundance VMR	$\log \mathrm{OH}$	-	-2.74
H_2O abundance VMR	$\log \mathrm{H_2O}$	-	-3.13
CO abundance VMR	$\log \mathrm{CO}$	-	-2.20
Reference temperature	T_1	K	4150
Reference pressure layer 1	$\log P_1$	bar	-5
Reference pressure layer 2	$\log P_2$	bar	1
Reference pressure layer 3	$\log P_3$	bar	2
Inversion gradient layer 1	α_1	-	0.25
Inversion gradient layer 2	α_2	-	0.35

Table 6.2: Free 1D model input parameters used to compute a synthetic exoplanet spectrum of WASP-18 A b. These parameters were either directly reported, or based on, the parameters inferred by Brogi et al. (2022).

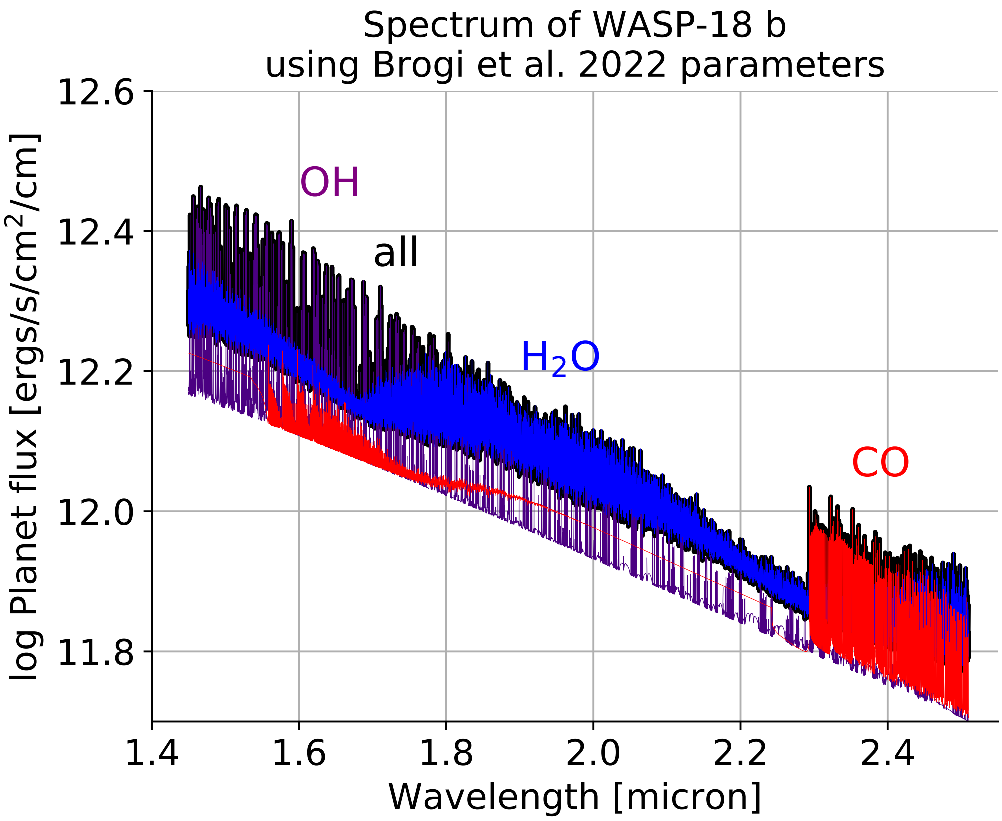

Figure 6.3: Synthetic spectrum of WASP-18 A b for the free 1D model in black based on atmospheric parameters inferred by Brogi et al. (2022) convolved to the observed spectral resolution of IGRINS of R=45,000. This spectrum was computed using the forward model in the HRCCS retrieval code by Line et al. (2021). The synthetic spectrum with only OH, only H_2O, and only CO are respectively indicated in indigo, blue, and red.

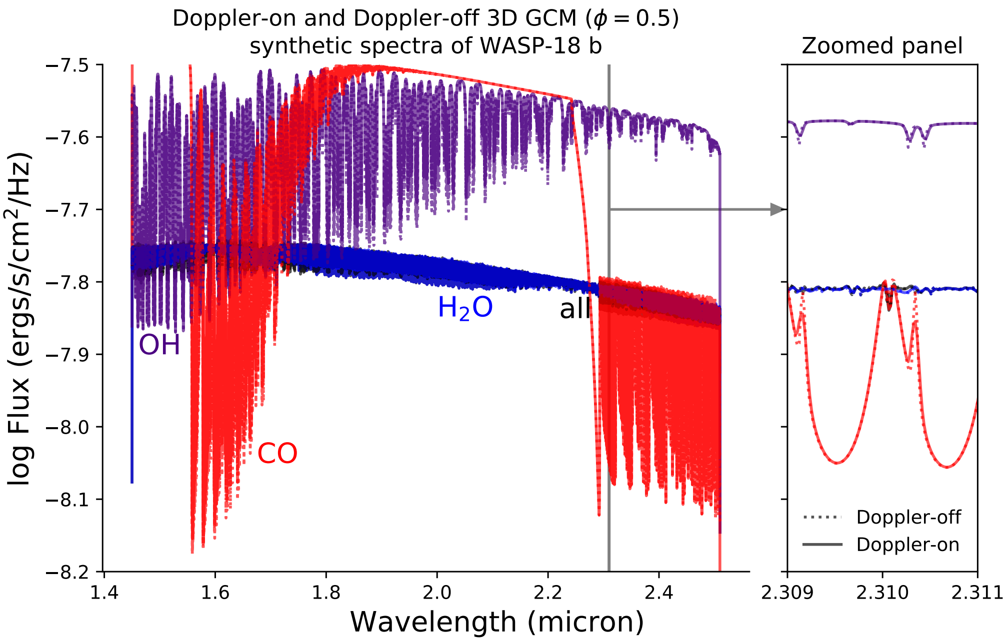

Figure 6.4: Doppler-on and Doppler-off 3D GCM synthetic spectra of WASP-18 A b convolved to the observed spectral resolution of IGRINS of R=45,000. *Left panel:* the Doppler-on spectra with only CO, only H_2O, only OH and all three included. *Right panel:* zoomed version to show the difference between the Doppler-on and Doppler-off spectra. The all included model is overlaps almost fully with the water only model.

6.2.2 The 3D GCM

The 3D GCM of WASP-18 A b was computed using a similar setup as described for another UHJ in section 2 of Beltz et al. (2022), but with the WASP-18 system parameters from Cortés-Zuleta et al. (2020b). I will briefly summarise their GCM setup here. The GCM solves for the set of Navier-Stokes equations as described in Rauscher & Menou (2012). This GCM's radiative transfer scheme has been updated by Roman & Rauscher (2017) to use the faster two-stream approximation from Toon et al. (1989). The GCM is capable of running in drag-free, uniform, or active drag mode (Rauscher & Menou, 2012, 2013). The uniform drag mode applies the same drag timescale globally[1], whereas the active drag mode has a local drag timescale τ_{mag} equal to

$$\tau_{\text{mag}}(B, \rho, T, \phi) = \frac{4\pi\rho\eta(\rho, T)}{|B^2 \sin\phi|}, \tag{6.3}$$

where B is the magnetic field strength, ϕ is the latitude, ρ is the density, T the temperature and η the magnetic resistivity (Beltz et al., 2022). The magnetic resistivity is computed following Menou (2012) as

$$\eta = 230\sqrt{T}/x_e \text{ cm}^2\text{s}^{-1}, \tag{6.4}$$

[1]In this case 10^4 s, following Beltz et al. (2022)

where x_e is the ionisation fraction calculated from the Saha equation. The active-drag mode is used and a magnetic field strength of $B = 20$ Gauss was assumed, appropriate given the mass of WASP-18 A b (Yadav & Thorngren, 2017).

The output from the GCM produces spatial maps of the P-T structures and winds. In each layer, the chemistry was assumed to be in local chemical equilibrium with a gas composition at solar elemental abundances. Opacities of OH, H_2O, and CO were included and their line list is the same as for the free 1D model. Using the two-stream approximation (Toon et al., 1989) the radiative transfer equation is solved following Zhang et al. (2017). The spectra are computed from the sum of the fluxes of the outer layers, taking into account the geometrical orientation of the exoplanetary disk at each observed orbital phase. This calculation can be done in Doppler-on and Doppler-off mode. The Doppler-on mode includes the effects of Doppler-shifted wavelengths due to the contribution of winds along the observed line of sight.

In total nine synthetic spectra were computed at equally spaced orbital phases ϕ between 0.323-0.697. These cover the pre-eclipse phase range of the Brogi et al. (2022) observations. To compute a synthetic spectrum at intermediate orbital phases, I linearly interpolate between the two spectra closest in the orbital phase. I use this to create half-phase ($\phi = 0.5$) synthetic spectra. These half-phase templates are computed, to investigate the effect of comparing a 3D simulated dataset with a phase-independent cross-correlation template. I do this for both the Doppler-on 3D GCM and the Doppler-off 3D GCM and for the models with respectively OH+H_2O+CO included, only OH, only H_2O, and only CO. The final result is eight synthetic half-phase spectra which are shown in Fig. 6.4.

The Doppler-on 3D GCM spectrum with all opacities included is dominated by water absorption lines. Some OH lines are visible towards shorter wavelengths and some CO lines are visible for the longer wavelengths. The difference between the Doppler-on and Doppler-off spectra is mainly an additional broadening term due to the projected rotational velocity of WASP-18 A b.

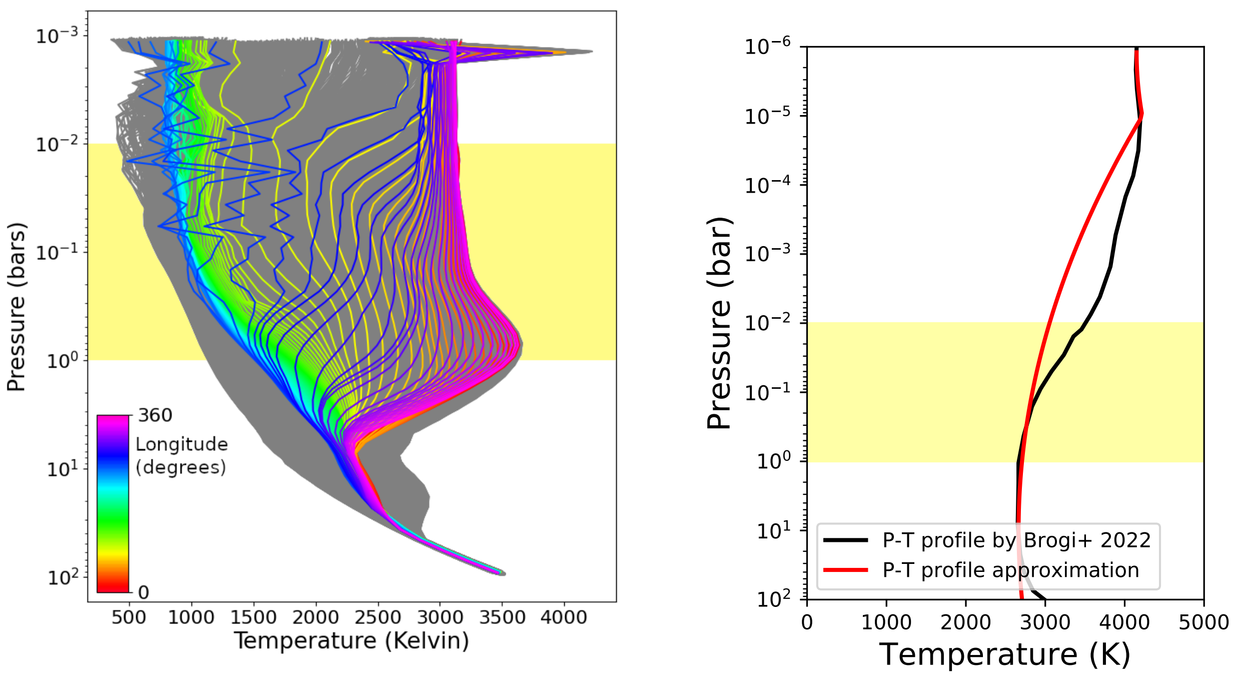

Figure 6.5: P-T profiles of the 1D model and 3D model of WASP-18 A b. The yellow shaded region in both plots indicates the estimated pressure range probed by the IGRINS observations from Brogi et al. (2022) between 0.01-1 bar. *Left panel:* P-T profiles of the 3D GCM model. The colours indicate longitude, seen from the substellar point at 0° increasing in eastward direction. *Right panel:* P-T profile inferred from pre-eclipse IGRINS data by Brogi et al. (2022) and the approximation used here using the parametrisation from Madhusudhan & Seager (2009).

6.2.3 Comparison between the 1D and 3D synthetic spectra

A striking difference between the free 1D model and the 3D GCM of WASP-18 A b is that the first shows emission lines, whereas the latter shows absorption lines. As shown in Fig. 6.5, this is a natural consequence of their different P-T structures.

The free 1D model assumes a parametrised inverted P-T structure, approximating the retrieved P-T structure by (Brogi et al., 2022). The inversion layer approximately covers pressures between $10^{-}5$ - 1 bar. Brogi et al. (2022) estimate the region where the HRS observations probe from the optical depth τ, as where the optical depth is equal to $\tau = 2/3$. This is at pressures of 0.01 - 1 bar. Thus the HRS observations are indeed sensitive to the region of the atmosphere where the inversion occurs, resulting in emission lines.

The 3D GCM also predicts inverted dayside P-T profiles. However, the GCM predicts an inversion layer at higher pressure levels in between 1 - 10 bar. These pressures are too deep into the atmosphere to be probed by the HRS observations. Instead, they cover the isothermal/slightly non-inverted regions of the P-T profile, resulting in muted absorption lines.

Another difference between the two models is that the free 1D model shows strong features for each of the three molecules included. However, the 3D GCM spectrum largely follows the H_2O spectrum with muted OH and CO lines. This is most likely again a consequence of the much shallower temperature gradient in the 3D GCM for those regions probed by the HRS observations.

Lastly, the 3D GCM includes a structure with much broader CO and OH features compared to the 1D model. This can be seen clearly in the zoomed panel of Fig. 6.4, where there are broad CO absorption features, that are not present in the all included model. In the 1D free model, all included spectrum and molecular templates are much more similar in the wavelength regions where the features overlap.

This is likely an artifact of how the 3D model's radiative transfer scheme computes spectra for single opacity sources. With only all opacity sources included, the atmosphere becomes optically thick at higher pressure layers, mainly set by the opacity of H_2O. However, when only a single opacity source is included, deeper regions of the atmosphere contribute to the synthetic spectrum. This may explain the broad and deep features in the only CO synthetic spectrum compared which are absent in the all included synthetic spectrum, as seen in the zoomed right panel of Fig. 6.4.

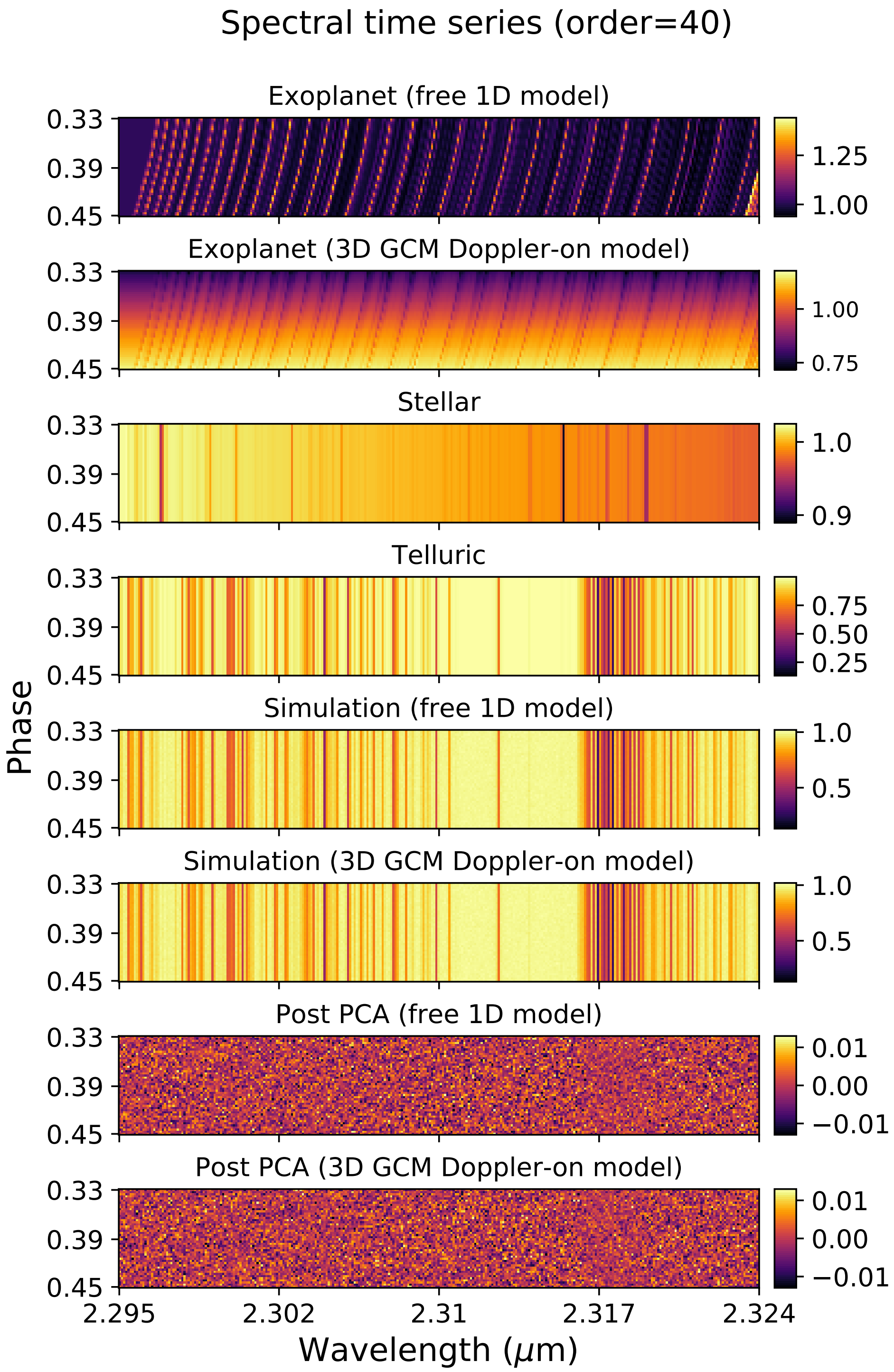

Figure 6.6: Simulated spectral time series of WASP-18 A b for the 40th IGRINS spectral order. The top panel shows the phase-independent free 1D model, shifted to the expected Doppler velocity. The second panel shows the same but for the phase-dependant 3D GCM Doppler-on model. The third panel shows the stationary stellar spectral time series. The fourth panel shows the telluric spectral time series. The fifth and sixth panels show the simulated data set for each of the models respectively. They are dominated by the telluric lines. The seventh and last panel show the simulated datasets after processing with PCA with five removed components. The colour bars in the top three panels were normalised with respect to the median value of the spectral time series. The colour bars of the other panels where normalised with respect to the telluric transmission spectrum continuum.

Parameter	Value
Phase coverage	0.326-0.452
Number of spectral channels	1848
Spectral resolution	45,000
Total number of frames	57
Continuum SNR	200
Total number of spectral orders	44
Wavelength range	1.45-2.45 μm

Table 6.3: Relevant observational parameters and conditions as reported by Brogi et al. (2022). These were used to simulate the HRS datasets.

6.3 Simulating the HRS datsets

To simulate the observations by Brogi et al. (2022) I use the observational parameters summarised in Table 6.3. I simulate 57 frames over a phase range from 0.326-0.452 for each of IGRINS 44 spectral orders covering wavelengths between 1.45-2.45 μm. Both the planet and stellar model are convolved to the instrumental resolution of IGRINS at $R = 45,000$ by convolution with a Gaussian kernel at the appropriate FWHM. The spectral time series for the exoplanet, stellar, and telluric components are shown in the top panels of Fig. 6.6.

For the 1D free model, I assume a phase-independent model, thus the same model is used at each orbital phase to simulate a spectral time series. For the 3D GCM, I assume a phase-dependant model, thus the model spectra are linearly interpolated at each orbital phase to simulate a spectral time series.

The exoplanet spectral time series is shifted to its expected Doppler velocity using equation 2.17. This assumes a circular orbit, which is a good approximation given the small eccentricity of WASP-18 A b's orbit of $e = 0.008$ (Nymeyer et al., 2011). The stellar spectrum $F_\star$ is a PHOENIX stellar spectrum template at the stellar effective temperature (T=6400 K) with Solar elemental abundances. I assume the stellar velocity around the system center of mass is negligible such that the stellar lines are stationary. These simulations are performed in the barycentric rest frame, thus the net barycentric velocity is zero at each orbital phase. Telluric spectrum T is simulated using the TELFIT code at a relative humidity $RH = 0.5$ and elevation angle $\theta = 45°$. The noiseless observed spectra are calculated using

$$F = \left(1 + \frac{F_{\mathrm{p,shifted}}}{F_\star}\frac{R_\mathrm{p}^2}{R_\star^2}\right) \times T. \quad (6.5)$$

White noise is added to each observed spectrum. The noise level N is computed from the continuum SNR reported by Brogi et al. (2022). First, F is normalised to the continuum, by fitting a polynomial to the brightest 200 pixels and division of this fit from each spectrum. I simulate noise using a Gaussian distribution with $\mu = 0$ and $\sigma = F_{\mathrm{normalised}}/SNR$. The noise is added to each spectrum in the simulated spectral time series.

The simulated data set is cleaned using PCA with five components. The final results are shown in the last two panels of Fig. 6.6.

6.4 Methods

6.4.1 Cross-correlation analysis

I compute CCF time series and SNR-maps similarly to how I computed those for WASP-33 b, as described earlier in Section 3.7.2. To estimate the errors on the velocity offsets from the 2D (v_{sys}, K_{p}) grid, I calculate the contour where the $\mathrm{SNR}_{\mathrm{max}}$ - SNR = 1. The velocity offsets and errors correspond with the center and outer bounds of this contour.

I do this for both the (i) free 1D model simulated dataset and (ii) the 3D Doppler-on GCM simulated dataset. I use the synthetic model spectra with all opacities included, only OH, only H_2O, and only CO respectively as cross-correlation templates. To avoid diluting the signal with orders where few lines are present, I only select certain orders for each of the three molecules: for only OH I select spectral orders with $\lambda_{\mathrm{min}} < 1.85\ \mu$m, for only H_2O, I select spectral orders with $1.70\ \mu\mathrm{m} < \lambda_{\mathrm{min}} < 2.30\ \mu$m, and for only CO I select spectral orders with $\lambda_{\mathrm{min}} > 2.30\ \mu$m. For the 3D GCM dataset, this is done with the Doppler-off cross-correlation templates, to ensure no velocity offsets are inherently present in the templates. Thus if velocity offsets are present in the simulated dataset, they should be offset in cross-correlation (v_{sys}, K_{p})-space when cross-correlated with the Doppler-off templates. I also compute a SNR map for cross-correlation of the dataset with the Doppler-on all-included case, to check if the injected model is retrieved.

6.4.2 The HRCCS retrieval

To understand how well HRCCS retrieval with a built-in 1D free model can infer constraints on a 'real' 3D exoplanet, as I first step I run the HRCCS retrieval by Line et al. (2021) on the free 1D model simulated dataset, similar to the methods used to characterise the water abundance of τ Böo A b, as has been described in Section 4.4.2.

Running the retrieval on the free 1D model simulated dataset is a basic test to ensure the retrieval code is working correctly. This is because the forward model to create the synthetic exoplanet spectrum is the same as the one used by within the HRCCS retrieval. The input parameters to create the simulated dataset should match the output parameters of the HRCCS retrieval on that simulated dataset. The prior ranges used in this retrieval are shown in Table 6.4 and the system parameters from Table 6.1.

Parameter	Symbol	Unit	Prior range	Result
OH abundance VMR	$\log \mathrm{OH}$	-	[-12, -1]	$-7.89^{+2.22}_{-2.17}$
H_2O abundance VMR	$\log \mathrm{H_2O}$	-	[-12, -1]	$-4.35^{+0.02}_{-0.02}$
CO abundance VMR	$\log \mathrm{CO}$	-	]-12, -1]	$-7.83^{+2.12}_{-2.02}$
Reference temperature	T_1	K	[3500, 4500]	3516^{+14}_{-9}
Reference pressure layer 1	$\log P_1$	bar	[-6, -4]	$-5.99^{+0.01}_{-0.01}$
Reference pressure layer 2	$\log P_2$	bar	[0, 2]	$0.50^{+0.10}_{-0.07}$
Reference pressure layer 3	$\log P_3$	bar	[1, 3]	$2.07^{+0.49}_{-0.53}$
Inversion gradient layer 1	α_1	-	[0.2, 0.4]	$0.24^{+0.03}_{-0.02}$
Inversion gradient layer 2	α_2	-	[0.2, 0.4]	$0.26^{+0.00}_{-0.00}$
System velocity offset	Δv_{sys}	km/s	[-20, 20]	$1.97^{+8.51}_{-10.11}$
Keplerian velocity offset	ΔK_{p}	km/s	[-20, 20]	$-6.21^{+11.53}_{-8.01}$
Scale parameter	$\log a$	-	[-1, 2]	$-0.99^{+0.01}_{-0.00}$
Phase offset	$d\phi$	-	[-0.01, 0.01]	$0.00^{+0.00}_{-0.00}$

Table 6.4: Prior ranges on the input parameters of the HRCCS retrieval on the 1D simulated HRS datasets of the WASP-18 A system. The results from the HRCCS retrieval are shown in the rightmost column. Expected values were listed in Table 6.4.

Template	SNR	Δv_{sys} (km/s)	ΔK_{p} (km/s)
1D free model simulated dataset			
OH + H_2O + CO	21.4	0.2±4.5	0.9±5.3
only OH	13.4	1.8±6.8	2.4±10.6
only H_2O	10.1	-1.0±7.6	3.5±11.6
only CO	12.5	-1.5±8.2	1.1±11.0
3D Doppler-on GCM simulated dataset			
OH + H_2O + CO (Doppler-on)	7.2	-2.4±10.0	-1.0±17.2
OH + H_2O + CO (Doppler-off)	7.3	-1.8±9.4	-1.6±17.5
only OH (Doppler-off)	Non-detection	-	-
only H_2O (Doppler-off)	6.2	-1.8±13.0	7.4±15.1
only CO (Doppler-off)	Non-detection	-	-

Table 6.5: Results from the cross-correlation analysis with the simulated WASP-18 A HRS datasets. The velocity offsets and errors correspond with the center and outer bounds of the contour where the SNR - $\mathrm{SNR_{max}}$ = 1.

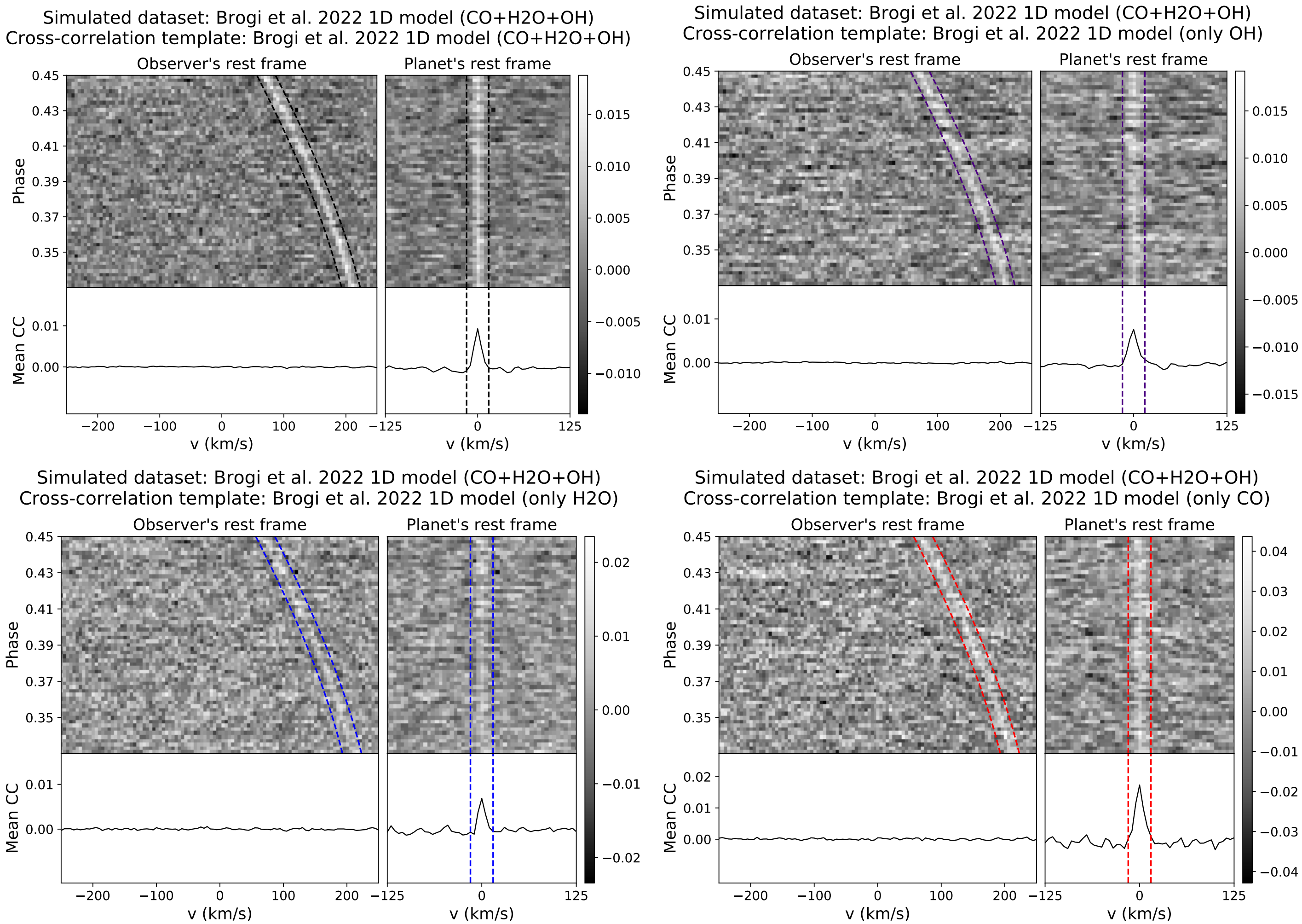

Figure 6.7: Cross-correlation trail plots for the simulated free 1D model WASP-18 A b dataset (similar to Fig. 3.13). The cross-correlation templates use the same 1D models with OH + H_2O + CO (top-left), only OH (top-right), only H_2O (bottom-left) and only CO (bottom-right). In each of the CCF time series, the planet trail is visible as a white trace of the observer's rest frame around the expected Doppler velocity of WASP-18 A b.

6.5 Results

6.5.1 Results from the cross-correlation analysis

The results for the 1D free model simulated dataset are summarised at the top of Table 6.5. The CCF time series are shown in Fig. 6.7. For all four cross-correlation templates, namely the OH+H_2O+CO case, the only OH case, only H_2O case, and only the CO case, the trail is visible around the expected exoplanetary Doppler velocity. The corresponding SNR maps in (v_{sys}, K_{p})-space are shown in Fig. 6.8. As expected, the velocities at the maximum SNR on the grid are close to WASP-18 A b's (v_{sys}, K_{p}) values. This is because no velocity offsets were introduced in simulating the free 1D model dataset and the cross-correlation template is the same as the injected model.

The results for the 3D Doppler-on GCM simulated dataset are summarised at the bottom of Table 6.5. The CCF time series for the Doppler-on 3D GCM simulated dataset cross-correlated with itself at half-phase ($\phi = 0.5$) is shown in Fig. 6.9. The exoplanet's trail is visible as a white trail around the expected (v_{sys}, K_{sys})-location. The corresponding SNR map is shown in Fig. 6.10 with a strong detection $SNR = 7.2$ around the expected (v_{sys}, K_{sys})-value.

The CCF time series for the 3D GCM Doppler-off half-phase (ϕ=0.5) OH+H_2O+CO case, the only OH case, only H_2O case and only CO case are shown in Fig. 6.11. The all included and H_2O only cases show a clear exoplanet trail around the expected Doppler velocity. However, no trails are visible for the OH and CO templates.

This is reflected by their corresponding SNR maps, which are shown in Fig. 6.12. The all included Doppler-off template has a strong detection at a SNR=7.3. This is slightly higher than the all included Doppler-on template. The broadened lines in the Doppler-on template may smear the trail across multiple velocity bins, diluting the signal when summed over a single pixel-wide trail. The H_2O Doppler-off model is detected at a SNR=6.2. CO is not detected, but interestingly the SNR map does show anti-correlation of SNR=-3.1 around the expected Doppler velocity. OH is not detected. From all three single molecular templates, the H_2O non-detection is closest to the all-included model (see Fig. 6.4), which most likely explains why this is the only molecule that has been detected in the simulated data set.

To visually compare the velocity offsets between the different templates, I plotted their contours around their maximum SNR all in the same Fig. 6.13. The water signal and all included cases are in agreement within 1σ. Since the templates with OH and CO were not detected, their velocity offsets are unconstrained.

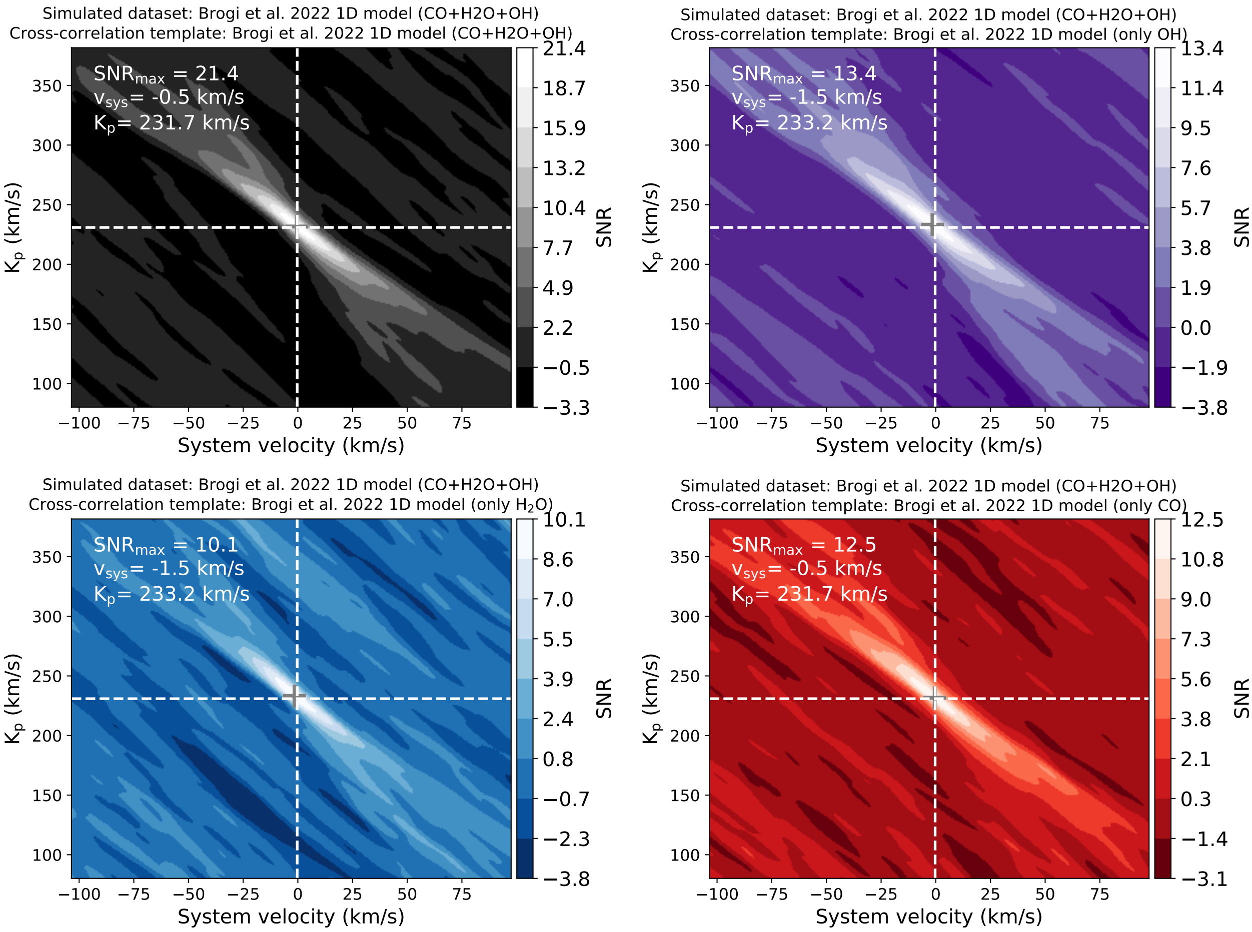

Figure 6.8: SNR maps computed for the simulated free 1D model WASP-18 A b dataset. The cross-correlation templates use the same 1D models with OH + H_2O + CO (top-left), only OH (top-right), only H_2O (bottom-left) and only CO (bottom-right). All show a strong detection (SNR>5) around the expected exoplanet velocity offset indicated by the white dashed grid. The gray plus symbol marks the SNR peak on the explored 2D grid, and the SNR value and velocities at this location are annotated on the left-top of each plot.

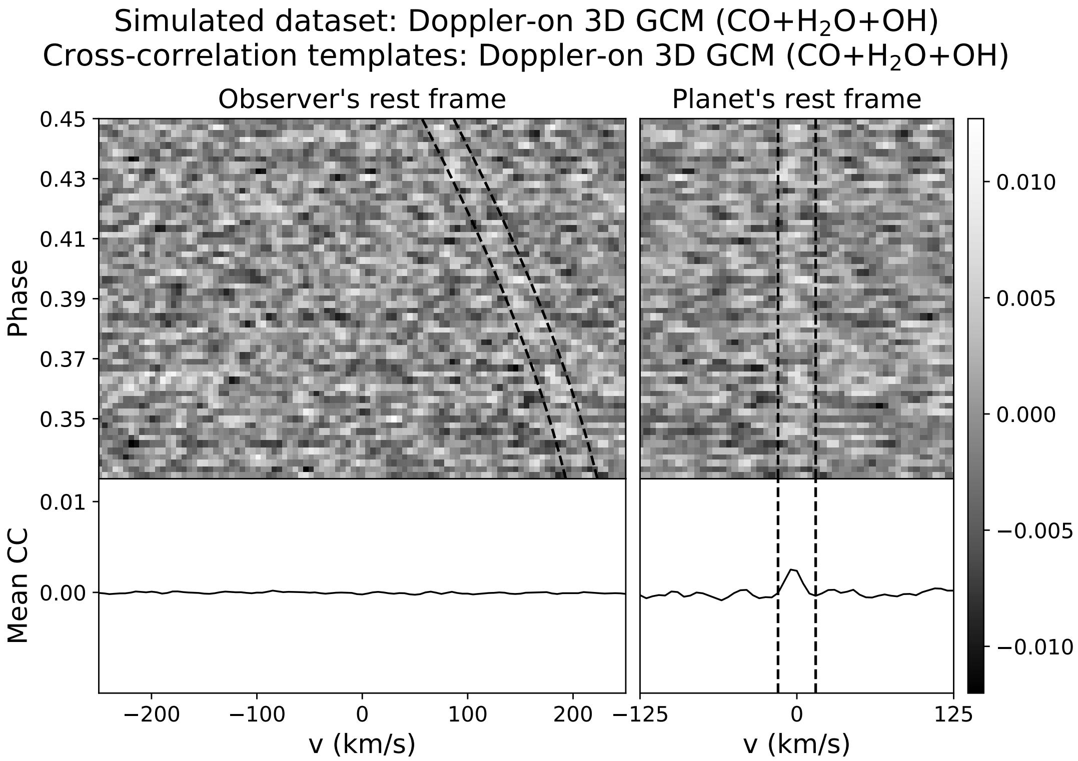

Figure 6.9: Cross-correlation time series for the simulated Doppler-on 3D GCM dataset of WASP-18 A b cross-correlated with itself at half-phase. The exoplanetary signal is visible as a faint white trail at the expected Doppler velocity, which is indicated by the black dashed lines.

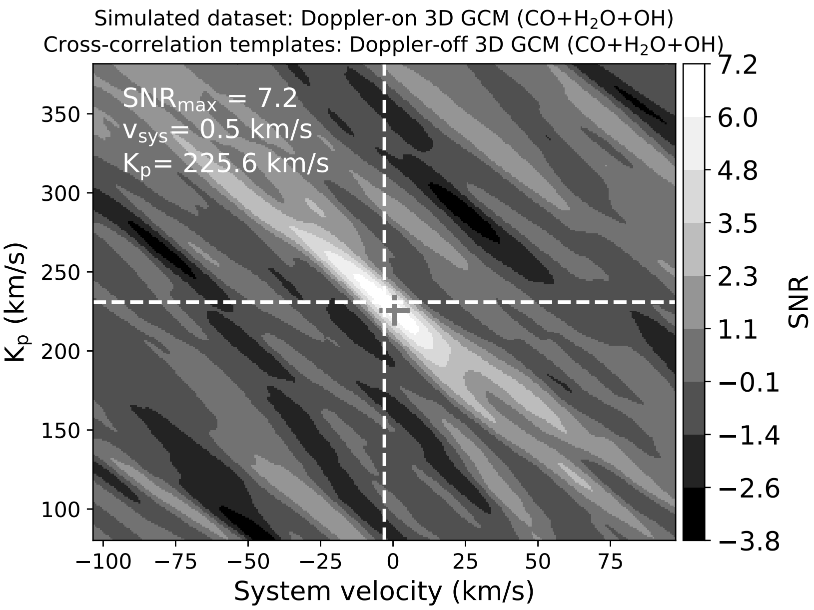

Figure 6.10: SNR map for the simulated Doppler-on 3D GCM dataset of WASP-18 A b cross-correlated with itself at half-phase. The gray plus symbol marks the SNR peak on the explored 2D grid, and the SNR value and velocities at this location are annotated on the left-top of each plot. It shows a strong detection expected location in velocity space at SNR=7.2.

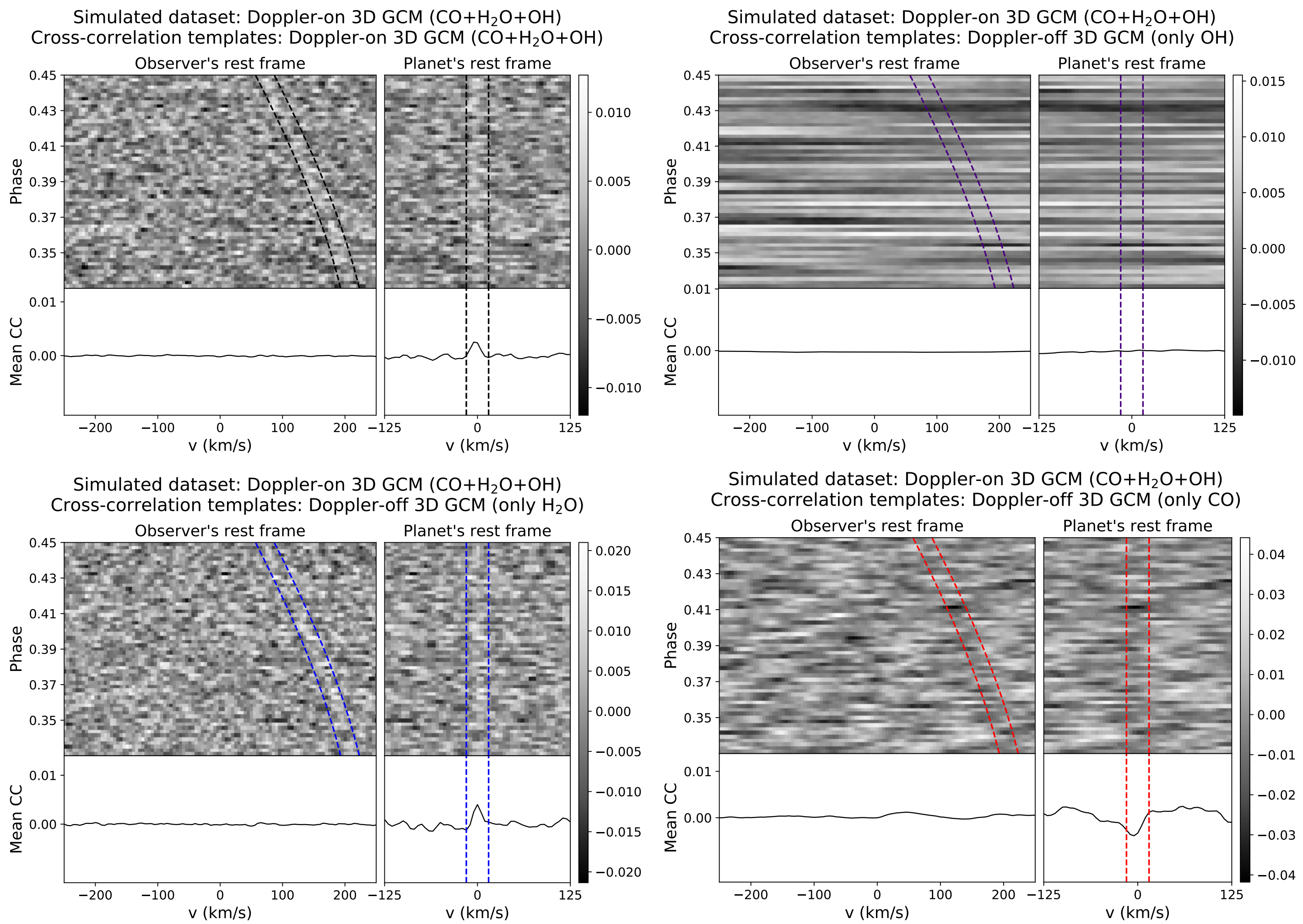

Figure 6.11: Cross-correlation trail plots for the simulated 3D Doppler-on GCM WASP-18 A b dataset (similar to Fig. 3.13). The cross-correlation templates are the 3D Doppler-off GCM WASP-18 A b models at half-phase. The models shown are OH + H_2O + CO (top-left), only OH (top-right), only H_2O (bottom-left), and only CO (bottom-right). In the all-included and H_2O CCF time series, the planet trail is visible as a white trace of the observer's rest frame around the expected Doppler velocity of WASP-18 A b. The CO CCF time series and OH CCF time series show a non-detection of the exoplanetary signal.

6.5.2 Results from the HRCCS retrieval

The results from the mock retrieval, running the HRCCS retrieval on the simulated 1D free model are shown in the rightmost column of Tab. 6.4. The posterior distributions are shown in Fig. 6.14, where the expected parameters are indicated by the dashed black lines. Only a few of the inferred parameters line up with the simulation's input parameters. Notably, the constraints on P_1 and $\log a$ are on the edge of their prior ranges, suggesting an incorrect scaling between the model and the simulated data. I will discuss this in more detail in the next section.

6.6 Discussion

6.6.1 Comparison of the SNRs with Brogi et al. 2022

The SNR values for the individual molecular detections in my free 1D model simulation are qualitatively similar to Brogi et al. (2022) but quantitatively different. Brogi et al. (2022) reported a SNR=6.0 for (OH+H_2O+CO), SNR=4.8 for OH, SNR=4.0 for CO and a SNR=3.3 for H_2O. Quantitively, the SNR detections from my simulation are much higher. This can be attributed to (i) the difference in synthetic model spectra used as cross-correlation templates and (ii) the idealised setup of the simulations. First, my forward models predict a larger continuum flux from the exoplanet compared to the one reported in Brogi et al. (2022). Therefore, the injected contrast ratio is higher, hence higher SNRs are expected. Second, the simulations only assume white noise, stationary telluric, and stellar lines, and do not include effects of correlated noise due to instrumental systematics. Qualitatively, the order from weakest to strongest detection SNR agrees with Brogi et al. (2022), as I find the strongest signal for the all-included cases, followed by OH, CO, and H_2O. This strong detection for OH is due to a combination of the IGRINS wavelength range covering a dense forest of strong OH lines and the relatively high OH abundance inferred by Brogi et al. (2022).

The SNR results from the 3D Doppler-on GCM dataset are quantitatively closer to values reported by Brogi et al. (2022), but differ qualitatively. Quantitatively, the overall lower SNR values are closer to those observed by Brogi et al. (2022). The overall weaker SNR values, especially compared to the free 1D model is likely can be attributed to the lower continuum flux of the 3D GCM spectra compared to the free 1D spectrum. This is due to the cooler temperatures predicted by the GCM at the pressure range probed by these HRS observations. Close to quadrature phases the 3D GCM produces even lower continuum flux values as more of the cooler night-side becomes visible. This is not accounted for in the free 1D model simulation. Qualitatively, I find the strongest SNR for the all-included cases, followed by H_2O and non-detections for CO and OH, which differs from the result from

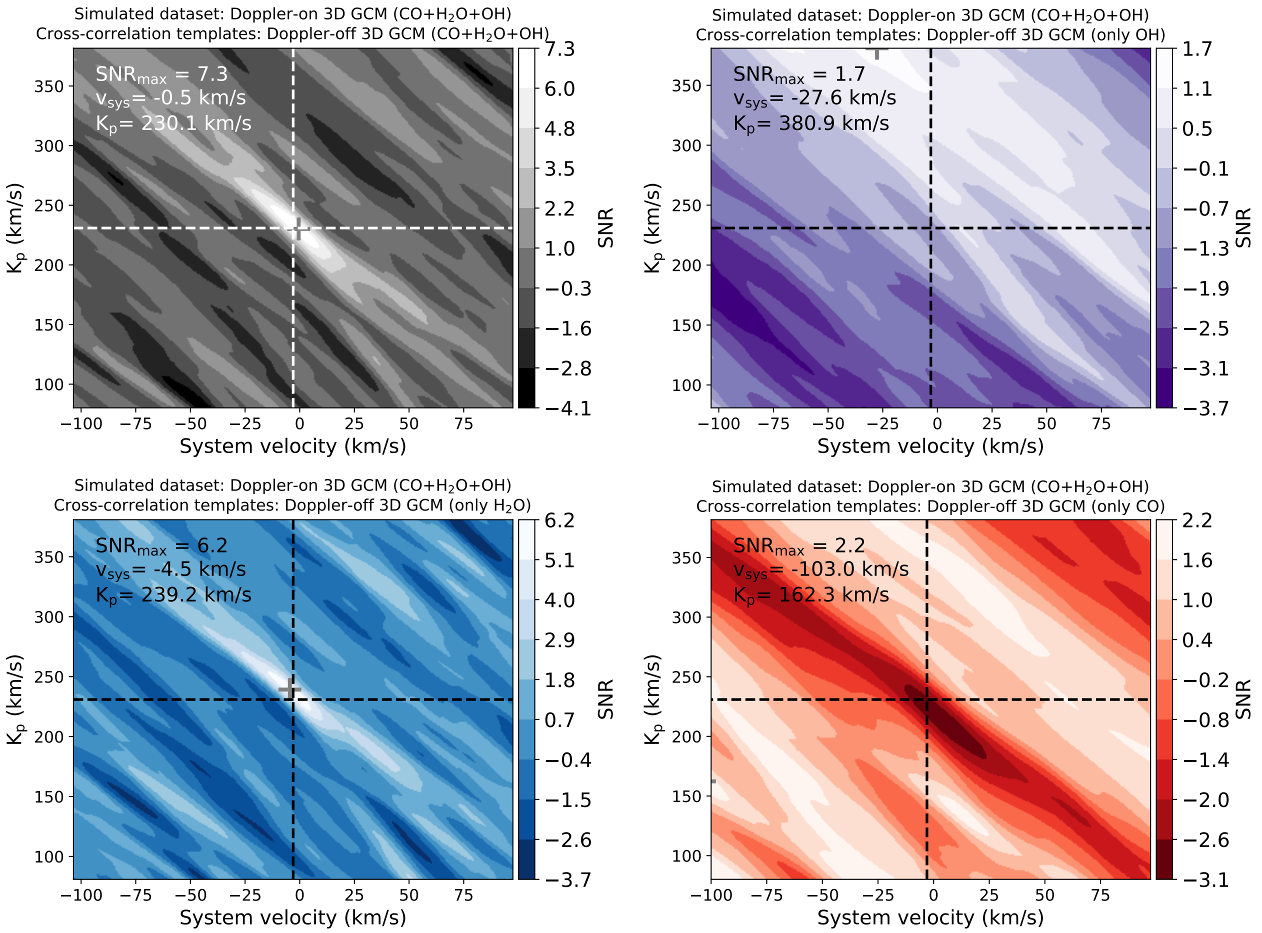

Figure 6.12: SNR maps computed for the simulated 3D Doppler-on GCM of WASP-18 A b dataset. The cross-correlation templates use the Doppler-off 3D GCM models at half-phase. The models shown are OH + H_2O + CO (top-left), only OH (top-right), only H_2O (bottom-left), and only CO (bottom-right). The all-included model and H_2O model show a detection (SNR>5) around the expected exoplanet velocity offset indicated by the white dashed grid. The OH and CO models show non-detections. The gray plus symbol marks the SNR peak on the explored 2D grid, and the SNR value and velocities at this location are annotated on the left-top of each plot.

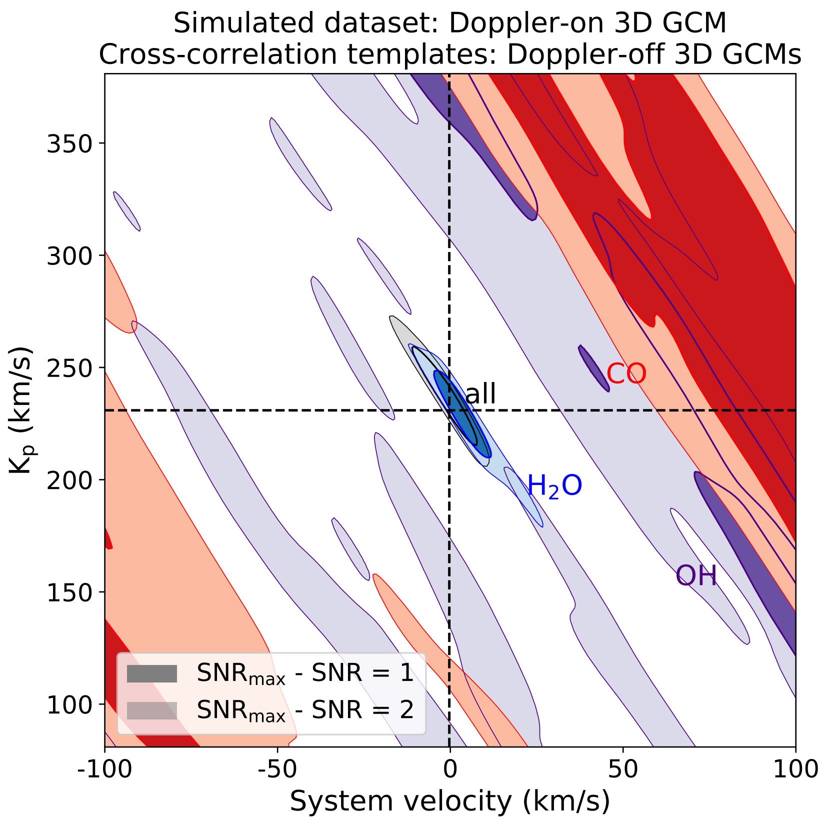

Figure 6.13: Velocity offsets observed in simulated Doppler-on 3D GCM of WASP-18 A b when cross-correlated with the Doppler-off 3D GCM models at half-phase. The models shown are: OH + H_2O + CO (all), only OH, only H_2O and only CO. Contours levels correspond to regions where the difference between the SNR and the maximum SNR are within 1σ and respectively 2σ.

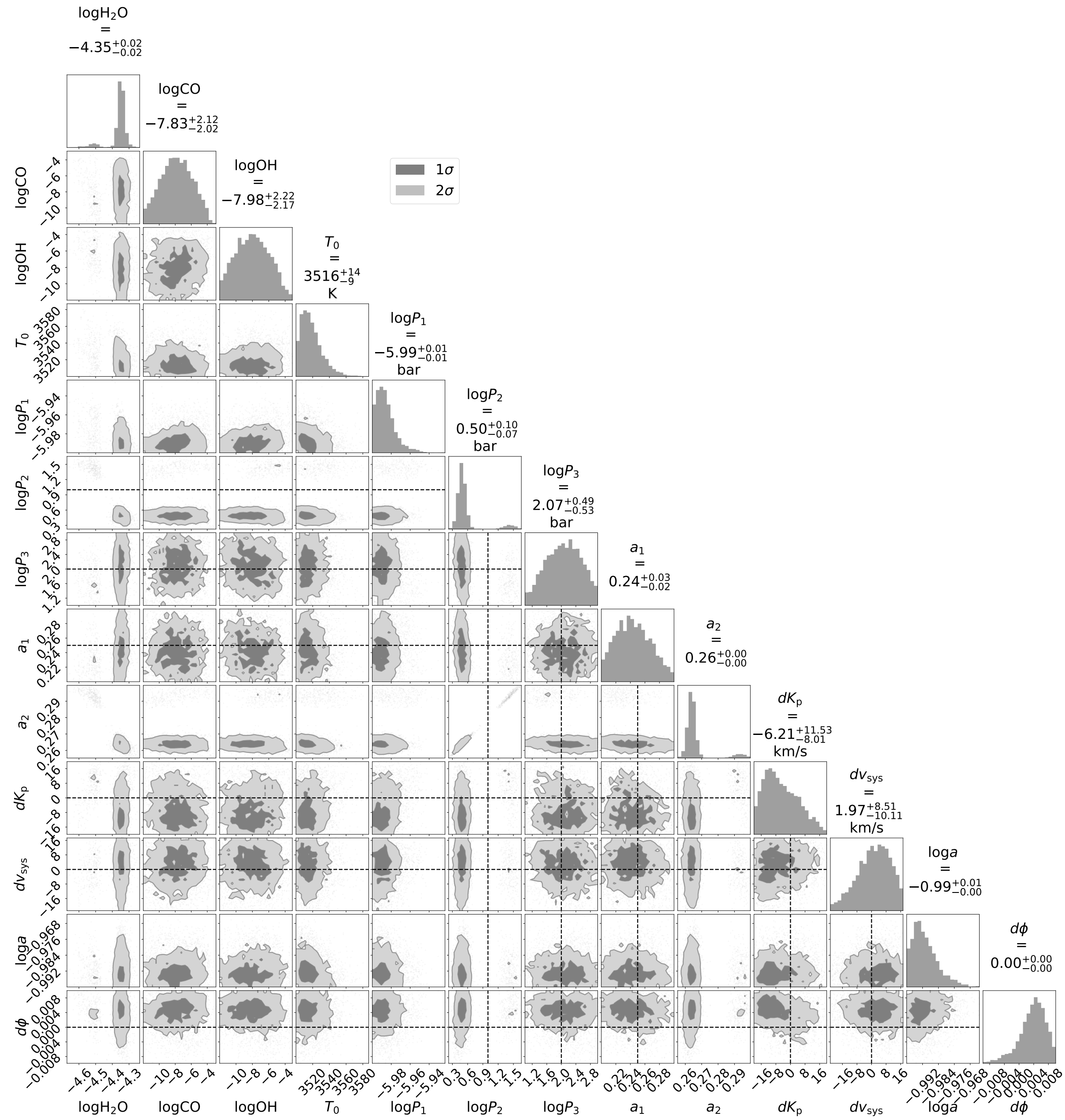

Figure 6.14: Overview of all posterior distributions and parameter constraints produced as output by the retrieval framework for the simulated free 1D WASP-18 A b dataset. Expected values are indicated by the dashed black lines.

Brogi et al. (2022). The strong detection for H_2O, but non-detections for CO and OH is likely due to the all-included spectrum and H_2O spectrum being the most similar and the OH and CO spectra being less similar.

Thus the differences between the 1D and 3D simulated datasets are for the most part due to the differences between the predicted synthetic spectra from a free 1D modelling code and a full 3D GCM. Most strikingly, the GCM predicts absorption lines whereas the 1D model predicts emission lines. The HRCCS retrieval analysis by Brogi et al. (2022) did include a P-T parametrisation which also allowed for non-inverted or isothermal structure. Thus assuming their inferred inverted P-T structure is correct, it hints that perhaps some physics is missing from my 3D GCM setup, which makes it predict non-inverted P-T profiles instead. This thus highlights the importance of understanding the differences between 1D and 3D modelling codes, especially in HRCCS, where are detections and results inherently depend on the model templates by cross-correlation.

6.6.2 Comparison of the velocity offsets with Brogi et al. 2022

A comparison between Fig. 6.2 and Fig. 6.13 shows my velocity offsets for the 3D GCM simulated dataset are qualitatively different from those observed by Brogi et al. (2022). The non-detections of OH and CO in my simulation mean their velocities are unconstrained and thus cannot be compared to those from Brogi et al. (2022). In my simulation, I find a slight positive difference in ΔK_{p} between the all-included and only H_2O models, but they agree within 1σ. They have a very similar Δv_{sys}, well within 1σ. However, Brogi et al. (2022) find a significant red-shifted water signal relative to the all-included case a slightly lower K_{p}. Thus my 3D GCM simulations do not reproduce the observed velocity offsets by Brogi et al. (2022).

To investigate the velocity offsets between the different molecules in the GCM, I cross-correlated each of the phase-dependant 3D GCM spectra with the half-phase 3D GCM Doppler-off spectrum. The results are shown in Fig. 6.15. For the spectra with all opacities included and only H_2O, there is no observed offset in the peak of the CCF as a function of orbital phase. Since the spectra themselves show no velocity offsets between the spectral lines, the observed similar location in (v_{sys}, K_{p}) location is also expected. On the contrary, the OH lines and CO lines do show a slight velocity offset as a function of orbital phase. This is in line with the previous result for a GCM of another UHJ by Beltz et al. (2022) where H_2O lines show a relative blue-shift compared to CO lines for pre-eclipse phases. However, since these molecules are not detected in the simulated dataset, I cannot compare if this translates into a (v_{sys}, K_{p}) for the simulated HRS observations.

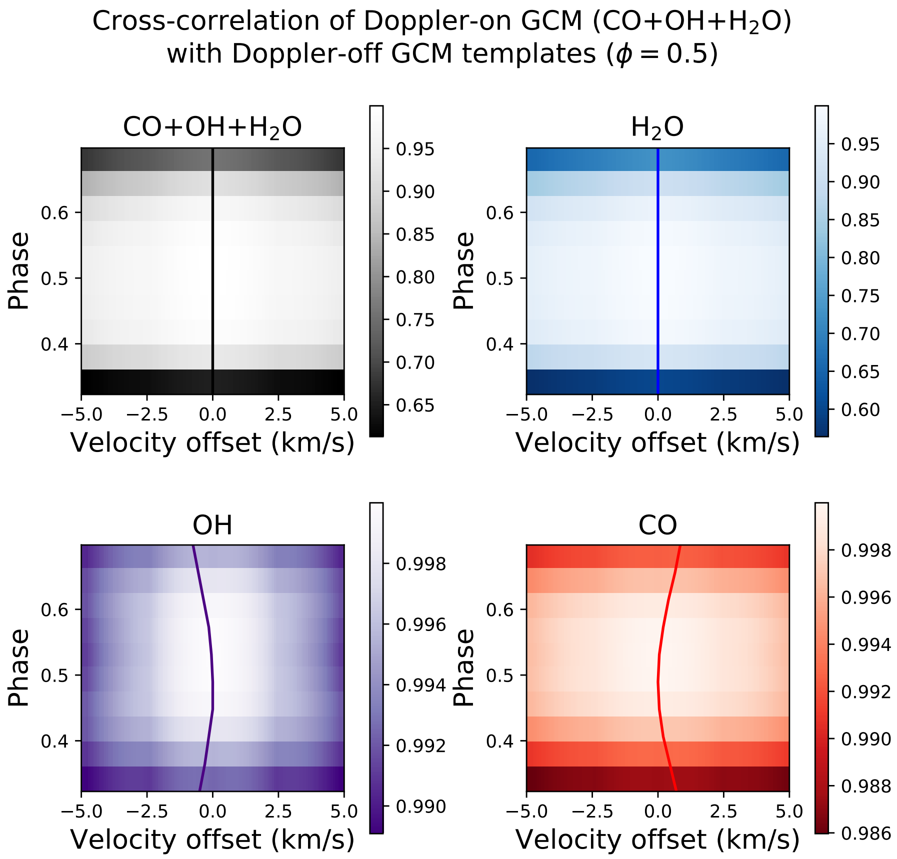

Figure 6.15: Cross-correlation of the 3D GCM Doppler-on model only with the Doppler-off model only at half-phase for all opacities included, and only OH, only H_2O and only CO included. The colours indicate the strength of the CCF at each orbital phase. The trail in each plot connects the maxima of each CCF in the orbital phase. The OH and CO templates show a net velocity offset at pre-eclipse and post-eclipse phases.

A possible explanation for the small velocity offsets in the Doppler-on model is the inclusion of magnetic drag in the GCM. This mainly impacts three things: (i) it reduces the hot spot offset in the GCM model, (ii) it changes the global circulation pattern from one dominated by an eastward jet to one dominated by day-to-night-side winds over the poles, and (iii) it affects the speed of the wind flow with altitude. First, as the local temperature affects the local chemistry, this possibly affects where on the disk the molecular lines form. Second, the wind flow over the poles produces winds with a smaller radial component in the direction of the observer. Third, if lines form at pressures where the wind flow is altered, this also affects their velocity offsets.

6.6.3 Results from the HRCCS mock retrieval

The first results from the mock retrieval are concerning as the input parameters to create the simulations are not inferred by the HRCCS retrieval. It is reassuring that the SNR-analysis shows strong detections of CO, H_2O, and OH at the expected exoplanet Doppler velocity, thus there is a sufficiently strong signal at the expected velocity in the simulated dataset from which the HRCCS retrieval should be able to constrain the model parameters. The fact that the cross-correlation analysis does work, suggests that perhaps there is incorrect scaling of the model in the simulated dataset. Correct scaling in HRS is often complex, due to the normalisation and telluric removal processing steps. Incorrect scaling of the model will still result in a strong cross-correlation signal due to the normalisation of the Pearson coefficient (see equation (2.11)). However, the retrieval is very sensitive to incorrect scaling of the data with respect to the model, leading to very different P-T parametrisation and chemical abundances. The inferred scale parameter of $\log a = -0.99^{+0.01}_{-0.00}$ at the edge of the prior range also hints towards an incorrect scaling of the simulated dataset. This highlights correct scaling is critical within a HRCCS framework.

Since the 3D GCM simulations did not show a significant velocity offset between the all-included case and H_2O case, this suggests HRCCS retrieval that includes a single (v_{sys}, K_{p}) used for all opacity sources is sufficient to constrain chemical abundances of this dataset. This is somewhat reassuring for current common setups for HRCCS retrievals, however, there are velocity offsets predicted for OH and CO as shown in Fig. 6.13. Thus when analysing a dataset with these opacity sources detected, a single (v_{sys}, K_{p}) might not be sufficient. Moreover, if the velocity offsets in the observations by Brogi et al. (2022) are real, it might still be necessary to introduce a molecule-dependant Δv_{sys}, and ΔK_{p} parameter in the HRCCS retrieval to correctly constrain abundances as their H_2O signal is offset from their all-included case. I also intend to run the HRCCS on the 3D GCM dataset.

The interpretation of such results is less straightforward, as the model used to generate the dataset is more complex than the forward model internal to the HRCCS retrieval. A 1D model might not be able to replicate the complexities of 3D P-T profiles and spatially distinct chemical profiles. For example, Beltz et al. (2021) found a 1D model resulted in an overall lower SNR compared to their 3D model for the HJ HD 209458 b. However, Beltz et al. (2021) did not compare the impact of a 1D model versus a 3D model on inferred parameters from a HRCCS retrieval. Running a HRCCS on simulations from a 3D GCM with known P-T profiles and chemical structures will therefore be a good test to evaluate the ability of a HRCCS with a fast 1D model to constrain atmospheric parameters of a 'real' 3D exoplanet. As part of van Sluijs et al. 2023b, in prep., I am currently investigating these results from the HRCCS retrieval and future ideas in more detail.

6.7 Conclusions

In this chapter, I explored the interplay of chemistry and dynamics in the atmosphere of an UHJ. I did this by investigating the climate of WASP-18 A b. In particular, Brogi et al. (2022) find molecule-dependant velocity offsets between CO, H_2O, and OH in the atmosphere of WASP-18 A b. I simulated a pre-eclipse HRS dataset with the same observing conditions. I showed I recovered these molecules using a 1D free model with the inferred chemical abundances and P-T structure by Brogi et al. (2022). However, similar simulations using a 3D GCM of WASP-18 A b are only sensitive to H_2O, and no molecule-dependant velocity offsets are found. The main conclusions are the following:

1. There is a striking difference between the inferred chemistry and structure inferred by Brogi et al. (2022) from their pre-eclipse observations of WASP-18 A b and those reproduced by the 3D GCM of WASP-18 A b. Brogi et al. (2022) inferred an inverted P-T profile with near-equal abundances of CO, OH and H_2O, whereas the 3D GCM predicts a non-inverted P-T profile with a water-dominated atmosphere. This highlights a need to understand the important physics that has to be included in realistic simulations of UHJs.

2. The inclusion of atmospheric dynamics in the 3D GCM does not reproduce the velocity offsets observed by Brogi et al. (2022). This is because the 3D GCM does not predict large Doppler shifts of spectral lines as a function of the orbital phase nor between the different molecular species. Possibly this can be explained by the active magnetic drag assumed in the GCM.

3. The non-retrieval of the model input parameters from the mock HRCCS retrieval, alongside the simultaneous strong detection in the cross-correlation analysis, highlights the need for careful normalisation in the processing and simulation of HRS datasets. The insignificant velocity offsets between the all-included case and the H_2O only case for different 3D GCM templates suggest HRCCS retrieval methods with the same (v_{sys}, K_{p})-value for H_2O and the exoplanet Doppler velocity is sufficient to correctly constrain its chemical abundance. That is at least in this dataset where only H_2O is detected, however, the phase-dependent velocity offsets of the OH and CO 3D GCM spectra suggest this may not be the case when constraining the abundances of these molecules.

7
Conclusions

"The mystery of life isn't a problem to solve, but a reality to experience. "
-Frank Herbert, Dune

7.1 Thesis summary

In this thesis, I explored how to characterise exoplanet atmospheres using HRCCS. Detailed characterisation of the atmospheres of these faraway worlds is crucial to understanding extreme atmospheric physics, planet formation pathways, climate and habitability on other worlds, and the possibility of extraterrestrial life. In the past decade, HRCCS has proven a powerful method to detect new species in the atmospheres of close-in giant exoplanets.

In **Chapter 2** I introduced the reader to HRCCS. This method uses HRS to resolve a unique spectral signature of species in the atmospheres. Spectra are calibrated against themselves in flux by means of continuum normalisation and telluric lines are removed using an algorithm such as SVD. This processed spectral time series is compared against a synthetic model spectrum. This synthetic model spectrum is the output of a forward modelling code. A hierarchy of levels of complexity exists, from free 1D models to free 1D self-consistent models to full 3D GCMs. The processed spectral time series and synthetic model spectrum are combined by means of cross-correlation, where a true exoplanetary signal maximises its SNR at its expected Doppler velocity. Bayesian frameworks are used to directly constrain model input parameters, such as P-T parametrisation and chemical abundances.

In **Chapter 3**, I introduced MEASURE, a survey with MMT/ARIES covering eleven exoplanets with a range of effective temperatures, stellar irradiance, orbital periods, masses, and radii. Characterisation of these individual worlds therefore enables comparative exoplanetology on a small population of worlds to test our theories of close-in giant exoplanet atmospheres. I successfully developed a pre- and post-processing pipeline for this survey. In the atmosphere of the UHJ WASP-33 b I reported the first detection of CO emission lines in an exoplanet atmosphere. This provides unambiguous evidence of a thermal inversion layer in this UHJ, in line with predictions from giant exoplanet models at these effective temperatures. It also demonstrates that HRCCS can be successfully used even at a spectral resolution of $R = 15,000$. This is potentially interesting for close-in terrestrial lava planets and UHJs, where spectral resolving power can be traded for photon collecting power.

In **Chapter 4**, I further explored the chemistry of WASP-33 b and two other exoplanets: the non-transiting HJ τ Boö A b observed with CRIRES/VLT and the non-transiting warm sub-Saturn HD 46375 b observed with MMT/ARIES. Despite, the non-detection of the atmospheres of τ Boö A b and HD 46375 b in their datasets, I demonstrate how injection-recovery test can be used to assess the constraining power of these observations. Moreover, I show that Bayesian frameworks are powerful structures to provide upper limits on chemical abundances even in the case of a non-detection. For a strong detection, such as CO emission lines in the atmosphere of WASP-33 b, I show Bayesian frameworks can constrain model input parameters, such as P-T parametrisation, heat-redistribution efficiency and metallicity.

In **Chapter 5**, I show that the scale parameter from the Brogi & Line (2019) CC-to-log(L) mapping is sensitive to the gradient of the P-T structure. The inclusion of a free phase-dependent scale parameter therefore has the potential to map spatial variation of the gradient of the P-T structure across the exoplanet's disk. I apply this novel idea to pre- and post-eclipse observations of WASP-33 b. A comparison of the scale parameter pre- and post-eclipse is consistent with an eastward hot spot offset scenario in the atmosphere of WASP-33 b. This also demonstrates for the first time that even at a spectral resolving power of $R = 15,000$ hot spot offsets can be constrained, despite being insensitive hot-spot-induced velocity offsets.

In **Chapter 6**, I investigate the observed velocity offsets of CO, H_2O and OH in the atmosphere of WASP-18 A b reported by Brogi et al. (2022). By simulating observations of WASP-18 A b using a 3D GCM, I show these offsets can be in part explained by the inherent 3D nature of its atmosphere. The retrieved velocity offsets highlight the importance of fitting abundances with at the correct $(v_{\text{sys}}, K_{\text{p}})$-location, which can differ from the Doppler velocity of the exoplanet itself. This has important implications for the design of HRCCS retrieval frameworks.

In conclusion, this thesis demonstrates that HRCCS combined with Bayesian frameworks are a powerful way to characterise both the chemistry and dynamics of exoplanet atmospheres. This was done for a range of exoplanets, thus paving the way towards comparative exoplanetology on a small population of worlds using HRCCS.

7.2 Ideas for future work

7.2.1 Analysing other MEASURE targets

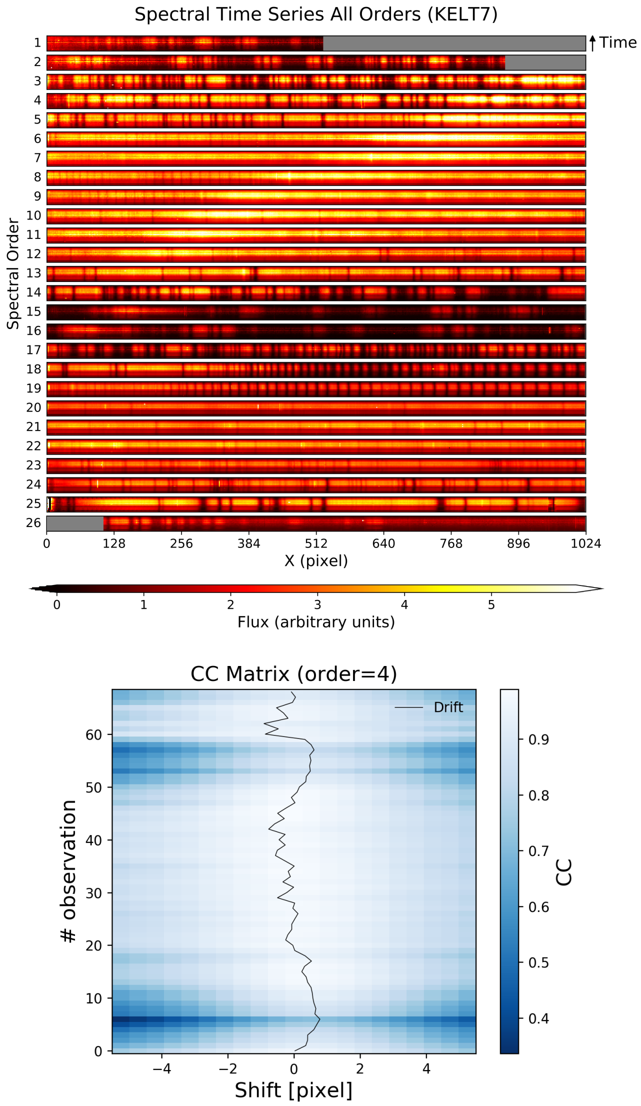

Figure 7.1: *Top panel:* Pre-processed spectral time series of KELT-7 b. Variability of the continuum is seen throughout all spectral orders. *Bottom panel:* a cross-correlation of the spectral time series of the fourth spectral order with the first observed spectrum. Misalignment on the order of a pixel is seen.

Alongside, the UHJ WASP-33 b and sub-Saturn HD 46375 b, nine more exoplanets have been observed as part of MEASURE. I will highlight the potential of future analysis of the MMT/ARIES dataset for three of these targets. Analysis of the datasets of the other seven targets will be challenging due to the short total observing time on their daysides (see Table 3.1), but may be worth pursuing depending on the result of checking the overall data quality after pre-processing the raw data. A good dataset should have a relatively stable alignment, small continuum variations, a high spectral resolving power, and a high continuum SNR.

KELT-7 b is a giant exoplanet at the transition region between HJs and UHJs (see Fig. 3.1). Therefore, investigation of whether the P-T structure is inverted or not can test theoretical predictions of at which temperature this transition occurs. Furthermore, its effective temperature is close to the dissociation temperature of H_2O. Therefore, constraints on the presence or chemical abundances of H_2O, OH, and H^- are of interest. Using HST/WFC Pluriel et al. (2020) found evidence for H_2O and H^- and observed no strong absorption feature. A recent study searched for absorption features of Hα, Li I, Na I, Mg I, and Ca II, but only provided upper limits (Tabernero et al., 2022).

A first look at the pre-processed MEASURE data for this target shows a large variation of the continuum and a large drift of the extracted spectra with respect to each other (see

Fig. 7.1). This is likely due to an open AO loop during part of the observing run. Nonetheless, novel ways to correct for this in the post-processing may prove beneficial to characterise the chemistry and dynamics of this exoplanet as a total of 15.5 observing hours on the dayside have been obtained (see Table 3.1).

HD 143105 b is another HJ, and as for KELT-7 b, this exoplanet is in the transition region between HJs and UHJs. A large amount of 21.5 hours is available on the dayside of this target. No previous studies on the characterisation of the atmosphere of this exoplanet exist.

τ Böo A b has also been observed with MMT/ARIES. In chapter 4 I reported the non-detection of water vapour in its atmosphere, which is likely due to a lack of constraining power of the one night of CRIRES/VLT observations. Adding the 16.5 hours of observed dayside with MMT/ARIES has the potential to improve constraints on the chemical abundance of water vapour in the atmosphere of this exoplanet. This remains a big job since due to the short exposure time on this target, there are a total of 2,504 high-resolution spectra to reduce and analyse.

7.2.2 The inclusion of 3D effects in HRCCS retrievals

To understand the interplay between chemistry and dynamics, the inclusion of 3D effects in HRCCS retrievals is crucial. The challenge is to design Bayesian frameworks at higher physical complexity, but yet sufficiently fast to compute. An example of this in this thesis is the inclusion of the scale parameter within a Bayesian framework and the binning of the dataset in the orbital phase.

One potential avenue for this is to characterise hot spot offsets in other HJ atmospheres using HRCCS by measuring line contrast variations as a function of the orbital phase. At sufficiently high spectral resolution, this can be combined with information from the velocity offsets. These results can be compared to the phase curve offsets observed from LRS. Thus HRCCS can potentially provide an independent way of measuring hot spot offsets and heat redistribution efficiency. I advocate for a study simulating exoplanets with different hot spot offsets to assess the feasibility of constraining hot spot offsets with HRS. Such a study can be compared against archival or new HRS observations.

Another way forward is to include a species-dependant additional velocity offset in $(v_{\mathrm{sys}}, K_{\mathrm{p}})$-space to account for spatial variations of the P-T structure and chemical abundances. I am continuing to explore this, building on the results presented in Chapter 6 (van Sluijs et al. 2023, in prep.). This work is important to better understand what biases are present in existing HRCCS retrievals and how they impact their ability to constrain the atmospheric abundances and the P-T structure.

7.2.3 Towards a unified theory of HJs

To establish a unified theory of hot Jupiters, we need to understand how their global circulation patterns, heat re-distribution efficiency, cloud decks, rotations, and chemistry change as a function of their effective temperatures and masses. The results of the exoplanet studies as part of this thesis work can be combined with other existing studies to form a small population of exoplanets. As highlighted throughout this thesis, such a sample is required to test our understanding of the extreme atmospheric physics in the atmospheres of close-in giants.

7.2.4 The JWST opportunity

Since we have entered the era of JWST, combining HRS with JWST spectra provides an unprecedented opportunity to combine LRS and HRS from the optical to the mid-infrared. However, there are some remaining challenges in how to best combine LRS and HRS data. Equation (2.33) assumes all LRS and HRS data points are independent and carry equal weight, but this is unlikely to be true for real data and needs further exploration. Conducting a study by simulating synthetic spectra of a benchmark exoplanet in low resolution for JWST and high resolution for a state-of-the-art ground-based HRS spectrograph (e.g. CRIRES+ or IGRINS) would be beneficial to test how to best combine LRS and HRS in an unbiased way. This has been done for HST and CRIRES by Brogi et al. (2017), but not specifically for JWST. Another challenge is to optimise observing strategy and processing for high-resolution spectra beyond $\lambda > 5$ μm from the ground, due to the thermal background. Successful HRS in this wavelength region is valuable if compared with the LRS coverage from JWST at those wavelengths to constrain hypothesized cloud emission features such as from SiO.

7.2.5 Preparing for the next generation of extremely large telescopes

The under-construction next generation of extremely large telescopes such as the ELT, GMT, and TMT will revolutionise the study of exoplanet atmospheres. The unprecedented photon-collecting power of the ELT will dramatically increase the SNR with HRS in the optical and infrared. For some of the benchmark HJs the ELT will enable resolving individual spectral lines at a $SNR_{\text{line}} > 1$ resulting in an unparalleled sensitivity to spectral line shape, depth, and position. A future project of interest is to simulate spectra for the ELT using a 3D GCM to assess the sensitivity of such observations to the 3D nature of exoplanet atmospheres. Moreover, our current line list from laboratory measurements or quantum mechanical computations might not be sufficiently accurate to be compared to the high SNR observations with extremely large telescopes. An investigation into whether our current line lists are sufficiently accurate or not, by simulating how current line list inaccuracies affect the constraining power of ELT data would be helpful to identify those line lists that require refinement.

The increased sensitivity can be used to push toward fainter and cooler targets. For gas giants at further orbital periods, where tidal synchronisation may not have happened, there is a need to understand how to characterise and map their inherent 3D chemistry and dynamics with an unknown rotational period. For even smaller worlds, Serindag & Snellen (2019) estimate an Earth-twin transiting a nearby M-dwarf can be detected in 20-50 transits with the ELT. There's also potential to combine HRS with high contrast imaging techniques to detect the reflected light from an Earth-sized planet around Proxima Centauri (e.g. Snellen et al., 2015).

Bibliography

Ahrer E., et al., 2023, MNRAS, 521, 5636

Allard F., Homeier D., Freytag B., 2011, in Johns-Krull C., Browning M. K., West A. A., eds, Astronomical Society of the Pacific Conference Series Vol. 448, 16th Cambridge Workshop on Cool Stars, Stellar Systems, and the Sun. p. 91 (`arXiv:1011.5405`)

Allart R., et al., 2023, arXiv e-prints, p. arXiv:2307.05580

Alonso R., et al., 2004, ApJ, 613, L153

Amundsen D. S., et al., 2016, A&A, 595, A36

Anderson E., Francis C., 2012, Astronomy Letters, 38, 331

Anglada-Escudé G., et al., 2016, Nature, 536, 437

Arcangeli J., et al., 2018, ApJ, 855, L30

Asplund M., et al., 2009, ARA&A, 47, 481

Azevedo Silva T., et al., 2022, A&A, 666, L10

Bakos G. Á., et al., 2007, ApJ, 656, 552

Baliunas S. L., et al., 1997, ApJ, 474, L119

Barber R., et al., 2006, MNRAS, 368, 1087

Barber R. J., et al., 2014, MNRAS, 437, 1828

Barge P., et al., 2008, A&A, 482, L17

Barman T. S., Hauschildt P. H., Allard F., 2001, ApJ, 556, 885

Barman T. S., et al., 2011, ApJ, 733, 65

Barnes R., et al., 2010, ApJ, 709, L95

Baxter C., et al., 2021, A&A, 648, A127

Bell T. J., et al., 2021a, MNRAS, 504, 3316

Bell T. J., et al., 2021b, MNRAS, 504, 3316

Bello-Arufe A., et al., 2022, AJ, 163, 96

Beltz H., et al., 2021, AJ, 161, 1

Beltz H., et al., 2022, AJ, 164, 140

Beltz H., et al., 2023, AJ, 165, 257

Ben-Yami M., et al., 2020, ApJ, 897, L5

Birkby J. L., 2018, arXiv e-prints, p. arXiv:1806.04617

Birkby J. L., et al., 2013, MNRAS, 436, L35

Birkby J. L., et al., 2017, AJ, 153, 138

Bonfanti A., Ortolani S., Nascimbeni V., 2016, A&A, 585, A5

Borsa F., et al., 2021a, Nature Astronomy, 6, 226

Borsa F., et al., 2021b, A&A, 645, A24

Borsa F., et al., 2021c, A&A, 653, A104

Borsa F., et al., 2022, A&A, 663, A141

Borsato N. W., et al., 2023, A&A, 673, A158

Borucki W. J., et al., 2009, Science, 325, 709

Borucki W. J., et al., 2010, Science, 327, 977

Bourrier V., et al., 2020, A&A, 635, A205

Brahm R., Jordán A., Espinoza N., 2017, PASP, 129, 034002

Brogi M., Line M. R., 2019, AJ, 157, 114

Brogi M., et al., 2012, Nature, 486, 502

Brogi M., et al., 2013, ApJ, 767, 27

Brogi M., et al., 2016, ApJ, 817, 106

Brogi M., et al., 2017, ApJ, 839, L2

Brogi M., et al., 2022, arXiv e-prints, p. arXiv:2209.15548

Buchner J., et al., 2014, A&A, 564, A125

Butler R. P., et al., 1997, ApJ, 474, L115

Butters O. W., et al., 2010, A&A, 520, L10

Buzard C., et al., 2020, AJ, 160, 1

Buzard C., et al., 2021a, arXiv e-prints, p. arXiv:2109.13275

Buzard C., et al., 2021b, AJ, 162, 26

Buzard C., et al., 2021c, AJ, 162, 269

Cabot S. H. C., et al., 2019, MNRAS, 482, 4422

Cabot S. H. C., et al., 2020, MNRAS, 494, 363

Cabot S. H. C., et al., 2021, AJ, 162, 218

Caffau E., et al., 2011, Sol. Phys., 268, 255

Casasayas-Barris N., et al., 2018, A&A, 616, A151

Casasayas-Barris N., et al., 2019, A&A, 628, A9

Casasayas-Barris N., et al., 2022, A&A, 664, A121

Cauley P. W., et al., 2019, AJ, 157, 69

Cauley P. W., et al., 2021, AJ, 161, 152

Chakrabarty A., Sengupta S., 2019, AJ, 158, 39

Charbonneau D., et al., 1999, ApJ, 522, L145

Charbonneau D., et al., 2002, ApJ, 568, 377

Charbonneau D., et al., 2005, ApJ, 626, 523

Chen J., Kipping D., 2017, ApJ, 834, 17

Chene A.-N., et al., 2014, in Navarro R., Cunningham C. R., Barto A. A., eds, SPIE Conference Series Vol. 9151, Advances in Optical and Mechanical Technologies for Telescopes and Instrumentation. p. 915147 (arXiv:1409.7448), doi:10.1117/12.2057417

Cheverall C. J., Madhusudhan N., Holmberg M., 2023, MNRAS, 522, 661

Chiavassa A., Brogi M., 2019, A&A, 631, A100

Cho J. Y. K., Polichtchouk I., Thrastarson H. T., 2015, MNRAS, 454, 3423

Coles P. A., Yurchenko S. N., Tennyson J., 2019, MNRAS, 490, 4638

Collier Cameron A., et al., 1999, Nature, 402, 751

Collier Cameron A., et al., 2010, MNRAS, 407, 507

Cont D., et al., 2021a, arXiv e-prints, p. arXiv:2105.10230

Cont D., et al., 2021b, arXiv e-prints, p. arXiv:2112.10461

Cont D., et al., 2022a, A&A, 657, L2

Cont D., et al., 2022b, A&A, 668, A53

Cortés-Zuleta P., et al., 2020a, A&A, 636, A98

Cortés-Zuleta P., et al., 2020b, A&A, 636, A98

Cosentino R., et al., 2012, in McLean I. S., Ramsay S. K., Takami H., eds, SPIE Conference Series Vol. 8446, Ground-based and Airborne Instrumentation for Astronomy IV. p. 84461V, doi:10.1117/12.925738

Cridland A. J., et al., 2019, A&A, 632, A63

Crossfield I. J. M., et al., 2022, ApJ, 937, L17

Csizmadia S., Hellard H., Smith A. M. S., 2019, A&A, 623, A45

Dang L., et al., 2018, Nature Astronomy, 2, 220

Deeg H. J., Alonso R., 2018, in Deeg H. J., Belmonte J. A., eds, , Handbook of Exoplanets. Springer International Publishing AG, p. 117, doi:10.1007/978-3-319-55333-7˙117

Deibert E. K., et al., 2023, arXiv e-prints, p. arXiv:2307.16738

Deming D., Knutson H. A., 2020, Nature Astronomy, 4, 453

Deming D., et al., 2012, ApJ, 754, 106

Donati J. F., et al., 2023, MNRAS, 525, 2015

Dressing C. D., Charbonneau D., 2015, ApJ, 807, 45

Ehrenreich D., et al., 2020, Nature, 580, 597

Eistrup C., Walsh C., van Dishoeck E. F., 2018, A&A, 613, A14

Von Essen C., et al., 2019, A&A, 622, A71

Von Essen C., et al., 2020, A&A, 639, A34

Evans T. M., et al., 2018, AJ, 156, 283

Fabrycky D., Tremaine S., 2007, ApJ, 669, 1298

Feinstein A. D., et al., 2023, Nature, 614, 670

Finnerty L., et al., 2023, AJ, 166, 31

Fischer D. A., Valenti J., 2005, ApJ, 622, 1102

Fischer D. A., et al., 2014, in Beuther H., et al., eds, Protostars and Planets VI. pp 715–737 (arXiv:1505.06869), doi:10.2458/azu˙uapress˙9780816531240-ch031

Fisher C., et al., 2020, AJ, 159, 192

Flagg L., et al., 2019, ApJ, 878, L37

Flagg L., et al., 2023, ApJ, 953, L19

Fontanive C., et al., 2019, MNRAS, 485, 4967

Fortney J. J., Dawson R. I., Komacek T. D., 2021, Journal of Geophysical Research (Planets), 126, e06629

Fulton B. J., et al., 2017, AJ, 154, 109

Gaia Collaboration et al., 2021, A&A, 649, A1

Gandhi S., Madhusudhan N., 2019, MNRAS, 485, 5817

Gandhi S., Brogi M., Webb R. K., 2020, MNRAS, 498, 194

Gandhi S., et al., 2022, MNRAS, 515, 749

Gandhi S., et al., 2023, AJ, 165, 242

Gao P., et al., 2021, Journal of Geophysical Research (Planets), 126, e06655

Gaulme P., et al., 2010, A&A, 518, L153

Gautschy A., Saio H., 1996, ARA&A, 34, 551

Giacobbe P., et al., 2021, Nature, 592, 205

Gibson N. P., et al., 2020, MNRAS, 493, 2215

Gibson N. P., et al., 2022, arXiv e-prints, p. arXiv:2201.04025

Gillon M., et al., 2017, Nature, 542, 456

Goorvitch D., 1994, The Astrophysical Journal Supplement Series, 95, 535

Gordon I. E., et al., 2022, J. Quant. Spec. Radiat. Transf., 277, 107949

Gray R. O., Napier M. G., Winkler L. I., 2001, AJ, 121, 2148

Grieves N., et al., 2018, MNRAS, 481, 3244

Grimm S. L., et al., 2021, ApJS, 253, 30

Guillot T., 2010, A&A, 520, A27

Guilluy G., et al., 2019, A&A, 625, A107

Gullikson K., Dodson-Robinson S., Kraus A., 2014, AJ, 148, 53

Hale A., 1994, AJ, 107, 306

Hammond M., Lewis N. T., 2021, Proceedings of the National Academy of Science, 118, e2022705118

Hara N. C., Ford E. B., 2023, Annual Review of Statistics and Its Application, 10, 623

Hargreaves R., et al., 2019, in EPSC-DPS Joint Meeting 2019. pp EPSC–DPS2019–919

Hargreaves R. J., et al., 2020, ApJS, 247, 55

Hauschildt P. H., Baron E., Allard F., 1997, ApJ, 483, 390

Hauschildt P. H., Allard F., Baron E., 1999, ApJ, 512, 377

Haynes K., et al., 2015, ApJ, 806, 146

Hellier C., et al., 2009, Nature, 460, 1098

Heng K., Frierson D. M. W., Phillipps P. J., 2011, MNRAS, 418, 2669

Henry G. W., 2000, ApJ, 536, L47

Herman M. K., et al., 2020, AJ, 160, 93

Herman M. K., et al., 2022, arXiv e-prints, p. arXiv:2203.11188

Herrero E., et al., 2011, A&A, 526, L10

Hindle A. W., Bushby P. J., Rogers T. M., 2019, ApJ, 872, L27

Hindle A. W., Bushby P. J., Rogers T. M., 2021, ApJ, 922, 176

Hoch K. K. W., et al., 2023, AJ, 166, 85

Hoeijmakers H. J., et al., 2018a, Nature, 560, 453

Hoeijmakers H. J., Snellen I. A. G., van Terwisga S. E., 2018b, A&A, 610, A47

Hoeijmakers H. J., et al., 2019, A&A, 627, A165

Hoeijmakers H. J., et al., 2020a, A&A, 641, A120

Hoeijmakers H. J., et al., 2020b, A&A, 641, A123

Hoeijmakers H. J., et al., 2022, arXiv e-prints, p. arXiv:2210.12847

Holmberg M., Madhusudhan N., 2022, AJ, 164, 79

Horne K., 1986, PASP, 98, 609

Jensen A. G., et al., 2018, AJ, 156, 154

Jiang Z., et al., 2023, AJ, 165, 230

John T. L., 1988, A&A, 193, 189

Johnson M. C., et al., 2015, ApJ, 810, L23

Justesen A. B., Albrecht S., 2019, A&A, 625, A59

Karman T., et al., 2019, Icarus, 328, 160

Kasper D., et al., 2023, AJ, 165, 7

Keating D., et al., 2020, AJ, 159, 225

Kesseli A. Y., et al., 2020, AJ, 160, 228

Kesseli A. Y., et al., 2022, AJ, 163, 107

Khorshid N., et al., 2022, A&A, 667, A147

Kilpatrick B. M., et al., 2017, AJ, 153, 22

Knutson H. A., et al., 2007, Nature, 447, 183

de Kok R. J., et al., 2013, A&A, 554, A82

de Kok R. J., et al., 2014a, A&A, 561, A150

de Kok R. J., et al., 2014b, A&A, 561, A150

Komacek T. D., Showman A. P., 2016, ApJ, 821, 16

Komacek T. D., Showman A. P., Tan X., 2017, ApJ, 835, 198

Kong H., Akakin H. C., Sarma S. E., 2013, IEEE Transactions on Cybernetics, 43, 1719

Kotani T., et al., 2018, in Evans C. J., Simard L., Takami H., eds, Society of Photo-Optical Instrumentation Engineers (SPIE) Conference Series Vol. 10702, Ground-based and Airborne Instrumentation for Astronomy VII. p. 1070211, doi:10.1117/12.2311836

Kozai Y., 1962, AJ, 67, 591

Kreidberg L., et al., 2018, AJ, 156, 17

Lavail A., et al., 2016, in 19th Cambridge Workshop on Cool Stars, Stellar Systems, and the Sun (CS19). Cambridge Workshop on Cool Stars, Stellar Systems, and the Sun. p. 48, doi:10.5281/zenodo.55729

Lee E. K. H., et al., 2021, arXiv e-prints, p. arXiv:2110.15640

Lee E. K. H., et al., 2022, ApJ, 929, 180

Leigh C., et al., 2003, MNRAS, 344, 1271

Levine S. E., et al., 2018, in Marshall H. K., Spyromilio J., eds, SPIE Conference Series Vol. 10700, Ground-based and Airborne Telescopes VII. p. 107004P, doi:10.1117/12.2312380

Li G., et al., 2015, The AJ Supplement Series, 216, 15

Li C., et al., 2020, Nature Astronomy, 4, 609

Lidov M. L., 1962, Planet. Space Sci., 9, 719

Line M. R., et al., 2021, Nature, 598, 580

Lockwood A. C., et al., 2014, ApJ, 783, L29

Lodders K., Fegley B., 2002, Icarus, 155, 393

Lord S. D., 1992, A new software tool for computing Earth's atmospheric transmission of near- and far-infrared radiation, NASA Technical Memorandum 103957

Lothringer J. D., Barman T., 2019, ApJ, 876, 69

Lothringer J. D., Barman T., Koskinen T., 2018, ApJ, 866, 27

Lothringer J. D., et al., 2020, arXiv e-prints, p. arXiv:2011.10626

Madhusudhan N., 2012, ApJ, 758, 36

Madhusudhan N., Seager S., 2009, ApJ, 707, 24

Madhusudhan N., Amin M. A., Kennedy G. M., 2014, ApJ, 794, L12

Maguire C., et al., 2023, MNRAS, 519, 1030

Mansfield M., et al., 2020, ApJ, 888, L15

Marcy G. W., Butler R. P., Vogt S. S., 2000, ApJ, 536, L43

Marsh T. R., 1989, PASP, 101, 1032

May E. M., et al., 2021, AJ, 162, 158

May E. M., et al., 2022, AJ, 163, 256

Mayor M., Queloz D., 1995, Nature, 378, 355

Mayor M., et al., 2003, The Messenger, 114, 20

Mazeh T., Tamuz O., Zucker S., 2007, in Afonso C., Weldrake D., Henning T., eds, Astronomical Society of the Pacific Conference Series Vol. 366, Transiting Extrapolar Planets Workshop. p. 119 (arXiv:astro-ph/0612418)

McCarthy D. W., et al., 1998, in Fowler A. M., ed., SPIE Conference Series Vol. 3354, Infrared Astronomical Instrumentation. pp 750–754, doi:10.1117/12.317340

McCullough P. R., et al., 2005, Publications of the Astronomical Society of the Pacific, 117, 783

McLean I. S., et al., 1998, in Fowler A. M., ed., SPIE Conference Series Vol. 3354, Infrared Astronomical Instrumentation. pp 566–578, doi:10.1117/12.317283

Meech A., et al., 2022, MNRAS, 512, 2604

Mendonça J. M., et al., 2018, AJ, 155, 150

Menou K., 2012, ApJ, 745, 138

Merritt S. R., et al., 2021, MNRAS, 506, 3853

Mikal-Evans T., et al., 2022, Nature Astronomy,

Mollière P., et al., 2019, A&A, 627, A67

Mollière P., et al., 2022, ApJ, 934, 74

Mounzer D., et al., 2022, A&A, 668, A1

Moutou C., et al., 2023, arXiv e-prints, p. arXiv:2307.11569

Mugrauer M., et al., 2006, Astronomische Nachrichten, 327, 321

Noguchi K., et al., 2002, PASJ, 54, 855

Nugroho S. K., et al., 2017, AJ, 154, 221

Nugroho S. K., et al., 2020a, MNRAS, 496, 504

Nugroho S. K., et al., 2020b, ApJ, 898, L31

Nugroho S. K., et al., 2021, ApJ, 910, L9

Nymeyer S., et al., 2011, ApJ, 742, 35

Öberg K. I., Murray-Clay R., Bergin E. A., 2011, ApJ, 743, L16

Park C., et al., 2014, in Ramsay S. K., McLean I. S., Takami H., eds, SPIE Conference Series Vol. 9147, Ground-based and Airborne Instrumentation for Astronomy V. p. 91471D, doi:10.1117/12.2056431

Parmentier V., et al., 2018, A&A, 617, A110

Parmentier V., Showman A. P., Fortney J. J., 2021, MNRAS, 501, 78

Pearson K. A., 2019, AJ, 158, 243

Pelletier S., et al., 2021, AJ, 162, 73

Pelletier S., et al., 2023, Nature, 619, 491

Pepe F. A., et al., 2010, in McLean I. S., Ramsay S. K., Takami H., eds, SPIE Conference Series Vol. 7735, Ground-based and Airborne Instrumentation for Astronomy III. p. 77350F, doi:10.1117/12.857122

Pepper J., et al., 2008, AJ, 135, 907

Perez-Becker D., Showman A. P., 2013, ApJ, 776, 134

Perna R., Heng K., Pont F., 2012, ApJ, 751, 59

Pino L., et al., 2022, arXiv e-prints, p. arXiv:2209.11735

Piskorz D., et al., 2016, ApJ, 832, 131

Piskorz D., et al., 2017a, AJ, 154, 78

Piskorz D., et al., 2017b, AJ, 154, 78

Piskunov N. E., et al., 1995, A&AS, 112, 525

Pluriel W., et al., 2020, AJ, 160, 112

Pollacco D. L., et al., 2006, PASP, 118, 1407

Polyansky O. L., et al., 2018, MNRAS, 480, 2597

Prinoth B., et al., 2022, Nature Astronomy, 6, 449

Queloz D., et al., 2000, A&A, 354, 99

Quirrenbach A., et al., 2018, in Evans C. J., Simard L., Takami H., eds, SPIE Conference Series Vol. 10702, Ground-based and Airborne Instrumentation for Astronomy VII. p. 107020W, doi:10.1117/12.2313689

Radica M., et al., 2023, MNRAS, 524, 835

Ramkumar S., et al., 2023, MNRAS, 525, 2985

Rasio F. A., et al., 1996, ApJ, 470, 1187

Rauscher E., Menou K., 2012, ApJ, 750, 96

Rauscher E., Menou K., 2013, ApJ, 764, 103

Rayner J., et al., 2016, in Evans C. J., Simard L., Takami H., eds, SPIE Conference Series Vol. 9908, Ground-based and Airborne Instrumentation for Astronomy VI. p. 990884, doi:10.1117/12.2232064

Ricker G. R., et al., 2014, in Space Telescopes and Instrumentation 2014: Optical, Infrared, and Millimeter Wave. p. 914320 (`arXiv:1406.0151`), doi:10.1117/12.2063489

Ridden-Harper A., et al., 2023, AJ, 165, 211

Rodler F., Kürster M., Henning T., 2010, A&A, 514, A23

Rodler F., Lopez-Morales M., Ribas I., 2012, ApJ, 753, L25

Rodler F., Kürster M., Barnes J. R., 2013, MNRAS, 432, 1980

Rojas-Ayala B., et al., 2012, ApJ, 748, 93

Roman M., Rauscher E., 2017, ApJ, 850, 17

Rothman L. S., et al., 2009, J. Quant. Spec. Radiat. Transf., 110, 533

Rothman L. S., et al., 2010, J. Quant. Spec. Radiat. Transf., 111, 2139

Rothman L. S., et al., 2013, J. Quant. Spec. Radiat. Transf., 130, 4

Saha S., 2023, ApJS, 268, 2

Sánchez-López A., et al., 2019, A&A, 630, A53

Sánchez-López A., et al., 2022, A&A, 661, A78

Scandariato G., et al., 2023, A&A, 674, A58

Schwartz J. C., et al., 2017, ApJ, 850, 154

Schwarz H., et al., 2016, A&A, 593, A74

Seager S., Deming D., 2010, ARA&A, 48, 631

Seidel J. V., et al., 2019, A&A, 623, A166

Seidel J. V., et al., 2020a, A&A, 641, L7

Seidel J. V., et al., 2020b, A&A, 643, A45

Seifahrt A., et al., 2018, in Evans C. J., Simard L., Takami H., eds, SPIE Conference Series Vol. 10702, Ground-based and Airborne Instrumentation for Astronomy VII. p. 107026D (arXiv:1805.09276), doi:10.1117/12.2312936

Serindag D. B., Snellen I. A. G., 2019, ApJ, 871, L7

Serindag D. B., et al., 2021, A&A, 645, A90

Showman A. P., Guillot T., 2002, A&A, 385, 166

Showman A. P., et al., 2008, ApJ, 685, 1324

Showman A. P., et al., 2009, ApJ, 699, 564

Showman A. P., Tan X., Parmentier V., 2020, Space Sci. Rev., 216, 139

Sing D. K., 2018, arXiv e-prints, p. arXiv:1804.07357

Sing D. K., et al., 2016, Nature, 529, 59

van Sluijs L., et al., 2019, A&A, 626, A97

van Sluijs L., et al., 2023, MNRAS, 522, 2145

Smette A., et al., 2015, A&A, 576, A77

Smith A. M. S., et al., 2011, MNRAS, 416, 2096

Snellen I. A. G., et al., 2010, Nature, 465, 1049

Snellen I. A. G., et al., 2014, Nature, 509, 63

Snellen I., et al., 2015, A&A, 576, A59

Soubiran C., et al., 2018, A&A, 616, A7

Southworth J., et al., 2009, ApJ, 707, 167

Spring E. F., et al., 2022, arXiv e-prints, p. arXiv:2201.03600

Stangret M., et al., 2020, A&A, 638, A26

Steiner M., et al., 2023, A&A, 672, A134

Stevenson K. B., et al., 2017, in AAS/Division for Planetary Sciences Meeting Abstracts #49. p. 408.05

Stone J. M., et al., 2014, ApJ, 792, 56

Suárez Mascareño A., et al., 2020, A&A, 639, A77

Tabernero H. M., et al., 2021, A&A, 646, A158

Tabernero H. M., et al., 2022, MNRAS, 515, 1247

Talens G. J. J., et al., 2017, A&A, 601, A11

Tamuz O., Mazeh T., Zucker S., 2005, MNRAS, 356, 1466

Tan X., Komacek T. D., 2019, ApJ, 886, 26

Taylor J., et al., 2023, MNRAS, 524, 817

Temple L. Y., et al., 2017, MNRAS, 471, 2743

Tennyson J., Yurchenko S., 2018, Atoms, 6, 26

Terrien R. C., et al., 2012, ApJ, 747, L38

Thibault S., et al., 2012, in McLean I. S., Ramsay S. K., Takami H., eds, SPIE Conference Series Vol. 8446, Ground-based and Airborne Instrumentation for Astronomy IV. p. 844630, doi:10.1117/12.926697

Toon O. B., et al., 1989, J. Geophys. Res., 94, 16287

Tsai S.-M., et al., 2021, ApJ, 923, 264

Turner J. D., et al., 2020, ApJ, 888, L13

Van Eylen V., et al., 2018, MNRAS, 479, 4786

Vogt S. S., 1987, PASP, 99, 1214

Vogt S. S., et al., 1994, in Crawford D. L., Craine E. R., eds, SPIE Conference Series Vol. 2198, Instrumentation in Astronomy VIII. p. 362, doi:10.1117/12.176725

Wall M. E., Rechtsteiner A., Rocha L. M., 2003, Singular Value Decomposition and Principal Component Analysis. Springer US, Boston, MA, pp 91–109, doi:10.1007/0-306-47815-3˙5, `https://doi.org/10.1007/0-306-47815-3_5`

Wang J., Ford E. B., 2011, MNRAS, 418, 1822

Wardenier J. P., et al., 2021, MNRAS, 506, 1258

Wardenier J. P., et al., 2023, arXiv e-prints, p. arXiv:2307.04931

Webb R. K., et al., 2022, MNRAS, 514, 4160

Wheatley P. J., et al., 2018, MNRAS, 475, 4476

Wilkins A. N., et al., 2017, ApJ, 836, L24

Wilks S. S., 1938, The Annals of Mathematical Statistics, 9, 60

Wolszczan A., Frail D. A., 1992, Nature, 355, 145

Wyttenbach A., et al., 2017, A&A, 602, A36

Yadav R. K., Thorngren D. P., 2017, ApJ, 849, L12

Yan F., Henning T., 2018, Nature Astronomy, 2, 714

Yan F., et al., 2019, A&A, 632, A69

Yan F., et al., 2020, A&A, 640, L5

Yan F., et al., 2021, A&A, 645, A22

Yan F., et al., 2022, A&A, 661, L6

Yan F., et al., 2023, arXiv e-prints, p. arXiv:2302.08736

Yurchenko S. N., et al., 2020, MNRAS, 496, 5282

Zhang J., Kempton E. M. R., Rauscher E., 2017, ApJ, 851, 84

Zhang M., et al., 2018, AJ, 155, 83

Zhang Y., et al., 2022a, A&A, 666, A47

Zhang Y., et al., 2022b, A&A, 666, A47

Zhang M., et al., 2023, AJ, 165, 62

Zieba S., et al., 2022, A&A, 664, A79

Zucker S., 2003, MNRAS, 342, 1291

Zucker S., Mazeh T., 1994, ApJ, 420, 806